

Andrea Di Cicco  
Gabriele Giuli  
Angela Trapananti *Editors*

# Synchrotron Radiation Science and Applications

Proceedings of the 2019 Meeting  
of the Italian Synchrotron Radiation  
Society—Dedicated to Carlo Lamberti

# **Springer Proceedings in Physics**

Volume 220

Indexed by Scopus

The series Springer Proceedings in Physics, founded in 1984, is devoted to timely reports of state-of-the-art developments in physics and related sciences. Typically based on material presented at conferences, workshops and similar scientific meetings, volumes published in this series will constitute a comprehensive up-to-date source of reference on a field or subfield of relevance in contemporary physics. Proposals must include the following:

- name, place and date of the scientific meeting
- a link to the committees (local organization, international advisors etc.)
- scientific description of the meeting
- list of invited/plenary speakers
- an estimate of the planned proceedings book parameters (number of pages/articles, requested number of bulk copies, submission deadline).

***Please contact:***

For Americas and Europe: Dr. Zachary Evenson; [zachary.evenson@springer.com](mailto:zachary.evenson@springer.com)  
For Asia, Australia and New Zealand: Dr. Loyola DSilva; [loyola.dsilva@springer.com](mailto:loyola.dsilva@springer.com)

More information about this series at <http://www.springer.com/series/361>

Andrea Di Cicco · Gabriele Giuli ·  
Angela Trapananti  
Editors

# Synchrotron Radiation Science and Applications

Proceedings of the 2019 Meeting  
of the Italian Synchrotron Radiation  
Society—Dedicated to Carlo Lamberti

 Springer

*Editors*

Andrea Di Cicco  
Physics Division  
School of Science and Technology  
University of Camerino  
Camerino, Macerata, Italy

Gabriele Giuli  
Geology Division  
School of Science and Technology  
University of Camerino  
Camerino, Macerata, Italy

Angela Trapananti  
Physics Division  
School of Science and Technology  
University of Camerino  
Camerino, Macerata, Italy

ISSN 0930-8989

ISSN 1867-4941 (electronic)

Springer Proceedings in Physics

ISBN 978-3-030-72004-9

ISBN 978-3-030-72005-6 (eBook)

<https://doi.org/10.1007/978-3-030-72005-6>

© Springer Nature Switzerland AG 2021

This work is subject to copyright. All rights are reserved by the Publisher, whether the whole or part of the material is concerned, specifically the rights of translation, reprinting, reuse of illustrations, recitation, broadcasting, reproduction on microfilms or in any other physical way, and transmission or information storage and retrieval, electronic adaptation, computer software, or by similar or dissimilar methodology now known or hereafter developed.

The use of general descriptive names, registered names, trademarks, service marks, etc. in this publication does not imply, even in the absence of a specific statement, that such names are exempt from the relevant protective laws and regulations and therefore free for general use.

The publisher, the authors and the editors are safe to assume that the advice and information in this book are believed to be true and accurate at the date of publication. Neither the publisher nor the authors or the editors give a warranty, expressed or implied, with respect to the material contained herein or for any errors or omissions that may have been made. The publisher remains neutral with regard to jurisdictional claims in published maps and institutional affiliations.

This Springer imprint is published by the registered company Springer Nature Switzerland AG  
The registered company address is: Gewerbestrasse 11, 6330 Cham, Switzerland

# Dedication

To Carlo Lamberti  
Our friend, our colleague

This book is dedicated to the memory of Carlo Lamberti. Carlo passed away unexpectedly February 1st, 2019, only 54 years old.

Carlo (Prof. Carlo Lamberti) studied physics at the University of Turin, Italy. From 1988 to 1993, he worked at the CSELT laboratories (at that time Telecom Italia, then Avago Technologies) in Turin (Italy) on the characterization of the interfaces of III-V semiconductor heterostructures with 4K photoluminescence, high-resolution x-ray diffraction and x-ray absorption spectroscopy. He obtained his Ph.D. in solid state physics from the University of Rome, Italy, in 1993. Since 2006, he had been professor of Physical Chemistry at the University of Turin. He has been also Full Professor of Solid-State Physics and Scientific Director of the Smart Materials Research Institute at the Southern Federal University in the framework of a Mega-Grant project financed by the Russian Federation Government.

He and his team performed more than 200 experiments approved by international committees at large scale facilities, mainly synchrotron radiation sources in Europe and USA. His research covered different fields in materials science, chemistry and physics. His scientific impact is impressive, resulting in more than 400 authored publications and a running Hirsch index  $h = 84$  in mid 2020.

Carlo was also a solid teacher. He trained a generation of young researchers and most of them are now recognized scientists in different countries, both in public and industrial research institutions. He will be well remembered both for his kindness and eclectic soul and for his deep expertise in Physics and Chemistry.

We, your SILS colleagues and friends, will really miss you, ciao Carlo! (Fig. 1).



**Fig. 1** Carlo Lamberti in several (funny and official) moments of his life

# Preface

## The Italian Synchrotron Radiation Society

These proceedings include several contributions presented at the 2019 meeting of the Italian Synchrotron Radiation Society (Società Italiana di Luce di Sincrotrone, SILS), held in Camerino (Italy), in September 2019.

The Italian Synchrotron Radiation Society is the independent and multidisciplinary scientific society which represents expert researchers and users of synchrotron radiation and free electron lasers since 1992. Members are active in all major scientific fields as follows: physics, materials science, chemistry, earth sciences, biology and medicine. SILS is linked to the European Synchrotron Users Organization (ESUO) and is involved in several activities related to coordination and promotion of science at advanced radiation sources. SILS activities include the organization of the annual meeting or conference and an appreciated biannual synchrotron radiation school. Moreover, awards are given to distinguished scientists usually in three categories: outstanding scientist, young scientist and best Ph.D. thesis in the field.

In particular, these proceedings refer to the SILS annual conference which is playing a role of reference for the Italian community of experts and users of synchrotron radiation. Taking place yearly at different host sites, the SILS meeting has become a traditional gathering of scientists and students working in this field presenting the most recent achievements obtained by using state-of-the-art synchrotron radiation techniques as well as emerging applications and developments of synchrotron and free electron laser sources.

## The SILS 2019 Conference

The 2019 edition of the SILS meeting ([www.unicam.it/sils2019](http://www.unicam.it/sils2019)) was held during 9–11 September 2019 at the Campus of the University of Camerino (see Fig. 2). The small town of Camerino in central Italy hosted the SILS meeting for the third time,



**Fig. 2** Group picture of the participants to the SILS 2019 meeting held in Camerino

and this edition was particularly significant, taking place three years after the earthquakes which devastated the city, its historic centre and several surrounding areas in 2016. As in recent SILS conferences, the rich scientific programme was organized in three plenary lectures, four thematic micro-symposia (“multi-techniques approach for in situ/operando studies”, “synchrotron-based characterization of surfaces and interfaces”, “photon-based multi-dimensional (2D/3D/4D) imaging from VUV to X-rays”, “advanced radiation sources: state-of-the-art and future applications”), each providing invited keynote talks and contributed oral presentations, as well as two open sessions, a poster session, one session dedicated to updates on the current status and developments of large-scale facilities of interest for the Italian scientific community and a special session dedicated to the memory of Carlo Lamberti, to whom this book is dedicated. Plenary talks focused on the following topics: investigation of diamonds and their mineral inclusions by X-ray diffraction, micro-fluorescence and micro-tomography (by F. Nestola), synchrotron-based microscopes for the study of ancient materials (by M. Cotte) and high-resolution resonant inelastic X-ray scattering for the study of correlated materials (by G. Ghiringhelli). Short plenary presentations were delivered by the winners of the SILS awards. Special emphasis was placed on contributions from young participants, with a special “Young Investigators” session including a keynote and ten short talks delivered by the early-stage researchers. The scientific programme was further enriched by the satellite workshop “Coherence of UV-SoftX beams, a contribution to its exploitation” (chaired by S. Nannarone and G. Stefani).

About 120 participants attended SILS 2019, with 70 delivered talks, including 14 speakers from foreign institutions. The SILS 2019 conference has been a lively occasion for the Italian synchrotron radiation community to share results and gather information on recent progress in synchrotron radiation techniques and applications. It is worth noticing that due to the prolonged COVID-19 pandemic emergency in 2020, the SILS 2021 conference to be held in Bologna was postponed to June 2021 (virtual meeting).



## Content of This Volume

Contributions included in this volume are related to some topics discussed at the conference and within the satellite workshop that can be grouped into three main categories: (i) coherence, (ii) instrumentation, methods and experimental techniques and (iii) applications of synchrotron radiation in physics, material science, chemistry and earth science.

The first two contributions by Margaritondo and Natoli describe some general features and consequences of the introduction of coherence in X-ray experiments. In particular, Margaritondo describes how coherence obtained by high-energy sources revolutioned X-ray science. Natoli describes some odd and interesting consequences of self-coherence phenomena in the photo-diffraction and photo-absorption processes.

The successive contributions are related to instrumental developments in X-ray facilities of interest for the Italian SILS community. Angelucci and co-workers briefly discuss the DAΦNE-light synchrotron light facility at the INFN-LNF Frascati National Laboratory, providing information about the recent scientific activity. Angelucci and Cimino report about current synchrotron radiation research activity aimed at studying properties of materials used in high performance circular colliders, with the aim of improving the performances of high-energy particle accelerators. Puri and co-workers describe the user facilities and experimental techniques available at the LISA CRG Italian beamline of the ESRF, highlighting the interesting opportunities for material science studies.

Other two contributions are related to advances in methods and techniques that may be of general interest. Martini and co-workers present an original method for the analysis of time-resolved XANES (X-ray absorption near-edge structure) spectra using a transformation matrix-based approach. Di Cicco and co-workers revisit the problem of measuring and evaluating the electron mean free path in solids possibly opening new possibilities for accurate estimates of the probing depths of X-ray techniques based on total fluorescence or total electron yield measurements.

The successive contributions are related to interesting applications of synchrotron radiation in different fields of research. Giorgetti and co-workers discuss the occurrence of multiple scattering in XAFS (X-ray absorption fine structure) data analysis and the use of multi-edge analysis for the study of battery materials. Polisi and co-workers study the high-pressure behaviour of hybrid composite materials constituted by azobenzene molecules embedded in one-dimensional nano-channels of porous materials. De Giudici and co-workers describe the Zn distribution and speciation in marine biominerals (namely the shells of bivalves and foraminifera) from polluted sites. Tavani and co-workers propose a new method for studying reaction intermediates by coupled XAFS and UV-Vis spectroscopy. Carlomagno and co-workers study the structural profile of a MgO/CoO/MgO trilayer using soft X-ray resonant magnetic reflectivity. Schiesaro and co-workers report the XAFS study of metal coordination core in Cu complexes. Campi discusses how the new advanced features of the latest generation synchrotron sources allowed to study structural fluctuations at the

nanoscale in the fields of material science (high-temperature superconductors) and biology (myeline ultrastructure). Rezvani and co-workers report about the structural and electronic properties of porous silicon nanowires measured by soft X-ray spectroscopy and Raman scattering at high pressures. Zambrano and co-workers discuss the use of synchrotron-based X-ray micro-tomography for characterizing the pore network with the aim of modelling fluid dynamics in porous carbonate rocks. Benzi and co-workers present an application of X-ray absorption spectroscopy to vanadium bearing Na-phosphate glasses, reporting about an integrated approach including V-O distances derived by XAFS, V oxidation states and coordination geometries derived from the pre-edge peak.

Camerino, Italy

Andrea Di Cicco  
Gabriele Giuli  
Angela Trapananti

# Acknowledgements

Finally, the editors of this volume must express their gratitude to all those organizations and individuals that helped make this conference a success and bring the project of this volume to fruition.

First of all, we are very grateful to the University of Camerino that supported the SILS 2019 conference. The technical, financial and communication services of this University provided a very valuable and efficient assistance both before and during the event and gave a fundamental contribution to the success of the conference. We would like to acknowledge our industry partners Malvern Panalytical, QuantumDesign, T.E.E.S (Technology Equipment & Engineering Solution), X-SPECTRUM and Vacuum FAB, which sponsored the program and specific awards and helped supporting the participation of a number of postgraduate students.

Many colleagues should also be thanked for their participation at different stages of this work including conference organization and proceedings realization. In this regard, we would like to thank the members of the entire local organizing and scientific committees and the organizers of the satellite workshop (G. Aquilanti, R. Arletti, E. Chiadroni, S. Colonna, P. D'Angelo, C. Giannini, S. Gross, R. Gunnella, C. Masciovecchio, M. Minicucci, S. Nannarone, E. Paris, G. Stefani, F. Stellato) as well as those contributing in different ways (F. Arzilli, F. Boscherini, M. De Crescenzi, S. De Panfilis, A. Filipponi, P. Ghigna, M. Giorgetti, C. Meneghini, Y. Mijiti, C. R. Natoli, L. Paolasini, S. Quartieri, S. Pascarelli, F. Rocca, S. J. Rezvani) to the success of this work.

# Contents

|          |  |           |
|----------|--|-----------|
| <b>1</b> | <b>Coherence: Elementary Introduction to a Quantum Revolution in X-Ray Science</b> .....   | <b>1</b>  |
|          | Giorgio Margaritondo   |           |
| <b>2</b> | <b>Some Odd Consequences of Self-coherence in the Photo-Diffraction and Photo-Absorption Processes</b> .....   | <b>17</b> |
|          | Calogero Renzo Natoli  |           |
| <b>3</b> | <b>DAΦNE-Light: The INFN-LNF Synchrotron Radiation Facility</b> .....  | <b>33</b> |
|          | Marco Angelucci, Antonella Balerna, Roberto Cimino, Mariangela Cestelli-Guidi, Antonio Grilli, Marco Pietropaoli, Agostino Raco, Vittorio Sciarra, Vinicio Tullio, and Giacomo Viviani |           |
| <b>4</b> | <b>Synchrotron Radiation Studies of Relevance to Accelerator R&amp;D</b> .....   | <b>45</b> |
|          | Marco Angelucci and Roberto Cimino   |           |
| <b>5</b> | <b>The LISA CRG Beamline at ESRF</b> .....   | <b>57</b> |
|          | Alessandro Puri, Giovanni Orazio Lepore, Riccardo Signorato, Paolo Scarbolo, Gianni Di Maio, and Francesco d'Acapito   |           |
| <b>6</b> | <b>Estimating a Set of Pure XANES Spectra from Multicomponent Chemical Mixtures Using a Transformation Matrix-Based Approach</b> .....   | <b>65</b> |
|          | Andrea Martini, Alexander A. Guda, Sergey A. Guda, Anastasiia Dulina, Francesco Tavani, Paola D'Angelo, Elisa Borfecchia, and Alexander V. Soldatov                                    |           |
| <b>7</b> | <b>Revisiting the Probing Depths of Soft X-ray Absorption Techniques by Constant Initial State Photoemission Experiments</b> .....   | <b>85</b> |
|          | Andrea Di Cicco, Seyed Javad Rezvani, and Stefano Nannarone  |           |

|           |   |     |
|-----------|---|-----|
| <b>8</b>  | <b>Multi-edge and Multiple Scattering EXAFS Analysis of Metal Hexacyanoferrates: Application in Battery Materials</b> .....   | 99  |
|           | Marco Giorgetti, Angelo Mullaliu, Jasper R. Plaisier, and Giuliana Aquilanti  |     |
| <b>9</b>  | <b>High Pressure Behavior of the Hybrid Material <math>\text{AlPO}_4\text{-5}</math>+Azobenzene: An In-situ Synchrotron X-ray Diffraction Study</b> .....   | 111 |
|           | Michelangelo Polisi, Fabio Malagutti, Linda Pastero, Giovanna Vezzalini, and Rossella Arletti   |     |
| <b>10</b> | <b>Zn Distribution and Chemical Speciation in Marine Biominerals: An Example on Bivalve and Foraminifera Shells from Polluted Sites</b> .....   | 125 |
|           | Giovanni De Giudici, Carlo Meneghini, Carla Buosi, Ilaria Carlomagno, Giuliana Aquilanti, Tohru Araki, Diana E. Bedolla, Maria Antonietta Casu, Antonietta Cherchi, Alessandra Gianoncelli, Antonella Iadecola, Andrei C. Kuncser, V. Adrian Maraloiu, Olivier Mathon, Valentina Rimondi, Pierpaolo Zuddas, and Daniela Medas |     |
| <b>11</b> | <b>Insights into the Structure of Reaction Intermediates Through Coupled X-ray Absorption/UV-Vis Spectroscopy</b> .....   | 141 |
|           | Francesco Tavani, Andrea Martini, Francesco Sessa, Giorgio Capocasa, Giorgio Olivo, Osvaldo Lanzalunga, Stefano Di Stefano, and Paola D'Angelo  |     |
| <b>12</b> | <b>Structural Profile of a MgO/Co/MgO Trilayer Using Soft X-ray Resonant Magnetic Reflectivity</b> .....  | 155 |
|           | Ilaria Carlomagno, Adriano Verna, Thomas Forrest, and Carlo Meneghini   |     |
| <b>13</b> | <b>Metal Coordination Core in Copper(II) Complexes Investigated by XAFS</b> .....   | 169 |
|           | Irene Schiesaro, Iole Venditti, Maura Pellei, Carlo Santini, Luca Bagnarelli, Giovanna Iucci, Chiara Battocchio, and Carlo Meneghini  |     |
| <b>14</b> | <b>Structural Fluctuations at Nanoscale in Complex Functional Materials</b> .....   | 181 |
|           | Gaetano Campi   |     |
| <b>15</b> | <b>Structural Properties of Porous Silicon Nanowires: A Combined Characterization by Advanced Spectroscopic Techniques</b> .....  | 191 |
|           | Seyed Javad Rezvani, Yimin Mijiti, Federico Galdenzi, Luca Boarino, Roberto Gunnella, Augusto Marcelli, Nicola Pinto, and Andrea Di Cicco   |     |

- 16 The Use of Synchrotron-Based X-ray Microtomography for the Pore Network Quantitative and Computational Fluid Dynamics Experiments on Porous Carbonate Rocks** ..... 203  
Miller Zambrano, Lucia Mancini, and Emanuele Tondi
- 17 V K-Edge XANES Full Multiple Scattering Study of V-Bearing Phosphate Glasses** ..... 219  
Federico Benzi, Eleonora Paris, Stefano Della Longa, Consuelo Mugoni, Cristina Siligardi, and Gabriele Giuli

# Contributors

**Marco Angelucci** INFN-Frascati National Laboratory, Frascati (RM), Italy

**Giuliana Aquilanti** Elettra-Sincrotrone Trieste, Basovizza, Trieste, Italy

**Tohru Araki** Diamond Light Source, Diamond House, Oxfordshire, Didcot, UK

**Rossella Arletti** Dipartimento di Scienze Chimiche e Geologiche, Università di Modena e Reggio Emilia, Modena, Italy

**Luca Bagnarelli** School of Science and Technology, Chemistry Division, University of Camerino, Camerino, MC, Italy

**Antonella Balerna** INFN-Frascati National Laboratory, Frascati (RM), Italy

**Chiara Battocchio** Department of Science, University Roma Tre, Rome, Italy

**Diana E. Bedolla** Elettra-Sincrotrone Trieste, Basovizza, Trieste, Italy

**Federico Benzi** School of Science and Technology-Geology Division, University of Camerino, Camerino, Italy

**Luca Boarino** Advanced Materials Metrology and Life Science Division, INRiM (Istituto Nazionale di Ricerca Metrologica), Turin, Italy

**Elisa Borfecchia** Department of Chemistry, INSTM Reference Center and NIS and CrisDi Interdepartmental Centers, University of Torino, Turin, Italy

**Carla Buosi** Department of Chemical and Geological Sciences, University of Cagliari, Cagliari, Italy

**Gaetano Campi** Institute of Crystallography CNR, Monterotondo Rome, Italy

**Giorgio Capocasa** Dipartimento di Chimica, Università di Roma La Sapienza, Roma, Italy;  
Istituto CNR di Metodologie Chimiche (IMC-CNR), Sezione Meccanismi di Reazione, Roma, Italy

**Ilaria Carlomagno** Elettra-Sincrotrone Trieste, Basovizza, Trieste, Italy

**Maria Antonietta Casu** Institute of Translational Pharmacology, Scientific and Technological Park of Sardinia POLARIS, UOS of Cagliari, National Research Council, Pula, Italy

**Mariangela Cestelli-Guidi** INFN-Frascati National Laboratory, Frascati (RM), Italy

**Antonietta Cherchi** Department of Chemical and Geological Sciences, University of Cagliari, Cagliari, Italy

**Roberto Cimino** INFN-Frascati National Laboratory, Frascati, RM, Italy

**Giovanni De Giudici** Department of Chemical and Geological Sciences, University of Cagliari, Cagliari, Italy

**Stefano Della Longa** Department of Life, Health and Environmental Science, University of L'Aquila, Coppito, AQ, Italy

**Andrea Di Cicco** Physics Division, School of Science and Technology, University of Camerino, Camerino, MC, Italy

**Gianni Di Maio** CAEN S.p.A., Viareggio, LU, Italy

**Stefano Di Stefano** Dipartimento di Chimica, Università di Roma La Sapienza, Roma, Italy;  
Istituto CNR di Metodologie Chimiche (IMC-CNR), Sezione Meccanismi di Reazione, Roma, Italy

**Anastasiia Dulina** Dipartimento di Chimica, Università di Roma "La Sapienza", Rome, Italy

**Francesco d'Acapito** CNR-IOM-OGG, Grenoble, France

**Paola D'Angelo** Dipartimento di Chimica, Università di Roma La Sapienza, Roma, Italy

**Thomas Forrest** Diamond Light Source, Didcot, UK

**Federico Galdenzi** INFN—Laboratori Nazionali di Frascati, Frascati, RM, Italy;  
University of Roma Tre, Rome, Italy

**Alessandra Gianoncelli** Elettra-Sincrotrone Trieste, Basovizza, Trieste, Italy

**Marco Giorgetti** Department of Industrial Chemistry, University of Bologna, Bologna, Italy

**Gabriele Giuli** School of Science and Technology-Geology Division, University of Camerino, Camerino, Italy

**Antonio Grilli** INFN-Frascati National Laboratory, Frascati (RM), Italy

**Alexander A. Guda** The Smart Materials Research Institute, Southern Federal University, Rostov-on-Don, Russia



**Sergey A. Guda** The Smart Materials Research Institute, Southern Federal University, Rostov-on-Don, Russia;  
Institute of Mathematics, Mechanics and Computer Science, Southern Federal University, Rostov-on-Don, Russia

**Roberto Gunnella** School of science and technology, Physics division, University of Camerino, Camerino, Italy

**Antonella Iadecola** RS2E, Réseau Français Sur Le Stockage Electrochimique de L'Energie, Amiens, France

**Giovanna Iucci** Department of Science, University Roma Tre, Rome, Italy

**Andrei C. Kuncser** Laboratory of Atomic Structures and Defects in Advanced Materials, National Institute of Materials Physics, Magurele, Romania

**Osvaldo Lanzalunga** Dipartimento di Chimica, Università di Roma La Sapienza, Roma, Italy;  
Istituto CNR di Metodologie Chimiche (IMC-CNR), Sezione Meccanismi di Reazione, Roma, Italy

**Giovanni Orazio Lepore** CNR-IOM-OGG, Grenoble, France;  
Dipartimento di Scienze della Terra, Università degli Studi di Firenze, Firenze, Italy

**Fabio Malagutti** Dipartimento di Scienze Chimiche e Geologiche, Università di Modena e Reggio Emilia, Modena, Italy

**Lucia Mancini** Elettra-Sincrotrone Trieste S.C.p.A, Basovizza, Trieste, Italy;  
LINXS—Lund Institute of Advanced Neutron and X-ray Science, Lund, Sweden

**V. Adrian Maraloiu** Laboratory of Atomic Structures and Defects in Advanced Materials, National Institute of Materials Physics, Magurele, Romania

**Augusto Marcelli** INFN—Laboratori Nazionali di Frascati, Frascati, RM, Italy;  
International Center for Material Science Superstripes, RICMASS, Rome, Italy;  
CNR - Istituto Struttura della Materia and Elettra-Sincrotrone Trieste, Basovizza Area Science Park, Trieste, Italy

**Giorgio Margaritondo** Faculté des Sciences de Base, Ecole Polytechnique Fédérale de Lausanne (EPFL), Lausanne, Switzerland

**Andrea Martini** Department of Chemistry, INSTM Reference Center and NIS and CrisDi Interdepartmental Centers, University of Torino, Turin, Italy;  
The Smart Materials Research Institute, Southern Federal University, Rostov-on-Don, Russia

**Olivier Mathon** The European Synchrotron Radiation Facility (ESRF), Grenoble, France

**Daniela Medas** Department of Chemical and Geological Sciences, University of Cagliari, Cagliari, Italy

- Carlo Meneghini** Department of Sciences, University of Roma Tre, Rome, Italy
- Yimin Mijiti** School of science and technology, Physics division, University of Camerino, Camerino, Italy
- Consuelo Mugoni** Department Engineering Enzo Ferrari, University of Modena and Reggio Emilia, Modena, Italy
- Angelo Mullaliu** Department of Industrial Chemistry, University of Bologna, Bologna, Italy
- Stefano Nannarone** Consiglio Nazionale delle Ricerche (CNR), CNR-IOM, Bazovizza, TS, Italy
- Calogero Renzo Natoli** INFN Laboratori Nazionali di Frascati, Frascati, Italy
- Giorgio Olivo** Dipartimento di Chimica, Università di Roma La Sapienza, Roma, Italy
- Eleonora Paris** School of Science and Technology-Geology Division, University of Camerino, Camerino, Italy
- Linda Pastero** Dipartimento di Scienze della Terra, Università di Torino, Torino, Italy
- Maura Pellei** School of Science and Technology, Chemistry Division, University of Camerino, Camerino, MC, Italy
- Marco Pietropaoli** INFN-Frascati National Laboratory, Frascati (RM), Italy
- Nicola Pinto** School of science and technology, Physics division, University of Camerino, Camerino, Italy
- Jasper R. Plaisier** Sincrotrone Elettra, Basovizza, TS, Italy
- Michelangelo Polisi** Dipartimento di Scienze Chimiche e Geologiche, Università di Modena e Reggio Emilia, Modena, Italy
- Alessandro Puri** CNR-IOM-OGG, Grenoble, France
- Agostino Raco** INFN-Frascati National Laboratory, Frascati (RM), Italy
- Seyed Javad Rezvani** School of science and technology, Physics division, University of Camerino, Camerino, Italy;  
Advanced Materials Metrology and Life Science Division, INRiM (Istituto Nazionale di Ricerca Metrologica), Turin, Italy;  
INFN—Laboratori Nazionali di Frascati, Frascati, RM, Italy
- Valentina Rimondi** Department of Earth Sciences, University of Florence, Florence, Italy;  
CNR—Institute of Geosciences and Earth Resources, Florence, Italy
- Carlo Santini** School of Science and Technology, Chemistry Division, University of Camerino, Camerino, MC, Italy

**Paolo Scarbolo** CAEN ELS s.r.l., Basovizza, Trieste, Italy

**Irene Schiesaro** Department of Science, University Roma Tre, Rome, Italy

**Vittorio Sciarra** INFN-Frascati National Laboratory, Frascati (RM), Italy

**Francesco Sessa** Dipartimento di Chimica, Università di Roma La Sapienza, Roma, Italy;

Department of Chemistry and Chemical Engineering, Chalmers University of Technology, Göteborg, Sweden

**Riccardo Signorato** S.R.I. Tech, Vigonza, Italy

**Cristina Siligardi** Department Engineering Enzo Ferrari, University of Modena and Reggio Emilia, Modena, Italy

**Alexander V. Soldatov** The Smart Materials Research Institute, Southern Federal University, Rostov-on-Don, Russia

**Francesco Tavani** Dipartimento di Chimica, Università di Roma “La Sapienza”, Rome, Italy

**Emanuele Tondi** School of Science and Technology - Geology Division, University of Camerino, Camerino, Italy

**Vinicio Tullio** INFN-Frascati National Laboratory, Frascati (RM), Italy

**Iole Venditti** Department of Science, University Roma Tre, Rome, Italy

**Adriano Verna** Dipartimento di Scienze, Università Roma Tre, Rome, Italy

**Giovanna Vezzalini** Dipartimento di Scienze Chimiche e Geologiche, Università di Modena e Reggio Emilia, Modena, Italy

**Giacomo Viviani** INFN-Frascati National Laboratory, Frascati (RM), Italy

**Miller Zambrano** School of Science and Technology - Geology Division, University of Camerino, Camerino, Italy

**Pierpaolo Zuddas** Sorbonne Universités, METIS, Paris, France

# Chapter 1

## Coherence: Elementary Introduction to a Quantum Revolution in X-Ray Science



Giorgio Margaritondo

**Abstract** For a long time after the discovery of x-rays in 1895, the experimentalists largely ignored their coherence—which was, anyway, very low. This situation changed after the advent of synchrotron sources [1]. Coherence-based X-ray techniques progressively became well established and very productive, in particular microradiology, microtomography. Coherence-based X-ray techniques progressively became well established and very productive, in particular microradiology, microtomography [2–4] and, in general, coherent scattering. A basic knowledge of coherence is thus desirable for all scientists interested in X-rays. We present here an introduction based on very simple arguments. After a classical-physics review of basic notions and parameters, we explore the links between coherence and quantum physics. Such links are becoming very interesting because of the realization of seeded X-ray free-electron lasers (X-FELs) that reach extreme levels of peak brightness and coherence [5]. Indeed, these new sources can facilitate the detection of higher-order quantum electrodynamics (QED) effects, potentially useful for novel experiments [6, 7].

### 1.1 Introductory Remarks

Coherence is a basic ingredient of optics experiments in the visible range and in other parts of the electromagnetic spectrum. However, it did not play a significant role in X-ray experiments until the arrival of synchrotron radiation [1]. In fact, the conditions for coherence are much more challenging for X-rays than for longer-wavelength radiation [1], and require special sources. Furthermore, before synchrotrons it was very difficult to obtain highly monochromatic X-rays, as needed for coherence in the longitudinal direction [2].

With synchrotron radiation, coherence gradually became a very useful tool for X-ray experimentalists [1–4]. Still, many of them do not sufficiently master its properties. At present, most X-ray users are not physicists, and the standard formal

---

G. Margaritondo (✉)

Faculté des Sciences de Base, Ecole Polytechnique Fédérale de Lausanne (EPFL), 1015 Lausanne, Switzerland

e-mail: [giorgio.margaritondo@epfl.ch](mailto:giorgio.margaritondo@epfl.ch)

© Springer Nature Switzerland AG 2021

A. Di Cicco et al. (eds.), *Synchrotron Radiation Science and Applications*,

Springer Proceedings in Physics 220, [https://doi.org/10.1007/978-3-030-72005-6\\_1](https://doi.org/10.1007/978-3-030-72005-6_1)

treatments of coherence may not be suitable for many of them. However, simple approaches are not easy to find. Here, we propose an elementary picture accessible by X-ray users from all disciplines.

We begin with an intuitive derivation of the basic notions about coherence using a classical description of pinhole diffraction. Then, we briefly discuss some examples to illustrate how coherence can be applied to X-ray imaging.

Finally, we analyze the links between coherence and quantum physics [6, 7], again in very simple terms. We specifically consider coherence in the context of QED, making an interesting discovery. Because of the very high coherence and peak brightness of the recently implemented seeded X-FELs, higher-order QED effects may cease to be irrelevant. And they could offer excellent opportunities for new types of experiments [6].

## 1.2 A Simple Classical Picture of Coherence

Coherence for electromagnetic radiation can be intuitively defined as “*the property that makes it possible to detect wave-like phenomena such as interference and diffraction*”. The difference between coherent and incoherent light can be seen in everyday life. We occasionally observe interference and diffraction effects, but they are unusual since most of the visible light sources do not possess enough coherence.

What makes electromagnetic radiation coherent, i.e., capable to produce wave-like phenomena? The answer can be based on anyone of such effects: here, our choice is pinhole diffraction (Fig. 1.1). The first finding is the existence of *two* kinds of coherence: *transverse* and *longitudinal* [1].

Consider Fig. 1.1a: a point source emitting a single wavelength  $\lambda$  does produce a visible (Airy) pinhole diffraction pattern, i.e., it is coherent. But this can change if the source emits a wavelength band of width  $\Delta\lambda$  (Figs. 1.1b and 1.2), and/or if its size is not infinitely small (Figs. 1.1c and 1.3). In such cases, the pattern may be washed out.

This is easy to understand from a qualitative point of view. First, consider a point source emitting a finite bandwidth  $\Delta\lambda$  (Fig. 1.2, top): each wavelength produces a different diffraction pattern, and in the superposition of patterns the features may be too blurred to be visible. Likewise, each point in an extended (non-laser) source (Fig. 1.3, top) produces a different pattern, and the pattern superposition may again be featureless. These facts illustrate the dual nature of coherence: the spectral bandwidth corresponds to longitudinal coherence and the source geometry to transverse coherence [8].

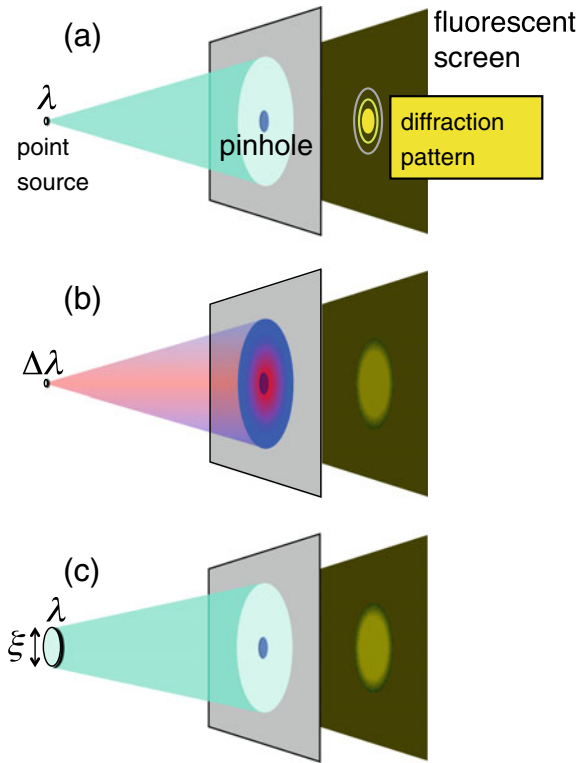


**Fig. 1.1** Diffraction by a circular pinhole reveals basic features of coherence. **a** A point source emitting only one wavelength is coherent and produces a visible (Airy) diffraction pattern. **b** When the point source is not monochromatic but emits a finite wavelength bandwidth  $\Delta\lambda$ , the pattern features may become too blurred to be visible: this leads to the notion of longitudinal (or time) coherence. **c** If a monochromatic source has a finite size, blurring may again result in a featureless pattern: this introduces the concept of transverse coherence

### 1.2.1 Longitudinal Coherence

Approximate quantitative conditions are also easy to derive for both aspects of coherence. We start with longitudinal coherence, considering again Fig. 1.2. The distance  $\eta$  between adjacent fringes on the detector is given by elementary optics:  $\eta \approx H\lambda/d$  ( $H$  and  $d$  are defined in the figure). The spread of wavelengths “blurs” this distance by  $\Delta\eta \approx H\Delta\lambda/d$ . When  $\Delta\eta$  is too big, i.e., if  $\Delta\eta > \eta$ , the blurring washes out the fringes. Hence, the condition for longitudinal coherence is  $H\Delta\lambda/d < H\lambda/d$ , or:

$$\Delta\lambda/\lambda < 1. \tag{1.1}$$

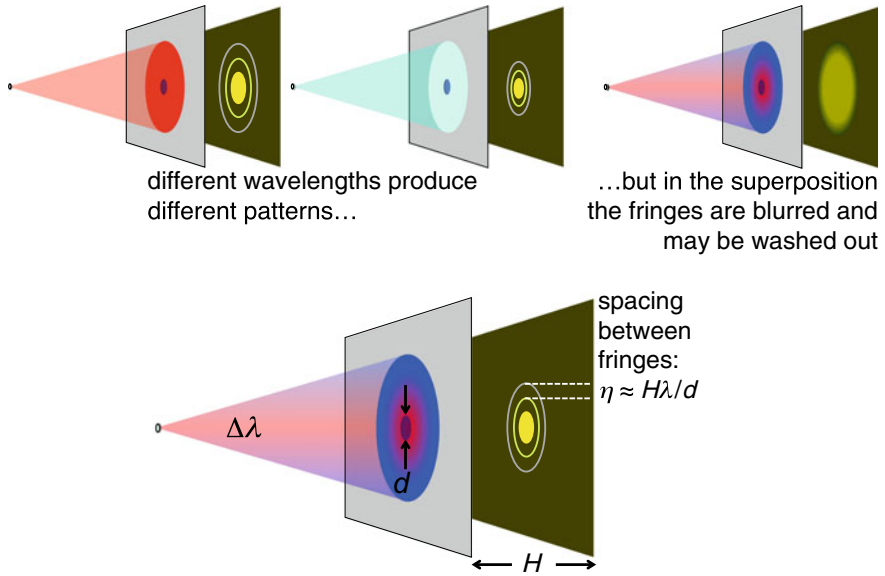


**Fig. 1.2** Longitudinal coherence. Top: if a point source emits different wavelengths, in the superposition of the corresponding diffraction patterns the fringes are blurred and may not be visible. Bottom: the pinhole size  $d$  and the pinhole-detector distance  $H$  used to derive Eq. 1.1

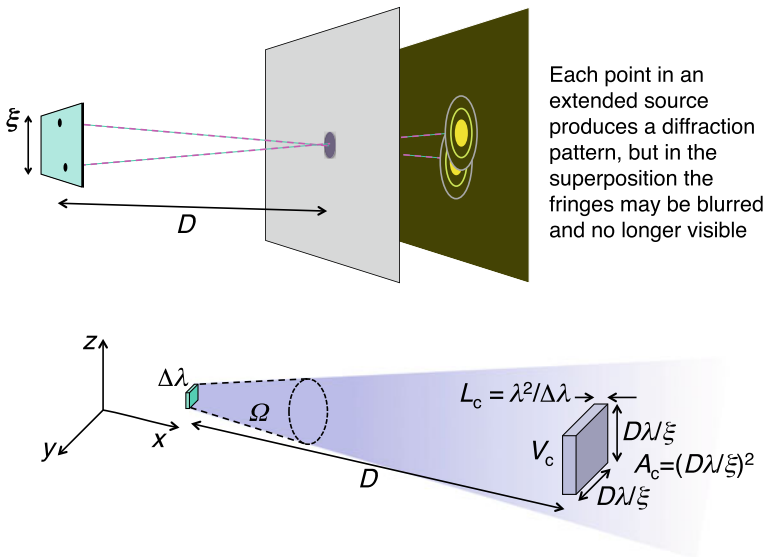


**Fig. 1.3** Transverse coherence of an extended (non-laser) source. Top: the superposition of patterns produced by different source points blurs the diffraction fringes. Bottom: the solid angle of emission  $\Omega$ , the coherence length  $L_c$ , the coherence area  $A_c$  and the coherence volume  $V_c$

Equation 1.1 is not a stringent condition: this is why we sometime see interference effects around us. In fact, our eyes filter the visible wavelengths and fulfill this requirement—so that we can enjoy, for example, the rainbow colors of soap bubbles.

The above condition can be also expressed in terms of the “coherence length”:

$$L_c = \lambda^2 / \Delta\lambda, \quad (1.2)$$

which transforms Eq. 1.1 into:

$$L_c < \lambda. \quad (1.3)$$

In general terms, if the wavelength bandwidth decreases, the coherence length increases and so does the level of longitudinal coherence.

### 1.2.2 Transverse Coherence, Coherence Area and Volume, Coherent Power

We now turn our attention to transverse coherence, using Fig. 1.3. Consider the diffraction patterns produced by different emitting points of an extended non-laser source—a square with sides of length  $\xi$  in the figure. The pattern centers are in different positions on the detector. If the source-pinhole distance is  $D$ , and  $d \ll D$ , then the maximum distance between two centers is of the order of  $\xi(H/D)$  (more accurately, it equals  $2^{1/2}\xi(H/D)$ ). The fringes are no longer visible if this maximum distance is bigger than the fringe spacing  $\eta \approx H\lambda/d$ . Thus, the approximate transverse coherence condition is  $\xi(H/D) < H\lambda/d$ , or:

$$d < \lambda D / \xi. \quad (1.4)$$

The immediate messages of Eq. 1.4 are simple: first, transverse coherence requires a small source size  $\xi$ . Second, diffraction can only involve radiation within an area in the plane of the pinhole smaller than  $\approx (\lambda D / \xi)^2$ . This is called the “coherence area” (Fig. 1.3, bottom):

$$A_c = (\lambda D / \xi)^2. \quad (1.5)$$

In addition, there is a subtler point: the diffraction pattern is clearly visible only if the signal-to-noise ratio is sufficiently high. For this, a large enough amount of radiation must participate to the diffraction. Suppose (Fig. 1.3, bottom) that the radiation is homogeneously emitted within a solid angle  $\Omega$ . Only a portion of this emission reaches the coherence area and can contribute to diffraction. The coherence area corresponds to a solid angle  $A_c/D^2 = (\lambda D / \xi)^2 / D^2 = (\lambda / \xi)^2$ . The fraction  $C$  of the emission that participates to diffraction corresponds to the ratio of the solid angles



$(\lambda/\xi)^2$  and  $\Omega$ :

$$C = \lambda^2/(\xi^2 \Omega), \quad (1.6)$$

which is called the “fraction of coherent power” [1].

In essence, a source possesses high transverse coherence if its coherent power is large,  $C \rightarrow 1$ . This requires a small source size and a narrow divergence.

Together (Fig. 1.3, bottom), the coherence area and the coherence length define the “coherence volume” [8]:

$$V_c = L_c A_c = (\lambda^2/\Delta\lambda)(\lambda D/\xi)^2 = \lambda^4 D^2/(\Delta\lambda \xi^2). \quad (1.7)$$

A large coherence volume corresponds to high overall coherence in all directions.

### 1.2.3 Diffraction Limit

The geometric parameters  $\xi$  and  $\Omega$  in Eq. 1.6 are affected by a fundamental limit. Consider in fact Fig. 1.4, which illustrates a simple (albeit ineffective) way to obtain a source with high transverse coherence: a shield blocks most of a radiation beam except the portion that passes through a pinhole of diameter  $\xi$ —which acts as a small-area source.

However, diffraction does not allow us to decrease the pinhole diameter  $\xi$  without increasing the angular spread  $\theta$ . Elementary optics shows that the minimum value for  $\theta$  is  $\approx \lambda/\xi$ , thus the minimum solid angle  $\Omega = \theta^2$  is of the order of  $(\lambda/\xi)^2$ . The resulting value for the coherent power fraction  $\lambda^2/(\xi^2 \Omega)$  is 1, corresponding to full transverse coherence.

We can thus re-interpret the fraction of coherent power, Eq. 1.6, as the ratio between the solid angle  $(\lambda/\xi)^2$ —within which the emission of any source has full transverse coherence—and the total spread  $\Omega$ .

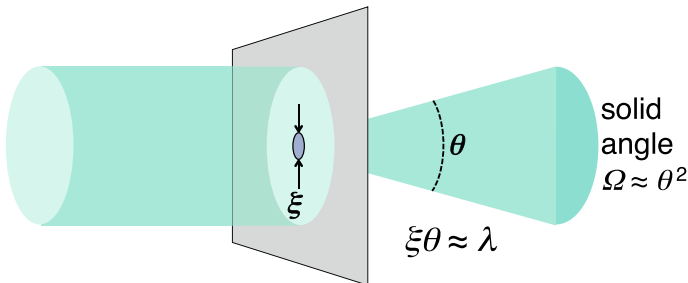


**Fig. 1.4** As we try to obtain a small-area source by using a shield with a pinhole, we discover the “diffraction limit” for the geometric parameters that determine the transverse coherence

Note that the “diffraction limit” is a fundamental property and not a technological barrier that could be overcome by better instrumentation. This limit—i.e., full transverse coherence—is now reached within large portions of the emission spectra of synchrotron radiation sources based on advanced storage rings and X-FELs.

### 1.2.4 *Measuring Coherence*

Although very simple, the arguments of Sects. 1.2.1 and 1.2.2 clarify to some extent longitudinal and transverse coherence. But they do not provide a way to *measure* their levels. For this, we must quantify the notion “*to detect wave-like phenomena such as interference and diffraction*”.

We can again use intuition. Wave-like phenomena can be observed by detecting the fringes in a diffraction or interference pattern. The fringes correspond to a sequence of high-intensity and low-intensity areas. Their “visibility” increases with the difference  $I_{\max} - I_{\min}$  between the maximum and minimum intensities. And it decreases if the overall intensity increases, putting the fringes on a strong background.

These concepts can be quantitatively expressed using the “visibility parameter”:

$$v = (I_{\max} - I_{\min}) / (I_{\max} + I_{\min}), \quad (1.8)$$

which can be adopted as a measure of the overall degree of coherence of the radiation.

### 1.2.5 *Coherence and Brightness*

The arguments of Sects. 1.2.2 and 1.2.3 illustrate, in particular, why coherence is much more difficult to obtain for X-rays than for visible or infrared light. Indeed, the conditions for longitudinal and transverse coherence are (1) a large coherence length  $L_c = \lambda^2 / \Delta\lambda$  and (2) a large coherent power fraction  $\lambda^2 / (\xi^2 \Omega)$ . Both parameters are proportional to  $\lambda^2$ , thus reaching high values is difficult for short X-ray wavelengths.

This handicap was progressively overcome after the advent of synchrotron sources. Longitudinal coherence was enhanced, for example, by the use of “undulators” [1], which emit rather narrow wavelength bandwidths. Furthermore, the very high intensity of synchrotron radiation compensated the strong flux losses caused by monochromators—which could thus be used to obtain narrow bandwidths and high longitudinal coherence not only from undulators but also from broadband emitters like bending magnets and wigglers [1].

The technical progress of synchrotron sources also enhanced the transverse coherence. To understand how, we must consider the relation between coherence and (spectral) “brightness” (or “brilliance”)  $B_S$ —the leading merit parameter for radiation sources [1]. Roughly speaking,  $B_S$  is proportional to the emitted flux  $F$  divided by the source size and by the solid angle of emission:

$$B_S \propto F/(\xi^2 \Omega). \quad (1.9)$$

Thus, the brightness increases as the geometric parameters in the denominator of Eq. 1.9 decrease. But these are the same parameters found in the denominator of the coherent power fraction, Eq. 1.6. Thus, the long-term technical efforts to decrease them boosted not only the brightness but also, as an important byproduct, the transverse coherence.

The analysis of the relation between coherence and brightness can be refined and expanded as follows. The spectral brightness  $B_S$  for synchrotron radiation is normally defined [1] as the number of photons emitted per unit time, per unit source area and per unit solid angle, within a relative bandwidth  $\Delta\lambda/\lambda$  centered at  $\lambda$ . Thus, if  $n = n(\lambda)$  is the number of photons that the source yields per unit time around  $\lambda$ , we have:

$$B_S \approx n/[\xi^2 \Omega (\Delta\lambda/\lambda)] = n\lambda/(\xi^2 \Omega \Delta\lambda). \quad (1.10)$$

On the other hand, the overall level of coherence can be characterized by the so-called “photon degeneracy parameter”  $N$  (a name borrowed from laser physics). This quantity, which takes into account the signal-to-noise ratio in coherence-based experiments, is defined as the number of photons that the source puts in the coherence volume. During a time  $\Delta t$ , the source emits  $n(\lambda)\Delta t$  photons around  $\lambda$ . Of them, those that pass through the coherence area and enter the coherence volume are  $n(\lambda)\Delta t$  multiplied by the fraction of coherent power,  $\lambda^2/(\xi^2 \Omega)$ . During the same time  $\Delta t$ , the photons travel at the speed of light  $c$  over a distance  $L = c\Delta t$ . Thus, those contained in the coherence volume are a fraction  $L_c/L = (\lambda^2/\Delta\lambda)/(c\Delta t)$ , and:

$$N = (n\Delta t)[\lambda^2/(\xi^2 \Omega)][(\lambda^2/\Delta\lambda)/(c\Delta t)] = (\lambda^3/c)[n\lambda/(\xi^2 \Omega \Delta\lambda)], \quad (1.11)$$

i.e.,

$$N = (\lambda^3/c)B_S. \quad (1.12)$$

Therefore, the photon degeneracy parameter that characterizes the overall coherence in all directions is proportional to the spectral brightness. This generalizes the notion that when the brightness increases so does the coherence. However, for the short wavelengths of X-rays the increase is mitigated by the  $\lambda^3$  factor in Eq. 1.12.

### 1.3 Exploiting Coherence

Regrettably, during the long-term increase of the synchrotron brightness many users did not notice the related enhancement of coherence, missing wonderful research opportunities. To appreciate such opportunities, consider for example the high-quality radiographs and tomographic pictures of Fig. 1.5, produced by synchrotron

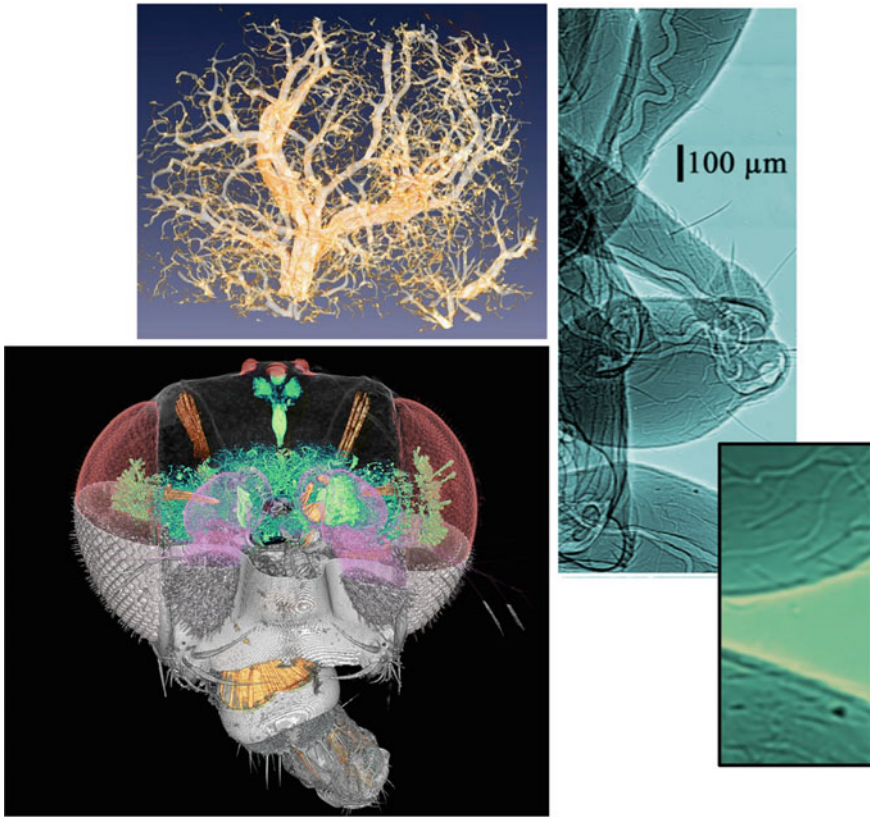


**Fig. 1.5** Examples of coherence-based radiology and tomography from [2] and [9]. Top left: cancer-related mouse microvasculature. Bottom left: tomography showing neurons and connections in the head of a *Drosophila* fly. Right: images of an ant leg; the zoomed-in portion at the bottom emphasizes the sharp edges that produce the high image quality

radiation with high transverse coherence [2, 9]. Extremely fine details are revealed with unprecedented spatial resolution that reaches subcellular levels.

A complete analysis of results like those of Fig. 1.5 requires an advanced theory of the image formation mechanism [10], which falls in the general class of “phase contrast radiography” and is related to holography. But many features can be understood, here again, with simple arguments [11, 12].

Note, for example (Fig. 1.5, bottom right picture), that the high quality of the coherence-based radiographs is mainly produced by marked edges between different regions of the specimen. Such edges are primarily caused by refraction, a typical wave phenomenon [11, 12]. As schematically illustrated in the top-left part of Fig. 1.6, X-rays reaching an object in regions outside a slanted edge are not affected by refraction (and are only weakly absorbed by the object). Instead, those passing through the edge are deviated, producing on the detector a characteristic dark-bright sequence, as seen

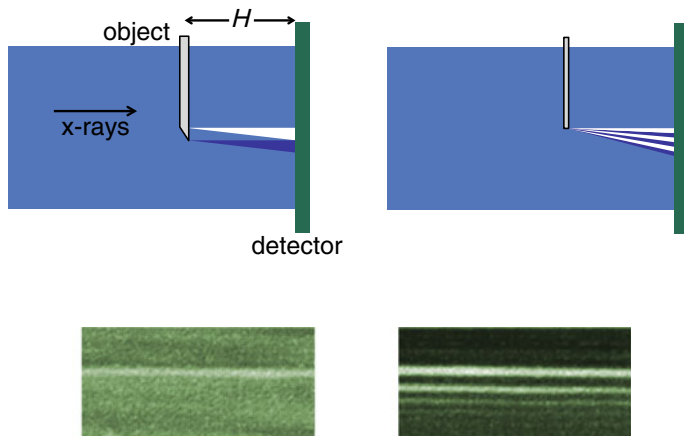


**Fig. 1.6** The two mechanisms that cause sharp edges in coherence-based radiographs [11, 12]: refraction by a slanted boundary (top left) and Fresnel edge diffraction (top right). The images show boundaries between an object and vacuum, but a similar analysis applies to those between different object regions. By changing the object-detector distance  $H$  one can emphasize [12] the effects of refraction over those of diffraction, or vice versa. This verifies the validity of the simplified approach of Ref. [12]; see for example the two versions of the same edge in the bottom part of the figure, obtained with different values of  $H$

in the images of Fig. 1.5. To detect this effect, the X-ray beam must have a well-defined direction, i.e., must be confined to a narrow solid angle and therefore possess high transverse coherence.

As discussed in Ref. [12], to fully understand the sharp boundaries in the images one must take into account not only refraction but also Fresnel edge diffraction, another wave-like effect—see Fig. 1.6, top right. This phenomenon occurs for any boundary and causes a series of fringes, whereas refraction works with slanted boundaries (Fig. 1.6, top left) and produces the aforementioned dark-bright fringe pairs. By changing the object-detector distance  $H$ , one can control the interplay between diffraction and refraction and emphasize one effect or the other. This was used to validate the approach of Ref. [12], with results like those shown in the bottom part of Fig. 1.6.

One important conclusion of this simple approach is that, contrary to transverse coherence, high longitudinal coherence is not required to obtain images with sharp edges [11, 12]. This realization in 1999 made it possible to avoid monochromators, boosting the available flux and opening the door to many interesting applications in diverse domains [2, 9, 11, 12].

One should note that phase-contrast techniques are much more diversified and flexible than the simple examples presented here [10]. Furthermore, they are only a portion of the wide spectrum of imaging techniques based on coherence. Overall, such techniques constitute now a formidable arsenal for the 3-dimensional microscopic analysis of the internal structure of specimens.

## 1.4 Coherence as a Quantum Property

The simplicity of the approach in the previous sections should not be mistaken as evidence that coherence is something trivial. This is far from the truth: coherence is one of the most fundamental and subtle properties of nature, intimately linked to quantum physics. We can get a hint of this connection by adopting again an intuitive approach.

Quantum physics treats electromagnetic radiation as photons [13], which under certain conditions can produce effects equivalent to those of waves in classical physics. These effects (as discussed below) are primarily caused by interactions of each photon with itself [6, 7, 13], as Dirac realized very early [14]. Therefore, coherence requires such self-interactions to produce detectable phenomena like interference and diffraction.

This imposes conditions on the photon “size”. To see how, consider the size  $\delta x$  in the longitudinal direction  $x$  of Fig. 1.3, given by Heisenberg’s position uncertainty:

$$\delta x \approx \hbar/\delta p_x, \quad (1.13)$$

where  $\delta p_x$  is the momentum uncertainty in the  $x$ -direction. The magnitude of  $p_x$  is  $\hbar/\lambda$ , therefore

$$\delta p_x \approx |d(\hbar/\lambda)/d\lambda|\Delta\lambda = \hbar\Delta\lambda/\lambda^2$$

and Eq. 1.13 gives:

$$\delta x \approx \lambda^2/\Delta\lambda = L_c. \quad (1.14)$$

This sheds new light on the notion of coherence length: it coincides with the longitudinal photon size according to the uncertainty principle. The condition for longitudinal coherence expressed by Eq. 1.3 implies that:

$$\delta x > \lambda, \quad (1.15)$$

a result that makes sense: to produce wave-like effects, a photon must have a sufficiently large “size” compared to the wavelength, so that its electromagnetic field (or, more accurately, its position probability amplitude) can sample at least one oscillation (see Fig. 1.7).

Consider now the transverse directions  $y$  and  $z$  of Fig. 1.3. Imagine a photon that reaches the pinhole. Because of the finite sizes of the pinhole and of the source, the direction of its momentum cannot be predicted with infinite accuracy. If the pinhole size is much smaller than that of the source,  $\xi$ , then the angular uncertainty is  $\approx \xi/D$ , and the momentum uncertainty in the  $y$ -direction is  $\delta p_y \approx (\hbar/\lambda)(\xi/D)$ , so that:

$$\delta y \approx \lambda D/\xi; \quad (1.16)$$

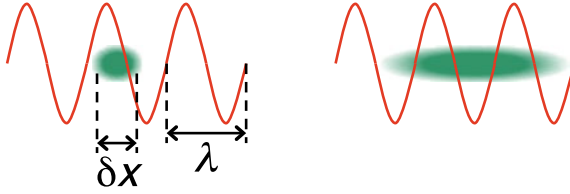


**Fig. 1.7** Left: when self-interacting, a photon cannot produce wave-like effects if its “size” is too small compared to the wavelength; right: such effects become possible when the “size” is larger than  $\lambda$

likewise:

$$\delta z \approx \lambda D / \xi, \quad (1.17)$$

and  $\delta y \delta z \approx (\lambda D / \xi)^2 = A_c$ . Thus, the coherence area approximately corresponds to the transverse cross section of a photon,  $\approx \delta y \delta z$ .

We can now re-visit in quantum terms the condition of Eq. 1.5,  $d < \lambda D / \xi$ : to produce visible diffraction, the pinhole must be smaller than the transverse size of the photon. This is reasonable: if, on the contrary, the photons are significantly smaller than the pinhole, then they pass through it as individual particles without generating wave-like effects.

As to the coherence volume, the above results imply that it corresponds to the three-dimensional size of a photon,  $\delta x \delta y \delta z \approx (\lambda^2 / \Delta \lambda) (\lambda D / \xi)^2 = \lambda^4 D^2 / (\Delta \lambda \xi^2) = V_c$ .

### 1.4.1 Coherence and QED

Recent and very interesting articles by Stöhr [6, 7] inspired this section: we address the readers to them for a complete and detailed discussion of the issues. Here, we summarize some relevant points in simplified terms, in particular the revolutionary implications of seeded X-FELs.

The initial history of quantum physics was marked by the notion that particle and wave natures coexist for the same phenomenon, most notably electromagnetic radiation. This duality, however, was removed by the advent of QED [13]—which considers electromagnetic radiation as made of photons and treats the classical wave-like phenomena as interactions between them.

As already mentioned, most wave-like phenomena are caused by interactions not between different photons but of each photon with itself [13, 14]. We can realize this point by studying interference or diffraction with different radiation fluxes. If the flux is sufficiently low, uncorrelated photons pass one-by-one through the experimental system and there are no interactions between them. At high fluxes, different photons pass simultaneously through the system—and photon-photon interactions

could hypothetically occur. However, the cumulative patterns of many photons are the same for both cases, so they must be dominated by self-interactions.

The reason for this dominance is that the corresponding wave-like effects are described by first-order QED, and higher-order terms are negligible as long as the peak spectral brightness—i.e., equivalently, the photon degeneracy parameter and the overall coherence—are not very high [6, 7]. Until very recently, this was generally true for X-rays.

Lately, X-FELs dramatically increased the peak brightness and the related parameters. However, the first sources in this class were affected by a serious handicap as far as time coherence was concerned. They were based on the optical amplification of stochastically emitted radiation (“*Self-amplified Spontaneous Emission*” or SASE) [15]—which produced time pulses of different shapes, limiting the time coherence.

The situation changed with the practical realization of the X-FEL “seeding” mechanism [5], in which radiation pulses with a well-defined shape are injected into an optical amplifier, producing X-rays with a narrow wavelength bandwidth and high time coherence. Seeded X-FELs thus reach excellent coherence levels in all directions, longitudinal and transverse (diffraction limit), and extremely high values of the peak brightness.

This could possibly trigger a revolution in X-ray physics, as the higher-order terms in the QED treatment of radiation are not necessarily negligible. Novel experimental techniques can emerge, mirroring what happened at longer wavelengths [6, 7].

Very interesting opportunities are also offered by the extension to X-rays of the strategies of “quantum imaging” [15]. For example, parametric down-conversion at short wavelengths [16–19] could be performed beyond the shot noise limit, with truly single photons.

We can appreciate, therefore, that X-ray coherence has far-reaching consequences well beyond the trivial impact of classical notions. Indeed, it touches the very foundations of quantum physics in fascinating and novel ways. And challenges the experimentalists to conceive innovative ways to exploit its potential.

## Appendix: A Second Look at the Coherence Length

The notions introduced in Sect. 1.2 coincide with those obtained with more conventional treatments of coherence. We present here, as an example, the case of the coherence length.

Figure 1.8 illustrates a simple case of multi-wavelength emission: two waves at a given time, with wavelengths  $\lambda$  and  $\lambda + \Delta\lambda/2$ . At  $x = 0$ , the two waves are in phase, whereas at  $x = x_0$  they are totally out of phase. This change occurs because between  $x = 0$  and  $x = x_0$  the first wave has  $q$  full oscillations and the second  $(q - 1/2)$  full oscillations,  $q$  being an integer number (in the figure,  $q = 7$ ). Thus,  $q\lambda = (q - 1/2)(\lambda + \Delta\lambda/2)$ , which gives  $q = (\lambda + \Delta\lambda)/(\Delta\lambda)$  and  $x_0 = q\lambda = \lambda^2/(\Delta\lambda) + \lambda$ . For  $\Delta\lambda \ll \lambda$ ,  $x_0 \approx \lambda^2/(\Delta\lambda) = L_c$ .



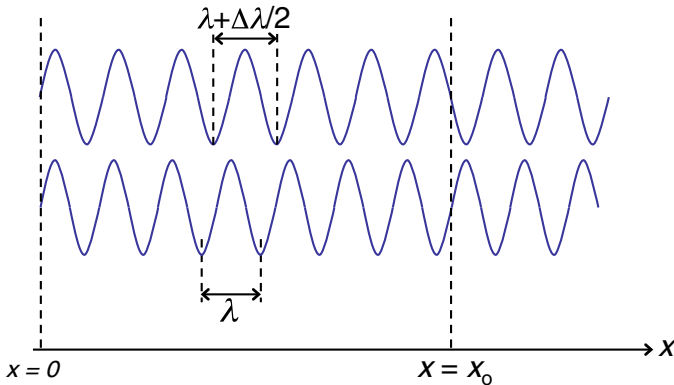


**Fig. 1.8** Two waves with different wavelengths change from being in phase to being totally out of phase over a distance  $x_0$ , approximately equal to the coherence length  $L_c$

Therefore, the coherence length is approximately the distance over which the phase difference between different wavelengths changes significantly. This coincides with the classical result of coherence theory: along a distance smaller than  $L_c$ , waves with different wavelengths can remain reasonably in phase with each other, and therefore capable to produce interference and diffraction effects.

Similar conclusions apply to other coherence parameters. For example, one can show that within the coherence volume waves from a non-monochromatic source with finite size and angular divergence are sufficiently in phase with each other to produce interference and diffraction effects.

## References

1. G. Margaritondo, *Elements of Synchrotron Light for Biology, Chemistry, and Medical Research* (Oxford University Press, New York, 2002).
2. G. Margaritondo, Y. Hwu, J.-H. Je, Nondestructive characterization by advanced synchrotron light techniques: spectromicroscopy and coherent radiology. *Sensors* **8**(12), 8378–8400 (2008)
3. M. Stamboni, A. Menzel, B. Watts, K.S. Mader, O. Bunk, Coherent X-ray imaging: bridging the gap between atomic and micro-scale investigations. *Chimia* **68**(1), 66–72 (2014)
4. P.R.T. Munro, Coherent X-ray imaging across length scales. *J. Contemp. Phys.* **58**(2), 140–159 (2019)
5. E. Allaria et al., Highly coherent and stable pulses from the FERMI seeded free-electron laser in the extreme ultraviolet. *Nat. Photonics* **6**, 699–704 (2012)
6. J. Stöhr, What are X-rays anyway: a modern view of the nature of lights and its implications for the future of X-ray science. *Synchrotron Radiat. News* **32**(4), 48–51 (2019)
7. J. Stöhr, Overcoming the diffraction limit by multi-photon interference: a tutorial. *Adv. Opt. Photon.* **11**(1), 215–313 (2019)
8. L. Mandel, E. Wolf, Coherence properties of optical fields. *Rev. Mod. Phys.* **37**(2), 231–287 (1965)
9. Y. Hwu, G. Margaritondo, A.S. Chiang, Why use synchrotron X-ray tomography for multi-scale connectome mapping. *BMC Biol.* **15**(1), 122 (2017)

10. F. Van der Veen, F. Pfeiffer, Coherent X-ray scattering. *J. Phys.* **16**(28), 5003–5031 (2004)
11. G. Margaritondo, G. Tromba, Coherence-based edge diffraction sharpening of X-ray images: a simple model. *J. Appl. Phys.* **85**(7), 3406–3408 (1999)
12. Y. Hwu et al., Coherence-enhanced synchrotron radiology: refraction versus diffraction mechanisms. *J. Appl. Phys.* **86**(8), 4613–4619 (1999)
13. R.P. Feynman et al., *The Feynman Lectures on Physics*, vol. 3 (Addison-Wesley, Reading, MA, 1965).
14. P.A.M. Dirac, *Quantum Mechanics*, 4th edn. (Oxford University Press, Oxford, England, 1958).
15. M.I. Kolobov, *Quantum Imaging* (Springer, New York, 2007).
16. S. Shwartz et al., X-ray parametric down-conversion in the Langevin regime. *Phys. Rev. Lett.* **109**, 013602 (2012)
17. D. Borodin, A. Schori, F. Zontone, S. Shwartz, X-ray photon pairs with highly suppressed background. *Phys. Rev. A* **94**, 013843 (2016)
18. D. Borodin, K. Schori, K. Tamasaku, S. Shwartz, Ghost imaging with paired X-ray photons. *Phys. Rev. A* **97**, 063804 (2018)
19. S. Sofer et al., Quantum enhanced X-ray detection. *Phys. Rev. X* **9**, 031033 (2019)

# Chapter 2

## Some Odd Consequences of Self-coherence in the Photo-Diffraction and Photo-Absorption Processes



Calogero Renzo Natoli

**Abstract** While the photo-emission process is inherently inelastic, in reality a closer investigation reveals that some coherence effects depending on the single photon and electron self-interference are indeed observable. All hinges on the Feynman's rule according to which, if the same final state can be reached by different pathways, the probability for its observation is obtained by taking the modulus squared of the sum of the probability amplitudes of the various paths, leading to the mechanism of self-interference. To this purpose we review the two-slit and the usual crystal (Bragg) diffraction experiments, highlighting that in both cases the interference patterns are due to the self-interference of the single incoming photon. Guided by these two examples, we construct the photo-emission equivalent of these experimental set-up in the case of delocalized initial states and discuss their related diffraction patterns using the language of Multiple Scattering (MS) Theory. In the general case this approach shows that coherent emission from atomic sites does not necessarily require their equivalence and new MS processes with different periodicity appear compared to the case of emission from a single localized site. In particular, the cross section for photo-emission from a valence band state factorizes, like in the diffraction counterpart, into an electronic part (photo-emission from a localized atom) and a modulating Bragg factor, where the momentum exchanged with the crystal involves the initial Brillouin Zone, the impinging photon and the final photoelectron wavevectors. Photo-emission from diatomic molecules is a particular case of this general framework. We show that, when the photoelectron is detected, the coherent emission from the two atomic centers realizes the analog of the Young's two-slit experiment, whereas in the case of photo-absorption the Cohen-Fano interference oscillations observed in the absorption cross section are to be ascribed to new MS paths joining the two sites.

---

C. R. Natoli (✉)

INFN Laboratori Nazionali di Frascati, c.p. 13, 00044 Frascati, Italy  
e-mail: [natoli@lnf.infn.it](mailto:natoli@lnf.infn.it)

© Springer Nature Switzerland AG 2021

A. Di Cicco et al. (eds.), *Synchrotron Radiation Science and Applications*,  
Springer Proceedings in Physics 220, [https://doi.org/10.1007/978-3-030-72005-6\\_2](https://doi.org/10.1007/978-3-030-72005-6_2)

## 2.1 Introduction

In the Feynman's approach to quantum mechanics the basic entities are processes or transitions rather than states [1, 2]. A process is an ordered event starting at a given initial state, proceeding possibly via intermediate states, and ending up at a definite final state. To each possible process one assigns a complex number called the probability amplitude for the process. The assigned number is assumed to depend only on the given process and to be independent of the past history (Markovian property).

One can state the rules for combining amplitudes and for calculating the associated probabilities as follows [3]:

1. The amplitude for processes occurring in succession is the product of the amplitudes for each part;
2. if a process can proceed in more than one way, the amplitude for the process is the sum of the amplitudes for the different alternatives,
3. the probability for a process is the absolute value squared of the amplitude for the process.

More concisely, probability amplitudes for alternative paths to the same final state are added, similar to the superposition principle for complex fields, and the detection probability is calculated as the absolute value squared. For composite events the associated amplitude probability for the process is the product of the amplitudes of the constituent events.

## 2.2 Some Illustrative Examples

### 2.2.1 *Two-Slit Experiment*

A clear illustration of the above laws is supplied by the familiar Young's two-slit experiment [1].

A photon emerging from a source  $S$  arrives at a detector placed behind a vertical screen through two horizontal parallel slits cut in the screen at a distance comparable or less its coherence length. In order to make contact with molecular emission treated below, we assume that each slit  $i$  reduces to a point with coordinates  $\mathbf{s}_i$  with respect to the origin of a planar system of coordinates chosen on the screen, located midway between the two points. The detector lies on a plane parallel to the screen intercepting the perpendicular to the plane of the screen at a distance  $z_0$ . This point is chosen to be the origin of a system of coordinates with axes congruent with those on the screen. In the detector plane the observation point is labeled by the vector  $\boldsymbol{\rho}$ .

In this framework, the photon can reach the detector passing through either points, which in turn become origin of a spherical wave the amplitude of which is given by

$e^{i\kappa r_{ix}}/r_{ix}$  where  $r_{ix}$  is the distance between the source point  $i$  on the screen and the point  $x$  on the detector plane, and  $\kappa$  is the photon wavevector.

At large average source-detector separation  $z_0$ , the so-called Fraunhofer diffraction limit, so that we can replace the distance  $r_{ix}$  by  $z_0$  in the denominator of the spherical wave, assuming also  $s, \rho \ll z_0$ , we can express the path length  $r_{ix}$  as

$$r_{ix} = \sqrt{z_0^2 + |\mathbf{s}_i - \boldsymbol{\rho}|^2} \approx z_0 \left( 1 + \frac{s_i^2}{2z_0^2} + \frac{\rho^2}{2z_0^2} - \frac{\mathbf{s}_i \cdot \boldsymbol{\rho}}{z_0^2} \right) \quad (2.1)$$

We further assume that  $\kappa s_i^2/2z_0 = \pi s_i^2/\lambda z_0 \ll 1$ , so that we can neglect the second term inside the parenthesis. Under these assumptions the amplitude to proceed from  $S$  to  $x$  via slit  $i$  is given by

$$\frac{1}{z_0} e^{i\kappa z_0(1 + \frac{\rho^2}{2z_0^2})} e^{-i\frac{\kappa}{z_0} \mathbf{s}_i \cdot \boldsymbol{\rho}} \quad (2.2)$$

and the total amplitude  $A$  for the photon to go from  $S$  to  $x$ , due to the indistinguishability of the source points, is given by

$$A = \frac{1}{z_0} e^{i\kappa z_0(1 + \frac{\rho^2}{2z_0^2})} (e^{-i\frac{\kappa}{z_0} \mathbf{s}_1 \cdot \boldsymbol{\rho}} + e^{-i\frac{\kappa}{z_0} \mathbf{s}_2 \cdot \boldsymbol{\rho}}) = \frac{1}{z_0} e^{i\kappa z_0(1 + \frac{\rho^2}{2z_0^2})} e^{-i\frac{\kappa}{z_0} \mathbf{s}_1 \cdot \boldsymbol{\rho}} (1 + e^{i\frac{\kappa}{z_0} (\mathbf{s}_1 - \mathbf{s}_2) \cdot \boldsymbol{\rho}}) \quad (2.3)$$

The detection probability on the screen is therefore

$$P = |A|^2 = \frac{2}{z_0^2} \left( 1 + \cos \left( \frac{\kappa}{z_0} (\mathbf{s}_1 - \mathbf{s}_2) \cdot \boldsymbol{\rho} \right) \right) \quad (2.4)$$

In the case of one photon at a time, the interference pattern on the detector screen is constructed cumulatively with time, pointing to a process of self-interference of the photon, whereas if many photons impinge on the slit screen the interference pattern is formed statistically at the same time. One observes the same phenomenon with electrons. It suffices to replace in the above formulas the photon wavevector  $\kappa$  with the electron wavevector  $k$ .

## 2.2.2 Bragg Diffraction

Another illustration of the same laws is provided by the Bragg diffraction patterns. The photon diffraction from a D-dimensional ( $D = 1, 2, 3$ ) periodic array of  $N$  equivalent atoms located at sites  $\mathbf{R}_j$  is simply calculated on the basis of the Feynman rules. We assume that there is only one atom per unit cell. The elementary process is the scattering by a single atom, located at site  $R_j$  inside the volume  $\Omega$ , of an impinging photon with momentum  $\kappa$  and polarization  $\boldsymbol{\epsilon}$  into a state with momentum  $\kappa'$  and polarization  $\boldsymbol{\epsilon}'$ . The amplitude from this process is given by

$$\begin{aligned}
\mathbf{F}_j(\mathbf{Q}) &= (\boldsymbol{\epsilon} \cdot \boldsymbol{\epsilon}') \int_{\Omega} d\mathbf{r}_j e^{i\mathbf{Q}\cdot\mathbf{r}} \rho(\mathbf{r}_j) \\
&= (\boldsymbol{\epsilon} \cdot \boldsymbol{\epsilon}') e^{i\mathbf{Q}\cdot\mathbf{R}_j} \int_{\Omega} d\mathbf{r}_j e^{i\mathbf{Q}\cdot\mathbf{r}_j} \rho(\mathbf{r}_j) \\
&= e^{i\mathbf{Q}\cdot\mathbf{R}_j} \mathbf{F}(\mathbf{Q})
\end{aligned} \tag{2.5}$$

where  $\mathbf{r}_j = \mathbf{r} - \mathbf{R}_j$ ,  $\rho(\mathbf{r}_j)$  is the charge density of the atom located at site  $\mathbf{R}_j$  and  $\mathbf{Q} = \boldsymbol{\kappa} - \boldsymbol{\kappa}'$  is the momentum transfer. The phase factor  $e^{i\mathbf{Q}\cdot\mathbf{R}_j}$  arises from the fact that the vector potential of the photon is referred to the common origin of the atomic coordinates  $\mathbf{R}_j$ . Notice the factorization of this amplitude into an electronic part  $\mathbf{F}(\mathbf{Q})$  equal for all atoms and a spatial part depending only on the atomic location.

In the single scattering approximation, the total probability  $P$  for photon scattering into the direction  $\hat{\boldsymbol{\kappa}}'$  by all the atoms of the array is obtained by taking the square modulus of the sum of all the individual scattering amplitudes representing alternative paths leading to the same final state. Therefore

$$P = |\mathbf{F}(\mathbf{Q})|^2 \left| \sum_j^N e^{i\mathbf{Q}\cdot\mathbf{R}_j} \right|^2 \tag{2.6}$$

where the second factor is the usual Bragg diffraction factor. Indeed, in the limit  $N \rightarrow \infty$  one has

$$\sum_j^{\infty} e^{i\mathbf{Q}\cdot\mathbf{R}_j} = \sum_{\mathbf{G}_D} \delta(\mathbf{Q} - \mathbf{G}_D) \tag{2.7}$$

where  $\delta$  is the usual Dirac's function and  $\mathbf{G}_D$  is any reciprocal lattice vector of the  $D$ -dimensional direct lattice.

The diffraction from a periodic charge distribution on the same lattice can be treated along similar lines. It is clear from the derivation of the phase factor  $e^{i\mathbf{Q}\cdot\mathbf{R}_j}$  in Eq. (2.5) that the diffraction patterns originate from a single photon self-interference, as also born out experimentally by their observation by Bragg, who was using photons coming from an x-ray tube inherently uncorrelated with each other.

### 2.2.3 Photo-Emission from a Localized Core State

In analogy with the Bragg diffraction process, we now try to construct the site amplitude of the photo-emission process as the product of the amplitudes of the constituent processes occurring in succession according to point (1) of the Feynman's rules described in the Introduction. We use the language of multiple scattering theory (MST) to write down this amplitude.

In the independent particle approximation, we need the wave function of the initial state localized within an atomic site (core state) and that of the photo-emission

final state which is the solution of the Schrödinger Equation (SE) with a positive energy corresponding to the kinetic energy of the photoelectron. This SE can be transformed into an integral equation with appropriate boundary conditions (the so-called Lippmann-Schwinger equation) which can be solved by the method of MST. This method of solution is implemented by dividing the space into non-overlapping domains  $\Omega_j$  (called cells, usually but non necessarily containing a physical atom), solving the differential equation separately in each of the cells and then assembling together the partial solutions into a global solution that is continuous and smooth across the whole region and satisfies the given boundary conditions [4, 5].

Under these assumption the PED cross section is given by

$$\frac{d\sigma}{d\hat{\mathbf{k}}} = 4\pi^2 \alpha \hbar \omega \left| \sum_L M_{LcL}(E) (B_L^c(\mathbf{k}))^* \right|^2 \quad (2.8)$$

where we have introduced the atomic transition matrix element

$$M_{LcL}(E) = \int_{\Omega_c} d\mathbf{r}_c (\Phi_L^c(\mathbf{r}_c; k))^* (e^{i\mathbf{k}\cdot\mathbf{r}_c} \boldsymbol{\epsilon} \cdot \mathbf{r}_c) \phi_{Lc}^c(\mathbf{r}_c) \quad (2.9)$$

and kept the exponential factor originating from the vector potential of the impinging photon with momentum  $\boldsymbol{\kappa}$ . Here  $\Phi_L^c(\mathbf{r}_c; k)$  is the local solution of the SE inside the cell  $\Omega_c$ , where the initial state  $\phi_{Lc}^c(\mathbf{r}_c)$  is localized, such that  $\sum_L (B_L^c(\mathbf{k}))^* \Phi_L^c(\mathbf{r}_c; k)$  is the local representation of the excited continuum photo-emission state, global solution of the SE with incoming wave boundary conditions [4, 5].

As usual,  $L$  stands for the pair  $l, m$  of angular momentum indices. Introducing a sum over  $m_c$  before the square modulus in Eq. (2.8) one obtains the unpolarized cross section. The scattering amplitude  $B_L^c(\mathbf{k})$  is given by

$$B_L^c(\mathbf{k}) = \sqrt{\frac{k}{\pi}} \sum_{jL'} \boldsymbol{\tau}_{LL'}^{cj} i^{j'} Y_{L'}(\hat{\mathbf{k}}) e^{i\mathbf{k}\cdot\mathbf{R}_j} \quad (2.10)$$

where  $\boldsymbol{\tau}_{LL'}^{ij}$  represents the full scattering path operator, giving the total amplitude of propagation of the photoelectron from site  $i$  to site  $j$ , starting with angular momentum  $L$  around site  $i$  and arriving with angular momentum  $L'$  at site  $j$ .

If we introduce the scattering matrix  $T_{LL'}^i \delta_{ij}$  of the cell  $i$  in an angular momentum basis, giving the scattering amplitude of the photoelectron impinging on the cell with angular momentum  $L$  into a state of angular momentum  $L'$ , and and the free spherical wave propagator  $G_{LL'}^ij$  from cell  $i$  to cell  $j$  [4], it is clear that  $\boldsymbol{\tau}_{LL'}^{ij}$  obeys the following equation

$$\boldsymbol{\tau}_{LL'}^{ij} = T_{LL'}^i \delta_{ij} + \sum_{\underline{LL}'k} T_{LL'}^i G_{\underline{LL}'}^{ik} \boldsymbol{\tau}_{\underline{L}'L'}^{kj} \quad (2.11)$$

which is derived from a resummation of the Born series in which the photoelectron first scatters from cell  $i$ , then propagates to cell  $k$  undergoing here another scattering

event, then to the next cell, and so on and so forth. The solution of this equation is given in terms of the inverse of the MS matrix ( $\mathbf{T}^{-1} - \mathbf{G}$ ) by

$$\boldsymbol{\tau} = (\mathbf{T}^{-1} - \mathbf{G})^{-1} = \sum_n (\mathbf{T}\mathbf{G})^n \mathbf{T} = \sum_n \mathbf{T} (\mathbf{G}\mathbf{T})^n \quad (2.12)$$

where the series expansion reproduces the original Born series (matrix multiplication in the appropriate indexes is implied) and converges if  $\rho(\mathbf{T}\mathbf{G})$ , the spectral radius (maximum eigenvalue) of  $\mathbf{T}\mathbf{G}$ , is less than one. This expansion will come handy in the following.

Due to the expression (2.10) we obtain the PED cross section by taking the product of the amplitude  $M_{L_c L}$  for creating a photo-electron in a state of spherical wave  $L$  selected according to the dipole selection rule from an initial core state  $L_c$ , times the amplitude of propagation from site  $c$  to any site  $j$ , starting with angular momentum  $L$  and ending with angular momentum  $L'$  after any number of scattering events, times the phase difference  $e^{i\mathbf{k}\cdot\mathbf{R}_j}$  between the initial and final sites  $c$  and  $j$ , times the spherical wave amplitude  $i^{l'} Y_{L'}(\hat{\mathbf{k}})$  for escaping toward the detector. All these amplitudes are to be summed together and squared to obtain the intensity of the photo-electron current at the detector, in keeping with the Feynman's rules for composite consecutive events introduced above and alternative paths to the same final state.

It is clear that the interference patterns so measured by the detector depend on the actual positions of the atoms in the sample and represent a three-dimensional hologram of the sample-object (i. e. the atomic positions in the system under study) in momentum and energy space, associated with the three degrees of freedom of the two polar and azimuthal emission angles and the final kinetic energy of the photo-electron as pointed out by Ref. [6]. For an in depth discussion on this aspect also from an experimental point of view see Ref. [7].

In case of real potentials the scattering amplitudes  $B_L^i(\mathbf{k})$  satisfy the relation

$$\int d\hat{\mathbf{k}} B_L^i(\mathbf{k}) \left[ B_{L'}^j(\mathbf{k}) \right]^* = -\frac{1}{\pi} \Im \boldsymbol{\tau}_{LL'}^{ij} \quad (2.13)$$

which is a kind of generalized optical theorem, consequence of the conservation of particle flux. This relation is very important, since it establishes the connection between the photo-emission and the photo-absorption cross section [5].

In fact, by integrating the PED cross section over all emission angles and exploiting Eq. (2.13) we get

$$\begin{aligned} \int d\hat{\mathbf{k}} \frac{d\sigma}{d\hat{\mathbf{k}}} &= 4\pi^2 \alpha \hbar \omega \int d\hat{\mathbf{k}} \left| \sum_L M_{L_c L}(E) (B_L^c(\mathbf{k}))^* \right|^2 \\ &= -4\pi \alpha \hbar \omega \sum_{LL'} M_{L_c L}(E) \Im \boldsymbol{\tau}_{LL'}^{cc} M_{L_c L'}^* \end{aligned} \quad (2.14)$$

which is equal to the absorption cross section, as shown below [4].



As a consequence, the integration process eliminates the physical detector located outside the sample and replaces it by the atomic emitter (since we count the number of holes), which becomes in this way both the source and the detector of the photo-electrons.

According to Feynman's rules we can interpret the second line of Eq. (2.14) as the imaginary part of the amplitude for creating an electron at the site of the photo-absorber, times the amplitude of propagation from this site to the same site after undergoing any number of multiple scattering by the atoms in the system, times the amplitude of being re-absorbed at the emitter atom.

The photo-emission amplitude  $\sum_L M_{L_c L}(E) (B_L^c(\mathbf{k}))^*$  is the sought amplitude for the site photo-emission process, analogous to the elementary process of the scattering of a photon by a single atom in the diffraction experiment.

### 2.3 Photo-Emission from Extended Valence States

We first consider periodic systems. In this case the initial state  $\phi_{\mathbf{k}_{bz}}(\mathbf{r})$  is a band state with wave vector  $\mathbf{k}_{bz}$  in a periodic lattice potential with one atom per unit cell, which according to Bloch's theorem can be written as

$$\phi_{\mathbf{k}_{bz}}(\mathbf{r}) = \frac{1}{\sqrt{N}} e^{i\mathbf{k}_{bz} \cdot \mathbf{r}} u_{\mathbf{k}_{bz}}(\mathbf{r}) \quad (2.15)$$

where  $u_{\mathbf{k}_{bz}}(\mathbf{r})$  has the periodicity of the lattice, such that

$$u_{\mathbf{k}_{bz}}(\mathbf{r} + \mathbf{R}_n) = u_{\mathbf{k}_{bz}}(\mathbf{r}) \quad (2.16)$$

for all lattice points  $\mathbf{R}_n$ . Therefore

$$\phi_{\mathbf{k}_{bz}}(\mathbf{r} + \mathbf{R}_n) = e^{i\mathbf{k}_{bz} \cdot \mathbf{R}_n} \phi_{\mathbf{k}_{bz}}(\mathbf{r}) \quad (2.17)$$

In Eq. (2.15)  $N$  is the number of unit cells in the volume  $V$  of the periodic lattice, so that  $u(\mathbf{r})$  is normalized to unity in the unit cell  $\Omega$ .

The PED cross section writes in this case

$$\frac{d\sigma}{d\hat{\mathbf{k}}} = 4\pi^2 \alpha \hbar \omega \frac{1}{N} \left| \sum_n e^{i(\mathbf{k}_{bz} + \kappa) \cdot \mathbf{R}_n} \sum_L M_L(E; \mathbf{k}_{bz}) (B_L^n(\mathbf{k}))^* \right|^2 \quad (2.18)$$

where now the cell transition matrix element

$$M_L(E; \mathbf{k}_{bz}) = \int_{\Omega} d\mathbf{r} (\Phi_L(\mathbf{r}; k))^* (e^{i\kappa \cdot \mathbf{r}} \boldsymbol{\epsilon} \cdot \mathbf{r}) u_{\mathbf{k}_{bz}}(\mathbf{r}) \quad (2.19)$$

is independent of the cell index  $n$ , but still dependent on the band wave vector  $\mathbf{k}_{bz}$ .

Note however that the propagation amplitude  $B_L^n(\mathbf{k})$  in Eq. (2.10) is not translationally invariant, since it is referred to the common origin of the lattice coordinates. If in the exponent of the last exponential factor we add and subtract the scalar product  $i\mathbf{k} \cdot \mathbf{R}_n$ , then the amplitude

$$B_L^n(\mathbf{k}) = \sqrt{\frac{k}{\pi}} \sum_{jL'} \tau_{LL'}^{nj} i^{j'} Y_{L'}(\hat{\mathbf{k}}) e^{i\mathbf{k} \cdot (\mathbf{R}_j - \mathbf{R}_n)} \quad (2.20)$$

is translationally invariant (independent of  $n$ ), since it depends only on the difference of lattice sites. Therefore we can rewrite Eq. (2.18) as

$$\begin{aligned} \frac{d\sigma}{d\hat{\mathbf{k}}} &= 4\pi^2 \alpha \hbar \omega \frac{1}{N} \left| \sum_n e^{i(\mathbf{k}_{bz} + \boldsymbol{\kappa} - \mathbf{k}) \cdot \mathbf{R}_n} \sum_L M_L(E; \mathbf{k}_{bz}) (B_L(\mathbf{k}))^* \right|^2 \\ &= 4\pi^2 \alpha \hbar \omega \frac{1}{N} \left| \sum_L \overline{M}_L(E) (B_L(\mathbf{k}))^* \right|^2 \left| \sum_n e^{i(\mathbf{k}_{bz} + \boldsymbol{\kappa} - \mathbf{k}) \cdot \mathbf{R}_n} \right|^2 \end{aligned} \quad (2.21)$$

the second equation being valid under the assumption of slow variation of the transition matrix element with  $\mathbf{k}_{bz}$ . This last expression is strongly reminiscent of its diffraction counterpart in Eq. (2.6), in that it factorizes into an electronic part (photo-emission from a localized atom) and a modulating Bragg factor. The similarity is even more striking since in this case  $\mathbf{Q}_{pe} = \mathbf{k}_{bz} + \boldsymbol{\kappa} - \mathbf{k}$  is the actual momentum transfer of the photo-emission process to the crystal, in complete analogy with the photon momentum transfer  $\mathbf{Q}$  in the diffraction experiment.

However one should keep in mind that the finite mean-free path  $\lambda$  of the final state photoelectron is much shorter than the coherent length of the photon in a diffraction experiment, so that the diffracting coherent volume in the two experiments is much different. In the PED case for a  $\lambda$  of the order of 15–20(Å) and in a lattice constant of the order of 3(Å) one can expect  $\approx 100$ –300 sites to contribute coherently to the modulating factor, whereas  $N$  in Eq. (2.21) is expected to be the number of cells inside a volume of linear dimensions of order of 1  $\mu\text{m}$ , the coherence length of the electron in the initial band state  $\phi_{\mathbf{k}_{bz}}(\mathbf{r})$ . In any case the predicted modulation as a function of  $\mathbf{Q}_{pe}$  and the maxima of the cross section when  $\mathbf{Q}_{pe}$  passes through a reciprocal lattice vector, could be checked experimentally.

The coherent emission from many centers collapses into a single site emission for photons in the x-ray regime. In this case the length of  $\mathbf{Q}_{pe}$  can easily be of the order of many reciprocal basis vectors long, “which leads to an effective averaging over a large part of the Brillouin zone due to a combination of finite angular resolution, short electron escape depth, and phonon-assisted indirect transitions” [8]. In fact, due to the relation

$$\frac{1}{N} \sum_{\mathbf{k}_{bz}} e^{i\mathbf{k}_{bz} \cdot \mathbf{R}} = \delta_{\mathbf{R},0} \quad (2.22)$$

we have

$$\frac{1}{N} \sum_{\mathbf{k}_{bz}} \left| \sum_n e^{i(\mathbf{k}_{bz} + \boldsymbol{\kappa} - \mathbf{k}) \cdot \mathbf{R}_n} \right|^2 = 1 \quad (2.23)$$

and the modulation of the coherent many center emission disappears [4, 9].

This is also what happens in the case of photo-emission from a localized core state, which can be considered a valence state with a flat band.

### 2.3.1 Photo-Emission from Homopolar Diatomic Molecules

Photo-emission from a homopolar diatomic molecule is a special case of Eq. (2.21) for  $N = 2$ ,  $\mathbf{R}_n = \pm \mathbf{R}/2$ ,  $k_{bz} = 0, \pi/R$ , if the origin of coordinates lies midway between the two equivalent atoms. We then have, under the assumption that the atomic matrix element  $\overline{M}_L$  be the same for the two band points,

$$\frac{d\sigma}{d\hat{\mathbf{k}}} = 4\pi^2 \alpha \hbar \omega \left| \sum_L \overline{M}_L(E) (B_L(\mathbf{k}))^* \right|^2 (1 \pm \cos(\boldsymbol{\kappa} - \mathbf{k}) \cdot \mathbf{R}) \quad (2.24)$$

where the  $+$  ( $-$ ) sign is for ‘gerade (ungerade)’ initial states, so that the summation over the initial ‘band’ states eliminates the interference term and the coherent emission from the two equivalent atoms collapses to a single site emission. The assumption that an homopolar diatomic molecule is a special case of Eq. (2.21) for  $N = 2$  neglects termination effects of the periodical array of centers, which might be not negligible in a chain of only two atoms. However Eq. (2.24) contains the essential physics.

Equation (2.24) represents the photo-emission realization for an oriented molecule of the celebrated Young’s two-slit experiment, as seen from the similarity with the Eq. (2.3), the photo-electron emission from the single atomic site of the molecule being modulated by the interference factor  $(1 \pm \cos(\boldsymbol{\kappa} - \mathbf{k}) \cdot \mathbf{R})$ . If the detector is placed on a plane parallel to the plane containing the molecule at distance  $z_0$  from this latter with coordinates  $\boldsymbol{\rho}$  with respect to the origin chosen in the same way, this factor reduces to Eq. (2.4), apart from an intensity factor. Note that the momentum  $\boldsymbol{\kappa}$  originates from the atomic matrix element for the creation of the photo-electron and represents the self-interference of the incoming photon. It can be neglected with respect to the photo-electron wave vector for energies up to  $10^4$  eV (see Appendix).

### 2.3.2 The Cohen-Fano Interference Term Revisited

The analogous relation for the photo-absorption cross section, leading to the Cohen-Fano interference term [10], could be derived with some effort from Eq. (2.24) by

integration over the photo-electron momentum  $\mathbf{k}$ , due to its presence in the interference term. More physical insight however could be gained by calculating directly the photo-absorption cross section from the knowledge of the Full Green's Function (FGF) of the molecule in the independent particle approximation.

A distinctive feature of MS theory is that one can write the FGF of the system under consideration in terms of the scattering path operator  $\tau$  and the local cell solutions  $\Phi_L^n(\mathbf{r}_n; k)$  as [11]

$$G^+(\mathbf{r}_i, \mathbf{r}'_j; E) = \sum_{LL'} \Phi_L^i(\mathbf{r}_i; k) \tau_{LL'}^{ij} \Phi_{L'}^j(\mathbf{r}_j; k) - \delta_{ij} \sum_L \Phi_L^i(\mathbf{r}_{<}; k) \Lambda_L^j(\mathbf{r}'_>; k) \quad (2.25)$$

where  $\Lambda_L^j(\mathbf{r}_{>}; k)$  is the irregular solution of the SE inside cell  $\Omega_j$  matching smoothly to the Bessel function  $J_L(\mathbf{r}; k) = j_l(kr) Y_L(\hat{\mathbf{k}})$  on the bounding sphere of the cell. As usual,  $\mathbf{r}_i = \mathbf{r} - \mathbf{R}_i$  where  $\mathbf{R}_i$  is the origin of cell  $\Omega_i$  and  $\mathbf{r}_{<}$  is the lesser of  $r_i, r'_j$ . For simplicity of presentation we assume here that the potential in the SE is real. In this case the singular part of the FGF is real, so that its imaginary part is zero. The general case of a complex potential describing inelastic processes is treated in Ref. [4]. However the conclusions derived here are very similar to those of the complex case, especially for what concerns the elastic processes describing coherent effects.

From the spectral representation of the FGF

$$G^+(\mathbf{r}, \mathbf{r}'; E) = \sum_n (\Psi_n(\mathbf{r}) \Psi_n^*(\mathbf{r}')) / (E - E_n + i\eta) \quad (2.26)$$

where  $n$  runs over all bound and continuum states of the SE it is easy to show that

$$\sigma_{abs}(\omega) = -4\pi\alpha\hbar\omega\theta(E - E_F) \times \int \langle \phi_{L_c}^c(\mathbf{r}) | e^{i\mathbf{k}\cdot\mathbf{r}} \boldsymbol{\epsilon} \cdot \mathbf{r} | \mathfrak{I} G^+(\mathbf{r}, \mathbf{r}'; E) | e^{-i\mathbf{k}\cdot\mathbf{r}'} \boldsymbol{\epsilon} \cdot \mathbf{r}' | \phi_{L_c}^c(\mathbf{r}') \rangle d\mathbf{r} d\mathbf{r}' \quad (2.27)$$

from an initial core state localized at site  $c$ . The  $\theta$  function assures that transitions are possible only to unoccupied states above the Fermi energy  $E_F$  of the system, defined to lie between the HOMO and LUMO states of the molecule. The insertion of the expression (2.25) for the FGF into this last relation leads directly to the Eq. (2.14).

Now if the initial state  $\phi_{is}(\mathbf{r})$  is instead delocalized over the two equivalent sites 1 and 2 of the molecule such that ( $\mathbf{r}_i = \mathbf{r} \pm \mathbf{R}/2$ ;  $i = 1, 2$ )

$$\phi_{is}(\mathbf{r}) = \frac{1}{\sqrt{2}} (\phi(\mathbf{r}_1) \pm \phi(\mathbf{r}_2)) \quad (2.28)$$

we easily find

$$\sigma_{abs}(\omega) = -4\pi \alpha \hbar \omega \left( \sum_{LL'} M_L(E) \Im \tau_{LL'}^{11} M_{L'}^*(E) \pm \cos(\boldsymbol{\kappa} \cdot \mathbf{R}) \sum_{LL'} M_L(E) \Im \tau_{LL'}^{12} M_{L'}^*(E) \right) \quad (2.29)$$

due to the equivalence of the two sites. Again the + sign is for a ‘gerade’ initial state, the – for a ‘ungerade’ state. Notice the factor  $\cos(\boldsymbol{\kappa} \cdot \mathbf{R})$  arising from the photon self-interference terms  $e^{\pm i\boldsymbol{\kappa} \cdot \mathbf{R}}$  associated with the product  $M_L(E) M_{L'}^*(E)$ . We have assumed for simplicity that the orbitals  $\phi(\mathbf{r}_i)$  are confined inside the respective cells, but the generalization is straightforward.

In the independent particle approximation, Eq. (2.29) is the exact expression for the total absorption cross section of the molecule. It consists of two terms, the first of which is the usual term describing processes in which the emitting atom acts also as a detector, measuring the interference between the outgoing and the incoming photo-electron wave and leading to EXAFS-like oscillations in the cross section with maximum  $k$  period of  $\Delta k = 2\pi/2R = \pi/R$ . The second term instead describes processes where one atom acts as the emitter and the other as the detector (and viceversa), originating oscillations in the cross section with maximum period  $\Delta k = 2\pi/R$ . This is the lowest order feature of other higher order oscillations of this type present in the absorption cross section with period  $\Delta k = 2\pi/nR$ , where  $n$  is any odd integer number, although their intensity fades away quite rapidly with increasing photo-electron energy. From this point of view the comparison of this interference term with the Young’s two-slit experiment is misleading, since in this case one of the source points measures the intensity of the photo-electron wave arriving from the other.

In order to make contact with Cohen-Fano’s assumptions in deriving their expression, we work in the Born approximation, use the muffin-tin approximation for the atomic scattering amplitudes ( $T_{LL'} \approx t_l/k\delta_{LL'} = -1/k e^{i\delta_l} \sin \delta_l$ ), where  $\delta_l$  is the  $l$ th phase shift of the spherically averaged atomic potential, and assume initial  $\phi_{1s}(\mathbf{r}_i)$  orbitals, so that an  $l = 1$  final state is selected by the dipole transition matrix element.

In the Born approximation, according to Eq. (2.11),  $\tau_{LL'}^{ii} \approx t_l$  and  $\tau_{LL'}^{12} \approx t_l^2 G_{LL'}^{12}$ . Using the following approximation for the free spherical wave propagator[4]

$$G_{LL'}^{ij} \approx -4\pi \frac{e^{ikR_{ij}}}{kR_{ij}} Y_L(\hat{\mathbf{R}}_{ij}) Y_{L'}(\hat{\mathbf{R}}_{ij}) i^{(l-l')} \quad (2.30)$$

where  $R_{ij}$  is the length of the vector  $\mathbf{R}_{ij}$  joining the two sites  $i$  and  $j$  ( $\mathbf{R}$  in our case), from Eq. (2.29) we find

$$\sigma_{abs} \approx \sigma_{at} \left( 1 \pm \frac{\sin(kR + 2\delta_1)}{kR} \right) \quad (2.31)$$

where  $\sigma_{at} = |M_l|^2/k^2 \sin^2 \delta_l$  ( $l = 1$ ) is the atomic absorption. As in Ref. [10] we have taken  $\mathbf{R}_{ij}$  along the  $z$ -axis so that  $1/3 \sum_m |Y_{1m}(\hat{\mathbf{R}}_{ij})|^2 = 1/(4\pi)$ , and considered the unpolarized cross section.

Notice that we have also neglected the photon self-interference factor  $\cos(\boldsymbol{\kappa} \cdot \mathbf{R})$  to second order as done by Cohen and Fano (the first order was shown to be zero by these authors). Retaining this term would introduce further oscillations in the cross section related to the photon wave vector  $\boldsymbol{\kappa}$ .

The phase shift  $2\delta_1$  has the same origin as for the EXAFS term and was also found by Liu et al. [12] taking into account MS within the molecule. It was missed by Cohen and Fano due to their simplifying assumption on the final photo-emission state that was assumed to be a plane wave. It can be important though in the determination of the bond length since it might not be negligible. The fact that the bond length of  $N_2$  and  $O_2$  molecules measured from delocalized valence states was found shorter than the equilibrium one might be related to its omission [13]. Notice that vibrational effects may be treated as done customarily in the standard MS Theory.

## 2.4 Photo-Emission from Eteropolar Diatomic Molecules

The non periodic case (e.g. photo-emission from molecular valence states) can be treated, *mutatis mutandis*, along the same lines as in Sect. 2.3 and leads to the expression

$$\frac{d\sigma}{d\hat{\mathbf{k}}} = 4\pi^2 \alpha \hbar \omega \left| \sum_n e^{i\mathbf{k} \cdot \mathbf{R}_n} \sum_L M_L^n(E) (B_L^n(\mathbf{k}))^* \right|^2 \quad (2.32)$$

where we have partitioned the molecular volume in cells  $\Omega_n$  so that

$$M_L^n(E) = \int_{\Omega_n} d\mathbf{r}_n (\Phi_L^n(\mathbf{r}_n; k))^* (e^{i\mathbf{k} \cdot \mathbf{r}_n} \boldsymbol{\epsilon} \cdot \mathbf{r}_n) \phi_n^v(\mathbf{r}_n) \quad (2.33)$$

indicating in each cell by  $\phi_n^v(\mathbf{r}_n)$  the local solution of the initial valence state and by  $\Phi_L^n(\mathbf{r}_n; k)$ , as before, the local solution of the excited continuum photo-emission state.

Despite the fact that the various sites (cells) are not equivalent, there seems to be a sort of coherence between photo-emission from the various cells. We defer the discussion on this point until after treating the case of the eteropolar diatomic molecule.

Emission from valence molecular states in terms of photoelectron wave interference, caused by initial state delocalization and final state photoelectron scattering has also been treated by Krüger in Ref [14], but without making explicit the photon phase factor.

Specializing to eteropolar diatomic molecules, in the spirit of LCAO theory, we write the initial valence state as

$$\phi_{is}^v(\mathbf{r}) = c_1 \phi_1^v(\mathbf{r}_1) + c_2 \phi_2^v(\mathbf{r}_2) \quad (2.34)$$

Assuming for simplicity that the two orbitals  $\phi_i^v(\mathbf{r}_i)$  are localized inside the respective cell  $\Omega_i$ , the normalization condition reads

$$\sum_i c_i^2 \int_{\Omega_i} d\mathbf{r}_i |\phi_i^v(\mathbf{r}_i)|^2 = 1 \quad (2.35)$$

In order to get some insight into the physics, we treat directly the case of photoabsorption, using the expression for the FGF given in Eq. (2.25) and the formula for photoabsorption Eq. (2.27). It is easy to convince oneself that by integrating over  $d\hat{\mathbf{k}}$  Eq. (2.32) and using Eq. (2.13) one arrives at the same result.

Starting from the initial state Eq. (2.34) we find

$$\begin{aligned} \sigma_{abs}(\omega) = & -4\pi\alpha\hbar\omega \left( \sum_i^{1,2} c_i^2 \sum_{LL'} M_L^i(E) \Im \tau_{LL'}^{ii} (M_{L'}^i)^*(E) \right. \\ & \left. + \sum_{i \neq j}^{1,2} c_i c_j \cos(\boldsymbol{\kappa} \cdot \mathbf{R}_{ij}) \sum_{LL'} M_L^i(E) \Im \tau_{LL'}^{ij} (M_{L'}^j)^*(E) \right) \quad (2.36) \end{aligned}$$

due to the symmetry  $\tau_{LL'}^{ij} = \tau_{LL'}^{ji}$  holding in real Spherical Harmonic basis, which we use, and indicating by  $\mathbf{R}_{ij} = \mathbf{R}_i - \mathbf{R}_j$ .

As for the homopolar case, under the same assumptions and in the Born approximation for  $\tau$  we find a result very similar to the homopolar case:

$$\sigma_{abs} \approx \sum_i^{1,2} c_i^2 \sigma_{at}^i + 2c_1 c_2 \frac{\sin(kR + \delta_l^1 + \delta_l^2)}{kR} \sqrt{\sigma_{at}^1} \sqrt{\sigma_{at}^2} \quad (2.37)$$

where  $\sigma_{at}^i = |M_l^i|^2/k^2 \sin^2 \delta_l^i$  and  $R = R_{ij}$ . The oscillatory behavior with periodicity  $2\pi/R$  is not an artifact of the theory and was found experimentally in the  $1\pi^{-1}$  ionization of the eteropolar molecule CO. In this case the  $\phi_i^v(\mathbf{r}_i)$  orbitals are approximately  $2p$  Carbon and Oxygen atomic states so that the main transition is to  $l = 2$  [15]. This observation was termed ‘unexpected’ in Ref. [16].

Therefore we are forced to conclude that coherent emission from atomic sites does not necessarily require their equivalence. It is sufficient that the initial state be delocalized over different atomic sites as shown clearly by the expression (2.32). The Cohen-Fano oscillations are therefore the reflection of this fact, rather than the indication of the realization of a kind of microscopic Young type of experiment, although the indistinguishability of the various emitting sites, whether equivalent or not, is at the basis of the interference process.

In this respect MS Theory is the language of election for the description of such phenomena, because it brings to the fore the coherence of the various emission processes and their connection with the atomic structure. Other languages do not provide such insight. They solve the SE for continuum states with reference to a single center (usually the origin) and obviously provide the same answer as obtained by MS Theory, but without providing the same physical insight.

## 2.5 Conclusions

We have shown that when the initial state in a photo-emission process is extended over many atomic sites, whether equivalent or not, it generates new MS processes compared to the case of emission from a single localized site, due to the fact that emission from different sites is coherent, as dictated by the Feynman's rules. In photoabsorption, these processes are characterized by the fact that the emitter does not coincide with the detector, as in the case of a localized emitter (whereby EXAFS type of oscillations are generated in the cross section), but two atoms at a time share this role, giving rise to a propagation of the photo-electron wave between the two sites with maximum period longer than the EXAFS period. This case encompasses the emission from delocalized occupied states of diatomic molecules and characterizes the Cohen-Fano interference term as the lowest order of such new processes, rather than the realization of a microscopic Young type of experiment.

## Appendix

We list here for the benefit of the reader some useful relations between the photon and the electron wave lengths and wave vectors as a function of their energy expressed in eV.

### For electrons

$$\lambda_e(\text{\AA}) = 12.26/\sqrt{E_e(eV)} \quad k_e(\text{\AA}^{-1}) = 2\pi/\lambda_e(\text{\AA}) = 0.5123\sqrt{E_e(eV)} \quad (2.38)$$

### For photons

$$\lambda_{ph}(\text{\AA}) = 12398.4/E_{ph}(eV) \quad \kappa_{ph}(\text{\AA}^{-1}) = 2\pi/\lambda_{ph}(\text{\AA}) = 5.068 \times 10^{-4}E_{ph}(eV) \quad (2.39)$$



Therefore the numerical ratio of the photon and electron wave number expressed in ( $\text{\AA}^{-1}$ ) is

$$\kappa_{ph}(\text{\AA}^{-1})/k_e(\text{\AA}^{-1}) \approx 10^{-3} E_{ph}(eV)/\sqrt{E_e(eV)} \quad (2.40)$$

## References

1. R.P. Feynman A.R. Hibbs. *Quantum Mechanics and Path Integrals. International Series in Pure and Applied Physics* (McGraw-Hill, 1965)
2. R.P. Feynman, *QED: the Strange Theory of Light and Matter*. Princeton Science Library. pub-PRINCETON (2013)
3. Y. Tikochinsky, Feynman rules for probability amplitudes. *Int. J. Theoret. Phys.* **27**, 543–549 (1988)
4. D. Sébilleau, R. Gunnella, Z.-Y. Wu, S. Di Matteo, C.R. Natoli, Multiple-scattering approach with complex potential in the interpretation of electron and photon spectroscopies. *J. Phys. Condens. Matter* **18**(9), R175–R230 (2006)
5. K. Hatada, K. Hayakawa, M. Benfatto, C.R. Natoli, Full-potential multiple scattering theory with space-filling cells for bound and continuum states. *J. Phys.: Condens. Matter*, **22**(18):185501 (2010)
6. J.J. Barton. Photoelectron holography. *Phys. Rev. Lett.* **61**, 1356–1359 (1988)
7. C.S. Fadley, S. Thevuthasan, A.P. Kaduwela, C. Westphal, Y.J. Kim, R. Ynzunza, P. Len, E. Tober, F. Zhang, Z. Wang, S. Ruebush, A. Budge, M.A. Van Hove, Photoelectron diffraction and holography: Present status and future prospects. *J. Electron Spectrosc. Related Phenomena* **68**, 19–47 (1994)
8. J. Osterwalder, T. Greber, P. Aebi, R. Fasel, L. Schlapbach, Final-state scattering in angle-resolved ultraviolet photoemission from copper. *Phys. Rev. B* **53**, 10209–10216 (1996)
9. P. Krüger, F. Da Pieve, J. Osterwalder, Real-space multiple scattering method for angle-resolved photoemission and valence-band photoelectron diffraction and its application to cu(111). *Phys. Rev. B* **83**, (Mar 2011)
10. H.D. Cohen, U. Fano, Interference in the photo-ionization of molecules. *Phys. Rev.* **150**, 30–33 (1966)
11. D. Sébilleau, K. Hatada, H. Ebert. Multiple scattering theory for spectroscopies: a guide to multiple scattering computer codes—dedicated to C. R. Natoli on the occasion of his 75th birthday. *Springer Proceedings in Physics* (Springer International Publishing, 2018)
12. X.-J. Liu, N.A. Cherepkov, S.K. Semenov, V. Kimberg, F. Gelmukhanov, G. Prümper, T. Lischke, T. Tanaka, M. Hoshino, H. Tanaka, K. Ueda, Young’s double-slit experiment using core-level photoemission from  $N_2$ : revisiting Cohen-Fano’s two-centre interference phenomenon. *J. Phys. B: Atomic, Mol. Opt. Phys.* **39**(23), 4801–4817 (2006)
13. M. Ilchen, L. Glaser, F. Scholz, P. Walter, S. Deinert, A. Rothkirch, J. Seltmann, J. Viefhaus, P. Declava, B. Langer, A. Knie, A. Ehresmann, O.M. Al-Dossary, M. Braune, G. Hartmann, A. Meissner, L.C. Tribedi, M. AlKhalidi, U. Becker, Angular momentum sensitive two-center interference. *Phys. Rev. Lett.* **112**, (2014)
14. P. Krüger, Photoelectron diffraction from valence states of oriented molecules. *J. Phys. Soc. Jap.* **87**(6) (2018)
15. S.E. Canton, E. Plésiat, J.D. Bozek, B.S. Rude, P. Declava, F. Martin, Direct observation of Young’s double-slit interferences in vibrationally resolved photoionization of diatomic molecules. *Proc. Natl Acad. Sci. USA* **108**, 7302–7306 (2011)
16. U. Becker, Matter-wave interference made clear. *Nature* **474**, 586–587 (2011)

# Chapter 3

## DAΦNE-Light: The INFN-LNF Synchrotron Radiation Facility



**Marco Angelucci, Antonella Balerna, Roberto Cimino,  
Mariangela Cestelli-Guidi, Antonio Grilli, Marco Pietropaoli, Agostino Raco,  
Vittorio Sciarra, Vinicio Tullio, and Giacomo Viviani**

**Abstract** DAΦNE-Light is the Synchrotron Radiation Facility at the INFN-Frascati National Laboratory (LNF). The electron storage ring used is part of the 0.5 GeV DAΦNE electron-positron collider that, with a routinely circulating electron current over 1.5 A, provides a very high photon flux in the low energy region, from IR region to soft x-rays. The use of synchrotron radiation for interdisciplinary studies, in many different fields, was developed at the LNF from 1978 to 1993 with the beamlines built to use, as synchrotron radiation source, the old ADONE 1.5 GeV collider. At the DAΦNE-Light facility there are five beamlines that can work independently and a white beam XUV branch line. Three beamlines are operational, using in parasitic and dedicated mode the intense photon emission of DAΦNE while the two XUV bending magnet beamlines and also the white light branch line, are nowadays under commissioning. A presentation of the facility together with some information on recent projects and scientific results will be given.

### 3.1 Introduction: The DAΦNE-Light Facility

The National Institute of Nuclear Physics (INFN), the Italian agency devoted to fundamental research in nuclear and sub-nuclear physics, has in Italy four big laboratories and the Frascati National Laboratory (LNF) is the oldest and largest one. The LNF is also well known for many important studies performed, also in the past, and related to the use of synchrotron radiation. At the end of the high-energy physics program, the electron-positron collider ADONE was used as partially dedicated synchrotron radiation source (1978–1993) [1–3]. In 1993 the operation of ADONE ended and the DAΦNE (Double Annular  $\Phi$ -factory for Nice Experiments) high-luminosity, 0.51 GeV, electron-positron collider was built for high energy physics experiments. Due to its low electron energy and high current, the DAΦNE collider provides a

---

M. Angelucci · A. Balerna (✉) · R. Cimino · M. Cestelli-Guidi · A. Grilli · M. Pietropaoli ·  
A. Raco · V. Sciarra · V. Tullio · G. Viviani  
INFN-Frascati National Laboratory, Frascati (RM), Italy  
e-mail: [antonella.balerna@Inf.infn.it](mailto:antonella.balerna@Inf.infn.it)  
URL: <http://dafne-light.lnf.infn.it>

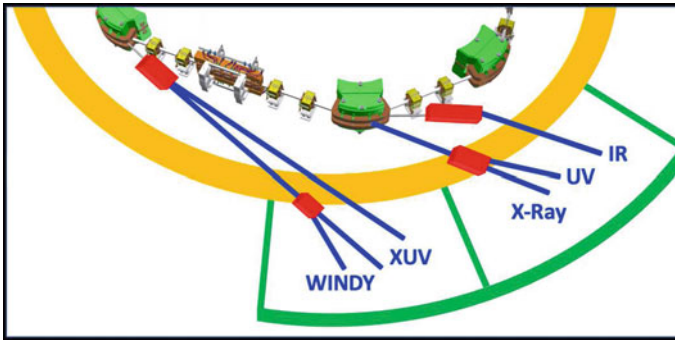


**Fig. 3.1** Schematic view of the DAΦNE-Light synchrotron radiation facility. In the figure the LEB and HEB XUV beamlines are indicated as XUV while X-Ray, UV and IR represent respectively the DXR1 (Soft X-ray), the DXR2 (UV-Vis) and the SINBAD-IR beamlines

very high flux in the low energy region and for this reason it is nowadays also being used as a not dedicated synchrotron radiation (SR) source [4, 5]. A schematic view of the DAΦNE-Light facility is reported in Fig. 3.1. In this small facility there are five independent beamlines. Three of them, the infrared (SINBAD-IR), the UV-Vis (DXR2) and the soft x-ray (DXR1) ones, are operational, while the two XUV (LEB and HEB) beamlines and the WINDY branch line are under commissioning. Only the DXR2 and the DXR1 beamlines have as synchrotron radiation source one of the DAΦNE 6-poles equivalent planar wiggler magnets while all the other beamlines collect the radiation produced by bending magnets. About 40 experimental teams, coming from Italian and European Universities and Research Institutions, receive beamtime at the DAΦNE-Light facility every year. The facility provides transnational access also within the H2020 EU Project CALIPSOplus [6]. A short overview of all beamlines and of some experimental results are herein reported.

### 3.2 SINBAD-IR Beamline

SINBAD (Synchrotron Infrared Beamline At DAΦNE) is the first Italian beamline operating with infrared radiation. The experimental activity at the SINBAD-IR beamline concerns micro-imaging and FTIR (Fourier Transform InfraRed) spectroscopy and imaging applied to different research and technological fields. The beamline is characterised by an optical system made of six Au-coated mirrors sending the IR radiation to an end station placed at about 25 m from the source [7]. The end station is a Bruker Vertex 70v interferometer coupled to a Hyperion 3000 IR microscope, equipped with a  $64 \times 64$  pixel Focal Plane Array (FPA) detector to perform chemical imaging with a diffraction-limited spatial resolution.

The Vertex 70v interferometer can operate in reflection, transmission and ATR (Attenuated Total Reflection) mode. The Hyperion 3000 microscope was upgraded

with a high-resolution visible camera, together with a faster image acquisition board and a 100micron MCT or mercury cadmium telluride narrow band detector. For offline analyses the laboratory is also equipped with a MID-IR Tensor II spectrometer, coupled to a High Throughput Scanner (HTS-XT) to perform analysis on multi-well silicon plates. For in-situ preparation of biological samples a clean chamber is available for cell culture growth.

The beamtime requests at the SINBAD IR beamline are mainly directed towards high-pressure studies, micro-spectroscopy in solid-state physics, earth science [8, 9], space science [10], biology [11], and live cell imaging [12, 13], reflectance-absorption studies related to material science [14], chemistry and cultural heritage [15–17].

Among the recent experimental results achieved and published, particular relevance must be given to mid-infrared studies of plasmons in three-dimensional nanoporous graphene [14]. It is well known that graphene is the first thermodynamically stable two-dimensional material found in nature and that it has very important properties like high electron mobility (Dirac electrons), strong interaction with the electromagnetic field, high thermal conductivity and high mechanical hardness. In recent years, research has focused on providing a third dimension in graphene. These topological structures [14] help to preserve the extraordinary electrical properties and thermodynamic properties of 2D graphene extending them to the third dimension. The porous or filamentous nature, and the high surface/volume ratio of these 3D architectures opens up interesting applications and fundamental physics scenarios: from superconductivity, for batteries and super-capacitors uses, flexible electronics, photonics up to infrared and terahertz and plasmonics. These electromagnetic properties have been studied through a collaboration between different Institutions [14]. 3D nano-porous graphene structures plasmonic absorption modes up to the mid-infrared were measured at the SINBAD beamline.

The SINBAD-IR beamline has been recently involved in research projects related to the study and characterisation of materials for cultural heritage. The ADAMO-DTC [18] project (Technologies of Analysis, Diagnostics and Monitoring for the preservation and restoration of Cultural Heritage), in partnership with other research institutions and universities, is funded by the Italian Lazio Region and is dedicated to the development of diagnostic technologies to be applied in archaeological sites in the Roman south-area. In the area of the large suburban Roman villa called “*Villa della Piscina*” numerous fragments of frescoes realised in different ages were found. The aim of the analyses carried out at DAΦNE-Light is to support the reconstruction of the frescoes fragments (see Fig. 3.2) and their dating from the materials composition and the realisation technologies.

### 3.3 DXR2 UV-VIS Beamline

The DXR2 beamline at DAΦNE-Light operates with UV radiation on an extended spectral range from 120 to 650nm (2–10 eV). A vertical Au-coated silicon mirror

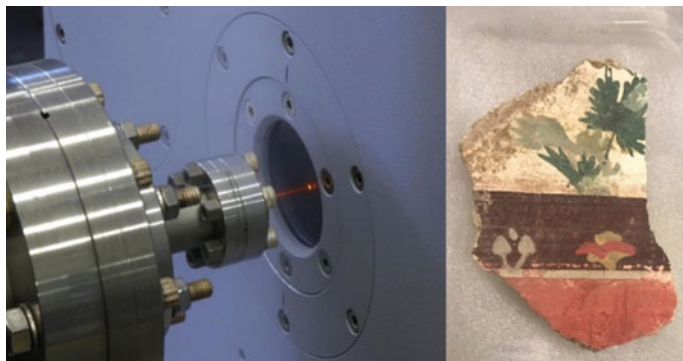
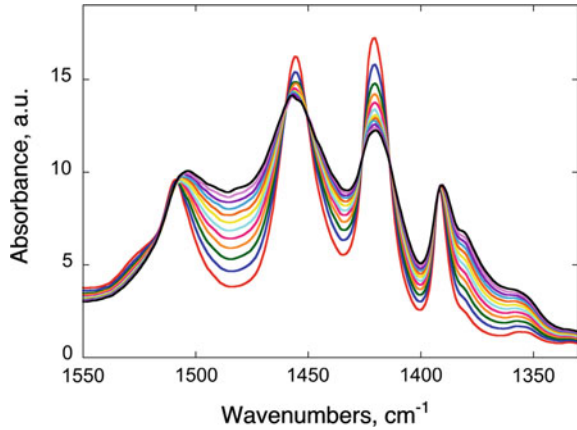


**Fig. 3.2** SINBAD-IR beam and one of the fragments of the frescoes studied

(80 cm  $\times$  10 cm) is used for deflecting, in the horizontal plane and at a grazing angle of about  $2.2^\circ$ , half of the synchrotron radiation photon beam produced by the same wiggler of the soft x-ray beamline, into this UV branch line ending with a 63 mm diameter  $\text{MgF}_2$  window. The experimental apparatus installed after the exit window of this branch line allow to work with the white beam, monochromatic radiations in the 180–650 nm range using a Czerny-Turner monochromator and with VUV radiation in the 120–250 nm range using a H20-UVL Horiba Jobin Yvon monochromator. An experimental chamber that can be installed at the end of the different optical systems was designed to perform many kind of measurements like reflectivity, absorption, scattering, detector calibration, etc. The UV light has been used at the DXR2 branch-line in many and different research fields from biological [19] to R&D for high energy physics experiments, to study solar-blind UV diamond-based detectors or UV aging effects on memory foam used as shock-absorbing foam also in space missions. Furthermore, coupling the UV radiation and IR spectroscopy [20] it was also possible to study the evolution of analysed samples in real time, measuring the variation of IR spectra during UV exposures and this has been used in the study UV irradiated nucleobases adsorbed on mineral surfaces related to the prebiotic evolution of complex chemical systems [21]. These studies are very important in the astrobiology context where the study of the interactions between electromagnetic radiation and bio-molecules is particularly relevant to investigate the physicochemical mechanisms that lead to the synthesis of complex chemical compounds in space. Electromagnetic radiation is one of the main responsible of bio-molecule chemical evolution in space promoting photochemical reactions on surfaces of planets, meteorite grains or cosmic and cometary dusts. In Fig. 3.3 the big changes in the IR spectra of the uracil molecules as a function of UV irradiation [21] are shown.

A UV-enhanced CCD camera is available at the beamline to perform experiments but also to achieve information on the UV spot size and distribution, to evaluate the presence and distribution of spurious signals, stray-light and the amount of unfocused or uncollimated light (depending on the position along the optical path).

**Fig. 3.3** IR absorbance spectra of uracil molecules plotted as a function of the UV irradiation time (from red to black after 72 min) [21]



Studies have also been performed on materials such as synthetic diamonds and tellurium-based ternary compounds to develop UV and IR radiation detectors with high sensitivity and temporal response. In order to read signals from these fast systems, a transimpedance preamplifier for ultrafast signals, of the order of 1 ns, with a very wide bandpass (4 GHz) and high gain (40 dB) and an oscilloscope (HDO9404 Teledyne LeCroy) which simultaneously offers a very wide bandwidth, an high sampling rate and low noise are available at the beamline.

In the control hutch of this beamline a SEM (Scanning Electron Microscope) microscope with a EDX (Energy Dispersive X-ray Spectroscopy) system was installed. This instrument allows nano- and micro-scale pre-analysis of samples to be measured providing morphological as well as elemental distribution information.

### 3.4 DXR1 Soft X-ray Beamline

The DXR-1 DAΦNE-Light soft X-ray beamline [22], is mainly dedicated to X-ray absorption spectroscopy (XAS). The X-ray source of this beamline is one of the 6-poles equivalent planar wiggler devices installed on the DAΦNE electron ring. This radiation source and the high electron current (higher than 1.5 A) give a useful X-ray flux well beyond ten times the critical energy (296 eV). The useful energy range goes from 900 eV up to 3000 eV where the lower limit is given by the Beryl crystals and the higher limit depends on the wiggler working conditions. The soft x-ray beamline accepts a vertical beam divergence of about 1 mrad and an horizontal one of 12 mrad.

From 2015, after some preliminary test, the beamline received the authorisation to work also during beam injections due to the stable beam conditions. The beamline is equipped with a Toyama double-crystal monochromator working in “boomerang” geometry and there are different sets of crystals (Beryl (10-10), KTP (011) InSb (111) Ge (111)) that can be used to cover the available soft X-ray range. An experi-



**Fig. 3.4** The finger-like structure of the ARDESIA 4-channel SDD

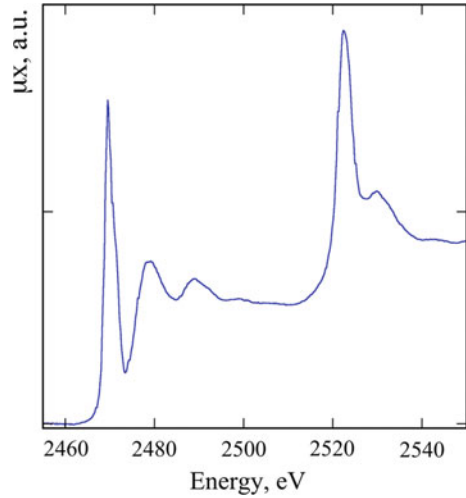
mental HV chamber can be used to allocate several samples for XAS measurements in transmission mode measuring the with two ionisation chambers the incoming monochromatic flux ( $I_0$ ) and the transmitted flux ( $I_1$ ). In the near future it will be also possible to perform XAS measurements in fluorescence mode. A 4-channel Silicon Drift Detector (SDD), named ARDESIA and developed by INFN, the Politecnico di Milano and FBK (Fondazione Bruno Kessler) [23–25], was tested at the beamline. The ARDESIA detector has a finger-like structure (Fig. 3.4) to be introduced in the experimental chamber using a specific vacuum-tight translating system and has a thin polymer entrance window with high transmission in the soft X-ray region [23, 24].

Beamtime at the DXR1 beamline is usually asked for XAS spectroscopy measurements but, as in the case of ARDESIA, it can also be used to test detectors and sometimes optical elements. XAS spectroscopy is useful to perform a local structural characterisation of different kind materials, being very sensitive to the formal oxidation states, coordination chemistry (Fig. 3.5), distances, coordination numbers of the atoms surrounding the selected atomic elements. Important studies were performed on anticancer metallodrugs [26], hydrogen storage materials [27] and many other fields like earth silicides [28].

### 3.5 XUV LEB and HEB Beamlines and the WINDY Branch Line

Two bending magnet XUV beamlines cover the photon energy range from 30 to 1000 eV and are under commissioning. The characteristics of DAΦNE as a synchrotron radiation source in this energy range are very interesting, mainly due to its very high flux ( $2 \times 10^{13}$  ph/s/mrad/0.1%bw at the critical energy) in the vacuum ultraviolet and soft x-ray region (5–1000 eV). The two beamlines get full advantage not only of the high beam current circulating in the ring (higher than 1.5 A) but also of the

**Fig. 3.5** XAS spectra at the S K-edge and Mo L<sub>3</sub>-edge in of a MoS<sub>2</sub> sample where  $\mu x = \ln(I_0/I_1)$



possibility of inserting their pre-optics very close to the electron source, in order to collect a significant fan of the horizontal radiation emitted by a bending magnet without the need of expensive and huge optical elements.

The beamline covering the low energy part of this energy range from 30 to 150 eV is called LEB (Low Energy Beam line) while the other covering the range from 60 to 1000 eV is called HEB (High Energy Beam line).

The location of the first optics of the LEB within the accelerator tunnel ensures the collection of a very high photon flux. The synchrotron light is then focused at the entrance slit of a grazing incidence spherical monochromator. Finally, a refocusing system collects the light from the monochromator exit slit and focuses it on the sample under study. The goal of this beamline is to deliver a high photon flux in the energy range 30 eV-150 eV with a resolution  $R \geq 3000$  (more details can be found in Ref. [29]).

The HEB is based on a plane grating monochromator equipped with two gratings (lower energy range (60–600) eV, higher energy range (250–1000) eV) to perform experiments of X-ray absorption, photoemission, resonant photoemission and photoelectron diffraction applied to bulk, surfaces, interfaces, and interdisciplinary research. The expected resolving power is ranging between 1000 and 5000 with a photon flux higher than  $10^{12}$  ph/s/1%bw in the entire energy range.

Both beamlines are in ultra high vacuum (UHV) and directly connected to the vacuum of the main DAΦNE ring and all their safety protocols and control systems have been tested. Being both under commissioning, up to now, after a careful alignment, their white light (WL) has been reflected/collimated by the ad hoc optics, inside accelerator building, to be transported into the 20 m far laboratory.

In June 2017 a Memorandum of Understanding (MoU) between CERN and INFN-LNF was signed concerning studies of reflectivity, photo-yield and photo induced desorption on small samples and on real beam pipes, by using the synchrotron radi-



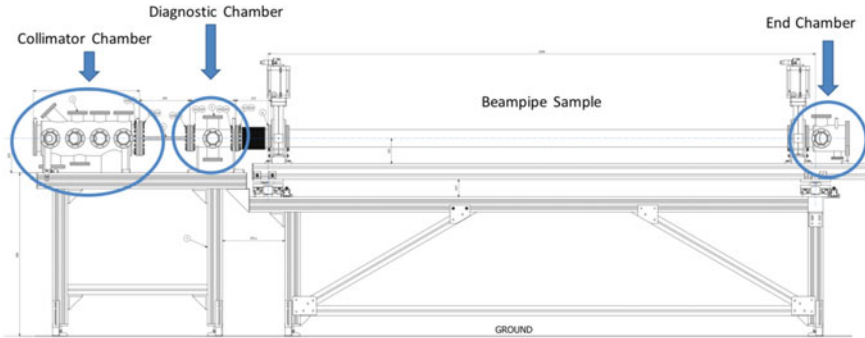


**Fig. 3.6** Schematic view of the WINDY branch line

ation white light of DAΦNE. The aim of this collaboration is to extract quantitative information for the optimisation of existing and planned accelerators like the Large Hadron Collider (LHC) and its High Luminosity planned upgrade (HL-LHC) and for planning and designing the future circular colliders (FCC) of various types. For this specific application a branch line fully devoted to white light studies of real beam pipes provided by CERN has been realised (see Fig. 3.6). A mirror chamber has been installed on the HEB to deflect the white beam into a new branch line WINDY (White lIght liNe for Desorption Yields) that will be used to irradiate long (up to 2–3 m) samples, to obtain complementary data to the ones obtainable on small surface samples from the other two beamlines. This would allow to extract quantitative information on surface reflectivity, electron and photo-induced desorption yield, secondary electron emission, chemical modifications etc., both on small samples and on real beam pipes, making the laboratory a powerful tool to study and qualify materials for accelerators. A photo of the two XUV beamlines and of the WINDY branch line is shown in Fig. 3.7. Two state-of-the-art end stations have been implemented and are successfully used at the moment with conventional sources to perform x-ray photoelectron spectroscopy (XPS) and secondary electron yield (SEY) [30–33] studies like the ones related to cryogenic vacuum and its stability upon photon, electron and/or ion irradiation. In order to perform these studies there was the need to measure all surface properties at very low operating temperatures. For this purpose, a cryogenic manipulator, is now available, on both systems, to routinely measure, at low temperatures, SEY on various cold surfaces in the presence of various adsorbates. At the moment it is possible to study desorption processes [34] thermally induced or induced by different irradiation processes (like electron or photon irradiation) on different surfaces but also use the experience gained in collaborations with other institutions [35]. The laboratory has been also equipped with an in air scanning tunneling microscope (STM), upgraded to be used at variable temperatures and in UHV, incrementing the analysis capabilities for funded studies as well as the general appeal and the available techniques of the laboratory.

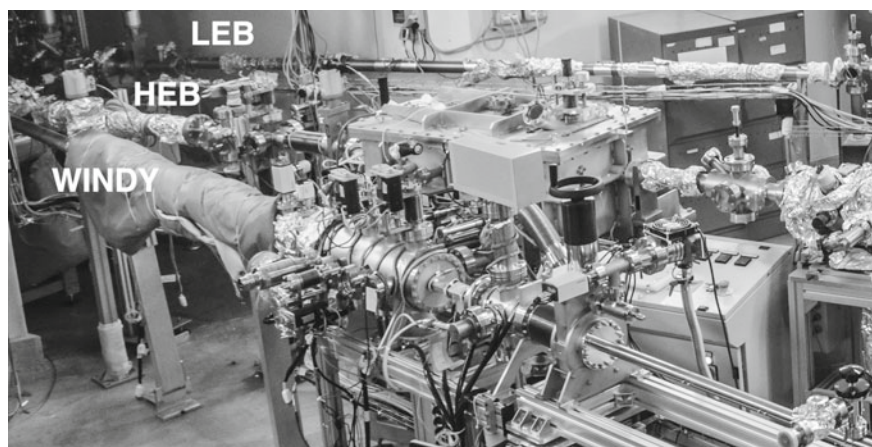


**Fig. 3.7** The two LEB and HEB XUV beamlines and the WINDY branch line

### 3.6 Conclusions

In the near future the DAΦNE-Light facility will continue giving beam-time to experimental proposals submitted by European users within the EU CALIPSOplus Transnational Access program, non EU and Italian users. Upgrades of the experimental setup will be performed and after the end of the commissioning of the the XUV lines there will be 5 beamlines and a branch line fully operational.

### References

1. E. Burattini, Synchrotron radiation research in Italy: the early years. *Synchrotron Radiat. News* **29**(2), 33–37 (2016). <https://doi.org/10.1080/08940886.2016.1149432>
2. A. Savoia, Frascati synchrotron radiation facility. *Synchrotron Radiat. News* **1**(3), 10–13 (1988). <https://doi.org/10.1080/08940888808602496>
3. R. Cimino, E. Burattini, S. Mobilio, The synchrotron radiation facility at Frascati. *Rev. Sci. Instrum.* **63**, 1613 (1992). <https://doi.org/10.1063/1.1142993>
4. A. Balerna, DAΦNE-light facility update. *Synchrotron Radiat. News* **27**(1), 21–24 (2014). <https://doi.org/10.1080/08940886.2014.869159>
5. A. Balerna, M. Cestelli Guidi, R. Cimino, M. Commisso, A. De Sio, L. Gambicorti, A. Grilli, D. Hampai, E. Pace, M. Pietropaoli, A. Raco, V. Sciarra, V. Tullio, G. Viviani, DAΦNE-Light INFN-LNF synchrotron radiation facility. *AIP Conf. Proc.* **1234**, 285 (2010). <https://doi.org/10.1063/1.3463191>
6. CALIPSOplus H2020 EU Project. <https://www.calipsoplus.eu/>
7. M. Cestelli Guidi, M. Piccinini, A. Marcelli, A. Nucara, P. Calvani, E. Burattini, Optical performances of SINBAD, the synchrotron infrared beamline at DAΦNE. *J. Opt. Soc. Am. A* **22**, 2810–2817 (2005). <https://doi.org/10.1364/JOSAA.22.002810>

8. G. Della Ventura, B. Mihailova, U. Susta, M. Cestelli Guidi, A. Marcelli, J. Schlüter, R. Oberti, The dynamics of Fe oxidation in riebeckite. A model for amphiboles. *Am. Mineralogist* **103**, 1103–1111 (2018). <https://doi.org/10.2138/am-2018-6382>
9. B. Cesare, F. Nestola, T. Johnson, E. Mugnaioli, G. Della Ventura, L. Peruzzo, O. Bartoli, C. Viti, T. Erickson, Garnet, the archetypal cubic mineral, grows tetragonal. *Sci. Rep.* **9**, 14672 (2019). <https://doi.org/10.1038/s41598-019-51214-9>
10. A. De Sio, L. Tozzetti, Z. Wu, A. Marcelli, M. Cestelli Guidi, G. Della Ventura, H. Zhao, Z. Pan, W. Li, Y. Guan, E. Pace, Physical vapour deposition synthesis of amorphous silicate layers and nanostructures as cosmic dust analogs. *Astron. Astrophys.* **589**, A4 (2016). <https://doi.org/10.1051/0004-6361/201527222>
11. I. Rago, C.R. Chandraiahgari, M.P. Bracciale, G. De Bellis, E. Zanni, M. Cestelli Guidi, D. Sali, A. Broggi, C. Palleschi, M.S. Sarto, D. Uccelletti, zinc oxide microrods and nanorods: differential antibacterial activity and their mode of action against gram-positive bacteria. *RSC Adv.* **4**, 56031–56040 (2014). <https://doi.org/10.1039/C4RA08462D>
12. C. Petibois, G. Déléris, M. Piccinini, M. Cestelli Guidi, A. Marcelli, A bright future for synchrotron imaging. *Nat. Photon.* **3**, 179 (2009). <https://doi.org/10.1038/nphoton.2009.31>
13. M. Cestelli Guidi, S. Yao, D. Sali, S. Castabno, A. Marcelli, C. Petibois, Experimental ATR device for real-time FTIR imaging of living cells using brilliant synchrotron radiation sources. *Biotechnol. Adv.* **31**, 402–407 (2013). <https://doi.org/10.1016/j.biotechadv.2011.11.009>
14. F. D'Apuzzo, A.R. Piacenti, F. Giorgianni, M. Autore, M. Cestelli Guidi, A. Marcelli, U. Schade, Y. Ito, M. Chen, S. Lupi, Terahertz and mid-infrared plasmons in three-dimensional nanoporous graphene. *Nat. Comm.* **8**, 14885 (2017). <https://doi.org/10.1038/ncomms1488>
15. G. Capobianco, M.P. Bracciale, D. Sali, F. Sbardella, P. Belloni, G. Bonifazi, S. Serranti, M.L. Santarelli, M. Cestelli Guidi, Chemometrics approach to FT-IR hyperspectral imaging analysis of degradation products in artwork cross-section. *Microchem. J.* **132**, 69–76 (2017). <https://doi.org/10.1016/j.microc.2017.01.007>
16. L. Monico, K. Janssens, C. Miliani, G. Van der Snickt, Brunetti, M. Cestelli Guidi, M. Radepon, M. Cotte, Degradation process of Lead chromate in paintings by Vincent van Gogh studied by means of spectromicroscopic methods. 3. Synthesis, characterization, and detection of different crystal forms of the chrome yellow pigment. *Anal. Chem.* **85**, 860–867 (2013). <https://doi.org/10.1021/ac3021592>
17. L. Pronti, M. Romani, G. Verona-Rinati, O. Tarquini, F. Colao, M. Colapietro, A. Pifferi, M. Cestelli-Guidi, M. Marinelli, Post-processing of VIS, NIR, and SWIR multispectral images of paintings. *New Discovery on The Drunkenness of Noah. Painted by Andrea Sacchi*, Stored at Palazzo Chigi (Ariccia, Rome) Heritage, vol. 2, pp. 2275–2286 (2019). <https://doi.org/10.3390/heritage2030139>
18. ADAMO-DTC Lazio Region Project. <http://progettoadamo.enea.it/english/>
19. R. Saladino, J.R. Brucato, A. De Sio, G. Botta, E. Pace, L. Gambicorti, Photochemical synthesis of citric acid cycle intermediates based on titanium dioxide. *Astrobiology* **11**, 815–824 (2011). <https://doi.org/10.1089/ast.2011.0652>
20. E. Pace, M. Cestelli Guidi, A. De Sio, L. Gambicorti, A. Grilli, M. Pietropaoli, A. Raco, G. Viviani, An innovative photochemical facility at DAΦNE-L. *J. Phys.: Conf. Series* **425**, 072024 (2013). <https://doi.org/10.1088/1742-6596/425/7/072024>
21. T. Fornaro, J.R. Brucato, E. Pace, M. Cestelli Guidi, S. Branciamore, A. Pucci, Infrared spectral investigations of UV irradiated nucleobases adsorbed on mineral surfaces. *Icarus* **226**, 1068–1085 (2013). <https://doi.org/10.1016/j.icarus.2013.07.024>
22. A. Balerna, DAΦNE-Light DXR1 Soft X-Ray synchrotron radiation beamline: characteristics and XAFS applications. *Condens. Matter* **4**, 7 (2019). <https://doi.org/10.3390/condmat401000>
23. I. Hafizh, G. Bellotti, M. Carminati, G. Utica, M. Gugiatti, A. Balerna, Tullio, G. Borghi, A. Picciotto, F. Ficorella, N. Zorzi, A. Capsoni, S. Coelli, L. Bombelli, C. Fiorini, ARDESIA: a fast silicon drift detector X-ray spectrometer for synchrotron applications. *X-Ray Spectrom.* **48**, 382–386. <https://doi.org/10.1002/xrs.3017>
24. I. Hafizh, G. Bellotti, M. Carminati, G. Utica, M. Gugiatti, A. Balerna, V. Tullio, G.O. Lepore, G. Borghi, F. Ficorella, A. Picciotto, N. Zorzi, A. Capsoni, S. Coelli, L. Bombelli, C. Fiorini,

- Characterization of ARDESIA: a 4-channel SDD X-ray spectrometer for synchrotron measurements at high count rates. *J. Instrum.* **14**, P06027 (2019). <https://doi.org/10.1088/1748-0221/14/06/P06027>
25. G. Bellotti, A. Butt, M. Carminati, C. Fiorini, L. Bombelli, G. Borghi, C. Piemonte, N. Zorzi, A. Balerna, The ARDESIA detection module: a 4-channel array of SDDs for Mcps X-Ray spectroscopy in synchrotron radiation applications. *IEEE Trans. Nucl. Sci.* **65**, 1355–1364 (2018). <https://doi.org/10.1109/TNS.2018.2838673>
  26. I. Ascone, L. Messori, A. Casini, C. Gabbiani, A. Balerna, F. Dell’Unto, A. Congiu Castellano, Exploiting soft and hard X-ray absorption spectroscopy to characterize metal/drug/Protein interaction. *Inorg. Chem.* **47**, 8629 (2008). <https://doi.org/10.1002/xrs.3017>
  27. A. Leon, A. Balerna, G. Cinque, C. Frommen, M. Fichtner, Al K Edge XANES measurements in NaAlH<sub>4</sub> Doped with TiCl<sub>3</sub> by ball milling. *J. Phys. Chem. C* **111**, 3795 (2007). <https://doi.org/10.1021/jp0645418>
  28. P. Zajdel, A. Kisiel, A. Szytula, J. Goraus, A. Balerna, A. Banas, P. Starowicz, J. Konior, G. Cinque, A. Grilli, Studies of valence of selected rare earth silicides determined using Si K and Pd/Rh L<sub>2,3</sub> XANES and LAPW numerical studies. *Nuclear Instrum. Methods Phys. Res. B* **364**, 76–84 (2015). <https://doi.org/10.1002/xrs.3017>
  29. G. Naletto, G. Tondello, R. Cimino, Design of a high-flux low-energy synchrotron radiation monochromator. *NIMA* **556**, 371–378 (2006). <https://doi.org/10.1016/j.nima.2005.10.012>
  30. R. Cimino, M. Comisso, D. Grosso, T. Demma, V. Baglin, R. Flammini, R. Larciprete, Nature of the decrease of the secondary-electron yield by electron bombardment and its energy dependence. *Phys. Rev. Lett.* **109**, (2012). <https://doi.org/10.1103/PhysRevLett.109.064801>
  31. L.A. Gonzalez, M. Angelucci, R. Larciprete, R. Cimino, The secondary electron yield of noble metal surface. *AIP Adv.* **7**, (2017). <https://doi.org/10.1063/1.5000118>
  32. R. Cimino, M. Angelucci, L.A. Gonzalez, R. Larciprete, SEY and low-energy SEY of conductive surfaces. *J. Elect. Spect. & Rel. Phen.* June (2019). <https://doi.org/10.1016/j.elspec.2019.06.008>
  33. R. Larciprete, D.R. Grosso, A. Di Trollo, R. Cimino, Evolution of the secondary electron emission during the graphitization of thin C films. *Appl. Surf. Sci.* **328**, 356–360 (2015). <https://doi.org/10.1016/j.apsusc.2014.12.046>
  34. L. Spallino, M. Angelucci, R. Larciprete, R. Cimino, On the compatibility of porous surfaces with cryogenic vacuum in future high-energy particle accelerators. *Appl. Phys. Lett.* **114**, (2019). <https://doi.org/10.1063/1.5085754>
  35. R. Dupuy, M. Bertin, G. Féraud, M. Hassenfratz, X. Michaut, T. Putaud, L. Philippe, P. Jeseck, M. Angelucci, R. Cimino, V. Baglin, C. Romanzin, J.-H. Fillion, X-ray photodesorption from water ice in protoplanetary disks and X-ray-dominated regions. *Nat. Astron.* **2**, 796–801 (2018). <https://doi.org/10.1038/s41550-018-0532-y>

# Chapter 4

## Synchrotron Radiation Studies of Relevance to Accelerator R&D



Marco Angelucci and Roberto Cimino

**Abstract** To correctly design recent and future high performance energy colliders, the knowledge of their vacuum walls material and surface properties is an essential prerequisite. Synchrotron radiation, produced by the circulating particles, interacts with the machine vacuum walls and induce gas desorption, photoelectrons and heat load which may affect vacuum and beam stability. Moreover, such interaction may chemically modify the surface and its behavior, affecting stability of the machine during its operation. Hence, most surface properties have to be quantitatively determined as a function of operation time and history. Photon reflectivity, photo yield, photo stimulated desorption and their geometrical distribution are essential ingredients to simulation codes. Such parameters must be studied not only on realistic “technical materials”, but also in conditions as close as possible to the operative ones. This implies that a significant effort is needed to go, whenever possible, at very grazing angle of incidence (as low as  $0.08^\circ$ ) and at very low operating temperatures (from 10 to 70 K). Here we will introduce the problem and present some results of a still ongoing experimental campaign carried out at BESSY2 and at the DAΦNE-L facility at LNF.

### 4.1 Introduction

An always vaster scientific community is successfully exploiting Synchrotron Radiation (SR) emitted by circular accelerators to probe the most diverse properties of matter, either in gas, liquid or solid state. [1, 2] Yet, there is still a vast community that continues to see SR as a nuisance and eventually a potential bottleneck for their scientific advances: the researchers working in R&D on high performance particles circular colliders. Not only SR cost power to be compensated but it also interacts with the accelerator walls causing a series of potentially detrimental phenomena.

---

M. Angelucci · R. Cimino (✉)  
INFN-Frascati National Laboratory, Frascati, RM, Italy  
e-mail: [Roberto.cimino@lnf.infn](mailto:Roberto.cimino@lnf.infn)

M. Angelucci  
e-mail: [marco.angelucci@lnf.infn.it](mailto:marco.angelucci@lnf.infn.it)

© Springer Nature Switzerland AG 2021  
A. Di Cicco et al. (eds.), *Synchrotron Radiation Science and Applications*,  
Springer Proceedings in Physics 220, [https://doi.org/10.1007/978-3-030-72005-6\\_4](https://doi.org/10.1007/978-3-030-72005-6_4)

Linear accelerators (like CLIC [3] and ILC [4]) have been proposed to solve those intrinsic problems, but there are evidences that, to a certain extent and energy, luminosity and beam stability are still better in circular machines. Therefore, not only LHC is going to be upgraded to High Luminosity (HL-LHC) [5, 6], but even more challenging machines like the High Energy (HE) LHC [7] and the Future Circular Collider (FCC) both for electrons (FCC-ee) [8] and protons (FCC-hh) [9] were studied and are nowadays proposed to the international community for fundings. Specially in proton machines like LHC, its HL upgrade, HE-LHC, and FCC-hh, SR not only costs electric power (since it reduces beam energy) but induces a series of unwanted effects that directly affect the accelerator construction and, if not properly mitigated, the actual possibility to reach the desired final beam performances. In all such machines, protons have such an high energy so that, the SR critical energy, (i.e. the energy that divides in two equal parts the SR power spectrum [10]) ranges from  $\sim 45$  eV (for LHC and its upgrade) pass to  $\sim 500$  eV (for the HE-LHC) and reach  $\sim 4.5$  keV for the FCC-hh.

The most severe effects SR may have are many and are briefly described in the following.

- SR will deposit additional Heat Load (HL) on the accelerator walls [5–7, 9]. Such HL is an extremely serious issue considering that all such proton machines uses cryogenic magnets (at 1.9 K) to produce the intense magnetic field to properly bend the heavy and energetic protons. SR deposited power per beam ranges from  $\sim 3.6$  (7.3) kW (for the LHC and its upgrade) pass to  $\sim 100$  kW (for the HE-LHC) and reach  $\sim 2400$  kW for the FCC-hh implying a local power deposition going from 0.17 W/m per beam (for the LHC) to  $\sim 40$  W/m per beam (for the FCC-hh). Such huge heat load cannot be dissipated at the cold bore held at 1.9 K and, already in the LHC, it is intercepted by a so called beam screen (BS) which is held at higher temperatures (at LHC it is at 20 K) and where the cryo-budget to dissipate the incoming SR (and other heat load sources) is granted at reasonable costs. For the FCC-hh, the BS is foreseen to operate at higher temperatures than in LHC ( $\sim 60$ – $70$  K) and the power needed to dissipate it is actually limiting the design performance of the machine.
- SR will induce photoelectrons that will interfere with the beam, inducing single bunch instabilities [11, 12]. Such effect can be simulated once the number, its time-evolution, the energy distribution and the geometrical position of the SR induced photoelectrons are known. It can be only partially tackled by a careful choice of beam parameters and ideally, the best solution would be to select wall materials or material coatings with a Photon Yield (PY) low enough to be compliant to the desired beam parameters.
- More than that, SR induced photoelectrons may trigger the so called electron cloud effect (ECE) [13, 14]. This phenomenon derives from the fact that the low energy photoelectrons (mainly secondaries of kinetic energies lower than 20 eV) will see the positive proton (or positron) bunch and will get accelerated towards the beam. Once the relativistic positive beam passes, the accelerated electrons will continue drifting and eventually hit the opposite wall. There, they will generate

other low energy electrons according to the material Secondary Electron Yield (SEY), which is defined as the number of electrons produced per incident electron as a function of its energy. Such newly produced secondaries will see again the next positive bunch and repeat the process, which may become resonant, causing a significant electron density increase in the beam pipe, which may destructively interfere with the accelerated beam. Also such phenomenon can be calculated as done for example by the PyECLOUD code at CERN [15] once the geometrical origin, the SEY (and its time-evolution) and the PY (and its time-evolution) of the wall material are known. ECE can be only partially taken care of by a correct choice of beam parameters (beam population, time spacing, etc.) but to avoid undesirable limitations to the machine performance a careful choice of constructive material possibly having an as small as possible SEY (ideally always below 1) should be performed.

- Of course, SR induced photoelectrons together with all the electrons generated by ECE, will induce additional gas desorption from the accelerator walls, through Photon Stimulated Desorption (PSD) and Electron Stimulated Desorption (ESD) potentially causing dynamic vacuum issues [16].
- Some of the irradiated SR impinging on the accelerator walls will be reflected and will cause SR irradiation, photoelectrons and gas desorption in regions where SR does not directly reach. At first sight any technical material is rough enough to significantly reduce reflectivity, but in reality, the very grazing SR incidence will indeed cause a potentially significant Reflectivity, both in its specular ( $R$ ) and scattered ( $R_t$ ) components. The study of SR Reflectivity ( $R$ ) is of paramount importance since it allows to follow SR in the machine and individuates all the geometrical places where photoelectrons and desorbed molecules will be produced. Different computer codes, as SYNRAD3D [17, 18] and Synrad+ [19] are used to calculate SR distributions in the machines and used to feed other programs like Molflow [20] and Molflow+ [21, 22], that will eventually calculate desorbed gas densities, heat load profiles, etc. All those programs are fundamental to properly design and operate high performance accelerators and indeed need realistic inputs from real technical materials in conditions (geometry, temperature, contaminants, etc.) as close as possible to the operational ones. This makes Reflectivity measurements quite challenging, since SR impinges on such long accelerators with a very small angle of incidence, ranging from  $\sim 0.28^\circ$  (4.8 mrad) for LHC-types machines and  $\sim 0.08^\circ$  (1.4 mrad) for FCC-hh. Actually, the use of reflectivity has been recently proposed as a method to reduce the SR heat load to be absorbed in FCC-hh cryogenic parts [23]. Even this proposal, adding sustainability to the entire project, will need a thorough experimental verification that would be only possible using state of the art set-ups now available in SR facilities around the world.
- Photo-desorption is one more essential parameter to correctly simulate vacuum behavior, using, for example, programs like Molflow [20] and Molflow+ [21, 22]. Those or similar codes are necessary to properly design and dimensionate any accelerator vacuum system. Indeed it is difficult to give values in numbers of molecules per incident photon and efforts are undergoing to measure PSD on

long pipes and beam screen structures [24]. It is also essential to study PSD at low temperatures since physisorbed gasses are expected to modify the values measured at RT. Working on very long samples held at temperatures between 20 and 60 K is a very challenging and costly approach. Nowadays efforts are pointing to study at grazing incidence long samples (up to 3 m) held at room down to liquid Nitrogen temperatures, while lower temperature studies will be performed on much smaller samples and at less grazing incidence, with the idea to scale all data in a organic database.

All simulations to correctly validate the design of any accelerator must input realistic data on all the aforementioned issues. The interaction between SR and technical materials in use in accelerators must be therefore studied with the needed accuracy. As said, quantitative PY, R,  $R_t$ , and PSD of all accelerator materials under direct or reflected SR should be measured in conditions as close as possible to the ones occurring in the real final system. Those parameters and their evolution with machine operation are key parameters to simulation and accelerator's operation.

Photoemission, adsorption spectra PSD and R of all the typical materials present in the inner surface of accelerator walls have been extensively studied but nearly no studies are performed in a quantitative way (reporting, for instance, the number of electrons produced per incident photon), on technical materials (dirty "as received" samples) and in condition in which those materials are in accelerators (grazing geometry and low temperature). At LNF and in collaboration with CERN, an extensive experimental campaign has been launched in recent years to tackle most of the aforementioned issues, either in single aspects and trying to combine different techniques and experimental conditions. The goal is to have a sufficient number of tiles to compose the general picture describing the interaction of SR with high performance particles colliders.

In the following we will briefly give some hints of what has been done and needs to be done in the near future.

## 4.2 Experimental Setup

For the research here presented, we used two different set-ups: one at the SR facility of the HMI in Berlin, and one under development at the Frascati National Laboratory. In Berlin there is a dedicated facility, the Optics Beamline, ideal to collect Reflectivity and PY data at very grazing photon incidence in the energy range from 35 eV to 2000 eV. Such Beamline is a dedicated SR laboratory for "at-wavelength" metrology of X-ray optical elements for soft X-rays and is normally used to study optical properties of gratings, multilayers optical components and to perform depth-profiling of microstructures, layered systems and buried layers [25–28]. The average spot-size at the sample is  $\approx 0.2 \times 0.3 \text{ mm}^2$  (v  $\times$  h). All the reflected and most of the scattered radiation can be detected by using the largest available photodiode ( $4 \times 4 \text{ mm}^2$ ). To study specular reflectivity R, we performed our experiments in a geometry where



$\theta_r = 2\theta_i$ .  $\theta_i$  is defined as the SR angle of incidence and  $\theta_r$  is defined as the angle at which photons are reflected from the surface. Both  $\theta_r$  and  $\theta_i$  are defined to be  $0^\circ$  when photons are parallel to the surface. This so called  $\theta/2\theta$  configuration was used to measure Specular Reflectivity (R) and PY as a function of  $\theta_i$  and photon energy. This geometry was used either keeping fixed the photon beam energy and scanning over the different impinging angles  $\theta_i$  varying accordingly  $\theta_r = 2\theta_i$ , or keeping a fixed  $\theta/2\theta$  geometry and varying the impinging photon energy. By fixing the photon beam energy and angle of incidence  $\theta_i$ , one can also scan the detector in order to cover as much solid angle  $\Omega$  as possible. This allows us measure the scattered light  $R_t$ . The experimental layout allows to measure PY along with all the reflectivity data. The sample under study is electrically insulated and connected to ground through a Keithley picoammeter, which then measures the number of photoelectrons produced by the sample surface at a given photon energy and experimental geometry. No bias was applied not to add unwanted noise to the measurements. The number of impinging photons is calculated multiplying the photodiode drain current by its tabulated energy-dependent quantum efficiency (GaAsP—G1127-02, Hamamatsu). This allows us to measure the absolute value of the PY, giving the number of emitted electrons per impinging photons.

Photo-desorption was performed by the “Material Science” Laboratory under development at DAΦNE-L INFN-LNF laboratory of Frascati, Rome [29]. The laboratory allows to study photo-desorption as a function of photon dose, both from monochromatic and focussed white light on small samples held at RT. In short it will also be possible to study the same small samples at temperature down to 10 K, and long samples (up to 3 m) at grazing incidence and down to liquid Nitrogen temperatures [29]. The data here shown have been collected at RT on small samples using white light radiation to test the technique and the set up. PSD have been performed by means of a quadrupole mass spectrometer (Hiden, HAL 3F PIC) during photon irradiation. SR can generate a total current of more than  $50 \mu\text{A}$  on the sample when the maximum electron current ( 1.4 Amps) is stored in the DAΦNE electron ring. The powerfulness of the set-up consist in its ability to perform multiple analysis on the “as received” as well as on the photo-irradiated surfaces. This allows to measure, for the first time in this context, the effect of photo irradiation on SEY and on surface chemistry. We recognize that this is the path to follow to unveil the cross-talk between the different phenomena occurring to the material surface to best mimic what is actually happening in the accelerator. The experimental setup for SEY and x-ray photoemission experiments is described in details elsewhere [13, 30, 31]. Briefly, the system consists in a  $\mu$ -metal chamber, with less than 5mGauss residual magnetic field, under ultra high vacuum (UHV) conditions, with a background pressure below  $2 \times 10^{-10}$  mbar. The system is equipped with an Omicron EA125 analyzer to reveal the photoelectrons excited by the non monochromatic radiation of an Al  $K\alpha$  ( $h\nu = 1486.7$  eV) source. SEY, being defined as the ratio of the number of electrons leaving the sample surface ( $I_{out}$ ) to the number of incident electrons ( $I_p$ ) per unit area, is measured as follows.  $I_p$  is measured by applying a positive bias on a faraday cup. To evaluate  $I_{out}$  we measure the sample current to ground  $I_s$ . Since  $I_{out} = I_p - I_s$ , then:

$$SEY = 1 - \frac{I_s}{I_p} \quad (4.1)$$

For this study we used as e-gun an ELG-2, from Kimball Physics, which uses a standard Ta disc cathode.

### 4.3 Selected Results

In this section, some selected Reflectivity (R), Photo Yield (PY), Photo Stimulated Desorption (PSD) results on Cu technical surfaces are presented. The results highlight the relationship between the surface properties (roughness, chemistry etc.) and the physical quantities of interest. As an example on what is possible to extract from R and PY data, we show those quantities in case of Technical Cu surfaces of various roughness confirming that it is indeed possible to obtain optical properties of interest for the simulations. Experimental data are mandatory since even a marginal change in roughness may seriously influence the parameters of interest.

The PSD measurements shown here confirm the importance to follow the surface evolution upon photo irradiation time and the interplay between the various relevant parameters.

#### 4.3.1 Reflectivity and Photo Yield

In the following section, we show some results for the specular reflectivity and the Photo-Yield as a function of incident photon energy for three different incidence angles ( $\theta_i = 0.25^\circ, 0.5^\circ, 1^\circ$ ). A more detailed description of the technique and more detailed studies can be found in the literature [32–36]. The studied surface are all “as received” Cu, which is the material coating of the inner part of the beam screen (to grant high conductivity and hence low impedance). The Cu surfaces have been chosen among typical flat technical copper surfaces with roughness  $R_a \approx 10, 15,$  and  $25$  nm to better understand its effect at very grazing geometry. Those roughnesses are far to be the ones usually available for optical elements, and we notice here, that the available simulation codes (as, for instance, REFLEC, RAY, CXRO, etc. [37, 38]) used to obtain optical reflectivity from surfaces can not correctly deal with such high  $R_a$  and R can not be therefore properly calculated. In Fig. 4.1, R (left panel) and PY (right panel) are shown as a function of photon energy from 35 to 1800 eV. The results show two opposite general trends for specular reflectivity and photon yield. In particular, R is higher at lower photon energies and at lower angle of incidence  $\theta_i$  while PY is higher at higher photon energies and lower at more grazing angle of incidence. In both R and PY data, the Cu-L<sub>2-3</sub> absorption edge at  $\sim 930$ – $950$  eV is visible and causes a drop in R and an increase in PY. In addition to this threshold, we measure a significant effect due to the absorption of C K-edge at  $\sim 280$  eV and O

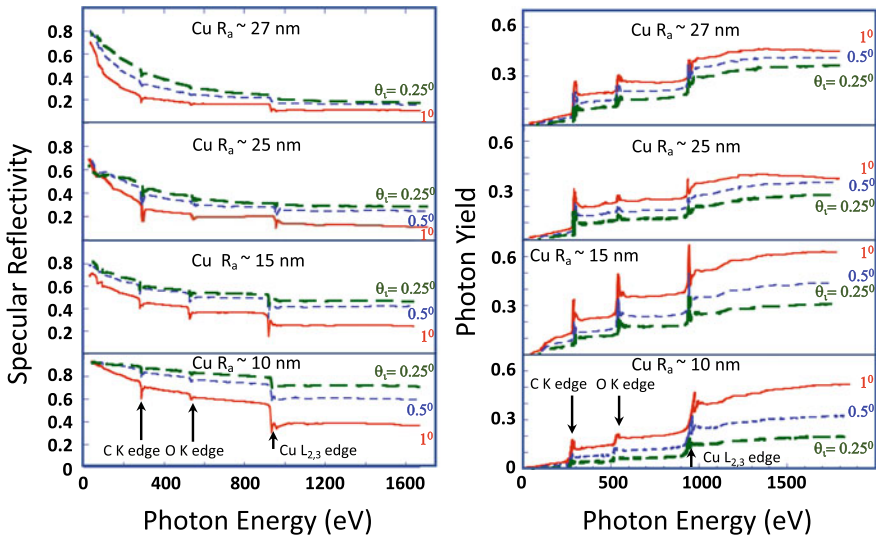


**Fig. 4.1** Specular reflectivity (left panel) and photon yield (right panel) obtained for samples with different roughness ( $R_a \approx 10, 15$  and  $25$  nm) at different incident angles ( $\theta_i = 0.25^\circ, 0.5^\circ, 1^\circ$ )

K-edge at  $\sim 530$  eV, which are known to be present, as contaminants, on the surface. This clearly shows that at such grazing incidence, the contaminant over-layer may have a role affecting R and PY. This calls for careful examination of such parameters on low temperature surfaces, where a physisorbed layers are expected to add up with time due to the cold surface pumping action. As expected,  $R_a$  plays a major role in determining the ability of a surface to specularly reflect impinging photons but also in influencing PY. The higher is  $R_a$ , the lower are the measured R and PY. This effect could become very significant when the sample are much more rougher or even nanostructured [35].

As previously mentioned the specular reflectivity R does not tell us the whole story. If, on one hand, R clearly decreases on increasing  $R_a$ , it does not necessarily means that all the photons that do not contribute to R are absorbed by the solid and disappear from the beam pipe. It can well be that they are off-specularly scattered, therefore still contributing to gas desorption and photoelectrons. In Fig. 4.2 we show the schematics of the experiment as well as the distribution, as a function of the reflection angle, of the normalized reflectivity at 1800 eV for Cu sample with  $R_a \approx 10$  and  $25$  nm. The lowest  $R_a$  sample shows a normalized reflectivity curve dominated by a very narrow peak centered at  $\theta_r = 2\theta_i$ . On the contrary, the same distribution measured, as a function of  $\theta_r$ , from the Cu sample with  $R_a \approx 25$  nm, shows not only a reduction in R but a significant increase in the diffuse component  $R_f$ . Without entering into details, these results show the importance to consider and experimentally measure the total reflectivity and not just the specular one when tracing photons in accelerators.

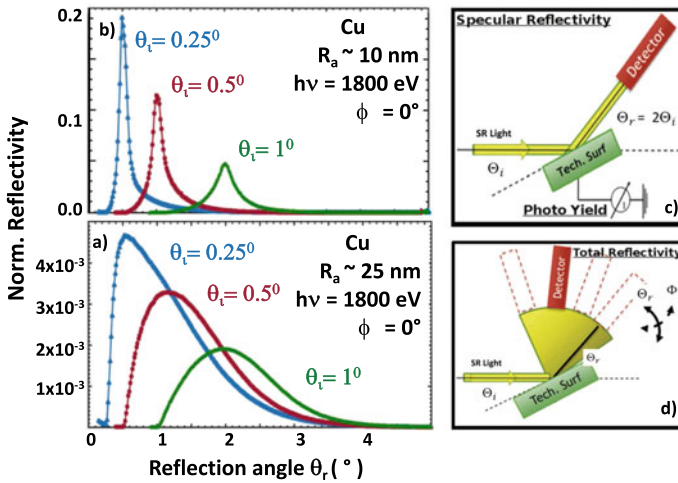


**Fig. 4.2** Normalized reflectivity versus reflection angle  $\theta_r$  at 1800 eV at incidence angles of  $1^\circ$ ,  $0.5^\circ$ ,  $0.25^\circ$  for Cu samples with  $R_a \approx 25$  (panel a) and 10 nm (panel b). In panel c) artistic view of the  $\theta/2\theta$  geometry used to measure R and PY. In panel d), schema of set-up used to measure the angular distribution of reflected and scattered radiation keeping fixed the photon beam energy and the angle of incidence  $\theta_i$  and by scanning the detector both in  $\theta_r$  and  $\Phi$ . Total reflectivity  $R_t$  is derived by 2-D integration of the angular-resolved data

### 4.3.2 Photodesorption

Synchrotron Radiation (SR) light from DAΦNE [29], has been used to perform some preliminary studies on small “as received” Cu samples at room temperature. In order to characterize the samples and their interactions with photons, Photo Stimulated Desorption (PSD), Photo-Yield (PY), X-Ray Photoemission (XPS) and Secondary Electron Yield (SEY) measurements were performed on the same surface. Figure 4.3 shows the measured PSD and PY data during irradiation, at normal incidence, with a white light spectrum containing photons between 0 and 1000 eV. In the left panel of Fig. 4.3, relevant molecular species ( $H_2$ ,  $H_2O$ ,  $CO/N_2$ ,  $O_2$ ,  $CO_2$ ) partial pressure are reported as a function of photon dose, together with the total pressure in the chamber. All the results are expressed in terms of dynamic pressures. The different partial and total pressures are normalized to the DAΦNE ring current to remove structures which are due to its variations. In the right panel of Fig. 4.3, we report PY variation collected simultaneously to the PSD data, measuring the sample current normalized to the number of incident photons.

Both PSD and PY values decrease with photon dose. PY halves quite suddenly, after very small doses, and then stays reasonably constant during additional doses. This indicates that the surface chemical modifications occurring at the surface and causing the difference in PY are effective after quite a small photon dose. PSD signals also undergo to a strong variation as soon as irradiation starts, then we observe a

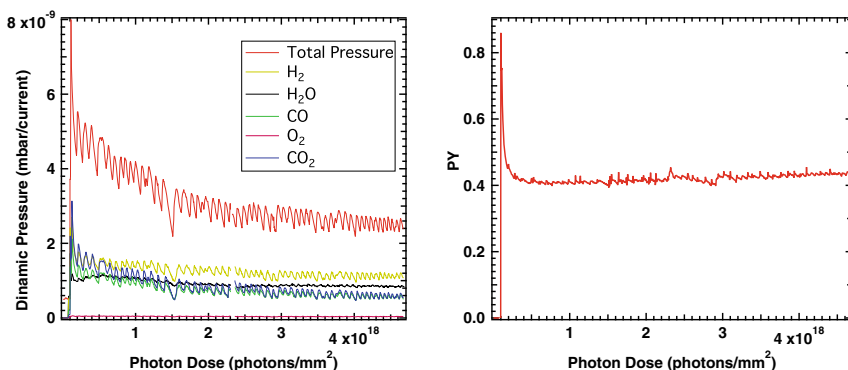


**Fig. 4.3** Photo Stimulated Desorption (left) and Photo-Yield (right) as function of photon dose for an “as received” copper sample at Room temperature under white light irradiation

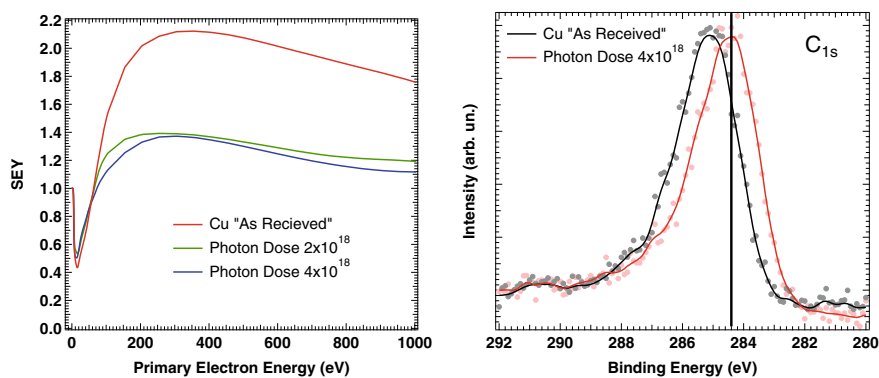


**Fig. 4.4** Surface characterization with Secondary Electron Yield (left panel) and X-Ray Photoemission (right panel) of an “as received” Cu sample before and after full dose irradiation

smoother progressive decrease. This seems to indicate that the initial PSD is the one modifying the surface PY while, after this small doses have been delivered, further desorption does not significantly alters surface composition.

To confirm that the photon dose significantly affects the surface properties and composition, we performed SEY and XPS measurements before and after irradiation. The obtained results are reported in Fig. 4.4. SEY shows a strong variation after the first SR irradiation ( $2 \cdot 10^{18}$ ph/mm<sup>2</sup>) dose. It decreases from 2.1 to 1.3 and after a subsequent irradiation of the same dose, the scrubbed system presents no relevant variation in the SEY maximum. Electron irradiation on an “as received” Cu is a well know process decreasing SEY [13, 39, 40] from  $\approx 2.1$  to less than 1.1. The physical process at the origin of this decrease has been individuated mainly by XPS analysis and in particular by looking at the C 1s core level [13, 31]. What has been seen to occur is that surface Carbon atoms change their bonding nature, passing from  $sp^3$ , as

in contaminant gasses, to  $sp^2$ , characteristic of in plane C–C bonding, as observable in graphite and a-C [41, 42].

On the right panel of Fig. 4.4, we show the C1s XPS spectra of the “as received” Cu sample before and after the final photon dose. The spectra show a very similar shift and modification observed when the sample is bombarded by electrons [41, 42] indicating a similar process at the base of the photo yield decrease. The noticeable difference between photon and electron irradiation seems to be affecting the final values reached by SEY. The puzzling origin of this difference is still under study being of great importance, since simulations tell us that ECE are mitigated once SEY is less than 1.1 and are not when SEY exceeds this value.

## 4.4 Conclusions

In this paper we report on the ongoing SR research activity to study material properties in use or to be used in high performance circular colliders. We briefly presented the challenge and the aim of this research together with some selected results. One main conclusion is that, indeed, to grant the necessary understanding and knowledge of the various parameters to be fed in simulation codes apt to validate colliders performances, a complex and significant experimental effort have to be pursued. We put into evidence here the importance to study SR interaction with samples in conditions and geometry as close as possible to what they have in the actual ring. Also we show that combining different measurements on the same surface may effectively enhance the understanding of the interplay between the many phenomena simultaneously occurring at the surface. Such combined approach has a very high potential to highlight the underlying physics driving surface photon and electron induced effects to be used for the proper design and operation of new high performances circular accelerator.

**Acknowledgements** This work was supported by INFN National committee V through the “MICA” project and by KE3724/TE/HL-LHC-Addendum n. 4 to Framework Collaboration Agreement KN3083 Between CERN and INFN. We thank HZB for the allocation of synchrotron radiation beamtime. Research leading to these results has also received funding by the project CALIPSO-plus, under the Grant Agreement 730872 from the EU Framework Programme for Research and Innovation HORIZON 2020. We thank DAΦNE-L technical support. We also thank P. Chiggiato, R. Kersevan, V. Baglin and the entire “e<sup>-</sup> cloud community” for continuous discussions and encouragements.

## References

1. P. Willmott, *An Introduction to Synchrotron Radiation: Techniques and Applications* (Wiley, 2011)
2. *Handbook on Synchrotron Radiation* (Series North-Holland, Amsterdam)

3. M. Aichele et al. *A Multi-teV linear Collider Based on CLIC Technology: CLIC Conceptual Design Report - CERN-2012-007*, SLAC-R-985, KEK-Report-2012-1, PSI-12-01, JAI-2012-001
4. C. Adolphsen et al., The International Linear Collider Technical Design Report - Volume 3.II: Accelerator Baseline Design - [arXiv:1306.6328](https://arxiv.org/abs/1306.6328) [physics.acc-ph] ILC-REPORT-2013-040, ANL-HEP-TR-13-20, BNL-100603-2013-IR, IRFU-13-59, CERN-ATS-2013-037, COCKCROFT-13-10, CLNS-13-2085, DESY-13-062, FERMILAB-TM-2554, IHEP-AC-ILC-2013-001, INFN-13-04-LNF, JAI-2013-001, JINR-E9-2013-35, JLAB-R-2013-01, KEK-REPORT-2013-1, KNU-CHEP-ILC-2013-1, LLNL-TR-635539, SLAC-R-1004, ILC-HIGRADE-REPORT-2013-003
5. G. Apollinari et al. *CERN Yellow Reports: Monographs "High-Luminosity Large Hadron Collider (HL-LHC): Preliminary Design Report" CERN Yellow Reports: Monographs* (2015)
6. G. Apollinari et al., CERN yellow reports: monographs "high-luminosity large hadron collider (HL-LHC): technical design report V. 0.1" CERN Yellow Reports: Monographs (2017)
7. J.L. Abelleira et al., High-Energy LHC design. *J. Phys. Conf. Ser.* **1067**, (2018)
8. A. Abada et al., FCC-ee: the lepton collider. *Eur. Phys. J. Spec. Top.* **228**, 261–623 (2019)
9. A. Abada et al., FCC-hh: the hadron collider. *Eur. Phys. J. Spec. Top.* **228**, 755–1107 (2019)
10. X-RAY DATA BOOKLET. Center for X-ray optics and advanced light source lawrence berkeley national laboratory. <https://xdb.lbl.gov/>
11. K. Ohmi, F. Zimmermann, *Phys. Rev. Lett.* **85**, 3821 (2000)
12. F. Zimmermann et al. Beam dynamics issues in the FCC, CERN-ACC-2016-0101, in *Proceedings, 57th ICFA Advanced Beam Dynamics Workshop on High-Intensity and High-Brightness Hadron Beams (HB2016)*: Malmö, Sweden, July 3–8 (2016)
13. R. Cimino, T. Demma, Electron cloud in accelerators. *Int. J. Mod. Phys. A* **29**(17), 1430023 (2014)
14. K. Ohmi, L. Mether, D. Schulte, F. Zimmermann, Study of electron cloud instabilities in FCC-hh, in *Proceedings, 6th International Particle Accelerator Conference (IPAC 2015)* Richmond, Virginia, USA, May 3-8, (2015)
15. G. Iadarola, G. Rumolo, in *Proceeding E-CLOUD12: Joint INFN-CERN-EuCARD-AccNetWorkshop on Electron-Cloud Effects, La Biodola, Isola d'Elba, Italy*, ed. by R. Cimino, G. Rumolo, F. Zimmermann, CERN-2013-002 (CERN, Geneva, 2013), pp. 189–194. <https://doi.org/10.5170/CERN-2013-002.189>
16. F. Perez, et al. Analysis of beam-induced vacuum effects. Tech. rep. EuroCirCol- P2-WP4-D4.4. ALBA, CERN (2018)
17. G. Dugan, D. Sagan, in *Proceedings of E-CLOUD 2010: 49th ICFA Advanced Beam Dynamics Workshop on Electron Cloud Physics*, ed. by K. Smolenski (Ithaca, NY 2010), Paper PST08
18. G.F. Dugan, K.G. Sonnad, R. Cimino, T. Ishibashi, F. Schäfers, Measurements of x-ray scattering from accelerator vacuum chamber surfaces, and comparison with an analytical model. *Phys. Rev. Spec. Top. - Accel. Beams* **18**(4) (2015)
19. R. Kersevan, in *Proceedings of IPAC 1993*, vol. C930517
20. R. Kersevan, J.-L. Pons, Introduction to MOLFLOW+: new graphical processing unit-based monte carlo code for simulating molecular flows and for calculating angular coefficients in the computer unified device architecture environment. *J. Vacuum Sci. Technol. A* **27**(4), 1017 (2009)
21. M. Ady, R. Kersevan, Introduction to the latest version of the test-particle monte carlo code molflow+. CERN Tech. Rep. **1993**, 3848–3850 (2014)
22. R. Kersevan, M. Ady, "Molflow+, Sinrad+" CERN 2018 <https://www.cern.ch/molflow>
23. R. Cimino, V. Baglin, F. Schäfers, Potential remedies for the high synchrotron-radiation-induced heat load for future highest-energy-proton circular colliders. *Phys. Rev. Lett.* **115**(26), 1–5 (2015)
24. L.A. Gonzalez, M. Gil-Costa, V. Baglin, P. Chiggiato, C. Garion, R. Kersevan, S. Casalbuoni, E. Huttel, I. Bellafont, F. Perez, Commissioning of a beam screen test bench experiment with a future circular hadron collider type synchrotron radiation beam. *Phys. Rev. Accel. Beams* **22**, (2019)




25. A. Sokolov, M.G. Sertsu, A. Gaupp, M. Lüttecke, F. Schäfers, J. Synchrotron Radiat. **25**, 100 (2018)
26. A. Sokolov, et al., At-wavelength metrology facility for soft X-ray reflection optics. Rev. Sci. Instrum. **87**(5) (2016)
27. F. Eggenstein et al., A reflectometer for at-wavelength characterisation of gratings. Nucl. Inst. Meth. Phys. Res. Sect. A Accel. Spectrometers, Detect. Assoc. Equip. **710**, 166–171 (2013)
28. A. Sokolov et al. An XUV optics beamline at BESSY II. Proc. SPIE2014 **February 2015**, 92060J (2014)
29. M. Angelucci, et al. DAΦNE-Light: the INFN-LNF synchrotron radiation facility, in *This proceedings*
30. L. Spallino, M. Angelucci, R. Larciprete, R. Cimino, On the compatibility of porous surfaces with cryogenic vacuum in future high-energy particle accelerators. Appl. Phys. Lett. **114**(15), (2019)
31. R. Cimino, M. Commisso, D. Grosso, T. Demma, V. Baglin, R. Flammini, R. Larciprete, Nature of the decrease of the secondary-electron yield by electron bombardment and its energy dependence. Phys. Rev. Lett. **109**, (2012)
32. N. Mahne, V. Baglin, I.R. Collins, A. Giglia, L. Pasquali, M. Pedio, S. Nannarone, R. Cimino, Photon Reflectivity distributions from the LHC beam screen and their Implications on the Arc Beam Vacuum System. Appl. Surf. Sci. **235**, 221–226 (2004)
33. F. Schäfers, R. Cimino, Soft X-ray reflectivity: from quasi-perfect mirrors to accelerator walls, *Proceedings of ECLLOUD12* (2013)
34. R. Cimino, F. Schäfers, Soft X-ray reflectivity and photoelectron yield of technical materials: experimental input for instability simulations in high intensity accelerators. Proceeding of IPAC2014, pp. 2335–2337
35. E. La Francesca et al. Photo reflectivity and photoelectron yield from copper technical surfaces, in preparation
36. R. Cimino, V. Baglin, I.R. Collins, VUV synchrotron radiation studies of candidate LHC vacuum chamber materials. Vacuum **53**(1–2), 273–276 (1999)
37. CXRO: X-Ray Interactions With Matter: <http://henke.lbl.gov/opticalconstants/>
38. F. Schäfers, Ray—the bessy raytrace program, in *Springer Series in Modern Optical Sciences: Modern Developments in X-Ray and Neutron Optics*, vol. 137, ed. by A. Erko, M. Idir, Th Krist, A.G. Michette (Springer, Berlin/Heidelberg, 2008), pp. 9–41
39. R. Cimino, I.R. Collins, M.A. Furman, M. Pivi, F. Ruggiero, G. Rumolo, F. Zimmermann, Can low energy electrons affect high-energy physics accelerators? Phys. Rev. Letter. **93**, 14801 (2004)
40. N. Hilleret, C. Scheuerlein, M. Taborrelli, Appl. Phys. A **76**, 1085 (2003)
41. R. Cimino, D.R. Grosso, M. Commisso, R. Flammini, R. Larciprete, Nature of the decrease of the secondary-electron yield by electron bombardment and its energy dependence. Phys. Rev. Lett. **2098**, 3 (2012)
42. R. Larciprete, D. Grosso, M. Commisso, R. Flammini, R. Cimino, Phys. Rev. ST Accel. Beams **16**, (2013)



# Chapter 5

## The LISA CRG Beamline at ESRF



Alessandro Puri , Giovanni Orazio Lepore , Riccardo Signorato, Paolo Scarbolo, Gianni Di Maio, and Francesco d'Acapito 

**Abstract** LISA, the Italian CRG beamline for X-ray Absorption Spectroscopy at ESRF, has been recently renewed and is currently in preparation for the new EBS source, with foreseen opening to users in September 2020. Here we describe some distinctive experimental techniques and user facilities available at the beamline.

### 5.1 Introduction

The LISA beamline [1] is the Italian CRG beamline operative at the European Synchrotron Radiation Facility (ESRF). It is an instrument dedicated to X-ray Absorption Spectroscopy and related techniques. LISA is open to users since April 2018 and collected data in its final configuration after a major upgrade for several months until the shutdown of the ESRF for the storage ring renewal. Reports concerning the beam parameters, standard data collection facilities and experimental activity have been presented elsewhere [2, 3]. Moreover, at LISA there is an ongoing program of development of innovative or peculiar XAS-related techniques. In this contribution, an overview will be given describing the related instrumentation and presenting some experimental examples. LISA also collaborates with Italian national

---

A. Puri (✉) · G. O. Lepore · F. d'Acapito  
CNR-IOM-OGG, c/o ESRF, 71 Avenue des Martyrs, Grenoble, France  
e-mail: [puri@esrf.fr](mailto:puri@esrf.fr)

G. O. Lepore  
Dipartimento di Scienze della Terra, Università degli Studi di Firenze, Via Giorgio La Pira 4,  
I-50121 Firenze, Italy

R. Signorato  
S.R.I. Tech, Viale Del Lavoro 42A, Vigonza, Italy

P. Scarbolo  
CAEN ELS s.r.l., c/o AREA Science Park—SS14 km 163.5, 34149 Basovizza, Trieste, Italy

G. Di Maio  
CAEN S.p.A., via Vetraia 11, Viareggio, LU, Italy

companies for the development and test of innovative instruments for beamline control, optimization and data collection.

## 5.2 XEOL

The XEOL technique (X-ray Excited Optical Luminescence) is a method that retrieves the XAS signal from the features appearing in the optical emission from the sample illuminated with X-rays across an absorption edge [4–6]. In particular cases, it can provide information about the local structure around luminescent species. The XEOL spectrometer consists in a lens (BK7 glass, 20 mm diameter) focusing the sample emission on a silica optic fiber (diameter 1 mm). The lens and the optic fiber tip are mounted on a manipulator inside the standard experimental chamber hence the experiments can be carried out in vacuum and/or at low temperatures. The optic fiber brings the signal to a fast photomultiplier tube (PMT) followed by a pulse forming electronic chain (amplifier, threshold, gate, shaper). The pulse gate can be synchronized with the storage ring Radio Frequency (RF) signal (see following section) in order to collect light pulses at a desired time delay respect to the impinging X-rays [6]. This device allowed the realization of XEOL experiments on Rare-Earths (Er, Yb) doped silica nanoparticles [7] and Ag nanoclusters in zeolite cages at the Ag-K edge [8, 9] (Fig. 5.1).

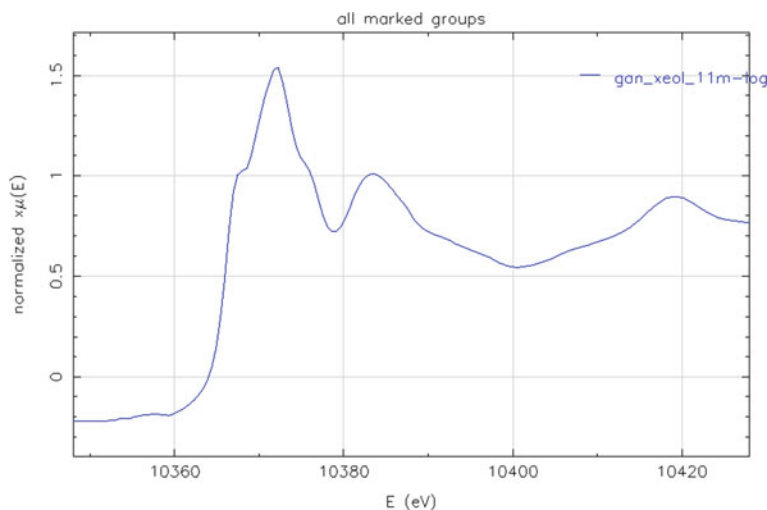


**Fig. 5.1** Example of a XEOL spectrum on a GaN sample at the Ga-K edge collected at 80 K. Data are collected with a PMT, (Hamamatsu H-3164-10, sensitivity range 300–650 nm, rise time 0.8 ns) and a set of optical bandpass filters (350–650 nm, width 10 nm, average transmissivity 40%) can be used to select a particular emission line from the sample

### 5.3 Pump and Probe

The ESRF storage ring is operated in several timing modes in order to allow the realization of time resolved experiments. In particular the 16 bunches mode and the 4 bunch mode are interesting as they provide a series of X-ray flashes equally spaced by 178 ns in the former case and 712 ns in the latter case. These regular flashes (probe) can be used in conjunction with a synchronized excitation (pump) signal on the sample realizing a stroboscopic data collection mode. The generation of the synchronized pulses is achieved by using a remotely programmable synchronization module (ESRF, BCDU8). LISA owns a laser diode for synchronized optical excitations with a wavelength of 404(2) nm, and pulse variable width  $W$ . At  $W = 1$  ns it can provide a pulse energy of 465 pJ at 1 MHz. The same optic fiber and lens used for XEOL are used to bring the laser pulses to the sample. The synchronization between the X-rays and the laser pulses can be achieved by placing a fast PMT in the sample position and collecting the two signals at the same time as shown in Fig. 5.2.

An example of use of the pump and probe technique at LISA can be found in [10].

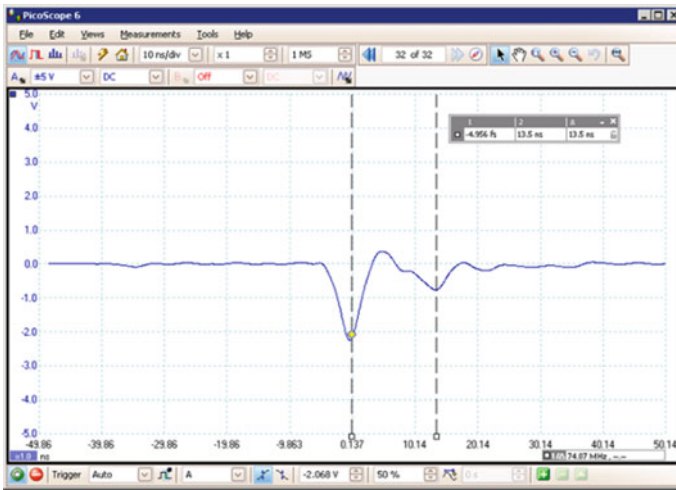


**Fig. 5.2** Plot showing the two signals on the PMT: on the left the laser diode signal, on the right the X-ray signal. The time scale is in ns so the distance between the two flashes in this case is about 10 ns. The delay between the two signals can be easily changed using the programmable BCDU8 unit. The module provides up to 8 outputs (TTL or NIM at choice) whose delays and width values can be varied in a wide range (delay from 11 ps to several ns, width from 2.8 ns to several ns). The signals width of 2.8 ns is due to the sum of the PMT rise time (0.8 ns) plus the scintillator (BC452) decay time (2 ns)



**Fig. 5.3** Microtomo furnace. The furnaces are provided by the sample environment pool of ESRF, together with their own power supply (Delta Electronika 75 V/22 A), water chiller and a remotely operated (RS232 port) temperature controller (Eurotherm 2408, rate 5°/min maximum)

## 5.4 Microtomo Furnace

A family of high-temperature X-ray microtomo furnaces has been developed at ESRF [11] in the past years. They cover a wide range of temperature (RT to 1000 °C) and are suitable for various X-ray techniques. They support operation both in vacuum and in controlled gas atmosphere, allowing in situ sample treatment. These furnaces are very compact and can be easily installed inside the LISA vacuum chambers. The maximum attainable temperature is 800 °C in gas atmosphere and 1000 °C under vacuum. Several gas types are supported (N<sub>2</sub>, He<sub>2</sub>, O<sub>2</sub>/He<sub>2</sub>, H<sub>2</sub>/He<sub>2</sub> mixtures, etc.). Automatic spectra acquisition at different temperatures is possible at LISA with a dedicated SPEC macro (Fig. 5.3).

The microtomo furnace has allowed the realization of experiments on thermal expansion switching in negative thermal expansion (NTE) materials [12]; studies on Metal-organic frameworks (MOFs) structural modification [13]; experiments on cerium oxide nanoparticles reduction [14]; studies on the synthesis of zeolites [15].

## 5.5 Elemental Mapping

With the newly installed mirrors, LISA provides a beam with dimensions down to  $\sim 100 \mu\text{m}$  (H)  $\times$   $60 \mu\text{m}$  (V) and a flux in the range of  $\sim 10^{10} - 10^{11} \text{ ph s}^{-1}$  (a further reduction of the horizontal dimension is expected following the EBS upgrade). It is then possible to perform elemental mapping, valence state mapping and full XAS measurements down to a few ppm. Such capabilities have potential impact in the study of complex materials belonging to several scientific fields, from environmental sciences to materials sciences and archaeometry.

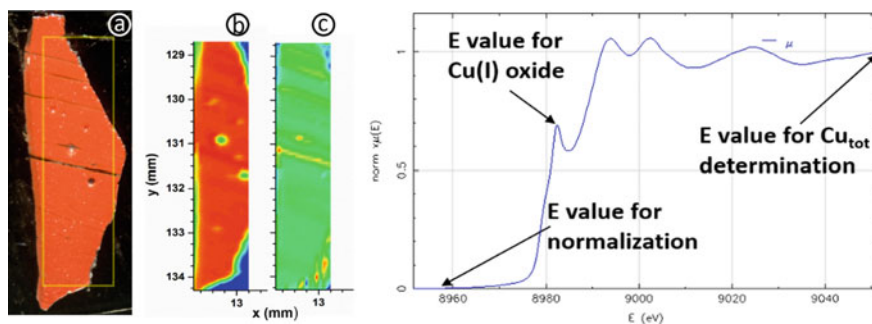


**Fig. 5.4** Left: **a** optical micrograph of the investigated sample and elemental maps (contoured region of the sample in **a**); **b** total Cu content; **c**  $\text{Cu}^{\text{I}}$  content (note: intensity increases in the sequence blue-green-yellow-red). Right: typical XANES Cu K edge spectrum with the energy values chosen for the XRF maps are indicated by arrows [16]

Figure 5.4a shows a thin polished section of a medieval mosaic tile, part of the original façade of the Santa Maria del Fiore cathedral in Florence (Italy) [16]. Figure 5.4b, c are elemental maps revealing the total Cu content distribution in the sample and the differences in oxidation state and structural features of Cu, respectively. The two elemental maps were obtained by the comparison of three raw maps, measured at specific energy values (Fig. 5.4 right: pre-edge, total Cu and  $\text{Cu}^{\text{I}}$ ).

## 5.6 FEXRAV

FEXRAV (Fixed Energy X-Ray Absorption Voltammetry, [17]) is an in situ XAS technique able to obtain fast information on electrode materials. This approach is based on the measurement of the absorption coefficient at a fixed energy while the electrode potential is varied. Similarly to the previously shown example for Cu maps, the measurement energy is chosen close to an X-ray absorption edge, in a way such as to give the maximum contrast between different oxidation states (or specific structural features) of an element. At LISA the standard ESRF voltammeter can be installed and operated inside the data collection macros.

Figure 5.5 shows, as an example, the study on  $\text{FeOOH}$  phases found as corrosion products of the steel cathode in the sodium chlorate process [18].

## 5.7 Conclusions and Perspectives

The new Italian CRG beamline at ESRF, LISA, is now in preparation for the EBS ring. In this paper some peculiar user facilities and experimental techniques available at the beamline have been presented. These techniques constitute interesting opportunities

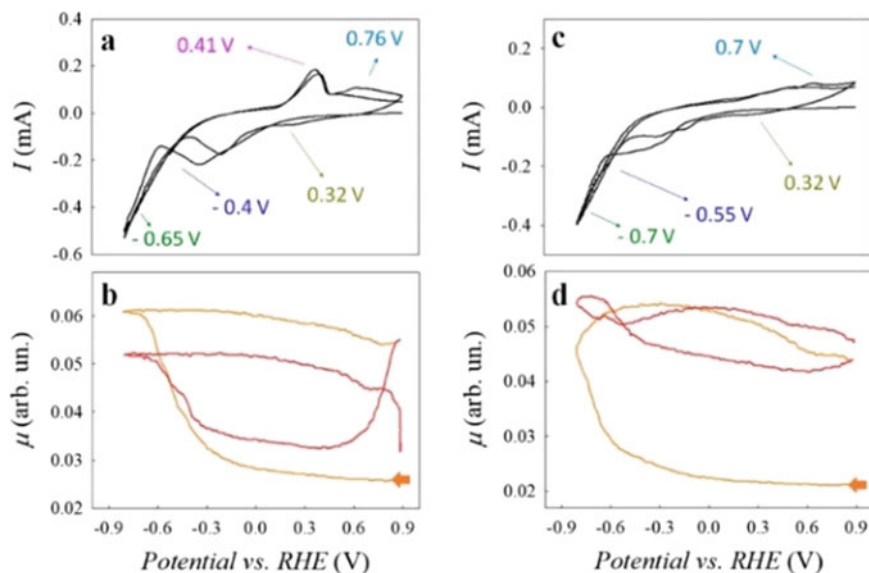


**Fig. 5.5** a, b Cyclic voltammetry and the FEXRAV for  $\gamma$ -FeOOH, respectively; c, d cyclic voltammetry and the FEXRAV for  $\alpha$ -FeOOH, respectively. From [18]

for luminescent materials, transient states, in situ chemical studies, in-homogeneous materials. With the advent of the new EBS ring, further developments such as an x-ray emission spectrometer or a  $\mu$ -focus end-station will be possible and are at present in a preliminary study phase.

**Acknowledgements** The LISA beamline is supported by CNR Department of Physical Sciences and Technologies of Matter project N. DFM.AD006.072. The instrumentation related to XEOL was obtained via the project “Collaborazione Scientifica CNR-FCT 2011-12” whereas the instrumentation for pump and probe experiment was obtained via the participation to projects EX-PRO-REL (Elettra Sincrotrone Trieste) and PRIN-2015 Project No. NEWLI-2015CL3APH.

## References

1. F. d’Acapito et al., The LISA beamline at ESRF. *J. Synchrotron Radiat.* **26**(2), 551–558 (2019)
2. F. d’Acapito et al., Activity report of the Italian CRG beamline at the European synchrotron radiation facility (ESRF). CNR-IOM-OGG, Grenoble (2018)
3. A. Puri, G.O. Lepore, F. d’Acapito, The new beamline LISA at ESRF: performances and perspectives for earth and environmental sciences. *Condens. Matter* **4**(1), 12 (2019)
4. G. Dalba et al., X-ray absorption spectroscopy on light emitting porous silicon by XEOL and TEY. *J. Non-Cryst. Solids* **232–234**, 370–376 (1998)
5. A. Rogalev, J. Goulon, X-ray excited optical luminescence spectroscopies, in *Advanced Series in Physical Chemistry. Chemical Applications of Synchrotron Radiation*, vol. 12 (World Scientific, Singapore, 2002), pp. 707–760

6. T.-K. Sham, R.A. Rosenberg, Time-resolved synchrotron radiation excited optical luminescence: light-emission properties of silicon-based nanostructures. *ChemPhysChem* **8**(18), 2557–2567 (2007)
7. L.M. Fortes et al., EXAFS study of Er, Yb doped hollow and dense SiO<sub>2</sub> microspheres. *J. Non-Cryst. Solids* **402**, 244–251 (2014)
8. W. Baekelant et al., Shaping the optical properties of silver clusters inside zeolite A via guest–host–guest interactions. *J. Phys. Chem. Lett.* **9**(18), 5344–5350 (2018)
9. D. Grandjean et al., Origin of the bright photoluminescence of few-atom silver clusters confined in LTA zeolites. *Science* **361**(6403), 686–690 (2018)
10. T. Baran et al., Operando and time-resolved X-ray absorption spectroscopy for the study of photoelectrode architectures. *Electrochim. Acta* **207**, 16–21 (2016)
11. D. Bellet et al., A 1300 K furnace for in situ X-ray microtomography. *J. Appl. Crystallogr.* **36**(2), 366–367 (2003)
12. Q. Gao et al., Switching between giant positive and negative thermal expansions of a YFe(CN)<sub>6</sub>-based Prussian blue analogue induced by guest species. *Angew. Chem. Int. Ed.* **56**(31), 9023–9028 (2017)
13. M. Todaro et al., Determination of geometry arrangement of copper ions in HKUST-1 by XAFS during a prolonged exposure to air. *J. Phys. Chem. C* **121**(44), 24853–24860 (2017)
14. J.S.P. Cresi et al., Contraction, cation oxidation state and size effects in cerium oxide nanoparticles. *Nanotechnology* **28**(49), 495702 (2017)
15. S. Sáez-Ferre et al., Use of alkylarsonium directing agents for the synthesis and study of zeolites. *Chem. Eur. J.* **25**(71), 16390–16396 (2019)
16. L. Capozzoli et al., Multi-analytical characterisation of a medieval red mosaic glass tessera of from the first facade of the Duomo of Florence Florentine manufacture, in *European Conference on Mineralogy and Spectroscopy*, Prague (2019)
17. A. Minguzzi et al., Fixed energy X-ray absorption voltammetry. *Anal. Chem.* **85**(15), 7009–7013 (2013)
18. M. Fracchia et al.,  $\alpha$ - and  $\gamma$ -FeOOH: stability, reversibility, and nature of the active phase under hydrogen evolution. *ACS Appl. Energy Mater.* **1**(4), 1716–1725 (2018)

# Chapter 6

## Estimating a Set of Pure XANES Spectra from Multicomponent Chemical Mixtures Using a Transformation Matrix-Based Approach



**Andrea Martini, Alexander A. Guda, Sergey A. Guda, Anastasiia Dulina, Francesco Tavani, Paola D'Angelo, Elisa Borfecchia, and Alexander V. Soldatov**

**Abstract** In this work, we propose a new method for the analysis of time-resolved X-ray absorption near edge structure (XANES) spectra. It allows to decompose an experimental dataset as the product of two matrices: a *pure* spectral matrix, composed by XANES spectra associable to well-defined chemical species/sites, and their related concentration profiles. This method combines the principal component analysis and the application of a transformation matrix whose elements are directly accessible by the user. We demonstrate the potential of this approach applying it to a series of XANES spectra acquired during the direct conversion of methane to methanol (DMTM) over a Cu-exchanged zeolite characterized by the ferrierite topology. Possibilities and limitations of this methodology are discussed together with a critical comparison with the Multivariate Curve Resolution Alternating Least Squares (MCR-ALS) algorithm that, in the field of X-ray absorption spectroscopy (XAS), is imposing itself as a widely used method for spectral decomposition.

---

A. Martini (✉) · E. Borfecchia  
Department of Chemistry, INSTM Reference Center and NIS and CrisDi Interdepartmental Centers, University of Torino, Via P. Giuria 7, 10125 Turin, Italy  
e-mail: [andrea.martini@unito.it](mailto:andrea.martini@unito.it)

A. Martini · A. A. Guda · S. A. Guda · A. V. Soldatov  
The Smart Materials Research Institute, Southern Federal University, Sladkova 178/24, 344090 Rostov-on-Don, Russia

S. A. Guda  
Institute of Mathematics, Mechanics and Computer Science, Southern Federal University, Milchakova 8a, 344090 Rostov-on-Don, Russia

A. Dulina · F. Tavani · P. D'Angelo  
Dipartimento di Chimica, Università di Roma "La Sapienza", P.le A. Moro 5, 00185 Rome, Italy



## 6.1 Introduction

One of the main dreams for researchers working in the field of chemistry and materials science consists in having a mathematical tool which allows to obtain an atomic-scale movie of a chemical reaction at realistic working conditions [1]. This request can be thought as the simultaneous determination of the spectra and concentrations of all the species involved in the analysed chemical reaction (i.e. reactants, intermediates and products), monitored by one or more characterization methods as a function of time. In this way, a reliable correlation between structure, kinetic and functionality can be properly identified. Focusing on the chemical speciation, X-ray absorption near edge structure (XANES) spectroscopy demonstrated to be an extremely useful technique, principally thanks to its local sensitivity and element selectivity, together with the possibility to simultaneously access both to the electronic and structural information of the material under study [2]. This fact led to the development of different strategies to decompose a dataset of XANES spectra acquired during a chemical/physical process, into a set of spectral and concentration profiles. However, most of them are based on the usage of particular constraints (i.e. the presence of a unique chemical specie at the beginning or at the end of the process) or references that, in some cases, are difficult or even impossible to measure, making their application unrealizable [3–5]. The work by Tauler et al. made a substantial contribution towards the solution of the spectral un-mixing problem. The authors proposed an automated data processing technique referred to as Multivariate Curve Resolution Alternating Least Squares (MCR-ALS) which has been largely used during the last two decades in different fields of research, ranging from chromatography to image analysis [6, 7]. MCR-ALS is basically an iterative algorithm which allows the separation of the experimental data set into pure, chemically/physically meaningful, spectra and their associated concentrations without the use of any reference. In the last years, an increasing numbers of research groups have begun to use it in the analysis of large XAS datasets relevant to different scientific fields, such as battery research [8], quantum-dots formation [9], solid-state chemistry [10] and heterogeneous catalysis [11–14]. However, the possibility retrieve, from this method, a proper set of pure spectra and concentration profiles having a spectroscopic meaning seems to depend on the amount of the variance of the XANES dataset and on the initialization of the MCR-ALS routine [15]. There are, in fact, some XANES dataset, such as the ones reported by Guda and Bugaev [16, 17], showing only the variation of small spectral features causing, in this way, the failure of the MCR-ALS analysis. This fact lead to the development of a new approach (part of the PyFitIt software [18]) based on the joined application of Principal Component Analysis (PCA) and of a user-defined transformation matrix. In general, no particular standards are required to drive the output of this method towards a meaningful solution. Nonetheless, some background knowledge of the system under study (e.g. from complementary characterization techniques or computational analysis) appears to be greatly helpful for a robust interpretation of the results. In Sect. 6.3.1.2, this new method is applied to a dataset constituted of a series of Cu K-edge XANES spectra, collected on Cu-exchanged

ferrite zeolite (Cu-FER) during the direct conversion of CH<sub>4</sub> to CH<sub>3</sub>OH. Finally, the obtained results are critically discussed and compared in Sect. 6.3.1.2.2 with the ones retrieved using the Multivariate Curve Resolution—Alternating Least Squares (MCR-ALS) method.

## 6.2 Method

### 6.2.1 The Transformation Matrix Approach

Let us consider an experimental XANES dataset  $\mu_{ij}$  composed by M energy points and L spectra (i.e.  $\dim(\mu_{ij}) = M \times L$ ), acquired during an experiment, where one or more physical or chemical variables are varying (e.g. time, temperature, pressure, pH ...). Each spectrum  $\mu_i$  of the dataset  $\mu_{ij}$  can be expressed as a linear combination of N *pure* spectral components  $s_j$  (with  $N < L$ ) as follow:

$$\mu_i = \sum_{j=1}^N c_{ij}s_j + \varepsilon_i \quad (6.1)$$

Equation (6.1) is the so-called Lambert and Beer equation [19]. Under this representation,  $\mu_i$  and  $s_j$  are one-dimensional vectors with length equal to M, while the scalar term  $c_{ij}$  is the fraction of the jth component acquired during the ith scan (with  $i = 0, 1, \dots, L$ ). Finally, the vector  $\varepsilon_i$  represents the experimental noise values associated to the ith vector in the dataset. It is worth noting that each of the N components must refer to a determined chemical species present in the analysed data mixture and must show some well-defined spectroscopic features able to visually characterize it (e.g. edge position, intensity/shape of the white line peak; number, energy position, and intensity and pre-edge and rising-edge peak ...).

Considering Eq. (6.1), one would recover, starting from each experimental spectrum  $\mu_i$ , the related pure spectra  $s_j$  and the associated concentration values  $c_{ij}$ . This request can be seen as an inverse problem. Herein, we present a mathematical method based on the usage of a transformation matrix able to find a solution of (6.1) realizing this kind of bilinear separation, entering in this way, in the family of the Multivariate Curve Resolution (MCR) methods [19, 20].

The first step of this approach foresees the application of the singular value decomposition (SVD) on the experimental dataset  $\mu_{ij}$  as follow:

$$\mu_{ij} = u_{ik}\sigma_{kl}v_{lj} \quad (6.2)$$

where  $u_{ik}$  is the absorption coefficient for the component  $k$ ,  $\sigma_{kl}$  is the element of a diagonal matrix, called singular values matrix, having the diagonal elements sorted in decreased order while the product  $w_{kj} = \sigma_{kl}v_{lj}$  can be considered as the concentration

value associated to the  $k$ th specie. Different statistical and empirical criteria can be employed, on the basis of the analysis of  $\sigma_{kl}$ , to define how many components correspond to the real pure species with different absorption coefficient (i.e.  $N$ ) and which of them are instead associated to the experimental noise ( $L-N$ ). Among all of them, due to its effective interpretability, we employed in this work the analysis of the scree plot, as reported afterwards in Fig. 6.4a.

It is worth noting that the decomposition of  $\mu_{ij}$  into the product of multiple spectral and concentration matrices is not unique. Equation (6.2) can be rewritten as:

$$\mu_{ij} = u_{ip} T_{pk} T_{kh}^{-1} w_{hj} \quad (6.3)$$

where  $T_{pk}$  is a square invertible matrix, called *transformation matrix*, having the property:  $T_{pk} T_{kh}^{-1} = \delta_{ph}$ . The inversion of  $T_{pk}$  can be used to realise decomposition (6.1) as:  $s_{ik} = u_{ip} T_{pk}$  and  $c_{kj} = T_{kh}^{-1} w_{hj}$ . This step is fundamental. In fact, following the Eckhart-Young theorem, it is possible to state that the spectral and concentration profiles obtained directly from the SVD decomposition are able to guarantee the best approximation of  $\mu_{ij}$  [21]. However, these values represent only a mathematical solution of (6.1) without any inherent chemical/physical meaning (see Fig. 6.4c). The transformation matrix allows, in this way, to convert the set of mathematical spectral and concentration profiles into a set of solutions of (6.1) having a physical/chemical interpretation. In the PCA section of the PyFitIt software [18], the elements of the transformation matrix are accessible by user and can be varied using sliders. Clearly, a proper set of constraints must be defined in order to reduce the number of elements of  $T_{pk}$  to be used (which goes as  $N^2$ ) and their range of variation. Dealing with XANES spectra, it is possible to include the non-negativity of the spectral and concentration profiles and the mass balance condition, as stated by Conti et al. in their pioneering work regarding the application of the MCR-ALS approach (see Sect. 6.3.1.2.2) to the analysis of a set of XAS data [8]. While the first two constraints can be implemented looking for a set of parameters  $T_{pk}$  able to provide absorption coefficients and concentration values that are non-negative, the mass balance condition is less straightforward to realise. Indeed, it requires the normalization of the experimental spectral profiles. For our analysis, we used the following formula:

$$\ell_i = \sqrt{\frac{1}{(E_{max} - E_{min})} \int_{E_{min}}^{E_{max}} dE \mu_i(E)^2} \quad (6.4)$$

where  $\ell_i$  is the normalization factor associated to the  $i$ th spectrum while  $E_{min}$  and  $E_{max}$  are respectively the minimum and maximum energy values of the XANES region. The requirement of the dataset normalization ensures the equality between the element of the first abstract concentration component of (6.3) (i.e.  $w_{h1}$ ) and the normalization coefficient related to the first abstract spectrum:  $w_{h1} = \ell_u$ , where

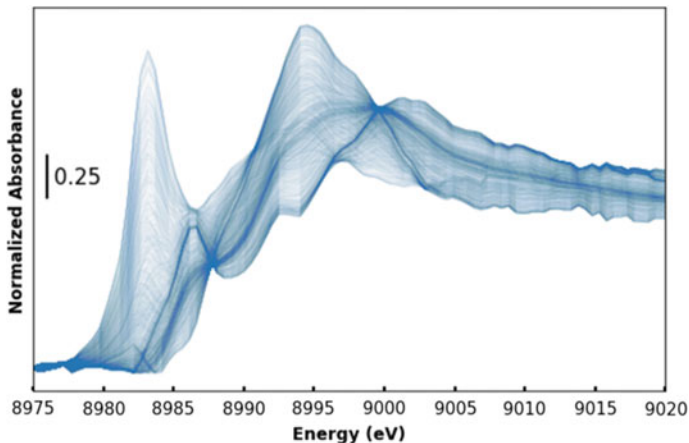


**Fig. 6.1** Set of theoretical spectra, solution of Eq. (6.1), obtained from the XANES dataset described in Sect. 6.3.1.2. In order to identify them, the following constraints have been adopted: non-negativity of the spectral and concentration profiles together with the mass-balance condition

$\ell_u = \sqrt{(1/(E_{max} - E_{min})) \int_{E_{min}}^{E_{max}} dE u_{1p}(E)^2}$ . This result can be used to guarantee the condition  $\sum_{j=1}^N c_{ij} = 1$ . In fact, it is possible to show that the normalization of the components reduces the number of matrix transformation elements from  $N^2$  to  $N^2 - N$  and determines the following simplification:

$$\sum_{j=1}^N c_{kj} = \sum_{j=1}^N T_{kh}^{-1} w_{hj} = w_{h1}/\ell_u = 1 \quad (6.5)$$

Similarly to the case of the Linear Combination Analysis (LCA) the uniform normalization of the experimental XANES spectra plays a fundamental role in the identification of spectroscopically interpretable results, in this case a set of pure spectral and concentration profiles. If the dataset is not properly normalised the condition reported in Eq. (6.5) cannot be satisfied leading to a set of concentration values whose sum for each scan can slightly differ from 1. At the same time it is possible to retrieve a series of pure spectra, characterized by a range of XANES points sited usually above the edge, which can deviate from the global profile of the XANES dataset, as described by Calvin in [22].

The presence of these constraints obviously limits the range of variation of the elements of  $T_{pk}$  and only the construction of a proper set of strongly selective constraints can lead to the isolation of a series of XANES components extremely close to the real physical/chemical solution. However, as showed, a unique solution of (6.1) cannot be identified. An ensemble of feasible XANES spectra is represented

in Fig. 6.1. Herein, this dataset has been generated considering the XANES data described in Sect. 6.3 and imposing the constraints described before.

The entire data analysis reported in this work has been realized using PYTHON 3.7. All the scripts can be provided by the corresponding author under request.

## 6.3 Case of Study

### 6.3.1 *Spectral Decomposition for Cu K-Edge XANES of Cu-FER During the DMTM Conversion*

#### 6.3.1.1 Experimental Setup and Description of the Protocol Followed

XAS data were collected during the DMTM conversion at beamline BM31 [23] of the European Synchrotron Radiation Facility (ESRF, Grenoble, France). For the measurements, we used 3 mg of a Cu-FER sample with  $\text{Cu}/\text{Al} = 0.20$  and  $\text{Si}/\text{Al} = 11$ . Details about the synthesis of this Cu-exchanged zeolite can be found in Ref. [24]. The sample was inserted in a 1 mm diameter quartz capillary with the powdered sample placed between glass wool plugs. The capillary was then fixed on a metal bracket and used as a fixed bed reactor. Finally, the gas inlet was connected to a dedicated gas flow setup. The process consisted of three steps:  $\text{O}_2$  activation at  $500\text{ }^\circ\text{C}$  (120 min, 100%  $\text{O}_2$ ),  $\text{CH}_4$  loading at  $200\text{ }^\circ\text{C}$  (180 min, 100%  $\text{CH}_4$ ) and  $\text{H}_2\text{O}$  assisted  $\text{CH}_3\text{OH}$  extraction at  $200\text{ }^\circ\text{C}$  (ca. 60 min). The temperature of the sample was controlled using a heat gun and the heating/ cooling ramps were performed with a  $5\text{ }^\circ\text{C}/\text{min}$  rate. The flow at each step was set to 2 ml/min using dedicated mass flow controllers (MFCs).

Cu K-edge XAS spectra were collected in transmission mode, using a water-cooled flat-Si (111) double crystal monochromator. The incident and transmitted X-ray intensities were detected using 30 cm long ionization chambers filled with He/Ar mixture. Scans in the range of 8800–9300 eV were continuously collected, binned with a constant energy step of 0.5 eV with the acquisition time being ca. 5 min/scan.

#### 6.3.1.2 Data Analysis

In order to obtain more insights into the conversion mechanism of  $\text{CH}_4$  to  $\text{CH}_3\text{OH}$  mediated by Cu-FER, we focused our analysis on the set of data acquired after the  $\text{O}_2$  activation (see Fig. 6.2), starting from the He flushing till the extraction of  $\text{CH}_3\text{OH}$  by means of steam. The collected dataset shown in Fig. 6.3 is composed by 30 XANES spectra properly normalized to the unity edge jump using the Athena software from the Demeter package [25].

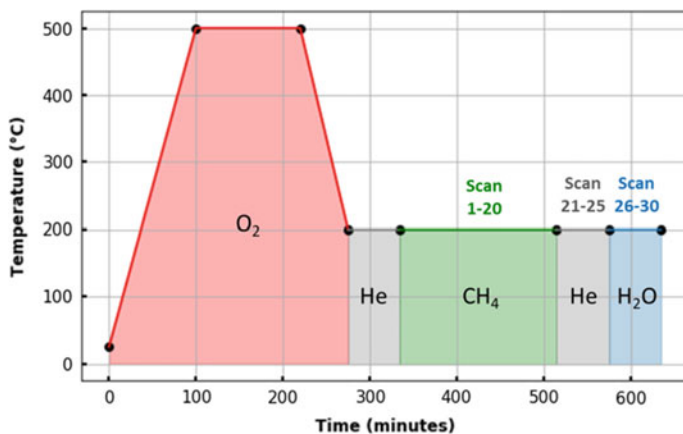


**Fig. 6.2** Graphical representation of the protocol followed: 120 min  $O_2$  activation at 500 °C (red), 180 min  $CH_4$  loading at 200 °C (green), steam-assisted  $CH_3OH$  extraction at 200 °C for ca. 60 min (blue). The sample and the lines were flushed with He (grey segments) after  $O_2$  activation and  $CH_4$  loading for ca. 60 min

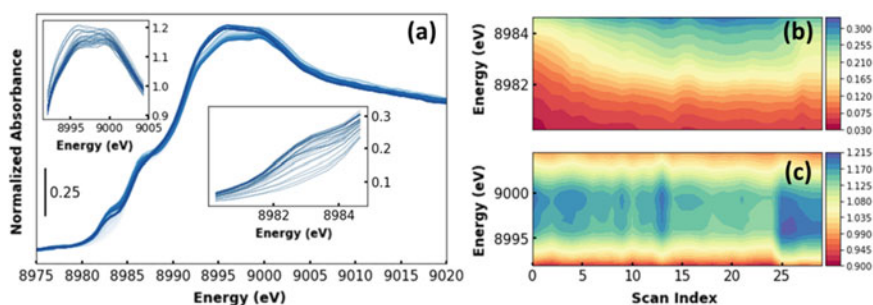


**Fig. 6.3** **a** Plot of the analysed time-resolved XANES dataset: the insets contain the magnification of the spectral regions showing the highest variations during the followed experimental protocol: white line variations (upper left inset), rising-edge peak variation (central inset). **b** Contour maps associates to the insets reported in Figure (a)

As it is possible to see from Fig. 6.3a, during the entire MTM process, only small variations in the XANES spectra occur. In particular, these variations involve the intensities of the XANES white line and the rising-edge transitions (see the insets of Fig. 6.3a). Analysing these spectral modifications together with the variation of the scan index (that can be imagined as a temporal variable, being the adopted sampling time in our experiment 5 min/scan) some interesting trends appear. By sending  $CH_4$ , scans 1–20, the energy edge is shifted progressively towards lower values, the XANES white line magnitude becomes lower, while the intensity of the  $1s \rightarrow 4p$  dipolar transition at ca. 8983 eV (characteristic of the Cu(I) ions) increases, as showed in Fig. 6.3b. This phenomenon can be interpreted as the reduction of a

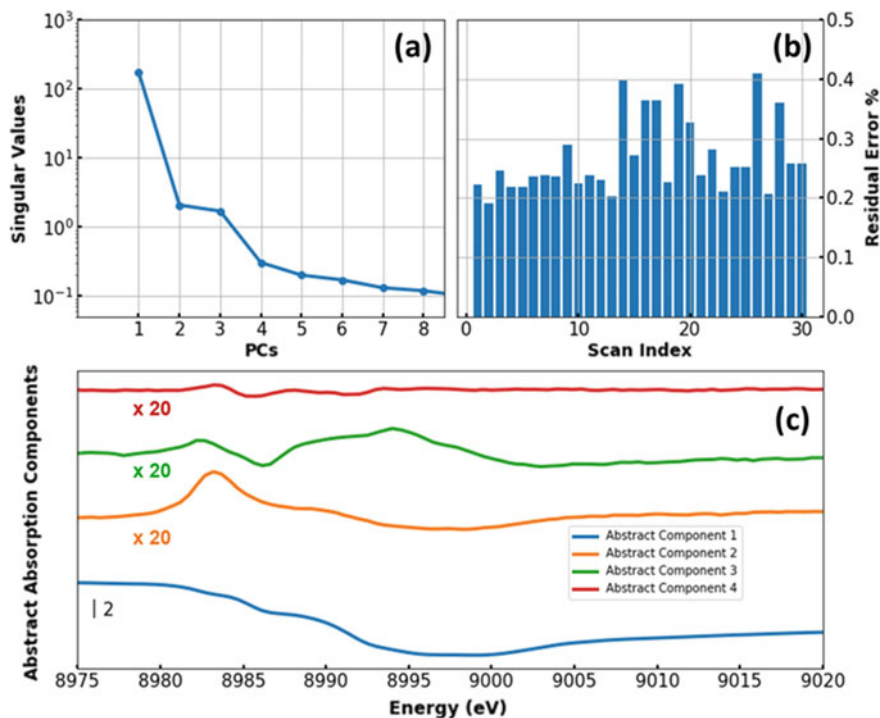


**Fig. 6.4** PCA output. **a** Scree plot (logarithmic plot of the singular values extracted by the SVD vs. the number of PCs). **b** %R-factor (residual error) associated to the reconstruction of each spectrum of the experimental dataset shown in Fig. 6.3a using three components. **c** First four abstract components retrieved by PCA. All the abstract components, except for the first one, have been multiplied for a factor 20 in order to enhance their main spectral features

certain quantity of framework-coordinated Cu(II) sites, previously formed during the activation process in the presence of  $O_2$ , to Cu(I) sites, always coordinated to the zeolite lattice oxygens [2, 24, 26]. During the extraction of  $CH_3OH$  with water, scans 26–30, the edge energy is re-shifted towards higher energy, the intensity of the Cu(I)  $1s \rightarrow 4p$  transition is abated and the XANES white line feature grows up again (see Fig. 6.3c). These evidences underline the presence of a higher abundance of Cu(II) sites in the chemical mixture, plausibly encompassing both Cu(II) aquo-complexes and framework-coordinated Cu(II) ions.

In order to identify the proper number of chemical species present in the analysed mixture, we applied the Principal Component Analysis (PCA) on the dataset showed in Fig. 6.3a. The results of this approach are reported in Fig. 6.4.

The analysis of the singular values, extracted by the SVD of the experimental dataset is reported in Fig. 6.4a. It is worth to note that each singular value is tight to the data variance explained by the related PC by the following relation:  $s_i = \sigma_{ii}^2 / (M - 1)$ , where the subscript  $i$  denotes the  $i$ th component [21]. It follows that those components, that are associated to the noise, contribute in the same way to the

dataset reconstruction and, for this reason, they are characterised by similar singular values. In the graph, an elbow is evident in proximity of the third component while from the fourth one onwards all the singular values lay approximately on a flat line. This trend suggests the presence of three PCs able to characterise the entire dataset. The fourth PC presents only some rather weak features if compared to the first three PCs, as evidenced in Fig. 6.4c and, for these reasons, it should be associated to some noise contribution or to the presence of a highly diluted specie. It is interesting to observe that the dataset reconstruction process with three PCs, shows an increase of the %R-factor values in proximity of two groups of scans: 14, 16, 17, 20 and 26, 28. The R-factor, for each scan, is defined as follows:

$$\%R_{Factor} = 100 \times \frac{\sum_{i=1}^M |\mu_{ij}^{PC} - \mu_{ij}|}{\sum_{i=1}^M |\mu_{ij}|} \quad (6.6)$$

where  $\mu_{ij}^{PC}$  is the dataset reconstructed with three PCs. For the first group of scans, it is interesting to underline the correlation between the higher error values with the increasing of the spectral white line and the shift of the edge energy, as showed in Fig. 6.3b, c. On the other hand, the error associated with the second group of scans seems to be related to the appearance of  $\text{CH}_3\text{OH}$  during the steam-assisted extraction step. This analysis suggests that some transient chemical species are present for the mentioned scans, influencing the experimental spectra. Probably, these small variations in the dataset could be represented by the fourth and fifth component. However, based on the scree plot analysis results and on the error on the reconstruction using three PCs (lower than 0.45%) we decided to retrieve only three PCs.

### Application of the Transformation Matrix Approach and Interpretation of the Results

We applied the transformation matrix approach on the experimental dataset showed in Fig. 6.3a. Each spectrum was initially normalised using Eq. (6.4). Then, employing the *target Transformation* function of PyFitIt [18] for three PCs, we defined a  $3 \times 3$  transformation matrix. Thanks to the normalization constraint, we reduced the number of sliders to adjust from nine to six. The analysis of the raw data shows that the background profile due to the atomic Cu K-edge absorption process is similar for all the recorded spectra. As already pointed out by Giorgetti et al. in [27], this behaviour indicates that there are no secondary processes such as the loss or dissolution of a part of the sample during the entire reaction process or the movement of the powder inside the capillary. This fact justified the application, in this case, of the mass balance condition closure described in Sect. 6.2.1. Finally, the elements of the transformation matrix were moved according to the non-negativity of the spectra and concentration profiles.



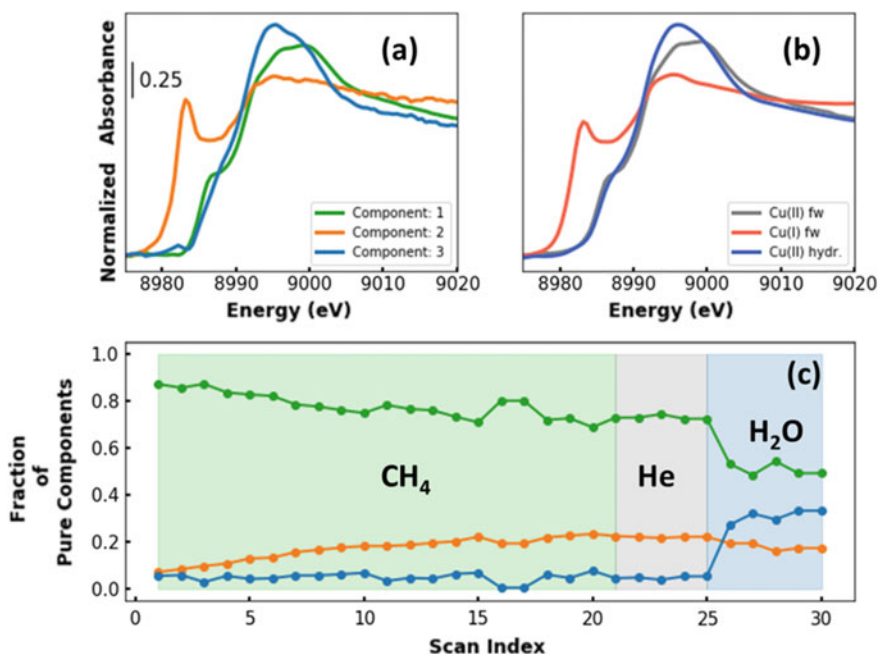


**Fig. 6.5** **a, c** Spectral and concentration profiles retrieved using the transformation matrix approach. **b** Cu-references used to test visually the goodness of the spectral decomposition

A retrieved solution of Eq. (6.1) having a well-defined chemical/physical meaning is given by matrix  $T_{pk} = \begin{pmatrix} 1/\ell & 1/\ell & 1/\ell \\ 3.40 & -1.05 & -0.70 \\ 0.45 & 1.50 & -0.30 \end{pmatrix}$ , with  $1/\ell = -0.18$  and it is showed in Fig. 6.5a, c.

It is possible to see that the identified spectral profiles are extremely similar to a set of references showed in Fig. 6.5b. These include a pseudo-octahedral Cu(II) aquo-complex (*Cu(II) hydr.*) as well as two framework-coordinated Cu(II) and Cu(I) species referred to as *Cu(II)* and *Cu(I) fw*, respectively. The *Cu(II) hydr.* was obtained measuring a Cu(II) acetate aqueous solution at RT. The *Cu(I) fw* reference was collected at RT after heating the sample up to 400 °C in vacuum. Finally the XANES acquired in He at 200 °C, just before the CH<sub>4</sub> loading step, was used as a *Cu(II) fw* reference.

The extracted profiles seem to be affected by a small amount of noise. This fact can be explained remembering that if the correct number of components is chosen, the PCA acts as a filter removing the highest amount of noise characterizing the dataset. However, as described by Malinowski [28], there is always a fraction of residual noise depending on the quality of the measurement mixed in the pure spectral and concentration profiles which cannot be removed deleting the unnecessary components.

The analysis of the concentration profiles associated to the pure spectra extracted showed in Fig. 6.5c and can lead to the following interpretation.

Scan 1 corresponds to the first state when the CH<sub>4</sub> is sent over the investigated Cu-FER sample at 200 °C. As it is possible to see from the concentration profiles (Fig. 6.5c), the amount of the second and third component is almost zero and it is possible to conclude that this scan is dominated by framework-coordinated Cu(II) sites (component n° 1, green spectrum in Fig. 6.5a). A precise assessment on the nature of this Cu(II) site is not straightforward. Depending on the zeolite topology, a number of Cu(II)-oxo species potentially active towards DMTM have been proposed to form during the high-temperature activation in O<sub>2</sub> and their structures are still debated in the literature [2, 24, 26, 29]. Among them, we can mention mono( $\mu$ -oxo) dicopper(II) cores, dicopper(II) peroxides and monocopper(II) superoxides. XANES simulations carried out on selected monomeric and dimeric Cu<sub>x</sub>O<sub>y</sub> moieties demonstrated that there is no sharp spectroscopic contrast in terms of spectral features among them [30, 31]. It follows that the first component profile is associated to a pure spectrum but it can be attributed to different Cu(II) species that, during the entire reaction, can coexist, making their identification impossible to be achieved using this technique.

During the sample interaction with CH<sub>4</sub>, we observe the partial reduction of Cu(II) to Cu(I) (component n° 2, orange spectrum in Fig. 6.5a), see scans 1–25 in Fig. 6.5c. Focusing on the Cu(I) species, it is interesting to note that the maximum development of the related concentration profile occurs relatively early, around scan n° 7. Subsequently, concentration values tend to stabilize, indicating saturation of some Cu(II) reactive species. The Cu(I) spectrum, retrieved by the transformation matrix approach, can be associated to a two-fold coordinated Cu(I) specie. In fact, assuming the mono( $\mu$ -oxo) dicopper(II) as the active site for the CH<sub>4</sub> oxidation, the Cu(I) site supports the opening of the Cu-( $\mu$ -O)-Cu bridge in the mono( $\mu$ -oxo) dicopper cores upon ( $\mu$ -O) methylation giving rise to the Z[Cu(I)(OCH<sub>3</sub>)Cu(II)]Z intermediate (where Z denotes coordination to two zeolite framework oxygen atoms in the proximity of a charge-balancing framework Al site) [26]. Starting from this last structure, a proposed scenario involves the di-copper core dissociation into proximal Cu(I)/Cu(II) units, e.g. a bare ZCu(I) ion, having a spectral signature equal to component 2 of Fig. 6.5a and a methoxide Z[Cu(II)(OCH<sub>3</sub>)] complex represented by a spectrum expected to be indistinguishable by *classic* XAS spectroscopy from the one associated to component 1. Novel insights about the identification of these intermediates could be obtained using High Energy Resolution Fluorescence Detected (HERFD) XANES, proven to be extremely helpful for the detection of the small variations of the XAS features that can characterize these species [15, 32].

Considering the scans associated with the CH<sub>3</sub>OH extraction (26–30), it is interesting to see from Fig. 6.5c the presence of two processes triggered by water: the diminution of components n° 1 and n° 2, associated to framework-coordinated Cu(II) and Cu(I) species, and the appearance of a third component (blue spectrum and concentration profile) associated to a Cu(II) hydrated state. The framework-coordinated Cu(II) fraction diminution can be explained by the hydrolysis mechanism involving the methoxide group of the Z[Cu(II)(OCH<sub>3</sub>)] complex while the small

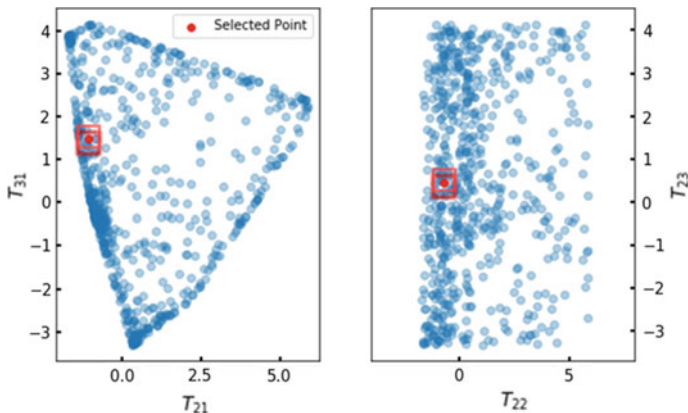


**Fig. 6.6** Graphical representation of two of the fifteen AFS, related to dataset showed in Fig. 6.3, for the couples of variables:  $(T_{21}, T_{31})$  and  $(T_{22}, T_{23})$ . These distributions have been obtained using a Monte Carlo approach, initializing and minimizing Eq. (6.7) for 1000 times. The initialization has been realized generating random numbers between  $-10$  and  $10$ , while for the minimization process, the Nelder-Mead algorithm has been employed [34]. With the red points are represented the sets of parameters able to provide the solution of Fig. 6.5, while the red cubes indicates, pictorially, the projections of a six-dimensional hypercube with a side of  $0.3$  over the 2D plane defined by these couples of parameters

abatement of the Cu(I) concentration values can be associated with  $H_2O$ -mediated re-oxidation pathways.

As previously discussed in Sect. 6.2.1, the solution obtained by the matrix transformation method depends on the values of the elements of  $T_{pk}$  and it is not unique. In order to quantify the maximum and minimum values of the spectral and concentration profiles for the solutions of (6.1) having a chemical/physical meaning, we proceeded with the following protocol:

First, we defined an objective function  $P$  as [33]:

$$P(T_{21}, T_{22}, T_{23}, T_{31}, T_{32}, T_{33}) = \sum_{i=1}^L \sum_{j=1}^N H_s(s_{ij}) s_{ij}^2 + \sum_{k=1}^M \sum_{j=1}^N H_c(c_{kj}) c_{kj}^2 \quad (6.7)$$

Due to the normalization constraint,  $P$  does not depend on the first row of  $T_{pk}$ , fixed to  $1/\ell$ . In (6.7)  $H_s$  is a Heaviside function that returns 0 if the spectral values  $s_{ij}$  are higher or equal to zero and 1 for their negative values, while  $H_c$  is a second function, associated with the concentrations profiles, that returns 0 for concentrations within 0 and 1 while it is equal to 1 if this last condition is not satisfied. Initializing randomly function  $P$  and minimizing it for a considerable number of iterations (i.e. 1000 or more) it is possible to obtain a graphical representation of all the combination of the elements of matrix  $T_{pk}$  satisfying the required constraints, called Area of Feasible Solutions (AFS), see Fig. 6.6. The ensemble of spectra associated to every minimum point of (6.7) is showed in Fig. 6.1.

The geometric shapes of the obtained AFS can be explained taking into account the portions of a  $\mathbb{R}^6$  space enclosed in a subspace limited by the conditions  $s_{ij} \geq 0$  and  $0 \leq c_{ij} \leq 1$  [33]. Despite the large range of variation of the elements of the transformation matrix, only a small number of combinations of these parameters are acceptable. The retrieved spectra must satisfy the imposed constraints as showed by Figs. 6.1 and 6.6, but, at the same time, they must be characterized by determined spectral features physically and chemically interpretable. This fact reduces drastically the number of spectra of Fig. 6.1 and consequently the related AFS showed in Fig. 6.6. Unfortunately, at the moment, there is no technique available able to automatically assess if a XANES spectrum, generated by a determined combination of parameters  $T_{pk}$ , has a physical/chemical meaning. The transformation matrix approach is not able to realize the so-called *blind source separation* of the experimental signal and only the user's intuition and the knowledge of the system under study can lead to a meaningful solution. It is opinion of the authors that the creation of a large dataset of reference XANES (experimental and simulated) spectra together with a solid Machine Learning algorithm for spectral comparison could improve the quality of the results. However, it is possible to select a region surrounding a feasible point and try to identify the maximum and minimum band boundaries of the feasible solutions having a physical/chemical meaning. To do this, we exploited the idea of Tauler [35] and we defined the following scalar function:

$$f_n(T_{ij}) = \frac{s_{in}(T_{ij})c_{nj}(T_{ij})}{\mu_{ij}} \quad (6.8)$$

where the operator  $\|\cdot\|$  indicates the Frobenius norm. This function gives the ratio between the contribution of a particular  $n$ th specie with respect to the total contribution coming from all the components  $\mu_{ij}$ . The optimization of this objective function, either maximized or minimized under the constraints, will give respectively the maximum and the minimum boundary for each chemical specie present in the dataset. In our case, we considered a subspace of AFS consisting of a six-dimensional hypercube having a side equal to 0.3 (six times the step variation used as a standard values in PyFitIt [18]) surrounding the point which provides the spectra and concentrations of Fig. 6.5. Afterwards, we minimised and maximised Eq. (6.8) changing progressively the components. This step was realised under constraints (described before) using the Sequential Least Squares Programming method [36].

The obtained results are showed in Fig. 6.7.

Analysing this picture, it is interesting to see that the lines constituting the spectral variation bounds are extremely close to each other. Some small differences appear in the rising-edge region (especially for the  $1s \rightarrow 4p$  peak of the Cu(I) component) and for the white line peak. Vice-versa, larger variations are observable for the related concentration profiles. The explanation must be found in the selection of the subspace of the  $T_{pk}$  parameters used for the minimization procedure [37]. The chosen hypercube has been defined in order to incorporate only the spectral profiles characterized by interpretable spectroscopic features. This '*user-based*' constraint limited

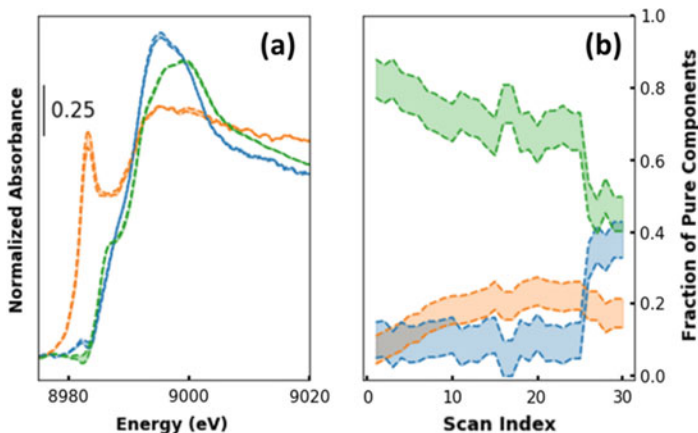


**Fig. 6.7** Spectral (a) and concentration (b) band boundaries calculated for the profiles of Fig. 6.5 minimizing and maximizing for six times Eq. (6.8)

the shape of the pure spectral profiles that can be isolated but not their concentrations that, in the selected range of variation of the  $T_{ij}$  can undergo significant variations. Possible strategies to reduce the concentration band boundaries amplitude could rely on the introduction of additional concentration constraints or by fixing a reference spectrum as a *pure* component in the analysed system.

#### Application of the MCR-Alternate Regression (MCR-AR) Method on the Analysed Dataset

For the sake of comparison, we performed the decomposition of the experimental dataset of Fig. 6.3 according to Eq. (6.1) using a different MCR method based on an alternate regression algorithm [38]. This technique is becoming extremely popular in the field of the XAS analysis, especially for time or space-resolved measurements when a large series of spectra must be analysed or when a high number of components (i.e.  $>3$ ) characterize the experimental dataset. The MCR algorithm requires an initial set of spectral  $s_{ih}^0$  or concentrations profiles  $c_{hj}^0$ . If, as an example, the algorithm is initialized using  $s_{ih}^0$ , then the concentration profiles related to step  $k = 1$  will be given by the following minimization:

$$c_{hj}^1 = \underset{c_{hj}^0}{\operatorname{argmin}}[\mathcal{F}_C(s_{ih}^0 c_{hj}^0)] \quad (6.9)$$

where  $\mathcal{F}_C$  is an objective function. Once the concentration profiles have been defined, a new set of spectral values can be retrieved minimizing a second objective function  $\mathcal{F}_S$ :

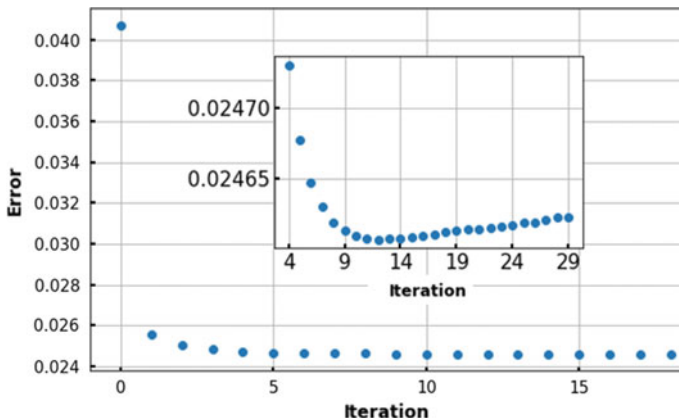


**Fig. 6.8** Plot of the error in the dataset reconstruction, calculated using Eq. (6.11), versus the number of iterations employed. The MCR-ALS routine has been initialized using spectra showed in Fig. 6.5b. The insets report the magnification of minimum region located at iteration n° 12

$$s_{ih}^1 = \underset{s_{ih}^0}{\operatorname{argmin}}[\mathcal{F}_S(s_{ih}^0 c_{hj}^1)] \quad (6.10)$$

Both the minimization processes (6.9) and (6.10) must be performed under constraints. Among all the different regressors available in Python, we found particularly suitable for the XANES decomposition the OLS (ordinary least squares) regressor, which minimizes the  $L_2$ -norm (residual sum of squares) among the original dataset  $\mu_{ij}$  and the reconstructed-one. In the literature, the MCR method based on the multiple OLS regression is usually named as MCR-ALS (where ALS stands for alternating least squares) [6]. Herein, the *classical* XANES constraints can be imposed (i.e. spectral and concentration non-negativity and mass balance condition) allowing one to drive the set of minimizations towards a feasible solution. The scheme of multiple regression described above can be easily extended to  $k$ -iterations. For each step, as a function of the retrieved  $s_{ih}^k$  and  $c_{hj}^k$ , an expression describing the goodness of the reconstruction can be calculated. In our analysis, we adopted  $\mathcal{E}_k$  described by the following equation [39]:

$$\mathcal{E}_k = 100 \times \left\langle \sqrt{\frac{\langle (\mu_{ij} - s_{ih}^k c_{hj}^k)^2 \rangle_i}{\langle \mu_{ij}^2 \rangle_i}} \right\rangle \quad (6.11)$$

where the operator  $\langle \cdot \rangle_i$  denotes the mean over the columns' matrix while  $\langle \cdot \rangle$  represents the mean calculated on a one-dimensional vector. Usually, if the difference between the errors associated to two consecutive iterations is lower than 0.1% the routine is stopped. In the case of the Cu-FER dataset in Fig. 6.3, the error trend related to the MCR-ALS method versus the iteration number is reported in Fig. 6.8. It is

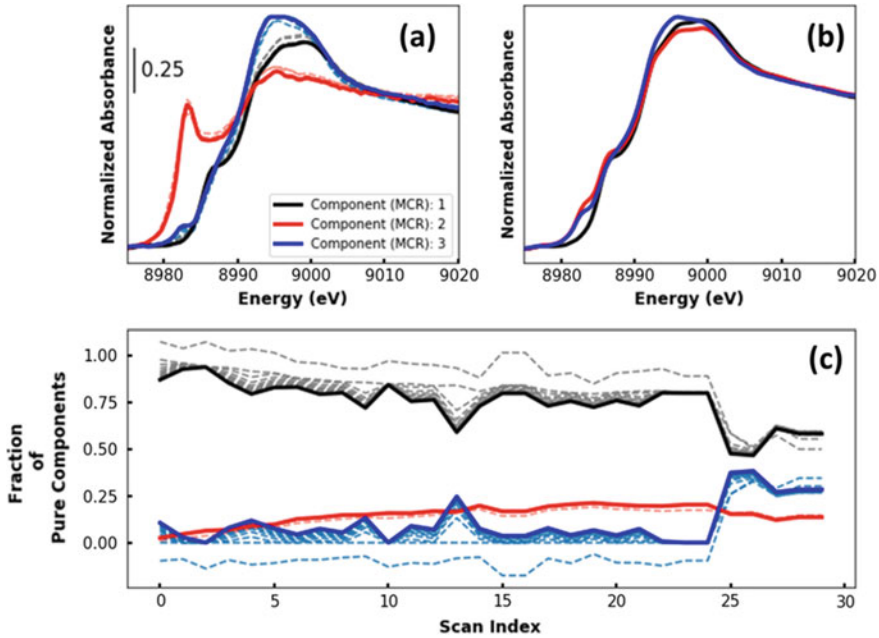


**Fig. 6.9** a, c Spectral and concentration profiles obtained by MCR-ALS algorithm initialized with the spectral references showed in Fig. 6.5b. The dashed lines represent the intermediate spectra and concentration before reaching the minimum values of the error in the dataset reconstruction process. **b** Set of spectral profiles obtained by the same method initialized using SIMPLISMA algorithm

interesting to see that after three iterations the difference  $\Delta\mathcal{E}_{23} = (\mathcal{E}_2 - \mathcal{E}_3) < 0.1\%$ ; after the third iteration only small variations occur, indicating that this set of spectra is already a good candidate to represent properly the dataset. However, for the sake of completeness, we assumed as the final state of the refinement process the one associated to the minimum value of the error function  $\mathcal{E}_k$ , that corresponds to the 12th iteration.

The power of this method stands principally in its *blindness* regarding the system under study. However, the entire routine is extremely sensitive to the kind of initialization used. Different statistical techniques such as EFA and SIMPLISMA can be applied to generate or isolate a proper set of spectra or concentration profiles suitable for the subsequent minimization routine [40, 41]. Nevertheless, these methods strongly depend on the amount of variation of spectra in the dataset [15]. If these variations are low, as for the dataset under study, MCR-ALS algorithm often fails, proposing a minimum characterized by spectra and concentrations, which minimize the error associated to the reconstruction but are still a mixture of pure components; see Fig. 6.9b.

The solutions to this problem are multiple but involve further measurements or a deeper knowledge of the system under study. Different datasets supposed to be characterized by the same components can be merged together in order to increase

the variance associated to the data, helping, in this way to identify a proper initial set of spectral and concentration profiles. An example where this strategy provided good results can be found in [42], where multiple XANES datasets collected on Cu-zeolites (chabazite) samples with different Si/Al and Cu/Al ratios, during the same activation process (from 25 to 400 °C) were joined in one larger dataset. Another strategy could be fixing some components to determined references (supposed to be present in the data mixture) or the initialization of the ALS routing using always selected references or some spectral profiles supposed to be connected with almost *pure* species. This last method, employing the reference spectra in Fig. 6.5b, was the one that we used to retrieve the set of spectral and concentration profiles, reported in Fig. 6.9a, c. Herein, the isolated components have a well-defined chemical-physical meaning and differ from the spectra used for the initialization only for small variations in the pre-edge and on the white-line. Finally, it is also interesting to note that the identified MCR-ALS concentration profiles lie in the band boundaries region showed in Fig. 6.7b, confirming the comparability of this method with the transformation matrix approach.

## 6.4 Conclusions

In this work, we firstly demonstrated that the transformation matrix approach is an efficient technique for the analysis of a generic experimental XANES dataset, even when characterized by small spectral variations, as it is the case for the Cu K-edge XANES dataset described in Sect. 6.3, collected during DMTM over Cu-FER. Afterwards, we compared the results obtained through the application of this method with the ones derived by the MCR-ALS approach. We showed that both techniques are able to isolate similar pure XANES spectra. However, we stressed the fact that the set of spectral and concentration profiles provided by the MCR-ALS approach seem to depend strongly on the degree of the variation characterizing the experimental dataset and on the methods adopted for the initialization of the routine. On the other hand, despite the inability to identify a unique solution, the application of constraints can drastically reduce the number of solutions provided by the transformation matrix approach, leading to a set of chemically/physically interpretable spectra and concentration profiles. At the same time, the multiple minimization and maximization of Eq. (6.8) provides a valid method to define the variation bounds associated to the pairs of spectral and concentration profiles identified by this new technique.

**Acknowledgements** AAG and SAG acknowledge the Russian Foundation for Basic Research (project № 20-32-70227) for the financial support. We are grateful to D. Pappas (University of Oslo) for the fruitful discussions about the chemical interpretation of the results obtained using the approach described in this article.



## References

1. G. Smolentsev, G. Guilera, M. Tromp, S. Pascarelli, A.V. Soldatov, Local structure of reaction intermediates probed by time-resolved X-ray absorption near edge structure spectroscopy. *J. Chem. Phys.* **130**, 9 (2009)
2. D.K. Pappas, E. Borfecchia, M. Dyballa, I.A. Pankin, K.A. Lomachenko, A. Martini, M. Signorelli, S. Teketel, B. Arstad, G. Berlier, C. Lamberti, S. Bordiga, U. Olsbye, K.P. Lillerud, S. Svelle, P. Beato, Methane to methanol: structure activity relationships for Cu-CHA. *J. Am. Chem. Soc.* **139**, 14961–14975 (2017)
3. T. Ressler, WinXAS: a program for X-ray absorption spectroscopy data analysis under MS-Windows. *J. Synchrotron Radiat.* **5**, 118–122 (1998)
4. Q. Wang, J.C. Hanson, A.I. Frenkel, Solving the structure of reaction intermediates by time-resolved synchrotron X-ray absorption spectroscopy. *J. Chem. Phys.* **129**, 7 (2008)
5. S.M. Webb, SIXpack: a graphical user interface for XAS analysis using IFEFFIT. *Phys. Scr.* **T115**:1011–1014 (2005)
6. J. Jaumot, R. Gargallo, A. de Juan, R. Tauler, A graphical user-friendly interface for MCR-ALS: a new tool for multivariate curve resolution in MATLAB. *Chemometr. Intell. Lab. Syst.* **76**, 101–110 (2005)
7. R. Tauler, Multivariate curve resolution applied to second order data. *Chemometr. Intell. Lab. Syst.* **30**, 133–146 (1995)
8. P. Conti, S. Zamponi, M. Giorgetti, M. Berrettoni, W.H. Smyrl, Multivariate curve resolution analysis for interpretation of dynamic Cu K-edge X-ray absorption spectroscopy spectra for a Cu doped V<sub>2</sub>O<sub>5</sub> lithium battery. *Anal. Chem.* **82**, 3629–3635 (2010)
9. B.L. Caetano, V. Briois, S.H. Pulcinelli, F. Meneau, C.V. Santilli, Revisiting the ZnO Q-dot formation toward an integrated growth model: from coupled time resolved UV–Vis/SAXS/XAS data to multivariate analysis. *J. Phys. Chem. C* **121**, 886–895 (2017)
10. H.W.P. Carvalho, S.H. Pulcinelli, C.V. Santilli, F. Leroux, F. Meneau, V. Briois, XAS/WAXS time-resolved phase speciation of chlorine LDH thermal transformation: emerging roles of isovalent metal substitution. *Chem. Mat.* **25**, 2855–2867 (2013)
11. W.H. Cassinelli, L. Martins, A.R. Passos, S.H. Pulcinelli, C.V. Santilli, A. Rochet, V. Briois, Multivariate curve resolution analysis applied to time-resolved synchrotron X-ray Absorption Spectroscopy monitoring of the activation of copper alumina catalyst. *Catal. Today* **229**, 114–122 (2014)
12. J.P. Hong, E. Marceau, A.Y. Khodakov, L. Gaberova, A. Griboval-Constant, J.S. Girardon, C. La Fontaine, V. Briois, Speciation of ruthenium as a reduction promoter of silica-supported Co catalysts: a time-resolved in situ XAS investigation. *ACS Catal.* **5**, 1273–1282 (2015)
13. A. Rochet, B. Baubet, V. Moizan, E. Devers, A. Hugon, C. Pichon, E. Payen, V. Briois, Intermediate species revealed during sulfidation of bimetallic hydrotreating catalyst: a multivariate analysis of combined time-resolved spectroscopies. *J. Phys. Chem. C* **121**, 18544–18556 (2017)
14. A. Voronov, A. Urakawa, W.V. Beek, N.E. Tsakoumis, H. Emerich, M. Rønning, Multivariate curve resolution applied to in situ X-ray absorption spectroscopy data: an efficient tool for data processing and analysis. *Anal. Chim. Acta* **840**:20–27 (2014)
15. A. Martini, E. Alladio, E. Borfecchia, Determining Cu-speciation in the Cu-CHA zeolite catalyst: the potential of multivariate curve resolution analysis of in situ XAS data. *Top. Catal.* **61**, 1396–1407 (2018)
16. A.L. Bugaev, O.A. Usoltsev, A.A. Guda, K.A. Lomachenko, I.A. Pankin, Y.V. Rusalev, H. Emerich, E. Groppo, R. Pellegrini, A.V. Soldatov, J.A. van Bokhoven, C. Lamberti, Palladium carbide and hydride formation in the bulk and at the surface of palladium nanoparticles. *J. Phys. Chem. C* **122**, 12029–12037 (2018)
17. A.A. Guda, A.L. Bugaev, R. Kopelent, L. Braglia, A.V. Soldatov, M. Nachtegaal, O.V. Safonova, G. Smolentsev, Fluorescence-detected XAS with sub-second time resolution reveals new details about the redox activity of Pt/CeO<sub>2</sub> catalyst. *J. Synchrotron Radiat.* **25**, 989–997 (2018)

18. A. Martini, S.A. Guda, A.A. Guda, G. Smolentsev, A. Algasov, O. Usoltsev, M.A. Soldatov, A. Bugaev, Y. Rusalev, C. Lamberti, A.V. Soldatov, PyFitit: the software for quantitative analysis of XANES spectra using machine-learning algorithms. *Comput. Phys. Commun.* 107064 (2019)
19. C. Ruckebusch, *Resolving Spectral Mixtures: With Applications from Ultrafast Time-Resolved Spectroscopy to Super-Resolution Imaging* (Elsevier, Amsterdam, 2016)
20. J. Timoshenko, A.I. Frenkel, "Inverting" X-ray absorption spectra of catalysts by machine learning in search for activity descriptors. *ACS Catal.* **9**, 10192–10211 (2019)
21. I. Markovsky, Structured low-rank approximation and its applications. *Automatica* **44**, 891–909 (2008)
22. S. Calvin, *XAFS for Everyone* (CRC Press, Boca Raton, 2013)
23. P.M. Abdala, O.V. Safonova, G. Wiker, W. van Beek, H. Emerich, J.A. van Bokhoven, J. Sa, J. Szlachetko, M. Nachtegaal, Scientific opportunities for heterogeneous catalysis research at the SuperXAS and SNBL beam lines. *Chimia* **66**, 699–705 (2012)
24. D.K. Pappas, E. Borfecchia, K.A. Lomachenko, A. Lazzarini, E.S. Gutterod, M. Dyballa, A. Martini, G. Berlier, S. Bordiga, C. Lamberti, B. Arstad, U. Olsbye, P. Beato, S. Svelle, Cu-exchanged ferrierite zeolite for the direct CH<sub>4</sub> to CH<sub>3</sub>OH conversion: insights on Cu speciation from X-ray absorption spectroscopy. *Top. Catal.* **62**, 712–723 (2019)
25. B. Ravel, M. Newville, ATHENA, ARTEMIS, HEPHAESTUS: data analysis for X-ray absorption spectroscopy using IFEFFIT. *J. Synchrotron Radiat.* **12**, 537–541 (2005)
26. K.A. Lomachenko, A. Martini, D.K. Pappas, C. Negri, M. Dyballa, G. Berlier, S. Bordiga, C. Lamberti, U. Olsbye, S. Svelle, P. Beato, E. Borfecchia, The impact of reaction conditions and material composition on the stepwise methane to methanol conversion over Cu-MOR: an operando XAS study. *Catal. Today* **336**, 99–108 (2019)
27. M. Giorgetti, S. Mukerjee, S. Passerini, J. McBreen, W.H. Smyrl, Evidence for reversible formation of metallic Cu in Cu<sub>0.1</sub>V<sub>2</sub>O<sub>5</sub> xerogel cathodes during intercalation cycling of Li<sup>+</sup> ions as detected by X-ray absorption spectroscopy. *J. Electrochem. Soc.* **148**, A768–A774 (2001)
28. E.R. Malinowski, *Factor Analysis in Chemistry* (Wiley, Hoboken, 2002)
29. E.M.C. Alayon, M. Nachtegaal, A. Bodi, J.A. van Bokhoven, Reaction conditions of methane-to-methanol conversion affect the structure of active copper sites. *ACS Catal.* **4**, 16–22 (2014)
30. A. Martini, I.A. Pankin, A. Marsicano, K.A. Lomachenko, E. Borfecchia, Wavelet analysis of a Cu-oxo zeolite EXAFS simulated spectrum. *Radiat. Phys. Chem.* 108333 (2019)
31. I.A. Pankin, A. Martini, K.A. Lomachenko, A.V. Soldatov, S. Bordiga, E. Borfecchia, Identifying Cu-oxo species in Cu-zeolites by XAS: a theoretical survey by DFT-assisted XANES simulation and EXAFS wavelet transform. *Catal. Today* (2019)
32. D.K. Pappas, A. Martini, M. Dyballa, K. Kvande, S. Teketel, K.A. Lomachenko, R. Baran, P. Glatzel, B. Arstad, G. Berlier, C. Lamberti, S. Bordiga, U. Olsbye, S. Svelle, P. Beato, E. Borfecchia, The nuclearity of the active site for methane to methanol conversion in Cu-mordenite: a quantitative assessment. *J. Am. Chem. Soc.* **140**, 15270–15278 (2018)
33. K. Sasaki, S. Kawata, S. Minami, Constrained nonlinear method for estimating component spectra from multicomponent mixtures. *Appl. Opt.* **22**, 3599–3603 (1983)
34. J.A. Nelder, R. Mead, A simplex method for function minimization. *Comput. J.* **7**, 308–313 (1965)
35. R. Tauler, Calculation of maximum and minimum band boundaries of feasible solutions for species profiles obtained by multivariate curve resolution. *J. Chemometr.* **15**, 627–646 (2001)
36. D. Kraft, *A Software Package for Sequential Quadratic Programming* (DFVLR, Köln, 1988)
37. A.C. Olivieri, R. Tauler, The effect of data matrix augmentation and constraints in extended multivariate curve resolution-alternating least squares. *J. Chemometr.* **31**, 10 (2017)
38. C.H. Camp, pyMCR: a python library for multivariate curve resolution analysis with alternating regression (MCR-AR). *J. Res. Natl. Inst. Stand. Technol.* **124**, 10 (2019)
39. A.A. Guda, S.A. Guda, K.A. Lomachenko, M.A. Soldatov, I.A. Pankin, A.V. Soldatov, L. Braglia, A.L. Bugaev, A. Martini, M. Signorile, E. Groppo, A. Piovano, E. Borfecchia, C. Lamberti, Quantitative structural determination of active sites from in situ and operando XANES spectra: from standard ab initio simulations to chemometric and machine learning approaches. *Catal. Today* **336**, 3–21 (2019)

40. M. Maeder, Evolving factor-analysis for the resolution of overlapping chromatographic peaks. *Anal. Chem.* **59**, 527–530 (1987)
41. W. Windig, J. Guilment, Interactive self-modeling mixture analysis. *Anal. Chem.* **63**, 1425–1432 (1991)
42. A. Martini, E. Borfecchia, K.A. Lomachenko, I.A. Pankin, C. Negri, G. Berlier, P. Beato, H. Falsig, S. Bordiga, C. Lamberti, Composition-driven Cu-speciation and reducibility in Cu-CHA zeolite catalysts: a multivariate XAS/FTIR approach to complexity. *Chem. Sci.* **8**, 6836–6851 (2017)

# Chapter 7

## Revisiting the Probing Depths of Soft X-ray Absorption Techniques by Constant Initial State Photoemission Experiments



Andrea Di Cicco, Seyed Javad Rezvani, and Stefano Nannarone

**Abstract** We have recently performed accurate constant initial state (CIS) Al  $2p$  photoemission experiments on Al films covered with layers of amorphous Ge of variable thickness, using synchrotron radiation in a variable photon energy range 100–1100 eV at the BEAR beamline at Elettra. Experiments were performed within the framework of a larger research effort aimed to obtain accurate and reliable measurements of the photoelectron mean free path (MFP) at variable kinetic energy and ultimately of the probing depth of the total electron yield and total fluorescence yield (TEY, TFY) techniques. Present MFP results are compared with previous experiments and simulations, improving our present knowledge of the MFP curve in amorphous germanium and opening new experimental possibilities for accurate measurements of the probing depth.

### 7.1 Introduction

An important parameter for correct usage and understanding of soft x-ray techniques and surface electron spectroscopes is the probing depth, which is naturally limited by the energy of the probe (electrons and/or photons). The evaluation of the probing depth of various surface-sensitive experimental techniques has been the focal point of a longstanding scientific activity in the last decades. In fact, the probing depth is intimately connected to the basic physics of the inelastic processes involving excited

---

A. Di Cicco

Physics Division, School of Science and Technology, University of Camerino,  
Via Madonna delle Carceri 9, 62032 Camerino, MC, Italy

e-mail: [andrea.dicicco@unicam.it](mailto:andrea.dicicco@unicam.it)

URL: <http://gnxas.unicam.it>

S. J. Rezvani (✉)

INFN Laboratori Nazionali di Frascati, Via Enrico Fermi 4, 00044 Frascati, RM, Italy

e-mail: [rezvani@iom.cnr.it](mailto:rezvani@iom.cnr.it)

S. J. Rezvani · S. Nannarone

Consiglio Nazionale delle Ricerche (CNR), CNR-IOM, Area Scienze Park,  
34149 Bazovizza, TS, Italy

© Springer Nature Switzerland AG 2021

A. Di Cicco et al. (eds.), *Synchrotron Radiation Science and Applications*,

Springer Proceedings in Physics 220, [https://doi.org/10.1007/978-3-030-72005-6\\_7](https://doi.org/10.1007/978-3-030-72005-6_7)

electrons in condensed matter but also to the useful range of different widely used spectroscopic techniques like for example x-ray photoemission (XPS) and x-ray absorption (XAS) spectroscopy.

A variety of surface-sensitive techniques have been used for many years, like total electron yield (TEY), partial and Auger electron yields, but some confusion about the actual probing depths of the experiments persists. Scattered values for probing depths, differing up to one order of magnitude, have been used in the literature depending on the particular technique and materials of choice [1, 2]. For example, effective probing depths in the 2–10 and 70–200 nm have been used in a recent experiment for the interpretation of TEY and TFY spectra aimed at studying the evolution of the solid electrolyte interface in Li-ion battery electrodes [3, 4]. Clearly, deeper understanding of the surface and interface properties could be obtained by using more precise estimates of the probing depths in different materials and in the typical energy ranges of the currently available soft x-ray techniques.

A primary information for a reliable estimation of the probing depth of photoemission-based techniques is the inelastic mean free path (MFP). However, there are issues in the determination of this fundamental quantity both using experimental techniques and simulation methods (see for example ref. [1]). Several advances in calculating the inelastic MFP have been carried out by several scientists in the last 50 years (see for example [2, 5–11]). Modern MFP calculations are presently considered quite accurate, although MFP curves are generally obtained by algorithms that take into account experimentally determined loss functions and simplified models for the inelastic scattering. On the other hand, several techniques have been used to measure the MFP of various substances including X-ray Photoelectron Spectroscopy (see for example ref. [1]). In particular, the overlayer-film method [1, 12, 13] has been used for decades although several source of uncertainties in the determination of the MFP have been soon identified. Another important source of MFP experimental data has been the application of the elastic peak spectroscopy method, which has clear advantages in using only electron spectrometers, for which the probing energy can be easily selected, and avoid the preparation of well-characterized overlayers. Although quite simple, this technique require simplified modelling of a complex transport and electron scattering phenomenon. For the above mentioned reasons, previous MFP experimental data are somewhat lacking and scattered, and often measurements are available for few kinetic energies and selected substances. At present, mean free path curves are almost always obtained by calculations [1, 14] the validity of which is based on selected experiments.

The possibility of performing accurate soft x-ray photoemission experiments using tunable photon energies provided by synchrotron radiation sources opened the way to new reliable MFP measurements in a wide kinetic energy range. In particular, the CNR-IOM BEAR (Bending for Emission Absorption and Reflectivity) beamline [15] at the Elettra synchrotron radiation facility offers a wide range of available techniques for performance of accurate photoemission and photoabsorption experiments in the typical range 30–1800 eV for the photon beam.

In this context, we have recently performed accurate constant initial state (CIS) photoemission experiments on selected samples at variable photon energy, within the

framework of a larger research effort aimed to obtain accurate and reliable measurements of the photoelectron inelastic MFP at variable kinetic energy, and ultimately of the probing depths of various surface-sensitive techniques (TEY and Auger yields). Investigated samples consisted in Al foils with partial overlayers of (amorphous) Ge of variable thickness. The intensity decay of the main Al peaks, in particular of the  $2p$  level, was measured as a function of the kinetic energy of the photoelectron and of different Ge overlayer thickness. In this work we present a new determination of the inelastic MFP curve of electrons in amorphous Ge which has been measured in a wide kinetic energy range 30–1000 eV and compared with previous results using different techniques.

## 7.2 Experimental

Samples used for the present experimental session were 15 mm diameter pure aluminum foils, initially cleaned by Aceton and ethylic alcohol and dried in  $N_2$  flow. Thin film overlayers of amorphous germanium (a-Ge) were deposited on Al foils by thermal evaporation using well-established procedures [16]. The evaporation chamber were kept in initial vacuum of  $10^{-6}$  mbar to avoid oxidation of the Al foils. The Al foils were only partially covered by the a-Ge overlayers (9 mm wide region) of variable thickness. In this way each sample can be used both for experiments related to both uncoated and a-Ge coated aluminum. The a-Ge films were obtained using evaporation rates as low as 1.0 nm/min, as monitored using a quartz oscillator balance, in order to ensure a uniform coverage of the films. Furthermore, the samples were kept at a sufficiently long distance from the evaporation source to ensure a uniform deposition on the Al foil. The thickness of the a-Ge overlayers ranged from 2 to 10 nms. In this study we present results for 2 nm films.

Photoemission experiments were carried out at the (IOM-CNR) BEAR beam line at Elettra synchrotron radiation centre (Trieste, Italy). The Elettra beam energy was 2 GeV with a typical current of 300 mA. The beam line is described in Fig. 7.1 and operates in the 2.8–1600 eV (443–0.775 nm) spectral region, delivering an intense photon beam of selectable ellipticity. The basic optical layout is based on the PMGM (Plane Mirror Grating Mirror) configuration (see ref. [17]). The beamline exploits three monochromators for different energy range (i.e., normal-incidence GNIM from 2.7–50 eV, grazing incidence G1200 for 40–1200 eV and G1800 for 600–1600 eV). In the present work, we have used only the G1200 monochromator of the grazing incidence channel, delivering typically a flux of  $\sim 10^{11}$  photons/s (100 eV) with a resolving power of about 3000 (at 400 eV). A detailed description of the beamline is reported in Fig. 7.1.

In the present experiments the samples were transferred to the experimental chamber of the beamline at a base pressure of  $10^{-9}$  via a primary load lock chamber. Particular care has been taken about the positioning and orientation of the samples in order to minimize variations of the distance between the sample and the electron analyzer (focus of the analyzer), keeping the same geometry between the sample surface

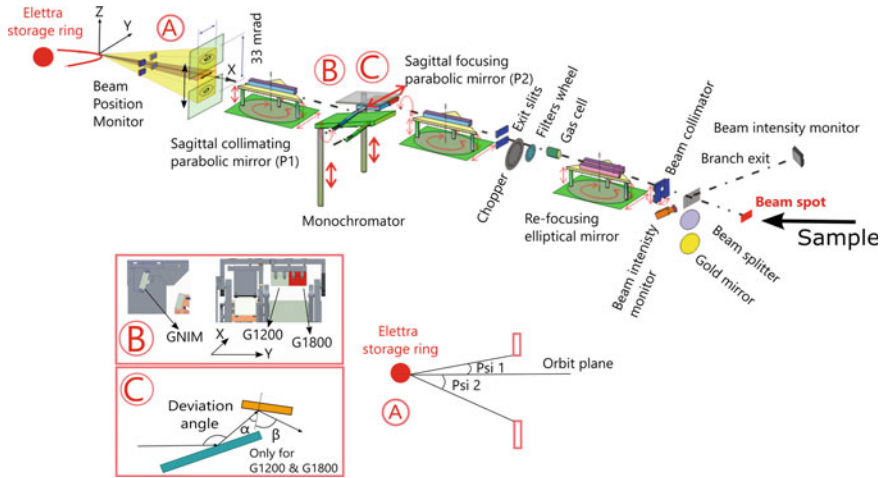


**Fig. 7.1** Layout of the BEAR beamline at the Elettra synchrotron radiation facility. A photon beam position monitor (BPM) is installed at the the beginning of the beamline. The device is based on four insulated Mo photoemitting plates, installed upstream of the beamline optics at 12m from the source. The current drained from the plates, typically of the order of some tens of  $\mu\text{A}$ , is read by four floatable ammeters (Indicated by A in figure). Photon polarization is controlled by moving a double slit device vertically to define the vertical acceptance of the bending magnet source, delivering either linear (*s* or *p*) or circular (elliptical) polarization. The BEAR Plane Mirror Grating Mirror (PMPG) configuration is based mainly on a first parabolic mirror, collimating the light emitted by the source, a monochromator working in parallel light at variable deviation angle, a second parabolic mirror focusing the dispersed beam onto the exit slit, and finally an elliptical mirror focussing the beam on the sample. The layout has been conceived to be theoretically aberration free. The bending magnet light is collimated on the monochromator by a platinum coated mirror, working in sagittal focusing. The monochromator is based on two different channels working in parallel light: the grazing incidence channel working in the 40–1600 eV energy range, and the normal incidence channel working in the 3–50 eV energy range. Both channels are mounted on the same mechanical stage, whose horizontal translation allows to select the different channel. The grazing channel is composed by a plane mirror and two plane laminar gratings G1200 and G1800, respectively with 1200 and 1800  $\text{ll/mm}$  (B). The grazing incidence channel is a based on a monochromator working in parallel light with variable deviation angle (C), related to the angles between the grating and mirror. The mirror collects the plane radiation from the first paraboloidal mirror. The monochromator works in the internal first order configuration. The optical layout allows to deliver the same wavelength following different Deviation Angles (the Deviation Angle is the angle between the incident and the reflected beam from the mirror), working in either optimization of the flux mode or in higher order rejection mode. The plane laminar grating G1200 works in the energy range 40–1400 eV, while G1800 is for the energy range 600–1600 eV. A second paraboloidal mirror P2 collects the radiation coming from the monochromator focusing it onto the exit slits. The beam is finally focused on the sample by a re-focusing elliptical mirror. The intensity of the photon beam at sample position is monitored by collecting the mirror drain current and by different detectors (beam intensity monitor, photodiode). Sample is positioned in the center of the experimental chamber and the optical set up focal point on a manipulator with six degrees of freedom of three translation and three rotation

and both the incoming photon beam and the axis of the analyzer. Samples have been thus mounted on the sample holder in the experimental chamber and rotated to be at 35 degrees with the X-axis which is the incident beam axis, as shown in Fig. 7.2. The electron analyzer was oriented with the axis parallel to the normal of the sample surface, and different sample positions (Al and Al+a-Ge) were probed using x-ray photoemission always keeping aligned the normal and the axis of the spectrometer at the same focal distance. This precise alignment procedure was found to be required to obtain reproducible intensities and shape of the photoemission signals, a feature needed in this kind of experiment.

Prior to photoemission experiments, preliminary X-ray absorption measurements at germanium M and N edges and as well as Al K and L edges were carried out in order to identify promptly the different regions of the loaded samples (positions of the a-Ge overlayers on Al) and their surface chemical characteristics (not shown here). XAS measurements were carried out in TEY (total electron yield mode) recording the drain current through an electrical contact connected to the sample holder. As described in the next Section, we carefully collected 2p Al X-ray photoemission spectra for both the raw (clean) Al surface and that covered by a thin 2nm a-Ge film, varying the photon energy with a 50 eV energy step in the 100–1050 eV range.

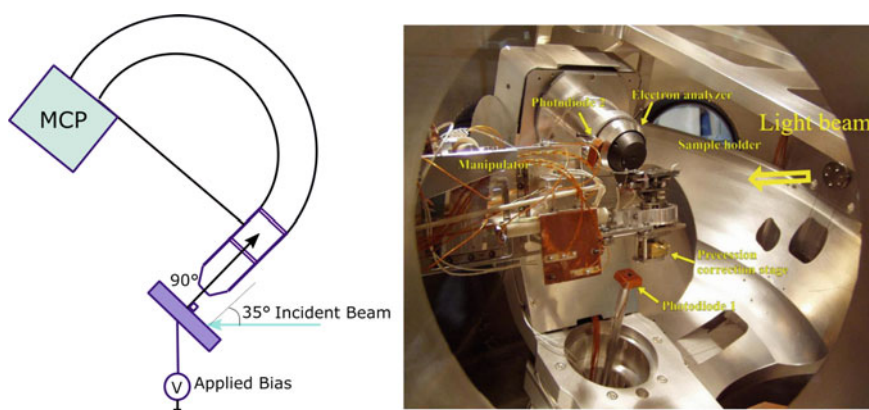


**Fig. 7.2** Left: experimental set up for photoemission measurements. The axis of the analyzer is placed normal to the sample surface which is tilted 35° with regards to the incident beam. A negative bias of 30 Volts was also applied to the back of the sample in order to improve the total photoemitted electron collection. The pass energy of the analyzer was kept fixed during the measurements ( $E_p = 20$  eV). Right: image of the inside of the experimental chamber of the BEAR beamline. The entrance of the hemispherical analyzer and sample manipulator (shown in the image) have been rotated to allow visualization of the internal components including the photodiodes for photon detection (see arrows) and the direction of the incoming photon beam (Light beam, big arrow)



### 7.3 Photoemission Spectra and Data-Analysis

Photoemission experiments were carried out at variable photon energy in the 100–1050 eV range (G1200) with a step of 50 eV, collecting accurate photoemission spectra in the Constant Initial State configuration (CIS), i.e. selecting the photoelectron kinetic energy region in the vicinity of the main Al  $2p$  peak (average binding energy 72.7 eV). As usual, the distance between the analyzer and the sample was scanned to identify the maximum photoemission signal and thus the focal point of the analyzer. This distance was kept fixed in different measurements of the Al  $2p$  photoemission peak related to clean Al and a-Ge coated regions. All the measurements were carried out using a constant pass energy ( $E_P=20$  eV) in selected kinetic energy regions. A bias of  $-30$  V was applied to the sample in order to optimize the collection of photoemitted electrons from the samples. All the measurements were carried out using proper filters regarding the selected photon energy range, in order to remove the higher order diffracted radiation by the monochromator. The exit slits defining the photon beam at sample position were  $200 \times 200 \mu\text{m}$  (lateral size), selected to optimize the photoemission signal. Typical acquisition times were 2–5 s for each kinetic energy, with a typical 0.3 eV energy step, collecting the intensity of the  $2p$  Al photoemission peaks in the 50–1000 eV kinetic energy range (corresponding to 100–1050 photon energy in CIS configuration). The kinetic energy of the collected photoelectrons is affected by the applied bias voltage ( $-30$  V).

Collected data at each photon energy included the photoemission signal obtained by the hemispherical analyzer and the current of the refocusing mirror used to monitor the flux of the incoming photon beam as discussed in the preceding Section (see Fig. 7.1). Fluctuations of the incoming photon beam intensity, although limited in the top-up running mode of the Elettra synchrotron, are important for a suitable normalization of the photoemission signal. However, the beam intensity at sample position depends on the characteristics of the beamline optics. Therefore proper normalization of the photoemission data to the incident photon flux requires separate measurements of the beam intensity at sample position that can be done using a photon detector (photodiode) normal to the incident beam (replacing the sample). The normalized photoemission signal for a given photon and electron kinetic energy ( $E_{ph}, E_{kin}$ ), collected for a given elapse of time  $\Delta t$  (here typically 2–5 s), has been thus obtained by:

$$I_{nor}(E_{ph}, E_{kin}) = \frac{I_{phot}(E_{ph}, E_{kin}, \Delta t)}{I_m(E_{ph}, \Delta t) \times \Delta t} \times \frac{I_m^a(E_{ph})}{I_0^a(E_{ph})} \quad (7.1)$$

where  $I_{phot}(E_{ph}, E_{kin}, \Delta t)$  and  $I_m(E_{ph}, \Delta t)$  are the photoemission signal and the mirror current respectively, while  $I_m^a(E_{ph})$  and  $I_0^a(E_{ph})$  are the mirror current and photodiode signal at sample position collected and averaged in separate experiments. The dark current (signal in absence of photon beam) has been subtracted for each measured signal in Eq. 7.1 ( $I_{phot}$ ,  $I_m$ ,  $I_0$ ). The normalized intensity obtained by Eq. 7.1 represents the photoemission counting rate (counts/s) in arbitrary units.

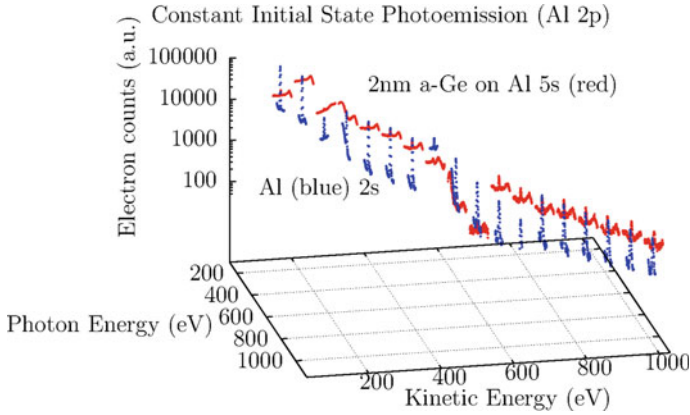


**Fig. 7.3** Photoemission data (Al  $2p$  peak) for different photon and kinetic energy showing the different intensity trends obtained in a wide range for the two samples (Al, blue line, 2nm overlayer of a-Ge on Al, red). Counting times were 2 and 5 seconds for clean Al and a-Ge on Al samples respectively

The complete data set obtained in the present experiments is reported in Fig. 7.3, where a 3D plot of the Al  $2p$  photoemission intensity as a function of photon and electron kinetic energies is presented for clean Al (blue) and the Al+2nm (Ge overlayer) samples. Besides the photoemission cross-section trend with photon energy and the attenuation of the photoemission intensity due to MFP effects, other sources of variation of the counting rate were the presence of oxygen (measurements were difficult in the 550–650 eV photon range) and other possible contamination sources (carbon) at the surface and within the thin film. In some cases, misalignments and line width broadenings were observed between the two samples, tentatively assigned to charging effects and/or to chemical shifts occurring at the interface. In order to obtain meaningful and reproducible results, we have found that experiments must be performed by keeping the samples in exactly the same geometrical configurations (same focus for the electron spectrometer, same illuminated area and same angular distributions). The manipulator of the BEAR beamline and the simple geometry chosen for the experiment (sample surface normal to the detector axis) allowed us to reproduce the sample position in space within a few  $\mu\text{m}$  of uncertainty, allowing very precise alignments and reproducible photoemission intensities.

In Fig. 7.4 we report selected normalized photoemission spectra showing the intensity change of the Al  $2p$  peak for the Al foil with and without a 2 nm overlayer of a-Ge. The reduction of the Al  $2p$  peak photoemission intensity for the 2 nm a-Ge overlayer region (blue in Fig. 7.4) as compared to clean Al is assigned to the inelastic MFP, while the background variation is assigned to the presence of germanium (and oxygen) in the overlayers. Photoemission spectra were collected in CIS mode so Al  $2p$  peaks appearing at a given kinetic energy correspond to well-defined incoming photon energies. As an example, the Al  $2p$  photoemission peak observed at  $\sim 200$  eV in Fig. 7.4 (lower panel) correspond to an incoming photon energy  $\hbar\nu = 250$  eV.

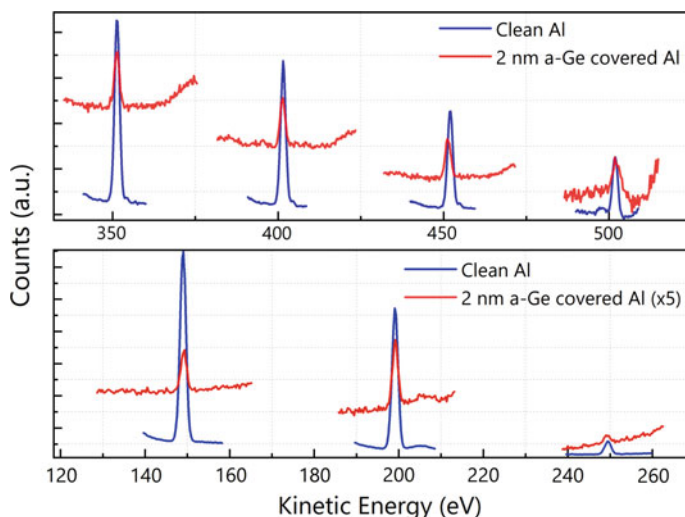


**Fig. 7.4** Measured photoemission spectra at the selected  $2p$  binding energy (Constant Initial State), obtained varying the incident photon energy. Data reported in the Figure correspond to both the clean Al surface (blue) and to the surface covered by a 2 nm thin film of amorphous germanium (a-Ge, red). Photoemission data shown in the upper and lower panels were recorded at different photon energies (200, 250, 300 eV, lower panel and 400, 450, 500, and 550 eV, upper panel), corresponding to selected  $2p$  photoelectron kinetic energies ( $\sim 150$ ,  $\sim 200$ ,  $\sim 250$ ,  $\sim 350$ ,  $\sim 400$ ,  $\sim 450$ ,  $\sim 500$  eV) as an effect of the applied bias voltage and work function. Data for the Al sample with a 2 nm a-Ge overlayer are reported with a suitable scale factor ( $\times 5$ ) in the lower panel

In general, due to the combined effect of the work function and applied bias voltage, the offset of the kinetic and photon energy is around 50 eV (Al  $2p$  binding energy is  $\sim 73$  eV).

CIS data shown in the two panels of Fig. 7.4 cover an intermediate range (150–500 eV) of kinetic energies for the Al  $2p$  photoelectrons. In the lower panel of Fig. 7.4, photoemission data of Al with the 2 nm a-Ge overlayer of a-Ge (red curves) show a reduced intensity mainly associated with the decrease of MFP and have been multiplied by a suitable factor for better visibility ( $\times 5$ ). Measurements at low kinetic energies (below  $\sim 100$  eV) were found to be extremely difficult due to the overwhelming secondary electron signal. Therefore, data collected at lower kinetic energies contain a large and increasing background contribution of the secondary electrons and were not reported in Fig. 7.4. On the other hand, the intensity of the  $2p$  photoemission peak was observed to decrease increasing the photon energy mainly due to natural decay of the  $2p$  absorption cross-section so data on a comparable scale are shown in the upper panel of 7.4 only for moderate kinetic energies (below  $\sim 500$  eV).

Data-analysis of the photoemission data was performed using standard procedures for XPS modelling. A Shirley [18] baseline was considered in the background removal process, while the Al  $2p$  photoemission peaks were modelled using a Voigt

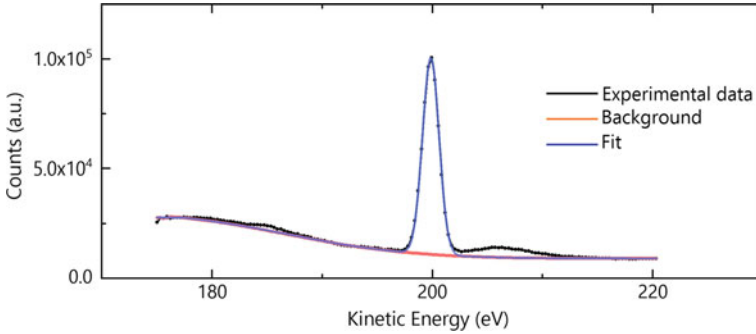


**Fig. 7.5** Example of the XPS refinement procedure carried out for the Al  $2p$  photoemission peak at 200 eV in clean aluminum (250 eV photon energy). The background function (orange line) and the final best-fit curve (blue) including a Voigt function are compared with the experimental spectrum. The agreement is remarkable

function obtained as a convolution of a Lorentzian and Gaussian profiles. A typical example of the peak-fitting procedure is shown in Fig. 7.5, where a background function and the final best-fit curve is compared with the Al  $2p$  photoemission data in pure Al. The same procedures have been applied to all of the photoemission data under consideration (see Fig. 7.3) obtaining the relevant parameters (height, width, area of each peak) for each kinetic energy with typical error bars of the order of 1–5%.

## 7.4 Results and Discussion

The inelastic MFP ( $\lambda$ ) of a-Ge was obtained using the overlayer method previously described, within a standard exponential attenuation model for the intensity of the photoemission signal related to the Al  $2p$  peak:

$$I_{Al_{2p}}^{Ge}(E_{kin}) = I_{Al_{2p}}(E_{kin}) \exp\left(\frac{-d}{\lambda \cos(\alpha)}\right). \quad (7.2)$$

In Eq. 7.2 the intensities  $I_{Al_{2p}}(E_{kin})$  and  $I_{Al_{2p}}^{Ge}(E_{kin})$  represent the photoemitted  $2p$  electron flux obtained by pure Al and through an a-Ge overlayer. Within this approach, a good approximation for those intensities are the normalized photoemission signals measured for the Al foil and for the Ge overlayer region (thickness  $d \sim 2$  nm) on Al, respectively. The geometry of our experiment was conceived to give  $\cos(\alpha) = 1$ . Solid-angle and bias voltage effects affecting the photoemission intensity were neglected in Eq. 7.2, because the photoelectron signals (from clean Al or through the overlayer) are collected in exactly the same experimental conditions.

Moreover, decay effects of the incoming photon beam through the overlayer thickness are neglected. A simple calculation using known photoabsorption cross-sections [19] shows that the photon beam decay in our a-Ge 2 nm overlayer is limited to less than 1% for photon energies above 500 eV, while is less than 5% in the 50–500 eV region, even considering possible oxidation processes. We have accounted for this small effect in calculating the actual intensity  $I_{Al_{2p}}(E_{kin})$  in Eq. 7.2, which anyway results in variations of the MFP within the measured uncertainty.

As discussed in the previous Sections, the Al 2*p* normalized photoemission intensities  $I_{Al_{2p}}^{Ge}(E_{kin})$ ,  $I_{Al_{2p}}(E_{kin})$  of Eq. 7.2 were obtained after isolation and background subtraction of the 2*p* peaks in all spectra and using the area of the peaks as representative of the collected number of electrons per unit surface and time. Using the entire set of data reported in Fig. 7.3 we were thus able to estimate the inelastic electron mean free path ( $\lambda$ ) of the electrons in the amorphous germanium (a-Ge) overlayer. The results are reported as a function of the physical kinetic energy of the photoelectrons (in the ~30–970 eV range) in Fig. 7.6. Error bars have been estimated by error propagation on the measured photoemission intensities.

Present results are compared with those of current models [1, 2, 14], presented as continuous lines in Fig. 7.6. Looking at Fig. 7.6 we see that there is an overall nice agreement in the trend of the present set of experimental data as compared with

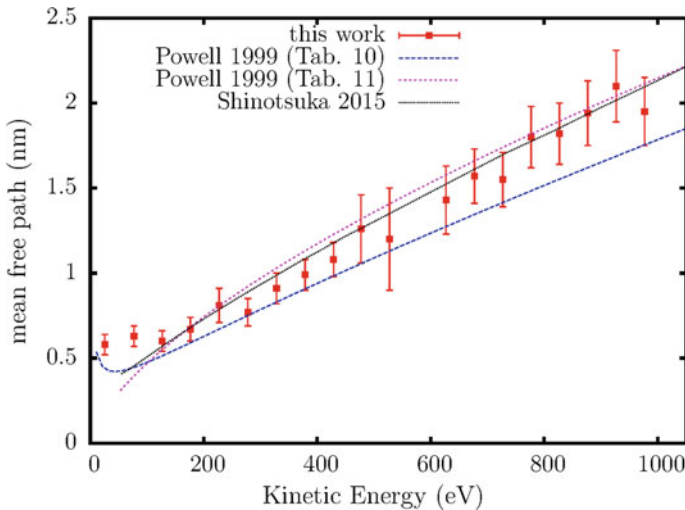


**Fig. 7.6** Electron inelastic mean free path (MFP) in amorphous germanium obtained in this work using the 2*p* Al (~73 eV binding energy) photoemission spectral intensity at different kinetic energies. In this figure the energy scale for experimental data has been shifted taking into account the extra-energy due to the applied bias voltage (30 V), accelerating the electrons toward the spectrometer, as well the effect of the work function. Present experimental data are compared with MFP curves obtained using empirical analytic functions (parameters can be found in ref. [1] by Powell and Jablonski published in 1999) and with the results of calculations using the relativistic Penn algorithm (see ref. [14])

previous models. However, it is possible to verify that current models for MFP in Ge [1, 2, 14] differ quite remarkably both at low and high kinetic energy, depending on the different choices and treatment of the optical data used for obtaining those calculations (this was already noted in ref. [1]).

Present experimental data are compared with MFP curves obtained using empirical analytic functions (parameters can be found in ref. [1] by Powell and Jablonski published in 1999) and with the results of calculations using the relativistic Penn algorithm (see ref. [14]).

Results reported in the review of Powell and Jablonski (Powell 1999 in ref. [1]) are based on simple empirical analytic functions as described in the original paper, and specific data for Ge were listed in Tables 10 and 11. The first MFP functional form (Table 10 [1]) is intended to describe also the behavior at low kinetic energy, indicating a minimum for the MFP at kinetic energies below 50 eV. This is to be expected as the MFP should increase approaching the Fermi energy, so at very low kinetic energies, while inelastic losses decreasing the MFP are important in the 10–100 eV energy region. However, this model (Powell 1999, Table 10) underestimates the experimentally determined MFP both at high ( $E \geq 500$  eV) and low energies ( $E \leq 200$  eV) and deviations up to 20% were also noted by the authors in the original publication. The MFP curves obtained by the other two models here reported (Powell 1999, Table 11 [1] and Shinotsuka [14]) are in nice agreement with each other and in reasonable agreement with present experimental data for kinetic energies larger than 100 eV (see Fig. 7.6). The first model results from a simple analytic expression for the MFP  $\lambda = k E^p$  ( $k = 0.02252$  nm/eV<sup>*p*</sup>,  $p = 0.6597$ ,  $E$  kinetic energy in eV, see Table 11 in ref. [1]). The  $k$  and  $p$  parameters for Ge were obtained optimizing the MFP curve for a set of measured data, at kinetic energies in the range 100–5000 eV. It is not surprising that this model can not reproduce the Ge experimental data below 100 eV, both for its functional form and for the region of optimization. The second MFP curve [14] was recently obtained in a tabular form by Shinotsuka and coworkers using a relativistic version of the full Penn algorithm [10, 11]. In the range of kinetic energies under investigation, this curve is in good agreement with the model already obtained in 1999 [1].

Present experimental data are in rather good agreement with those last two models especially at high kinetic energies ( $E_{kin} > 500$  eV) and in reasonable agreement in the 100–500 eV region. Of course, present data at lower kinetic energies (below 100 eV) are not explained by current models.

## 7.5 Conclusions

We successfully performed a series of constant initial state photoemission experiments using synchrotron radiation in a wide soft x-ray photon range, to the purpose of measuring the inelastic mean free path of simple substances using the so-called overlayer method.

The intensity attenuation of the secondary electron beam provided by photo-excited Al  $2p$  electrons ( $\sim 73$  eV binding energy) was measured using an Al foil partly covered by a 2 nm thin amorphous germanium film. By taking proper care of the experimental conditions, attenuation data could be carefully evaluated in a wide range of photon energies (100–1050 eV) corresponding to kinetic energies in the  $\sim 30$ –980 eV range. The inelastic mean free path in amorphous germanium was evaluated using a standard exponential attenuation model.

Present experimental data have been in substantial agreement with previous models for high kinetic energies (greater than 100 eV). On the other hand, currently accepted models have not been found to explain MFP data at lower kinetic energies.

Present measurements improve our present knowledge of the mean free path in Ge opening also new experimental possibilities for accurate measurements at variable energies in simple and complex substances. This information is seen to be very important for a correct evaluation and theoretical modelling of the probing depth in widely used surface-sensitive photoelectron-based techniques.

## References

1. C.J. Powell, A. Jablonski, Evaluation of calculated and measured electron inelastic mean free paths near solid surfaces. *J. Phys. Chem. Ref. Data* **28**, 19–62 (1999). <https://doi.org/10.1063/1.3243762>
2. W.S.M. Werner, Electron transport in solids for quantitative surface analysis. *Surface Interface Anal.* **31**(3), 141–176 (2001). <https://doi.org/10.1002/sia.973>. <https://onlinelibrary.wiley.com/doi/abs/10.1002/sia.973>
3. A. Di Cicco, A. Giglia, R. Gunnella, S.L. Koch, F. Mueller, F. Nobili, M. Pasqualini, S. Passerini, R. Tossici, A. Witkowska, Sei growth and depth profiling on zfo electrodes by soft x-ray absorption spectroscopy. *Adv. Energy Mater.* **5**(18), 1500,642 (2015). <https://doi.org/10.1002/aenm.201500642>. URL <https://onlinelibrary.wiley.com/doi/abs/10.1002/aenm.201500642>
4. S.J. Rezvani, F. Nobili, R. Gunnella, M. Ali, R. Tossici, S. Passerini, A. Di Cicco, Sei dynamics in metal oxide conversion electrodes of li-ion batteries. *J. Phys. Chem. C* **121**(47), 26379–26388 (2017). <https://doi.org/10.1021/acs.jpcc.7b08259>
5. J.J. Quinn, Range of excited electrons in metals. *Phys. Rev.* **126**, 1453–1457 (1962). <https://doi.org/10.1103/PhysRev.126.1453>. <https://link.aps.org/doi/10.1103/PhysRev.126.1453>
6. J. Shelton, Inelastic mean free paths for electrons in bulk jellium. *Surface Sci.* **44**(2), 305–309 (1974). [https://doi.org/10.1016/0039-6028\(74\)90119-8](https://doi.org/10.1016/0039-6028(74)90119-8). <http://www.sciencedirect.com/science/article/pii/0039602874901198>
7. C. Powell, Attenuation lengths of low-energy electrons in solids. *Surface Sci.* **44**(1), 29–46 (1974). [https://doi.org/10.1016/0039-6028\(74\)90091-0](https://doi.org/10.1016/0039-6028(74)90091-0). <http://www.sciencedirect.com/science/article/pii/0039602874900910>
8. J. Ashley, C. Tung, R. Ritchie, Electron inelastic mean free paths and energy losses in solids: I. aluminum metal. *Surface Sci.* **81**(2), 409–426 (1979). [https://doi.org/10.1016/0039-6028\(79\)90109-2](https://doi.org/10.1016/0039-6028(79)90109-2). <http://www.sciencedirect.com/science/article/pii/0039602879901092>
9. D.R. Penn, Electron mean-free-path calculations using a model dielectric function. *Phys. Rev. B* **35**, 482–486 (1987). <https://doi.org/10.1103/PhysRevB.35.482>. <https://link.aps.org/doi/10.1103/PhysRevB.35.482>
10. S. Tanuma, C.J. Powell, D.R. Penn, Calculations of electron inelastic mean free paths. ii. data for 27 elements over the 50–2000 eV range. *Surface Interface Anal.* **17**(13), 911–

- 926 (1991). <https://doi.org/10.1002/sia.740171304>. <https://onlinelibrary.wiley.com/doi/abs/10.1002/sia.740171304>
11. S. Tanuma, C.J. Powell, D.R. Penn, Calculations of electron inelastic mean free paths. ix. data for 41 elemental solids over the 50 ev to 30 kev range. *Surface Interface Anal.* **43**(3), 689–713 (2011). <https://doi.org/10.1002/sia.3522>. <https://onlinelibrary.wiley.com/doi/abs/10.1002/sia.3522>
  12. P.W. Palmberg, T.N. Rhodin, Auger electron spectroscopy of fcc metal surfaces. *J. Appl. Phys.* **39**(5), 2425–2432 (1968). <https://doi.org/10.1063/1.1656571>
  13. M.P. Seah, W.A. Dench, Quantitative electron spectroscopy of surfaces: a standard data base for electron inelastic mean free paths in solids. *Surface Interface Anal.* **1**(1), 2–11 (1979). <https://doi.org/10.1002/sia.740010103>. <https://onlinelibrary.wiley.com/doi/abs/10.1002/sia.740010103>
  14. H. Shinotsuka, S. Tanuma, C.J. Powell, D.R. Penn, Calculations of electron inelastic mean free paths. x. data for 41 elemental solids over the 50 ev to 200 kev range with the relativistic full penn algorithm. *Surface Interface Anal.* **47**(9), 871–888 (2015). <https://doi.org/10.1002/sia.5789>. <https://onlinelibrary.wiley.com/doi/abs/10.1002/sia.5789>
  15. S. Nannarone, A. Giglia, N. Mahne, A. De Luisa, B. Doyle, F. Borgatti, M. Pedio, L. Pasquali, G. Naletto, M. Pelizzo, G. Tondello, Bear: a bending magnet for emission absorption and reflectivity. *Notiziario Neutroni e Luce di Sincrotrone* **12**(1), 8–19 (2007). <https://www.fisica.uniroma2.it/~notiziario/2007/volume12n1.html>
  16. A. Di Cicco, A. Congeduti, F. Coppari, J.C. Chervin, F. Baudelet, A. Polian, Interplay between morphology and metallization in amorphous-amorphous transitions. *Phys. Rev. B* **78**(3), 033,309 (2008). <https://doi.org/10.1103/PhysRevB.78.033309>
  17. G. Naletto, G. Tondello, A high resolution monochromator covering wide ultraviolet spectral ranges with a single grating. *Pure Appl. Opt.: J. Eur. Opt. Soc. Part A* **1**(6), 347–358 (1992). <https://doi.org/10.1088/0963-9659/1/6/007>
  18. D.A. Shirley, High-resolution x-ray photoemission spectrum of the valence bands of gold. *Phys. Rev. B* **5**, 4709–4714 (1972). <https://doi.org/10.1103/PhysRevB.5.4709>. <https://link.aps.org/doi/10.1103/PhysRevB.5.4709>
  19. B. Henke, E. Gullikson, J. Davis, X-ray interactions: Photoabsorption, scattering, transmission, and reflection at  $e = 50\text{--}30,000$  ev,  $z = 1\text{--}92$ . *Atomic Data and Nuclear Data Tables* **54**(2), 181–342 (1993). <https://doi.org/10.1006/adnd.1993.1013>. <http://www.sciencedirect.com/science/article/pii/S0092640X83710132>



# Chapter 8

## Multi-edge and Multiple Scattering EXAFS Analysis of Metal Hexacyanoferrates: Application in Battery Materials



Marco Giorgetti , Angelo Mullaliu , Jasper R. Plaisier ,  
and Giuliana Aquilanti 

**Abstract** The occurrence of multiple scattering (MS) phenomena in the extended portion of the X-ray absorption spectrum permits to disclose details of the local atomic structure of the target atom. The high order MS paths become relevant only in peculiar structures, regardless the crystallinity of the investigated sample, such as in metal hexacyanoferrates. General guidelines and prescriptions are presented in order to give the authors a useful guide for a correct interpretation of the EXAFS spectra of this class of compounds, which is characterized by close, but sufficiently separated, discontinuities of the absorption coefficient due to the probed contiguous transition metal K-edges. The large number of experimental points, the occurrence of large four-body MS terms, and the presence of multiple probes are discussed in the frame of the renewed attention of these compounds for their use in the battery community.

### 8.1 Introduction

The extended X-ray absorption fine structure (EXAFS) arises from the quantum mechanical interference of the ejected photo electron of the target atom with its atomic surrounding. Unlike the primary probe, i.e., the X-rays, which are highly penetrating, the secondary probe, i.e., the photo electron, deeply interacts within the material not only through single scattering (SS) phenomena, but also by multiple scattering (MS) effects. The MS formalism represented the best approach for a correct X-ray absorption near-edge structure (XANES) interpretation since the pioneering work by Lee and Pendry [1], as well as the further developments by Natoli, Benfatto and co-workers [2, 3] regarding the EXAFS region. Here, the modulation of the

---

M. Giorgetti (✉) · A. Mullaliu  
Department of Industrial Chemistry, University of Bologna, 40138 Bologna, Italy  
e-mail: [marco.giorgetti@unibo.it](mailto:marco.giorgetti@unibo.it)

J. R. Plaisier · G. Aquilanti  
Sincrotrone Elettra, ss 14, km 163.5, 34149 Basovizza, TS, Italy

signal derives from the combination of the different multiple body terms, which may become more pronounced under specific circumstances. Indeed, the focusing effect concerns the enhancement of the three-body term involving three atoms and a planal angle in between [4], while in the case of four collinear atoms vibrating around the equilibrium position, the signal intensification goes under the name of superfocusing effect, being first observed for  $\text{FeF}_3$  [5]. Nowadays, the computational treatment of the MS effects in EXAFS is a consolidated practice [6–9].

Metal hexacyanoferrates (MHCF), also called Prussian blue Analogs (PBAs), represent a class of material that has recently sparked attention for their use as active materials in batteries [10, 11]. Structurally speaking, PBAs are three-dimensional bimetallic cyanides, whose lattice enables to host a wide variety of ions due to the large interstices and channels, as seen from Fig. 8.1. The rigid and open framework that characterizes PBAs allows for a facile and reversible ion-exchange, permitting their use not only in lithium- and sodium-ion batteries, but also in polyvalent-ion technologies. The intercalation and de-intercalation processes are accompanied by a structural modification as well as a change in the oxidation state of the metals constituting the framework. The presence of two (or more) transition metals in the compound and the 4-atoms collinearity trigger strong multiple scattering effects in the respective EXAFS spectra, whose inclusion is required to analyze properly an EXAFS spectrum of this class of materials.

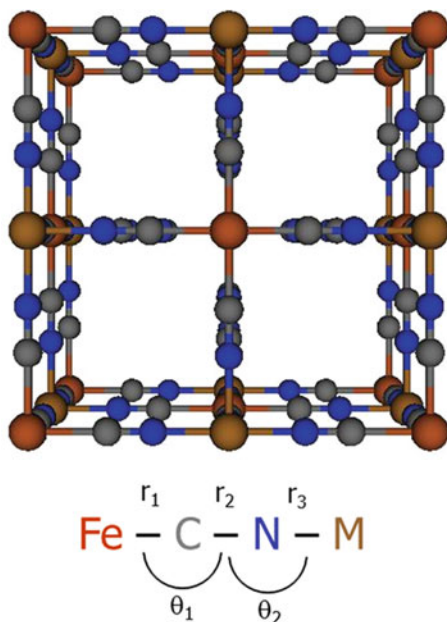


**Fig. 8.1** Graphical representation of a MHCF lattice. The 3D-structure is constituted by repeating  $\text{Fe}-\text{C}-\text{N}-\text{M}$  ( $\text{M}$  = generic transition metal), where the angles in between atoms, i.e.,  $\theta_1$  and  $\theta_2$ , are often equal to  $180^\circ$

The chapter is organized as follows. Section 8.2 reports examples of EXAFS in various metal hexacyanoferrates, while Sect. 8.3 introduces the inclusion of the MS contribution in these materials. Section 8.4 highlights some key features in batteries including tips for the data analysis.

## 8.2 EXAFS Spectrum in MHCF and Its Analysis

The structure illustrated in Fig. 8.1 implies some peculiarities in the analysis of the EXAFS spectrum: (1) the strong MS contribution, (2) the possibility of recording and analyzing multiple edges belonging to the structural transition metals, and (3) the possibility of using structural constraints, as the two metals centers being 5 Å apart. In Fig. 8.2 three typical situations where metals hexacyanoferrates are explored by EXAFS are displayed. In Panel a, a mixed Ni/Co hexacyanoferrate presents three contiguous edges, while the Cu hexacyanoferrate spectrum in Panel b is characterized by a larger separation of the two investigated K-edges, being the Fe K-edge at 7112 eV and the respective Cu edge at 8989 eV. In the case of cobalt hexacyanoferrate (or also iron hexacyanocobaltate), two close metal edges, i.e., Fe and Co, are recorded as shown in Panel c, whereas Cu hexacyanocobaltate features larger separated edges (cf. Panel d). Despite the relatively low separation of the two K-edges, the analysis of the EXAFS spectrum of the first metal is still feasible. In fact, a 600 eV energy separation in the examples displayed in both Panels a and c corresponds to a photoelectron wavevector of about 12–13 Å<sup>-1</sup>, and, by considering the large MS effects, oscillations appear along all the explored k-range. The strong multiple scattering effects contributing to the EXAFS signal are a consequence of the MHCF structure, characterized by an high degeneracy of the almost perfect linear –Fe–C–N–M chains coupled to an high degeneration of the atomic chains and a short distance between the two metals centers.

The bottom panels of Fig. 8.2, Panels e and f, report as example the Fourier transform of the EXAFS signal for the copper hexacyanoferrate material at both the Fe and Cu sites. The three peaks in each panel correspond to the first, second and third shells, i.e., –(Fe)–C–N–Cu– or –(Cu)–N–C–Fe– when considering Fe or Cu as photo absorber, respectively. By taking a closer look, the second and third peaks are interestingly comparable in intensity to the first one, due to the strong superfocusing effect found in this class of compounds. Additionally, each metal site is seen from the other one, as the third peak in at the Cu K-edge arises from the Cu–Fe long interaction, while the same holds true for the Fe K-edge.

The presence of two or more transition metal sites in MHCFs enables another key aspect of EXAFS analysis, i.e., the possibility of performing a multiple edge refinement at the all investigated metal K-edges. In such a case the data analysis can be carried out at the two edges simultaneously. The first example has been reported by Di Cicco [12] while studying the three L-edges (L<sub>III</sub>, L<sub>II</sub>, and L<sub>I</sub>) in liquid and crystalline Sn, and further extended to the analysis of K-edges by Zhang et al. [13] and Calvin et al. [14]. Giorgetti et al. [15] pioneered the use of multiple-edge

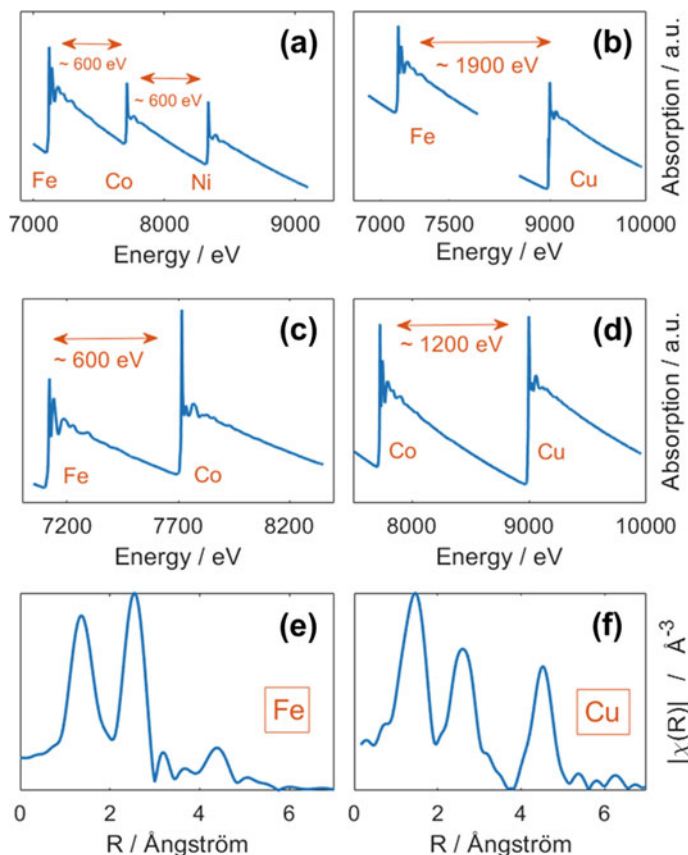


**Fig. 8.2** Absorption spectra of different metal hexacyanoferrates displaying the transition metal edges: **a** mixed Ni/Co hexacyanoferrate; **b** Cu hexacyanoferrate; **c** Co hexacyanoferrate; **d** Cu hexacyanocobaltate. Fourier transform of the  $k^2$ -weighted EXAFS signal for Cu hexacyanoferrate at the **e** Fe and **f** Cu sites

fitting in cobalt hexacyanoferrate. The main advantage of using the multiple-edge fitting versus the single-edge fitting, i.e., by doing the data analysis on the two edge separately, resides in the application of major constraints and on the overall number of experimental points that are being used to probe a specific structure. This approach strongly depends on the structure of the material under investigation, and it is very useful if correlated parameters are utilized in the simultaneous EXAFS analysis of the edges. The analysis of the EXAFS spectrum on nickel/cobalt hexacyanoferrate [16] offered the possibility of studying three contiguous metal edges while sharing the same structural parameters. In this case, the repeating  $-\text{Ni}(\text{Co})-\text{N}-\text{C}-\text{Fe}-$  structural fragment has been probed considering all the experimental data point along the three edges (about 1200 data points instead of 400 if a single edge approach had been used), thus allowing extending the number of experimental data points to a factor of

three leading to a very reliable EXAFS minimization. A comparison of the multiple edge refinement versus the single edge is available for metal hexacyanoferrates [16], and the data report substantially differs in the first shell quotation in the order of few hundredths of Å.

Eventually, is the single edge refinement an option? Normally it is not, but in case of multi-component systems it can be. If we consider systems consisting of two phases, each including the same photo-absorber. This is an example that frequently occurs while analyzing chemical reactions. In this situation, the EXAFS signal is an average of two environments around the same photo-absorber. On the contrary, if the two phases concern two different metals, a single-edge fitting at both metal K-edges would be the strategy of choice. A relevant example is the analysis of the EXAFS spectra of copper hexacyanoferrate thin films doped with Prussian blue (PB), where the CuHCF structure had to be investigated by single-edge fitting at the Cu data [17].

### 8.3 The MS EXAFS Analysis Using GNXAS

We present here the details of the EXAFS analysis on MHCs, with emphasis on some common traits. The GNXAS [18–20] code enables the possibility of the multiple edge approach and the proper extraction of the data, which are key features for a correct interpretation of the data. Figure 8.3 presents the details of the data analysis of two metal hexacyanoferrates, the copper and the cobalt analogs. The plots indicate the individual signals to the total theoretical one and the comparison to the experimental, in each panel. The individual theoretical signals, also called n-body terms, are derived from the decomposition of the EXAFS signal into a sum of several contributions. The explanation of each n-body term relevant for the analysis of hexacyanoferrate structures is reported in the Experimental section of several papers [21–25], therefore, we only briefly address it here. The theoretical signal is calculated ab initio and contains the relevant two-body  $\gamma^{(2)}$ , three-body  $\gamma^{(3)}$ , and four-body  $\gamma^{(4)}$  MS terms. The two-body terms are associated with pairs of atoms, probing their distances and variances. The three-body terms are associated with triplets of atoms and probe angles, and bond-bond and bond-angle correlations. The four-body terms are associated to chains of four atoms, and probe distances and the two angles in between, bond-bond and bond-angle correlations [15]. With reference to the linear  $-\text{Fe}-\text{C}-\text{N}-\text{Cu}-$  fragment indicated in the Fig. 8.1 (for the Cu analog case), the MS terms included in Fig. 8.3 are: the two body  $\gamma^{(2)}$  Fe–C with degeneracy of 6, the three body  $\gamma^{(3)}$  Fe–C–N with degeneracy of 6 and the four body  $\gamma^{(4)}$  Fe–C–N–Cu with degeneracy of 6 at the Fe site. Similarly, for the Cu site: the two body  $\gamma^{(2)}$  Cu–N with degeneracy of 4.5; the three body  $\gamma^{(3)}$  Cu–N–C with degeneracy of 4.5 and the four body  $\gamma^{(4)}$  Cu–N–C–Fe with degeneracy of 4.5. The Cu first shell also comprises of a second two body  $\gamma^{(2)}$  Cu–O signal with degeneracy of 1.5. This accounts for the “insoluble” structure of metal hexacyanoferrates that will be addressed later.

A close inspection of Fig. 8.3 reveals that all the MS signals are important in determining the total theoretical one and to reach a good match within the experimental

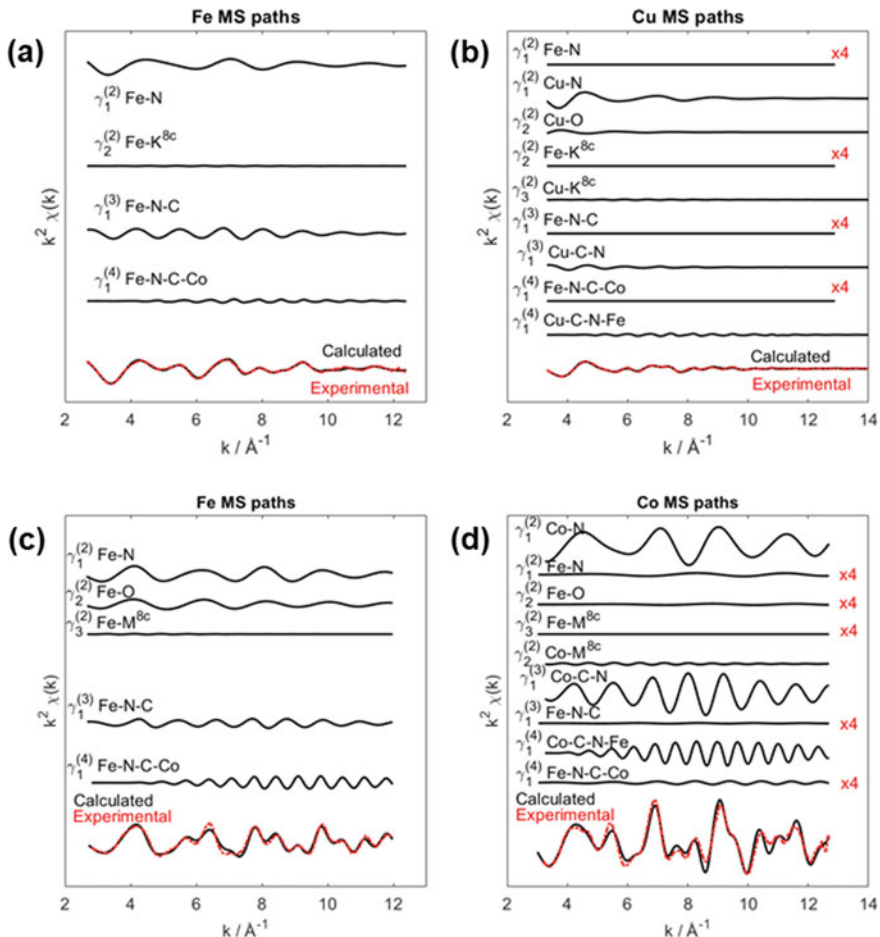


**Fig. 8.3** Multiple scattering paths for Cu hexacyanoferrate (upper panels) at the **a** Fe and **b** Cu sites; and for Co hexacyanoferrate at the **c** Fe and **d** Co sites

curves. In particular, the four-body term  $\gamma^{(4)}$  is highly relevant and modulates the entire spectrum. Which are the parameters probed by the two four-body terms, i.e., the  $\gamma^{(4)}$  Cu-N-C-Fe and the  $\gamma^{(4)}$  Fe-C-N-Cu? They coincide with what reported in Fig. 8.1, that are the three atomic distances (Fe-C, C-N, and Cu-N) with the respective bond variances ( $\sigma^2_{\text{Fe-C}}$ ,  $\sigma^2_{\text{C-N}}$ , and  $\sigma^2_{\text{Cu-N}}$ ), the angles in between atoms ( $\theta_{\text{Fe-C-N}}$  and  $\theta_{\text{Cu-N-C}}$ , or  $\theta_1$  and  $\theta_2$  as reported in Fig. 8.1) and their angle variances ( $\sigma^2_{\theta_1}$  and  $\sigma^2_{\theta_2}$ ), and the dihedral angle  $\varphi$  (the angle formed by the Fe-C-N and Cu-N-C planes) and its variance  $\sigma^2_{\varphi}$ . All these parameters can be modeled either by analyzing separately the Cu K-edge and the Fe K-edge or by fitting them simultaneously, by adopting a multiple edge fitting approach, as presented in Fig. 8.3. The

advantage of the multiple edge fitting is distinct: only few parameter (including structural and non-structural terms) are necessary to model the entire EXAFS spectra, as the typical cubic structure of most of the MHCFs permits to neglect some of the correlation parameters, such as the bond angle correlations. Indeed, the  $\theta_{\text{Fe-C-N}}$  and  $\theta_{\text{Cu-N-C}}$  angles are set to be  $180^\circ$ , hence the actual number of parameters used to define the three- and four-body MS terms is reduced by symmetry. Deviations from the planarity can be neglected; therefore, the corresponding correlations are set to be zero.

A second relevant aspect concerns the proper modelling of the atomic background of the second edge. The second edge background can be affected by the previous edge, if two consecutive edges are analyzed, as in the case of cobalt hexacyanoferrate where the Co edge closely follows the Fe (cf. Panels c, d). This can be evaluated by considering the  $\gamma^{(2)}$  Fe–C signal of the Fe K-edge as continuation in the Co K-edge. In other words, due to the vicinity of the Fe (7112 eV) and Co (7709 eV) edges, there is an overlay of the Fe–C first shell that extends over the Co edge. This picture highlights the effect of the proper account of XAFS signals continuation of previous edges, in contraposition to the copper hexacyanoferrate case (cf. Fig. 8.3, Panels a and b), where the energy gap between the edges is much higher.

A third relevant point refers to the degeneracy coefficient above mentioned for the first shell of the metal site linked to the N-end in MHCFs. In the CuHCF example, the number of N atoms coordinating the Cu site is set to 4.5, while an additional 1.5 oxygen atoms is considered to fill the octahedral coordination. This atypical parametrization comes from the “soluble” and “insoluble” forms of MHCFs. The “soluble” form has a typical face-centered cubic structure, and both the Fe and Cu are octahedrally coordinated to the C and N of the cyanide group, respectively. Unlike, the “insoluble” structure contains some  $\text{Fe}(\text{CN})_6$ -ion vacancies, despite featuring the same rigid cubic framework of linear –Fe–C–N–Cu– atomic chains. In the latter case, the octahedral coordination of Cu is filled by structural water molecules. The Cu atoms belong hence to two different sites, one being a pseudo planar coordinated  $\text{CuN}_4\text{O}_2$  and the other a perfect  $\text{CuN}_6$  octahedron. The proportion of the two sites depends on the number of vacancies in the structure. For instance, by assuming a  $\frac{1}{4}$  of hexacyanoferrate vacancies, this leads to the average values of 4.5 and 1.5 for the N coordination versus the O coordination. While analyzing and EXAFS spectrum, the degeneracy given by the above-mentioned MS terms can be set by the stoichiometry and by powder diffraction information, if available. This should be done in the input parametrization. Generally, these parameters are fixed in the minimization; optionally, they can be varied if a dynamic process is aimed to be studied, as in the case of operando monitoring of a battery material. For instance, the strategy has been used in the characterization of electrodeposited thin film of copper hexacyanoferrate [17]. Measurements at the Fe K-edge are not affected, as every Fe atom is octahedrally coordinated by six carbon atoms.

## 8.4 Application of the Extended XAFS Spectrum in Hexacyanoferrates-Based Batteries

The open-framework structure depicted in Fig. 8.1 allows for ion intercalation and release, thus making the MHCF lattice a very interesting host for ions. The position at the center of each cube (8c position) in a typical fcc structure can be occupied by an ion guest. This has not only favored the use of such materials in potentiometric sensors [25] and, in general, in ion exchange applications [26], but also in batteries [10]. Most of the XAS experiments involving batteries are aimed to revealing the electroactivity of the metals in the bulk of the material, by analyzing XANES spectra only. However, EXAFS experiments offer details on the local atomic environment of the selected atomic species. The location of these ions is a difficult task via an EXAFS experiment alone, but complementary information can be obtained by powder X-ray diffraction. This is generally done by studying the pristine material. When the following electrochemical reaction occurs:



where AM is a generic active materials and ION a generic ion for the insertion (and subsequent release) process, the site for the ion intercalation might also be verified. What is the sensitivity of the EXAFS probe regarding the ion located in the 8c position? This involves the inclusion of a scattering path, the  $\gamma^{(2)}$  Fe-ION and the  $\gamma^{(2)}$  Cu-ION signals, due to the contribution of the interstitial alkali cations. This approach is rarely followed when analyzing Li-ion batteries but some examples are available considering the Na-ion case [27], due to the differences in the multiple scattering contributions of the two alkali metals. The potassium-ion battery offers an additional edge to exploring the battery [28].

Operando monitoring of a battery material through XAFS spectroscopy, i.e., the step by step exploration of the electrochemical reaction expressed in Eq. (8.1), has some key advantages respect to the ex situ mode. Not only the battery is working while it is probed spectroscopically, but also the dynamics of the process (in terms of both charge and local structure modifications) can be revealed. While studying metal hexacyanoferrates as cathode materials, operando XANES spectroscopy infers about reduction and oxidation phenomena occurring at the metallic site (also to ligand [23]), generally. Figure 8.4a, b, for instance, reveals the variation of the first shell distances in iron hexacyanocobaltate [29] and their relative Debye–Waller factors during charge and discharge against lithium metal. While the Fe–N and Co–C distances are slightly modified, the large variation of the Debye Waller factors indicates structural disorder enhancement in the first polarization step. Additional information can be obtained by analyzing the number of –Fe–C–N–M– (M = generic transition metal) structural fragments during the electrode polarization. This is visible in Panel c of Fig. 8.4. The number of –Fe–C–N–M– chains ( $\text{CN}^{\text{chain}}$ ) changes during the electrochemical reaction, and this can be correlated to the stability of the overall structure upon ion-uptake and -release of the hexacyanoferrate network. After multiple cycling



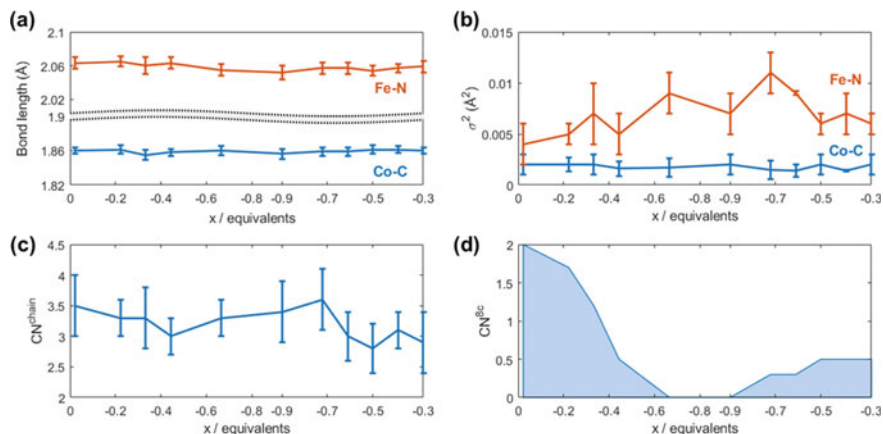


**Fig. 8.4** Relevant EXAFS fitting results for Fe hexacyanocobaltate: **a** first shell distances behavior: Fe–N and Co–C; **b** EXAFS Debye–Waller factors; **c** variation in Fe–N–C–Co chains degeneracy during lithiation; **d** variation in the coordination number of the 8c interstitial cation. Reproduced under CC Creative Commons license 4.0, Ref. [29]

this may trigger irreversibility of the overall electrochemical system, determining a capacity fade. Technically speaking, this analysis is performed by including a variable coordination number of the  $\gamma^{(4)}$  Fe–N–C–Co and  $\gamma^{(4)}$  Co–C–N–Fe four-body contributions, by using a multiple edge fitting approach.

Figure 8.4d displays the coordination number variation of the alkali metal in the 8c position regarding the same EXAFS dataset. Such number decreases upon charge and increases during discharge, as expected from Eq. (8.1). However, due to the limited scattering power of light ions that are commonly used in battery research (the lighter the shuffling ion involved in the electrochemical process, the higher the charge per unit mass of the device), the reliability of the test is weak. Indeed, the quotation of the parameter error is challenging.

## References

1. P.A. Lee, J.B. Pendry, Theory of the extended X-ray absorption fine structure. *Phys. Rev. B* **11**(8), 2795–2811 (1975)
2. M. Benfatto, C.R. Natoli, A. Bianconi, J. Garcia, A. Marcelli, M. Fanfoni, I. Davoli, Multiple-scattering regime and higher-order correlations in X-ray-absorption spectra of liquid solutions. *Phys. Rev. B* **34**(8), 5774–5781 (1986)
3. C. Brouder, M.F. Ruiz-López, R.F. Pettifer, M. Benfatto, C.R. Natoli, Systematic approach to the calculation of the polarization-dependent (and polarization-averaged) general term of the curved-wave multiple-scattering series in the X-ray-absorption cross section. *Phys. Rev. B* **39**(3), 1488–1500 (1989)
4. A. Filipponi, A. Di Cicco, Investigating local three-body correlations by means of a novel XAS data-analysis method. *Synchrotron Radiat. News* **6**(1), 13–19 (1993)

5. A. Kuzmin, Ph. Parent, Focusing and superfocusing effects in X-ray absorption fine structure at the iron K edge in  $\text{FeF}_3$ . *J. Phys. Condens. Matter* **6**, 435–4404 (1994)
6. M.A. Beckwith, W. Ames, F.D. Vila, V. Krewald, D.A. Pantazis, C. Mantel, J. Pécaut, M. Gennari, C. Duboc, M.N. Collomb, Y. Yano, J.J. Rehr, F. Neese, S. DeBeer, How accurately can extended X-ray absorption spectra be predicted from first principles? Implications for modeling the oxygen-evolving complex in photosystem II. *J. Am. Chem. Soc.* **137**, 12815–12834 (2015)
7. V.L. Aksenov, M.V. Koval'chuk, A.Y. Kuzmin, Y. Purans, S.I. Tyutyunnikov, Development of methods of EXAFS spectroscopy on synchrotron radiation beams: review. *Crystallogr. Rep.* **51**(6), 908–935 (2006)
8. A. Muñoz-Páez, S. Díaz-Moreno, E. Sánchez Marcos, J.J. Rehr, Importance of multiple-scattering phenomena in XAS structural determinations of  $[\text{Ni}(\text{CN})_4]_2$ -in condensed phases. *Inorg. Chem.* **39**(17), 3784–3790 (2000)
9. R. Sarangi, X-ray absorption near-edge spectroscopy in bioinorganic chemistry: application to M-O<sub>2</sub> systems. *Coord. Chem. Rev.* **257**(2), 459–472 (2013)
10. W.-J. Li, C. Han, G. Cheng, S.-L. Chou, H.K. Liu, S.-X. Dou, Chemical properties, structural properties, and energy storage applications of Prussian blue analogues. *Small* **15**(32), 1900470 (2019)
11. L. Jiang, Y. Lu, C. Zhao, L. Liu, J. Zhang, Q. Zhang, X. Shen, J. Zhao, Y. Yu, H. Li, X. Huang, L. Chen, Y.-S. Hu, Building aqueous K-ion batteries for energy storage. *Nat. Energy* **4**, 495–503 (2019)
12. A. Di Cicco, Multiple-edge EXAFS refinement: short range structure in liquid and crystalline Sn. *Phys. Rev. B* **53**(10), 6174–6185 (1996)
13. H.H. Zhang, A. Filipponi, A. Di Cicco, S.C. Lee, M.J. Scott, R.H. Holm, B. Hedman, K.O. Hodgson, Multiple-edge XAS studies of synthetic iron–copper bridged molecular assemblies relevant to cytochrome *c* oxidase. Structure determination using multiple-scattering analysis with statistical evaluation of errors. *Inorg. Chem.* **35**(17), 4819–4828 (1996)
14. S. Calvin, E.E. Carpenter, V.G. Harris, Use of multiple-edge refinement of extended X-ray absorption fine structure to determine site occupancy in mixed ferrite nanoparticles. *Appl. Phys. Lett.* **81**, 3828 (2002)
15. M. Giorgetti, M. Berrettoni, A. Filipponi, P.J. Kulesza, R. Marassi, Evidences for four body contribution in the EXAFS spectrum of  $\text{Na}_2\text{Co}[\text{Fe}(\text{CN})_6]$ . *Chem. Phys. Lett.* **275**, 108–112 (1997)
16. M. Giorgetti, M. Berrettoni, Structure of Fe/Co/Ni hexacyanoferrate As probed by multiple edge X-ray absorption spectroscopy. *Inorg. Chem.* **47**, 6001–6008 (2008)
17. M. Giorgetti, L. Guadagnini, D. Tonelli, M. Minicucci, G. Aquilanti, Structural characterization of electrodeposited copper hexacyanoferrate films by using a spectroscopic multi-technique approach. *Phys. Chem. Chem. Phys.* **14**(16), 5527–5537 (2012)
18. A. Filipponi, A. Di Cicco, C.R. Natoli, X-ray absorption and n-body distribution functions in condensed matter I. Theory. *Phys. Rev. B* **52**(2), 15122–15134 (1995)
19. A. Filipponi, A. Di Cicco, X-ray absorption and n-body distribution functions in condensed matter. II. Data analysis and applications. *Phys. Rev. B* **52**(2), 15135–15149 (1995)
20. F. Iesari, K. Hatada, A. Trapananti, M. Minicucci, A. Di Cicco, GNXAS: advances in the suite of programs for multiple-scattering analysis of X-ray absorption data, in *Multiple Scattering Theory for Spectroscopies*, 1st edn. (Springer, Berlin, 2018), pp. 221–256
21. M. Giorgetti, G. Aquilanti, M. Ciabocco, M. Berrettoni, Anatase-driven charge transfer involving a spin transition in cobalt iron cyanide nanostructures. *Phys. Chem. Chem. Phys.* **17**(35), 22519–32252 (2015)
22. A. Mullaliu, G. Aquilanti, P. Conti, J.R. Plaisier, M. Fehse, L. Stievano, M. Giorgetti, Copper electroactivity in Prussian blue-based cathode disclosed by operando XAS. *J. Phys. Chem. C* **122**(28), 15868–15877 (2018)
23. A. Mullaliu, G. Aquilanti, L. Stievano, P. Conti, J.R. Plaisier, S. Cristol, M. Giorgetti, Beyond the oxygen redox strategy in designing cathode material for batteries: dynamics of a Prussian blue-like cathode revealed by operando X-ray diffraction and X-ray absorption. *J. Phys. Chem. C* **123**(14), 8588–8598 (2019)

24. A. Mullaliu, J. Asenbauer, G. Aquilanti, S. Passerini, M. Giorgetti, Highlighting the reversible manganese electroactivity in Na-rich manganese hexacyanoferrate material for Li- and Na-ion storage. *Small Methods* **4**, 1900529 (2020)
25. M. Giorgetti, E. Scavetta, M. Berrettoni, D. Tonelli, Nickel hexacyanoferrate membrane as a coated wire cation-selective electrode. *Analyst* **126**(12), 2168–2171 (2001)
26. A. Mullaliu, M. Giorgetti, Metal hexacyanoferrates: ion insertion (or exchange) capabilities, in *Applications of Ion Exchange Materials in the Environment* (Springer, Berlin, 2019), pp. 109–133
27. B. Xie, L. Wang, J. Shu, Y. Zhou, Z. Yu, H. Huo, Y. Ma, Y. Cheng, G. Yin, P. Zuo, Understanding the structural evolution and lattice water movement for rhombohedral nickel hexacyanoferrate upon sodium migration. *ACS Appl. Mater. Interfaces* **11**, 46705–46713 (2019)
28. D. Wardecki, D.O. Ojwang, J. Grins, G. Svensson, Neutron diffraction and EXAFS Studies of  $K_{2x/3}Cu[Fe(CN)_6]_{2/3} \cdot nH_2O$ . *Cryst. Growth Des.* **17**, 1285–1292 (2017)
29. A. Mullaliu, P. Conti, G. Aquilanti, J.R. Plaisier, L. Stievano, M. Giorgetti, Operando XAFS and XRD study of a Prussian blue analogue cathode material: iron hexacyanocobaltate. *Condens. Matter* **3**(4), 36 (2018)

# Chapter 9

## High Pressure Behavior of the Hybrid Material $\text{AlPO}_4\text{-5}$ +Azobenzene: An In-situ Synchrotron X-ray Diffraction Study



Michelangelo Polisi, Fabio Malagutti, Linda Pastero, Giovanna Vezzalini, and Rossella Arletti 

**Abstract** In this paper we present the results of a study aimed at the understanding of the high-pressure behavior of a hybrid composite constituted by azobenzene molecules embedded in 1-D nano-channels of  $\text{AlPO}_4\text{-5}$  porous material. In-situ synchrotron high pressure X-ray powder diffraction experiments have been performed on the hybrid material and the starting porous material  $\text{AlPO}_4\text{-5}$ . The “non-penetrating” silicone oil and the “penetrating” methanol:ethanol:water 16:3:1 mixture (m.e.w.) have been used as pressure transmitting media. Using silicone oil, the presence of dye molecules within the zeolite channels affect the pressure behavior of the material increasing its compressibility. In the m.e.w. experiment, the penetration of molecules in the channels influences the elastic behavior of the material, leading to a less compressible material. The reversibility of the unit cell parameters after the pressure treatment and the strong stability showed by the hybrid material suggest the possibility to extend the range of applicability of these composites.

### 9.1 Introduction

The design of hierarchically organized composite materials with photochemical properties has attracted the attention of many researchers in the last decades. The capability to elaborate the energy and the input information of photons, exhibited by organic/inorganic hybrids, allows these materials to be exploited in system for

---

M. Polisi · F. Malagutti · G. Vezzalini · R. Arletti (✉)  
Dipartimento di Scienze Chimiche e Geologiche, Università di Modena e Reggio Emilia, Via  
Campi 103, 41125 Modena, Italy  
e-mail: [rossella.arletti@unimore.it](mailto:rossella.arletti@unimore.it)

L. Pastero  
Dipartimento di Scienze della Terra, Università di Torino, Via Valperga Caluso 35, 10125 Torino,  
Italy

harvesting and transforming the solar energy, or for sensing at the nanoscale [1–3]. These peculiar properties make these materials suitable in strategic areas, from sustainable energy technologies to biomedical sciences [4, 5].

The regular pore systems of zeolite frameworks provide ideal space for the encapsulation, stabilization and organization of photoactive species, such as luminescent dyes. In particular, one-dimensional channel phases (such as Zeolite L,  $\text{AlPO}_4\text{-5}$ , ZSM-5) are suitable hosts for preparing hierarchically organized materials as artificial photonic antenna systems [6, 7]. In these systems, photoactive molecules, arranged in 1-D nanostructures inside the zeolite channels, are able to transfer energy via FRET (Förster Resonance Energy Transfer) mimicking a natural antenna system [8].

Among zeolites,  $\text{AlPO}_4\text{-5}$  with AFI topology, has been extensively studied with the aim to produce new hybrid materials with desired optical properties [9–12]. The incorporation and the linear alignment of dyes into this alumino-phosphate, characterized by a mono-dimensional channel system, led to new optical properties indicating laser action tunable over a wide range [11].

In a previous work [13], the characterization of the composite material  $\text{AlPO}_4\text{-5}$ +azobenzene dye was carried out combining diffractometric investigation (X-ray powder diffraction, XRPD) and spectroscopic investigation (IR and diffuse reflectance UV-Vis). The use of complementary techniques allowed to understand the localization of azobenzene molecules within the zeolite channels and their interaction with the host framework. From aforementioned study, the protonation of a consistent portion of the azobenzene molecules was evidenced, as a consequence of the Brönsted acidity showed by  $\text{AlPO}_4\text{-5}$  material.

Many studies [14–17] determined how the photophysical and photochemical properties of this kind of composite materials could be affected by the orientation and packing of the guest molecules in the zeolite channels.

Considering that host-guest and guest-guest interactions considerably influence the behavior of the organic/inorganic hybrids and that they can be tuned by an external stimulus (e.g. pressure) the exploration of properties of these hybrid materials under non-ambient conditions can open a new scenario in the exploitation of such innovative materials. The high-pressure behavior of zeolites has been largely studied in the last years [18–20], but very few studies are reported on how hybrid materials respond to compression. Recent study [21] explored the response of the composite material (zeolite L + fluorenone) to compression, demonstrating the very high stability of this hybrid under pressure (up to ~6 GPa).

The question arising from these studies is: how the confining environment of nanometric pores, combined with pressure, can influence the behavior of the guest molecules and hence the properties of the hybrid material?

This kind of investigations are crucial to enhance the application range of these materials, pointing out the stability and resilience of the supramolecular organization of dye molecules, and to unravel the effect of the pressure on the optical properties of the hyper-confined species in zeolite channels.

In the present work, the high pressure-behavior of the hybrid material  $\text{AlPO}_4\text{-5}$ +azobenzene dye has been studied. The hybrid was compressed during in-situ synchrotron X-ray powder diffraction experiments, using both penetrating

(methanol-ethanol-water mixture) and not-penetrating (silicone oil) pressure transmitting media (PTM), inside a diamond anvil cell (DAC) to verify the stability of the hybrid and the evolution of its structural features.

The structural response to the pressure of the hybrid system was compared with that of the original  $\text{AlPO}_4\text{-5}$  material, to evaluate how the presence of azobenzene dye within zeolite channels influences the compressibility of the  $\text{AlPO}_4\text{-5}$  phase.

## 9.2 Materials and Methods

### 9.2.1 $\text{AlPO}_4\text{-5}$ +Azobenzene Hybrid Material

The  $\text{AlPO}_4\text{-5}$  material with AFI framework-type [22] has been chosen as host for the dye molecules loading. The preparation of the composite material (from now on AFI-azo) was performed incorporating azobenzene within the zeolite channels via gas phase adsorption.

The  $\text{AlPO}_4\text{-5}$  (synthesis protocol reported in [23]) crystalline powder was preliminarily dehydrated at 150 °C. The activated material (100 mg) was mixed with trans-azobenzene (12 mg) and deposited inside a Teflon-lined autoclave in order to have a molar ratio zeolite/dye of 1:1. The mixture was heated at 150 °C for 12 h, then the sample was washed with a Soxhlet extractor for 24 h, using ethanol, in order to remove the azobenzene from the crystal surface. As reported by Polisi et al. [13] the characterization on the resulting hybrid material AFI-azo [s.g.  $P6cc$ ,  $a = 13.7727(8)$ ,  $c = 8.4095(5)$ ,  $V = 1383.1(1)$ ] shows that the amount of azobenzene within the  $\text{AlPO}_4\text{-5}$  pores is 0.5 molecules p.u.c. calculated from the thermal analysis, while a higher amount (0.9 molecules p.u.c.) was calculated from the Rietveld refinement.

### 9.2.2 High Pressure In-situ XRPD

Three in-situ synchrotron HP-XRPD experiments were carried out. Two experiments—one on the pristine  $\text{AlPO}_4\text{-5}$  sample and one on the hybrid AFI-azo—were performed using silicone oil as non-penetrating pressure transmitting media (PTM). A third one was performed on the hybrid sample AFI-azo, using a mixture of methanol-ethanol-water (16:3:1, m.e.w.) as penetrating PTM. In all experiments, a Merrill-Basset DAC was used to transmit the pressure to the system and pressure was calibrated using the ruby fluorescence method (estimated error 0.05 GPa) [24].

Although the hydrostatic limit of silicone oil reported by Angel et al. [25] is about 0.9 GPa, the comparison between results obtained by several authors [26–30], compressing different kind of samples at higher pressure showed that the hydrostaticity of silicon oil can be considered satisfactory at least up to about 5 GPa.

**Table 9.1** Pressure (in GPa) of the XRPD data collections (R indicate steps collected upon pressure release)

| AlPO <sub>4</sub> -5—s.o<br>(GPa) | AFI-azo—s.o<br>(GPa) | AFI-azo—m.e.w<br>(GPa) |
|-----------------------------------|----------------------|------------------------|
| P <sub>amb</sub>                  | P <sub>amb</sub>     | 0.55                   |
| 0.69                              | 0.72                 | 0.73                   |
| 1.15                              | 1.26                 | 0.92                   |
| 1.65                              | 1.73                 | 1.47                   |
| 2.21                              | 2.12                 | 1.94                   |
| 2.81                              | 2.72                 | 2.77                   |
| 3.39                              | 3.47                 | 3.98                   |
| 3.91                              | 3.98                 | 4.82                   |
| 4.44                              | 4.62                 | 6.04                   |
| 4.96                              | 5.2                  | R 3.14                 |
| R 3.67                            | R 3.7                | R P <sub>amb</sub>     |
| R 2.15                            | R P <sub>amb</sub>   |                        |
| R P <sub>amb</sub>                |                      |                        |

Both experiments performed using non-penetrating PTM were carried out at ALBA synchrotron (Cerdanyola del Vallès, Barcelona-Spain) on MSPD beamline in Debye–Scherrer geometry, using a fixed wavelength of 0.5340 Å and a SX165 (Rayonix) detector placed at 160 mm from the samples. The experiment carried out on AFI-azo with m.e.w. mixture was performed at ELETTRA Sincrotrone Trieste (Italy) on XPRESS beamline, using a fixed wavelength of 0.4957 Å and a MAR365 detector placed at 307 mm from the sample.

The pressure investigated in the different experiments are reported in Table 9.1.

### 9.2.3 XRPD Data Analysis

The one-dimensional diffraction patterns were obtained in the 2θ range 1–28° by integrating the bi-dimensional images with the software DIOPTAS [31].

Rietveld refinements were performed on all patterns collected in order to calculate the unit cell parameters. No structural refinement was performed due to the complexity of the systems compared to the quality of the data.

The Rietveld profile fitting was performed in the 2θ range 1–26 using the GSAS package [32], with EXPGUI interface [33]. The structure reported [13] was used as starting model for all the refinements. The structural model was fixed during the refinements. The pseudo-Voigt profile function proposed by Thompson et al. [34] and cut-off of the peak intensity were applied. The background curve was fitted by a Chebyshev polynomial with an average of 21 coefficients.

AlPO<sub>4</sub>-5 crystallizes in the P6cc space group, all refinements were performed in this space group since no changing in the symmetry or appearance of new peaks was observed.

### 9.3 Results and Discussion

Figures 9.1a, b and 9.2 show the evolution of the XRPD data in the three pressure-ramps collected. No evidence of new peaks or symmetry changes are detected in all experiments. A notable decrease of the intensities is visible in the silicone oil experiments (Fig. 9.1) due to several factors as: reduction of the average crystallite size, increasing in the long-range structural disorder, or presence of micro-strain caused by deviatoric stress in the quasi-hydrostatic pressure-transmitting medium silicone oil. This pressure-induced amorphization is less marked in the m.e.w. experiment (Fig. 9.2) due to the penetrating nature of media able to sustain the framework during compression. Upon decompression, the original intensities are completely restored in the m.e.w. experiments, while using silicone oil, broader and less intense peaks are visible once pressure is released, especially in the  $\text{AlPO}_4\text{-5}$  sample.

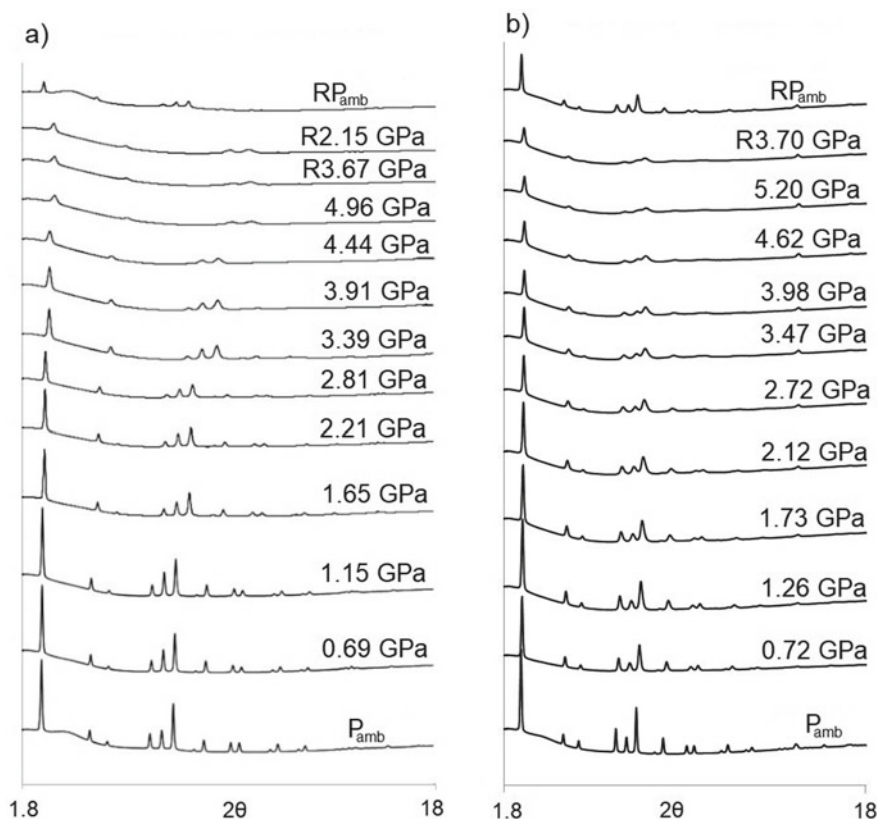


**Fig. 9.1** Evolution of the XRPD patterns as a function of pressure in the two experiments on  $\text{AlPO}_4\text{-5}$  (a) and AFI-azo (b) materials, compressed in silicone oil. Pressure increase from the bottom to the top, R indicate patterns collected upon pressure release



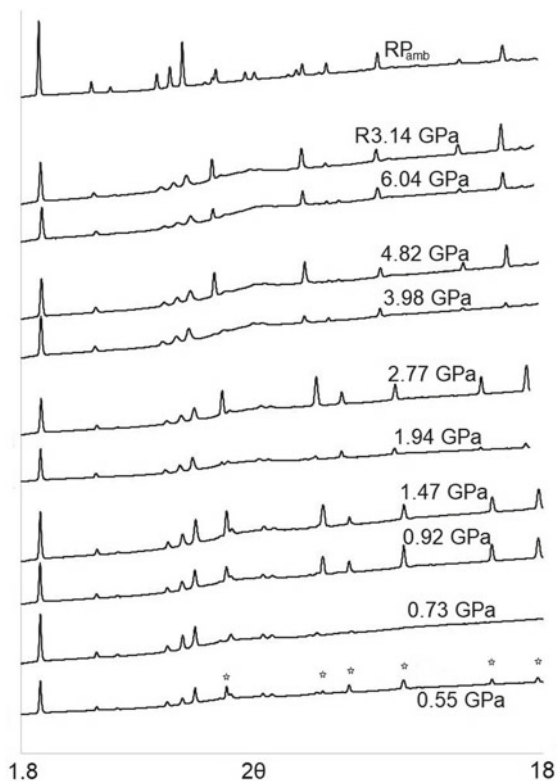


**Fig. 9.2** Evolution of the XRPD patterns as a function of pressure of AFI-azo compressed in m.e.w. Pressure increase from the bottom to the top, R indicate patterns collected upon pressure release. Star symbols indicate ruby diffraction peaks

### 9.3.1 $AlPO_4-5$ Compressed in S.O.

Figure 9.3 shows the unit cell parameters and volume variation of the  $AlPO_4-5$  sample compressed in silicone oil (reported in Appendix). The maximum variations of the  $a$  and  $c$  cell parameters at the highest pressure (4.96 GPa) are 5.0% and 3.6%, respectively and the maximum variation of volume is 12.9%.

Up to 2.8 GPa the compressibility of  $a$  and  $c$  is almost isotropic, then the  $c$  parameter remains almost constant up to 5 GPa, while  $a$  continues to decrease. Above 3.4 GPa an overall hardening of the structure is observed.

In a previous study [35], the high-pressure behavior of the  $AlPO_4-5$  zeolite was studied by single crystal X-ray diffraction using two different PTMs: silicone oil as non-penetrating PTM and m.e.w. as penetrating one. Comparing the behavior of the powder sample analyzed in the present study with the one of  $AlPO_4-5$  compressed in silicone oil [35], a slightly different behavior can be observed. In the single crystal (SC) experiment the  $c$  parameter is more compressible than  $a$  parameter up to

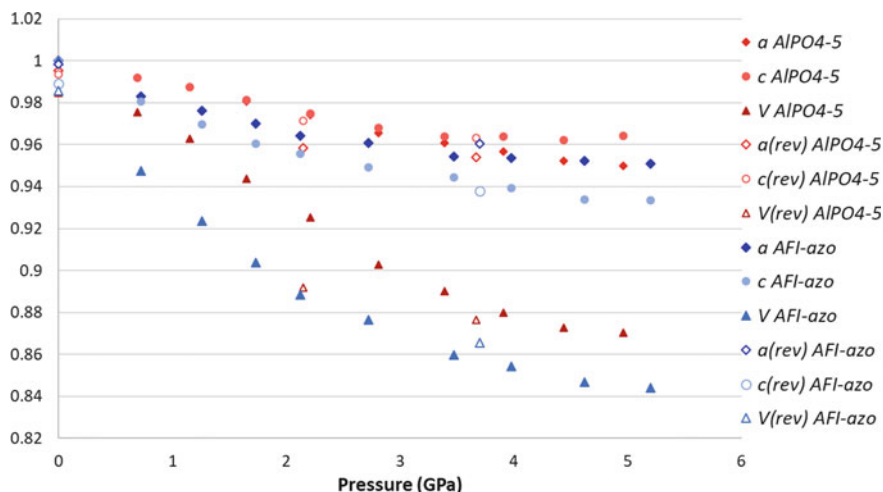


**Fig. 9.3** High pressure evolution of the normalized unit cell parameters and volume of  $\text{AlPO}_4\text{-5}$  and AFI-azo compressed in silicone oil. (rev) indicates data collected upon pressure release. Error bars not reported since they are smaller than the symbols

1.65 GPa (highest reached pressure), contrarily to what observed in the present study, where  $a$  and  $c$  parameters describes a very similar trend up to 2.8 GPa (Fig. 9.3). A further discrepancy is represented by the volume variation in the two experiments: at 1.65 GPa, the unit cell volume variation for SC experiment is about 9.2%, while in the powder one is about 5.6%.

Without a deep structural study, it is not possible to offer a straightforward interpretation of these different elastic behaviors. However, it is possible to suppose that the different compressibility derives from a difference in the extraframework content reported for the two  $\text{AlPO}_4\text{-5}$  samples. It is known, in fact that the  $\text{H}_2\text{O}$  content within  $\text{AlPO}_4\text{-5}$  porosities, can easily and largely variate depending on the environmental conditions [23]. In fact, from the structural refinement reported by Lotti et al. [35], 6.4(4)  $\text{H}_2\text{O}$  molecules are hosted p.u.c. (per unit cell), while in the powder sample, the value reported by Polisi et al. [23] is 13.1. We can thus attribute the lower compressibility verified for the powder experiment to the larger  $\text{H}_2\text{O}$  amount that stiffen the structure, thus contrasting the pressure effect and acting as framework support.

### 9.3.2 AFI-Azo Compressed in S.O.

The unit cell parameters and volume behaviour of the hybrid sample AFI-azo compressed in silicone oil are reported in Appendix and shown in Fig. 9.3. The maximum compressions of the  $a$  and  $c$  parameters are 4.9% and 6.6%, respectively,

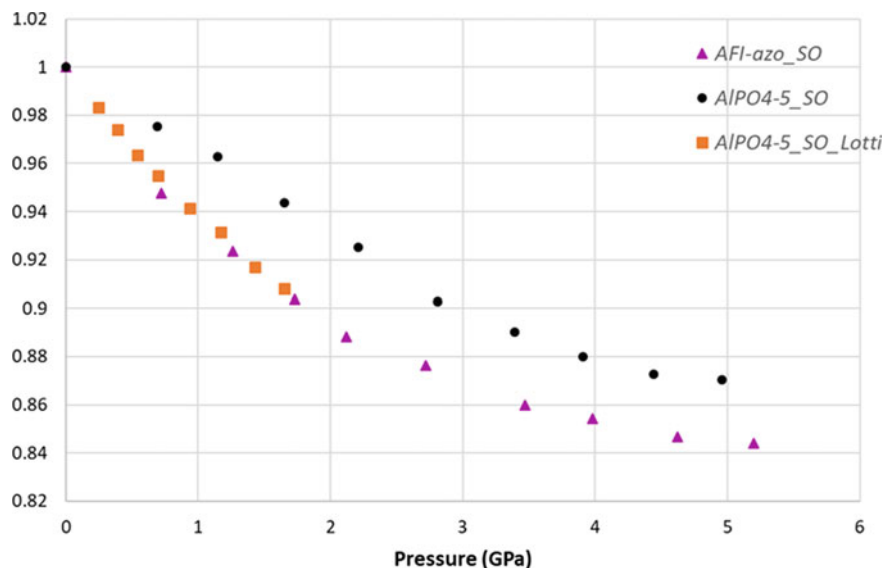


**Fig. 9.4** Comparison of the HP normalized unit-cell volume behavior of the  $\text{AlPO}_4\text{-5}$ , AFI-azo and the  $\text{AlPO}_4\text{-5 SC}$  [35], compressed in silicone oil

while the unit cell volume decreases of 15.6% at the highest investigated pressure (5.2 GPa).

Contrarily to what observed from the pristine sample, it is possible to observe, even from the early stage of compression, an anisotropic behaviour, being  $c$  the more compressible axe.

Comparing the unit cell volume trend of the AFI-azo sample with that of  $\text{AlPO}_4\text{-5}$  (Fig. 9.4), the hybrid sample resulted to be more squeezable. We can deduce that the dye molecules sustain the AFI framework in a different way respect to the  $\text{H}_2\text{O}$  molecules, as also visible from the different behavior of the  $a$  and  $c$  parameters in the two materials. In fact, the guest-guest and host guest interactions are always strongly linked to compressibility, however in this case it is difficult to propose further hypothesis justifying the different elastic behavior of the two samples due to the absence of structural data.

The patterns collected upon pressure release show an almost completely reversible behavior.

### 9.3.3 AFI-Azo Compressed in M.E.W.

Figure 9.5 shows the unit cell parameters and volume trend of the AFI-azo compressed in m.e.w. (values reported in Appendix). The  $a$  and  $c$  parameters show a similar elastic behaviour and at the highest investigated pressure (6.04 GPa) the

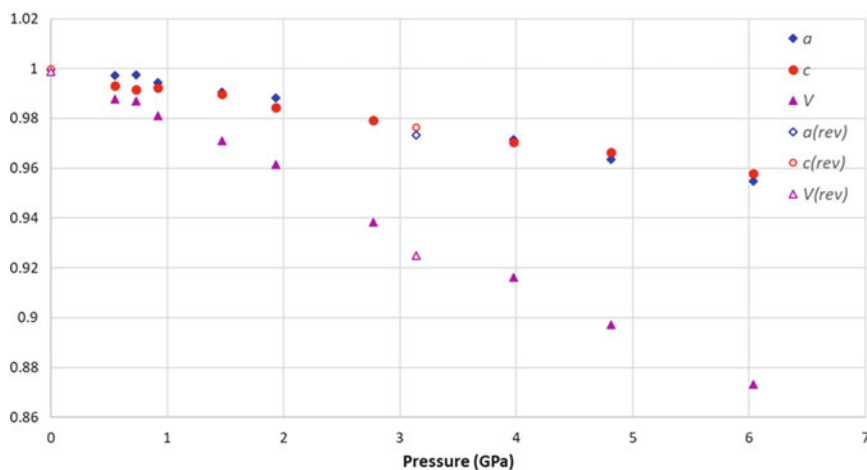


**Fig. 9.5** High pressure evolution of the normalized unit cell parameters and volume of the AFI-azo hybrid material compressed in m.e.w. (rev) indicates data collected upon pressure release

maximum variations are 4.5% and 4.2%, for  $a$  and  $c$ , respectively. The maximum unit cell volume contraction is 12.7% and the general trend of the unit cell parameters is quite linear. The slight variation between the two points at 0.55 and 0.73 GPa is inside the error of the values as reported in table in Appendix.

The lower compressibility observed for AFI-azo in m.e.w. (12.7%) with respect to s.o. (15.6%) is due to the different nature of the two fluids: penetrating versus non-penetrating medium. In fact, it is well known that the penetration of molecules of the PTM in zeolites channels tend to stiffen the structure.

From the points collected during pressure release it can be observed that the process is completely reversible and the starting unit cell parameters are restored. This clearly indicate that a possible pressure induced penetration of medium molecules inside the hybrid pores is completely reversible.

The HP behavior of  $\text{AlPO}_4\text{-5}$  in m.e.w. was reported by Lotti et al. [35] on the basis of SC X-ray diffraction and by Kim et al. [36] on the basis of XRPD experiment. Figure 9.6 shows the unit cell volume trend of the three samples compressed in m.e.w.

As visible, the AFI-azo compressibility is intermediate between the two  $\text{AlPO}_4\text{-5}$  samples reported in literature. The different behavior between the two samples reported by Kim et al. [36] ( $\text{Al}_{12}\text{P}_{12}\text{O}_{48} \cdot 9.9\text{H}_2\text{O}$ ) and [35] ( $\text{Al}_{12}\text{P}_{12}\text{O}_{48} \cdot 6.4\text{H}_2\text{O}$ , from structural refinement) could be due to: (i) a more pronounced intrusion of fluid molecules into micropores of the polycrystalline  $\text{AlPO}_4\text{-5}$ , likely for the higher surface/volume ratio, with respect to the single crystal and to the (ii) different amount of water molecules hosted in the pores (9 vs. 6) and stiffening the structure.

In the case of a penetrating PTM as m.e.w., several factors could influence the HP behavior of the material. In particular the amount, the type, the disposition of the extraframework species, and the way in which they interact with the intruded molecules of the PTM, can modify the compressibility of the various phases. A deep

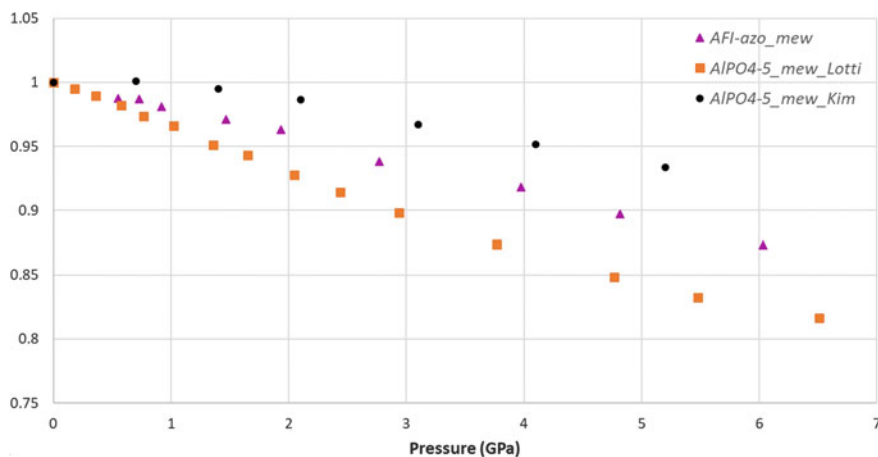


**Fig. 9.6** Comparison among the HP normalized unit-cell volume versus P of AFI-azo, AlPO<sub>4</sub>-5 single crystal [35] and AlPO<sub>4</sub>-5 powder [36] compressed in m.e.w

structural investigation would be necessary to understand the mechanisms behind these differences.

## 9.4 Conclusions

We investigated the compressibility of the AlPO<sub>4</sub>-5 material with AFI framework type and of the hybrid material AFI-azo (AlPO<sub>4</sub>-5+azobenzene dye), in three in situ high pressure synchrotron XRPD experiments using silicone oil as non-penetrating and m.e.w. as penetrating PTM.

From the HP unit cell parameters and volume behavior, a different compressibility is appreciable between the composite material and the starting sample. The presence of azobenzene inside the AlPO<sub>4</sub>-5 channels influences the HP behavior in both experiments performed with non-penetrating and penetrating PTM. In fact, when compressed in non-penetrating PTM AFI-azo seem more compressible than the starting AlPO<sub>4</sub>-5 sample. The reversibility of the process, concerning the restoration of initial unit cell parameters after pressure release, was observed for all the materials, with only a small loss of crystallinity in some cases. These results indicate the strong stability of these hybrids even in high pressure regime. Further studies targeted to the understanding of their photophysical behavior in these conditions are foreseen and may reveal new unexpected properties of these systems.

## Appendix

See Table 9.2.

**Table 9.2** Unit cell parameters of  $\text{AlPO}_4\text{-5}$  and AFI-azo in all HP experiments

| P (GPa)                                  | <i>a</i>   | <i>c</i>  | <i>V</i>  |
|--|------------|-----------|-----------|
| <i>AlPO<sub>4</sub>-5 (silicone oil)</i> |            |           |           |
| Ambient                                  | 13.7144(8) | 8.4065(5) | 1369.3(2) |
| 0.69                                     | 13.6009(5) | 8.3379(3) | 1335.7(1) |
| 1.15                                     | 13.5420(5) | 8.3012(3) | 1318.3(1) |
| 1.65                                     | 13.4501(8) | 8.2484(4) | 1292.1(2) |
| 2.21                                     | 13.361(1)  | 8.1954(6) | 1267.0(2) |
| 2.81                                     | 13.244(2)  | 8.1370(8) | 1236.0(3) |
| 3.39                                     | 13.179(3)  | 8.104(1)  | 1219.0(4) |
| 3.91                                     | 13.119(3)  | 8.102(2)  | 1205.0(6) |
| 4.44                                     | 13.062(5)  | 8.090(2)  | 1195.1(8) |
| 4.96                                     | 13.027(7)  | 8.106(4)  | 1192(1)   |
| 3.67 R                                   | 13.082(4)  | 8.096(4)  | 1200(1)   |
| 2.15 R                                   | 13,142(9)  | 8.167(5)  | 1221(1)   |
| Ambient R                                | 13.652(3)  | 8.354(1)  | 1348.3(5) |
| <i>AFI-azo (silicone oil)</i>            |            |           |           |
| Ambient                                  | 13.7365(8) | 8.4129(5) | 1374.8(2) |
| 0.72                                     | 13.5033(6) | 8.2502(7) | 1302.8(1) |
| 1.26                                     | 13.407(1)  | 8.158(1)  | 1269.8(2) |
| 1.73                                     | 13.326(1)  | 8.080(1)  | 1242.7(2) |
| 2.12                                     | 13.244(2)  | 8.039(2)  | 1221.2(3) |
| 2.72                                     | 13.198(7)  | 7.987(1)  | 1204.8(2) |
| 3.47                                     | 13.107(9)  | 7.946(1)  | 1182.2(2) |
| 3.98                                     | 13.102(1)  | 7.901(2)  | 1174.6(3) |
| 4.62                                     | 13.080(2)  | 7.857(2)  | 1164.1(5) |
| 5.2                                      | 13.061(2)  | 7.854(3)  | 1160.3(5) |
| 3.7 R                                    | 13.195(2)  | 7.892(2)  | 1190.0(4) |
| Ambient R                                | 13.714(1)  | 8.321(1)  | 1355.3(2) |
| <i>AFI-azo (m.e.w.)</i>                  |            |           |           |

(continued)

**Table 9.2** (continued)

| P (GPa)   | <i>a</i>   | <i>c</i>  | <i>V</i>  |
|-----------|------------|-----------|-----------|
| 0.55      | 13.699(3)  | 8.357(1)  | 1358.2(5) |
| 0.73      | 13.703(1)  | 8.3454(5) | 1357.0(2) |
| 0.92      | 13.658(3)  | 8.352(1)  | 1349.1(5) |
| 1.47      | 13.605(3)  | 8.330(2)  | 1335.3(6) |
| 1.94      | 13.586(2)  | 8.283(1)  | 1324.1(5) |
| 2.77      | 13.446(4)  | 8.240(2)  | 1290.2(7) |
| 3.98      | 13.362(3)  | 8.168(1)  | 1262.9(5) |
| 4.82      | 13.235(3)  | 8.132(3)  | 1233.5(5) |
| 6.04      | 13.116(4)  | 8.060(5)  | 1200.9(7) |
| 3.14 R    | 13.369(3)  | 8.217(3)  | 1272.3(9) |
| Ambient R | 13.7293(8) | 8.4129(4) | 1373.3(2) |

## References

1. V. Balzani, A. Credi, M. Venturi, Photochemical conversion of solar energy. *ChemSuschem* **1**, 26–58 (2008)
2. V. Vohra, G. Calzaferri, S. Destri, M. Pasini, W. Porzio, C. Botta, Toward white light emission through efficient two-step energy transfer in hybrid nanofibers. *ACS Nano* **4**(3), 1409–1416 (2010)
3. G. Calzaferri, R. Méallet-Renault, D. Brühwiler, R. Pansu, I. Dolamic, T. Dienel, P. Adler, H. Li, A. Kunzmann, Designing dye-nanochannel antenna hybrid materials for light harvesting, transport and trapping. *ChemPhysChem* **12**, 580–594 (2011)
4. R. Koeppel, O. Bossart, G. Calzaferri, N.S. Sariciftci, Advanced photon-harvesting concepts for low-energy gap organic solar cell. *Sol. Energy Mater. Sol. Cells* **91**, 986–995 (2007)
5. H. Lülfi, A. Devaux, E.A. Prasetyanto, L. De Cola, Porous nanomaterials for biomedical applications. *Org. Nanomaterials Synth. Charact. Device Appl.* **22**, 487–507 (2013)
6. G. Calzaferri, Nanochannels: hosts for the supramolecular organization of molecules and complexes. *Langmuir* **28**, 6216–6231 (2012)
7. G. Tabacchi, Supramolecular organization in confined nanospaces. *ChemPhysChem* **19**, 1249–1297 (2018)
8. G. Calzaferri, H. Li, D. Brühwiler, Dye-modified nanochannel materials for photoelectronic and optical devices. *Chem. Eur. J.* **14**, 7442–7449 (2008)
9. Z. Lei, A. Vaidyalngam, P.K. Dutta, Photochemistry of azobenzene in microporous aluminophosphate AlPO<sub>4</sub>-5. *J. Phys. Chem. B* **102**, 8557–8562 (1998)
10. I. Braun, F. Ihlein, F. Laeri, J.U. Nöckel, G. Schultz-Ekloff, F. Schüth, U. Vietze, Ö. Weiß, D. Wöhrle, Hexagonal microlaser based on organic dyes in nanoporous crystals. *Appl. Phys. B* **70**, 335–343 (2000)
11. Ö. Weiß, J. Loerke, U. Wüstefeld, F. Marlow, F. Schüth, Host-guest interactions and laser activity in AlPO<sub>4</sub>-5/laser dye composites. *J. Solid State Chem.* **167**, 302–309 (2002)
12. C. Seebacher, C. Hellriegel, C. Bräuchle, M. Ganschow, D. Wöhrle, Orientational behavior of single molecules in molecular sieves: a study of oxazine dyes in AlPO<sub>4</sub>-5 crystals. *J. Phys. Chem. B* **107**, 5445–5452 (2003)
13. M. Polisi, R. Arletti, S. Morandi, M. Fabbiani, G. Martra, S. Quartieri, L. Pastero, G. Vezzadini, Zeolite/dye hybrid composite: organization of photoactive azobenzene molecules inside AlPO<sub>4</sub>-5. *Microporous Mesoporous Mater.* **268**, 25–30 (2018)

14. S. Megelski, A. Lieb, M. Pauchard, A. Drechsler, S. Glaus, C. Debus, A.J. Meixner, G. Calzaferri, Orientation of fluorescent dyes in nano channels of zeolite L. *J. Phys. Chem.* **105**, 25–35 (2001)
15. G. Schulz-Ekloff, D. Wöhrle, B. van Duffel, R.A. Schoonheydt, Chromophores in porous silicas and minerals: preparation and optical properties. *Microporous Mesoporous Mater.* **51**, 91–138 (2002)
16. H.S. Kim, K.W. Sohn, Y. Jeon, H. Min, D. Kim, K.B. Yoon, Aligned inclusion of n-propionic acid tethering hemicyanine into silica zeolite film for second harmonic generation. *Adv. Mater.* **19**, 260–263 (2007)
17. E. Fois, G. Tabacchi, G. Calzaferri, Orientation and order of xanthene dyes in the one-dimensional channels of zeolite L: bridging the gap between experimental data and molecular behavior. *J. Phys. Chem. C* **116**, 16784–16799 (2012)
18. R. Arletti, O. Ferro, S. Quartieri, A. Sani, G. Tabacchi, G. Vezzalini, Structural deformation mechanisms of zeolite under pressure. *Am. Miner.* **88**, 1416–1422 (2003)
19. D.G. Gatta, Y. Lee, Zeolites at high pressure: a review. *Mineral. Mag.* **78**(2), 267–291 (2014)
20. D.G. Gatta, P. Lotti, G. Tabacchi, The effect of pressure on open-framework silicates: elastic behaviour and crystal-fluid interaction. *Phys. Chem. Miner.* **45**, 115–138 (2018)
21. L. Gigli, R. Arletti, E. Fois, G. Tabacchi, S. Quartieri, V. Dmitriev, G. Vezzalini, Unravelling the high-pressure behaviour of dye-zeolite L hybrid materials. *Curr. Comput.-Aided Drug Des.* **8**(2), 79 (2018)
22. C. Baerlocher, L.B. McCusker, D.H. Olson, *Atlas of Zeolite Framework Types*, 6th edn. (Elsevier, Amsterdam, 2007).
23. M. Polisi, R. Arletti, S. Quartieri, L. Pastero, C. Giacobbe, G. Vezzalini, Dehydration mechanism of  $\text{AlPO}_4\text{-5}$ : a high-resolution synchrotron X-ray powder diffraction study. *Microporous Mesoporous Mater.* **261**, 137–143 (2018)
24. H.K. Mao, J. Xu, P.M. Bell, Calibration of the ruby pressure gauge to 800 Kbar under quasi-hydrostatic conditions. *J. Geophys. Res.* **91**, 4673–4676 (1986)
25. R.J. Angel, M. Bujak, J. Zhao, G.D. Gatta, S.D. Jacobsen, Effective hydrostatic limits of pressure media for high-pressure crystallographic studies. *J. Appl. Cryst.* **40**, 26–32 (2007)
26. T. Le Bihan, S. Heathman, S. Darracq, C. Abraham, J.-M. Winand, U. Benedict, High pressure X-ray diffraction studies of UX3 (X = Al, Si, Ga, Ge, In, Sn). *High Temp. High Pressures* **27**(28), 157–162 (1996)
27. P. Comodi, G.D. Gatta, P.F. Zanazzi, High-pressure structural behaviour of heulandite. *Eur. J. Mineral.* **13**, 497–505 (2001)
28. P. Comodi, G.D. Gatta, P.F. Zanazzi, Effects of pressure on the structure of bikitaite. *Eur. J. Mineral.* **15**, 267–295 (2003)
29. G. Vezzalini, S. Quartieri, A. Sani, D. Levy, The structural modifications induced by high pressure in scolecite and heulandite: in-situ synchrotron X-ray powder diffraction study, in *Studies in Surface Sciences and Catalysis*, vol. 135, ed. by A. Galarneau, F. Di Renzo, F. Fajula, J. Védrine (2001)
30. O. Ferro, S. Quartieri, G. Vezzalini, E. Fois, A. Gamba, G. Tabacchi, High-pressure behaviour of bikitaite: an integrated theoretical and experimental approach. *Am. Miner.* **87**, 1415–1425 (2002)
31. C. Prescher, V.B. Prakapenka, DIOPTAS: a program for reduction of two-dimensional X-ray diffraction data and data exploration. *High Pressure Res.* **35**, 223–230 (2015)
32. A.C. Larson, R.B. Von Dreele, General structure analysis system “GSAS”. Los Alamos National Laboratory Reports. LAUR, 86-748 (1994)
33. B.H. Toby, EXPGUI, a graphical user interface for GSAS. *J. Appl. Crystallogr.* **34**, 210–213 (2001)
34. P. Thompson, D.E. Cox, J.B. Hastings, Rietveld refinement of Debye-Scherrer synchrotron X-ray data from  $\text{Al}_2\text{O}_3$ . *J. Appl. Crystallogr.* **20**, 79–83 (1987)
35. P. Lotti, D.G. Gatta, D. Comboni, M. Merlini, L. Pastero,  $\text{AlPO}_4\text{-5}$  zeolite at high pressure: crystal-fluid interaction and elastic behavior. *Microporous Mesoporous Mater.* **228**, 158–167 (2016)



36. T. Kim, Y. Lee, Y.-N. Jang, J. Shin, S.H. Hong, Contrasting high-pressure compression behaviors of AlPO<sub>4</sub>-5 and SSZ-24 with the same AFI framework topology. *Microporous Mesoporous Mater.* **169**, 42–46 (2013)

# Chapter 10

## Zn Distribution and Chemical Speciation in Marine Biominerals: An Example on Bivalve and Foraminifera Shells from Polluted Sites



**Giovanni De Giudici, Carlo Meneghini, Carla Buosi, Ilaria Carlomagno, Giuliana Aquilanti, Tohru Araki, Diana E. Bedolla, Maria Antonietta Casu, Antonietta Cherchi, Alessandra Gianoncelli, Antonella Iadecola, Andrei C. Kuncser, V. Adrian Maraloiu, Olivier Mathon, Valentina Rimondi, Pierpaolo Zuddas, and Daniela Medas**

**Abstract** Biominerals are widespread in Nature and they precipitate to respond to different physiological purposes. A broad knowledge of their chemical and structural properties offers a unique opportunity to improve our capability to reconstruct actual and paleoenvironment. In this work, we show two case studies, bivalves and foraminifera grown in polluted sites that were characterized by applying different

---

G. De Giudici · C. Buosi · A. Cherchi · D. Medas (✉)

Department of Chemical and Geological Sciences, University of Cagliari, Cagliari, Italy  
e-mail: [dmedas@unica.it](mailto:dmedas@unica.it)

C. Meneghini

Department of Sciences, University of Roma Tre, Rome, Italy

I. Carlomagno · G. Aquilanti · D. E. Bedolla · A. Gianoncelli

Elettra-Sincrotrone Trieste, Basovizza, Trieste, Italy

T. Araki

Diamond Light Source, Diamond House, Harwell Science and Innovation Campus, Oxfordshire, Didcot, UK

M. A. Casu

Institute of Translational Pharmacology, Scientific and Technological Park of Sardinia POLARIS, UOS of Cagliari, National Research Council, Pula, Italy

A. Iadecola

RS2E, Réseau Français Sur Le Stockage Electrochimique de L'Energie, Amiens, France

A. C. Kuncser · V. A. Maraloiu

Laboratory of Atomic Structures and Defects in Advanced Materials, National Institute of Materials Physics, Magurele, Romania

O. Mathon

The European Synchrotron Radiation Facility (ESRF), Grenoble, France

V. Rimondi

Department of Earth Sciences, University of Florence, Florence, Italy

CNR—Institute of Geosciences and Earth Resources, Florence, Italy

© Springer Nature Switzerland AG 2021

A. Di Cicco et al. (eds.), *Synchrotron Radiation Science and Applications*,

Springer Proceedings in Physics 220, [https://doi.org/10.1007/978-3-030-72005-6\\_10](https://doi.org/10.1007/978-3-030-72005-6_10)

and complementary synchrotron radiation-based investigation techniques, mainly focused on the investigation of Zn incorporation in the biomineralized shells. Using scanning transmission X-ray microscopy (STXM) and X-ray micro-fluorescence ( $\mu$ -XRF), we found the colocalization of elements across the shells, while we obtained information on chemical speciation of Zn by applying X-ray absorption spectroscopy (XAS). Noticeably, instead of metal dispersion in the Ca-carbonate shells, we found traces of several independent phases, in particular for Zn, dispersed generally as microscopic minerals. This work provides fundamental insight into the structural properties, coordinative and chemical environment of some marine biominerals. This new knowledge is fundamental to understand the biogeochemical processes and to develop effective environmental proxies.

## 10.1 Introduction

Biomaterials are biogenic composite materials, made up of organic and mineral phases, produced by living organisms for different purposes, such as defense against predators, protection of the vital organs, support of the body, and others [1]. Biomaterials are spread everywhere in the biosphere and in the geological record, and often include impurities and defects due to interactions between the organism and the surrounding environment [2–5], therefore they can bring important information about local biogeochemical conditions.

Bivalve and foraminiferal shells, ubiquitous biominerals in modern and paleo-marine environments, are often used as environmental proxies [6–9]. Bivalve shells are formed by an extracellular biomineralization made up of different layers, resulting in an organo-mineral biocomposite, where the Ca-carbonate mineral (calcite, aragonite or vaterite, [10]) represents up to 95–99% [11]. The bivalve shell consists of three layers. The outmost one is the periostracum made up of conchiolin, an unmineralized protein layer that covers the external surface of the shell, enhancing abrasion resistance and acting as a barrier against predation. The periostracum provides the nucleation site for calcium carbonate [12]. Below the periostracum grows a prismatic layer that is secreted by the outer mantle fold [13], containing organic matrices consisting of chitin and proteins [14, 15]. Finally, the nacreous layer is deposited; it is a micro-laminate composite material with highly oriented aragonite crystals [16]. The organic matrix consists of several macromolecules, polysaccharides and proteins, located in both intercrystalline and intracrystalline positions within the nacre [13].

Foraminifera are mainly marine organisms and can live on the seafloor sediments (i.e., benthic species), or can float in the water column at various depths (i.e., planktonic species) [17]. Foraminifera produce their own shell, characterized either by one or multiple chambers commonly made up of calcium carbonate, through a controlled biomineralization process. Magnesium content is related to the biomineralization

mechanism. Shells precipitated by Rotaliida through an extracellular biosynthesis are characterized by low-Mg contents, small crystallites and generally a spiral form. Miliolida form their own shell by an intracellular biomineralization mechanism, precipitating calcite inside the cell and extruding crystals externally into an organic matrix. These are characterized by high-Mg contents and have a porcelaneous shell with calcite growing in form of large needle-like crystallites [18].

Bivalve and foraminiferal shells are useful environmental proxies because variations in the shell structure or composition reflect physicochemical variations in the surrounding environment [19–21]. The evolution of the watershed (annual cycles in rainfall and soil erosion and/or sediment inputs) can be understood looking at the trace element profiles of bivalves by laser ablation inductively coupled plasma mass spectrometry (LA ICP-MS) [22]. The measurement of Mg/Ca ratio and Ca isotopes in foraminifera represents a relevant proxy for the evaluation of paleotemperature [21], and B/Ca ratio is used as a paleo-pH proxy to investigate the evolution of the carbonate saturation state in the oceans [2, 23].

Previous literature has shown that bivalves accumulate trace elements from the external environment and that metal detoxification can occur by their deposition in the mineral structures (shell and/or microspherules [24]) leading to structural alterations in the nacreous layer [25]. In foraminifera, morphological deformities were observed both in fossils and in modern specimens, probably in response to environmental stress [26].

Among trace elements, Zn is relevant for natural healthy biochemical processes, and it is an essential nutrient in many phytoplankton enzymes, particularly those of eukaryotes [27], playing an important role in marine primary production. Determination of Zn and other trace or major elements in carbonates allows to develop sensitive proxies to reveal paleocean characteristics. For instance, Liu et al. [28] have demonstrated that Zn/Fe ratio in shallow marine carbonate rocks has potential to provide a quantitative tracer for the long-term redox evolution of the oceans. Also, the Zn/Ca ratio of benthic foraminifera has been successfully used to reconstruct past deep ocean nutrient concentrations, providing insights into the changes in the physical circulation of the ocean through Earth history [4].

Zinc may result toxic in high concentrations originating from natural and/or anthropological contamination sources [29, 30]. Despite the rapid development of the research addressed to trace metals in marine (micro)organisms, the coordination chemistry and mineral speciation of Zn incorporated into the biomineralized shell of bivalve and foraminifera have been over-looked compared to other more harmful elements, though they represent a fundamental knowledge in order to assess the nature of Zn biomineral phases and the biological mechanisms involved in the detoxification. These have important implications to achieve information on the biomineralization mechanism, helpful to understand the biogeochemical processes and to develop effective biomonitoring techniques. In our studies, we have developed a research topic aimed to understand the fate of Zn in foraminiferal and bivalve shells [31, 32] through a multi-technique approach that combines state of the art complementary techniques namely: i) transmission electron microscope (TEM), ii) scanning transmission X-ray microscopy (STXM), and iii) X-ray micro-fluorescence ( $\mu$ -XRF) to

localize Zn at the micro and nanoscale; iv) X-ray absorption spectroscopy (XAFS) to individuate the Zn coordination chemistry; v) X-ray diffraction (XRD) to identify mineralogical phases. As representative examples, we describe in detail the Zn incorporation in different bivalve genera (*Donax*, *Lentidium* and *Chamelea*) and in the shells belonging to two benthic foraminiferal species (*Elphidium aculeatum* belonging to the Rotaliida order, and *Quinqueloculina seminula* belonging to the Miliolida order), collected from polluted environments. Specifically, bivalves were collected from the abandoned mining site of Malfidano (SW Sardinia, Italy), and foraminifera from La Maddalena Harbour (N Sardinia, Italy), an area characterized by past military activity.

## 10.2 Investigated Areas and Samples

### 10.2.1 Bivalve Samples

The Malfidano area is located in the Iglesias mining district (SW Sardinia, Fig. 10.1a–point 1, and Fig. 10.1b). The main deposits consist of Paleozoic formations represented by Cambrian–Ordovician rocks. The Lower Cambrian successions are made up of siliciclastic sedimentary rocks, carbonate intercalations (Nebida Group) and shallow water platform carbonate rocks (Gonnesa Groups [33]). The Middle and Upper Cambrian–Lower Ordovician successions comprise nodular limestones and slates (Campo Pisano Formation, Iglesias Group). Aeolian dunes along the coast and fluvial deposits in the internal area are the main Quaternary outcrops.

The mine was active from 1870 to 1980, and ore deposits consisted both of primary sulfides, resulting from the metamorphism and magmatism of the Variscan Orogeny [34], and calamine deposits. In the Iglesias mining district, the primary sulfides included sphalerite (ZnS) and galena (PbS), with a normal Zn grade of about 8–12 wt%, that occurred in columnar, massive, lens- and vein-like shapes in the carbonatic formations [34]. The calamine deposits formed from different weathering events that developed within the Dolomia Gialla (hydrothermal Dolomia Geodica). The principal Zn-bearing minerals were smithsonite ( $\text{ZnCO}_3$ ) and hemimorphite ( $\text{Zn}_4\text{Si}_2\text{O}_7(\text{OH})_2 \cdot \text{H}_2\text{O}$ ), associated with nodules of supergene or remnant galena and sphalerite [35, 36] with an overall Zn grade exceeding 20–22 wt% [34].

In June 2016, bivalve shells of similar sizes were collected from surface sea-bed sediments along Buggerru and San Nicolò beaches (Fig. 10.1a–c). The most abundant genera were *Donax*, *Lentidium* and *Chamelea* (Fig. 10.1d). At least 50 specimens for each genus were collected, immediately stored in bags and transported to the laboratory. About 20 specimens per genus for each beach were selected, pooled into one sample and ground for mineralogical investigation, chemical analysis, and XAS analysis.

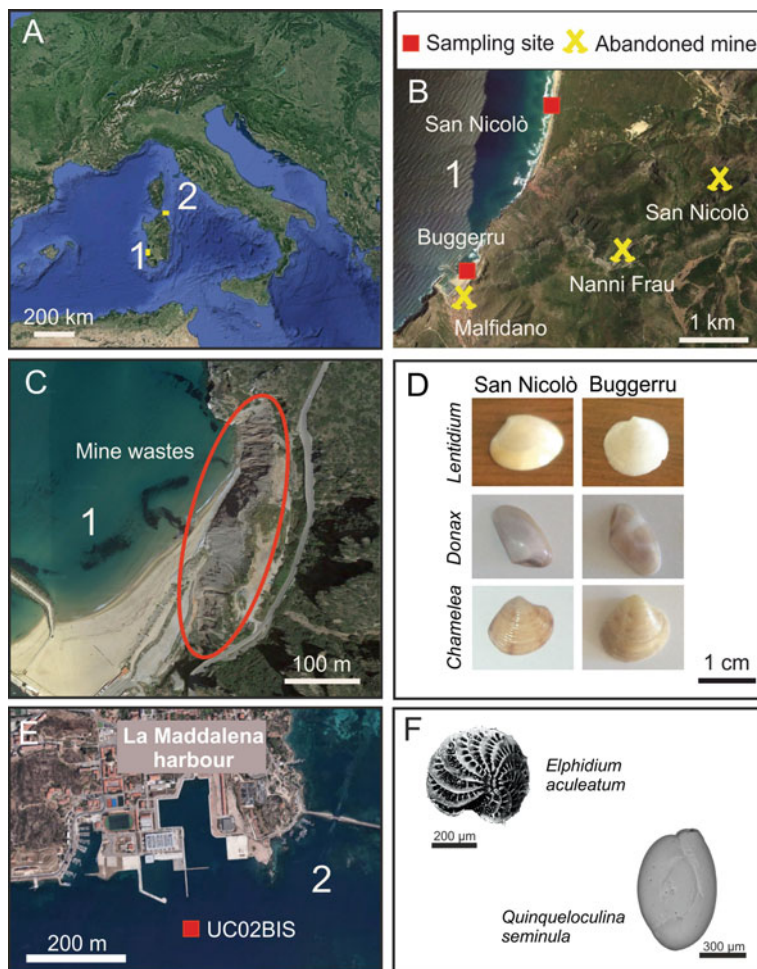


**Fig. 10.1** Localization of Sardinia island (a); bivalve sampling site (b); detail on mining wastes disposed near the Buggerru beach (c); selected photos of bivalve genera collected at Buggerru and San Nicolò beaches (d); foraminiferal sampling site (e), and selected photos of *Elphidium aculeatum* and *Quinqueloculina seminula* collected near the La Maddalena harbor (f)

### 10.2.2 Foraminiferal Samples

La Maddalena Harbour is located in the La Maddalena Island (NE Sardinia; Fig. 10.1a-point 2). This island belongs to the La Maddalena Archipelago. The archipelago, with a surface of about 200 km<sup>2</sup>, is characterized by a complex system of inlets, promontories, bays, channels and paleo-fluvial valleys (*rias*) [37]. It represents the uppermost part of the NNE Hercynian plutonic basement, and mainly consists of leucogranites, crossed by a N-S-trending late dyke system.

The La Maddalena Archipelago is minimally affected by intense industrial activity [38], the anthropogenic impact is limited to the La Maddalena and S. Stefano military harbors [38–40]. Specifically, La Maddalena Harbour was devoted to military activities for more than a century, as refined in preparation for the G8 meeting in 2009. The superficial sediments of the La Maddalena Harbour show an enrichment in pollutants such as As, Hg, Zn, Cu, Pb, Cd and hydrocarbons ( $C > 12$ ), with a maximum concentration of Zn in sediments of around 1600 ppm [40].

Surface sediment samples for the investigation of the Zn incorporation in foraminiferal shells were collected at one station (UC02BIS) from a short core with a length of 3 m in October 2011 (Fig. 10.1e). Only the topmost sediment layer (0–2 cm) was used for analysis. Sediments were preserved in ethanol and Rose of Bengal (2 g of Rose of Bengal in 1000 ml of ethyl alcohol) for foraminiferal recognition [41]. A constant volume of approximately 50 cm<sup>3</sup> was dried at 50 °C and weighed. After drying and sieving the residues on a 63- $\mu$ m mesh, the foraminifera were examined under a binocular microscope. At least 300 living benthic foraminifera from each sample were picked for micropalaeontological analysis. Benthic foraminifera were identified according to several taxonomic works [42–45]. Specifically, we investigated the Zn coordinative environment in individual tests of two species of benthic foraminifera, *Elphidium aculeatum* (Rotaliida, low-Mg calcite) and *Quinqueloculina seminula* (Miliolida, high-Mg calcite) (Fig. 10.1f).

## 10.3 Analytical Methods

### 10.3.1 Bivalve Analysis

Shell samples were washed in laboratory with deionized water and were brushed with a nylon toothbrush to eliminate sand, algae and other impurities. Samples were then washed several times in Milli-Q water and dried at room temperature for one week. Samples were ground in an agate mortar and analyzed by XRD using laboratory  $\theta$ - $\theta$  equipment (Panalytical) with Cu K $\alpha$  radiation ( $\lambda = 1.54060 \text{ \AA}$ ), operating at 40 kV and 40 mA, and an X'celerator detector.

Acid digestions were performed by EPA method 3050 with slight modifications according to Connors et al. [46]. Zinc and Fe concentrations were quantified by inductively coupled plasma optical emission spectroscopy (ICP-OES, ARL Fisons ICP Analyzer 3520 B), and inductively coupled plasma mass spectrometry (ICP-MS, Perkin-Elmer, Elan 5000/DRC-e, USA). For the acid digestion method, potential contamination, precision and accuracy were evaluated processing blank solutions, duplicate samples and the certified reference material B.C.S. No. 368—dolomite. For ICP-OES and ICP-MS analysis, reference solutions (SRM 1643e and EnviroMAT Drinking Water, High EP-H-3 and Low EP-L-3) were analyzed every five samples to estimate method precision and accuracy.

Zinc and Fe distributions were investigated by scanning transmission X-ray microscope (STXM) at the TwinMic beamline, at Elettra-Sincrotrone Trieste (Trieste, Italy) [47–53] and by Energy-dispersive X-ray spectroscopy transmission electron microscopy (EDS TEM) at the NIMP (Laboratory of Atomic Structures and Defects in Advanced Materials, Magurele, Romania). Calcium and sulfur distributions were further investigated by STXM combined with XRF elemental mapping analysis at the I08-SXM beamline in Diamond Light Source, Didcot, UK (for details in sample preparation and instrument characteristics see Medas et al. [31]). The linear correlation  $\rho_{A-B}$  between the fluorescence intensities of A and B elements in the maps was calculated to evaluate the relative distribution of selected elements in the shells. The correlation analysis was carried out using a python script based on the numpy [54] and scipy [55] libraries.

XAS measurements were carried out at the XAFS beamline of Elettra synchrotron radiation facility (Trieste, Italy [56]) at the Zn K-edge (9.659 keV) to probe the Zn coordination chemistry. The XAFS data analysis was performed in the near edge region (XANES) using the linear combination analysis (LCA) method [57, 58]. High quality XAS spectra were acquired in transmission geometry on a set of Zn reference compounds for sake of comparison and used for LCA, including organic (e.g. Zn malate, Zn citrate, Zn cysteine, etc.) and inorganic (e.g. Zn sulfide—sphalerite, Zn hydroxycarbonate—hydrozincite, Zn phosphate— $Zn_3(PO_4)_2$ , etc.) compounds. Zn K-edge raw XAS data were treated following the standard procedure for data treatment, normalization and extraction of structural signal [59].

### 10.3.2 Foraminiferal Analysis

Foraminiferal specimens were divided in two groups accordingly to the Mg-calcite shell composition: *Elphidium aculeatum* (Rotaliida, low-Mg calcite) and *Q. seminula* (Miliolida, high-Mg calcite). The low- and high-Mg calcite composition is related to differences in the biomineralization mechanisms: *E. aculeatum* provides the calcite shell from extracellular synthesis, on the contrary *Q. seminula* builds its own shell through intracellular mechanism ([18] and references therein).

The foraminiferal specimens were washed and rinsed three times in ultrasonic bath with ultrapure water for 3 min in order to remove impurities and to avoid the contribution of small sediments grains. Selected foraminiferal shells had been previously investigated by ESEM (environmental scanning electron microscopy) in low-pressure mode for morphological and chemical composition analyses (without any Au or C surface coating). Mineralogical analysis was performed by laboratory XRD as for bivalves.

The Zn K-edge XAS measurements were carried out on bulk samples while Zn K-edge  $\mu$ -XAS measurements were carried out on single specimens of *E. aculeatum* and *Q. seminula*. Bulk measurements were conducted in fluorescence geometry at the Elettra-XAFS beamline (Trieste-Italy; [56]) on two independent sample sets each one comprising about 50 mg (corresponding to approximately 300 specimens)



of *Elphidium* spp. and *Quinqueloculina* spp. tests belonging to different species. The foraminiferal shells were ground and mixed with cellulose matrix and pressed in order to obtain homogeneous pellets suitable for careful handling. Measurements were carried out keeping the samples at liquid N<sub>2</sub> temperature in a wide energy range (up to 10.640 keV), suitable for extended X-ray absorption fine structure (EXAFS) signal analysis.

The  $\mu$ -XAS measurements were carried out at the ESRF-BM23 beamline (Grenoble-France; [60]) using a  $4 \times 4 \mu\text{m}^2$  X-ray spot. Each specimen was firstly explored on the basis of fluorescence maps (at 12 keV X-ray beam energy) to individuate the metal distribution (mainly Ca, Fe and Zn). The Zn K-edge  $\mu$ -XAS data were collected in the near edge (XANES) region (from -100 to 150 eV range around the Zn K-edge) in selected Zn rich spots.

## 10.4 Results

Investigated bivalve shells are mainly made up of aragonite (Table 10.1) with Zn concentration varying between 2 and 80 mg/kg and the highest values were observed in samples from Buggerru, where mining tailings are dispersed in the marine sediments or near to the beach (Fig. 10.1c). Iron shows variable concentrations in all the analyzed samples (8–30 mg/kg).

Selected representative STXM-XRF maps (TwinMic beamline) of thin cross sections of the bivalve shells are shown in Figs. 10.2a, b. The Pearson linear correlation coefficient  $\rho_{ij}$  between *i* and *j* fluorescence intensities (*i, j* = Ca, Zn, Fe) has been calculated to depict the relationship among Zn, Fe and Ca distribution within the shell. Correlation analysis reveal that Zn and Fe are weakly correlated ( $\rho_{\text{Zn-Fe}} = 0.09\text{--}0.15$ ) suggesting that they are located in different phases. Also, Zn and Fe are weakly correlated to Ca ( $\rho_{\text{Zn-Ca}} = 0.23$ ,  $\rho_{\text{Fe-Ca}} = 0.08$ ), indicating that Zn and Fe are not homogeneously dispersed in the aragonite matrix but may likely occur in Fe or Zn rich specific phases embedded into the shell matrix [31]. Accordingly, TEM analysis (Fig. 10.3a–f) reveals that Zn and Fe clusters occur in different regions of the aragonite biocomposite matrix, resulting in a low correlation coefficient ( $\rho_{\text{Zn-Fe}}$

**Table 10.1** List of bivalve samples, sampling locality, mineralogical composition and concentration of Zn and Fe from the Malfidano area

| Sample           | Locality   | Mineralogy | Zn (mg/kg) | Fe (mg/kg) |
|------------------|------------|------------|------------|------------|
| <i>Donax</i>     | San Nicolò | Aragonite  | 2.5        | 10         |
| <i>Lentidium</i> | San Nicolò | Aragonite  | 3.6        | 10         |
| <i>Chamelea</i>  | San Nicolò | Aragonite  | 8.3        | 20         |
| <i>Donax</i>     | Buggerru   | Aragonite  | 27         | 7.7        |
| <i>Lentidium</i> | Buggerru   | Aragonite  | 29         | 20         |
| <i>Chamelea</i>  | Buggerru   | Aragonite  | 81         | 30         |

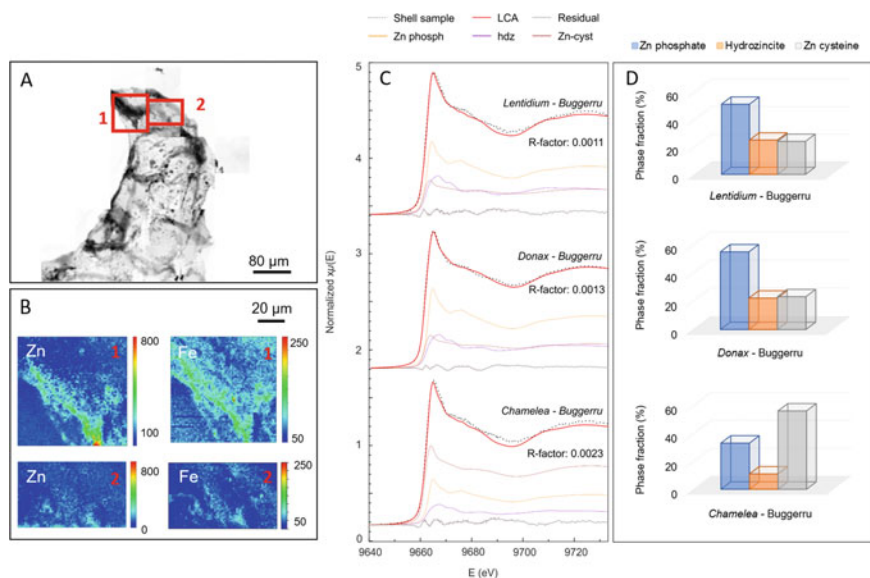


**Fig. 10.2** STXM analysis (a and b) of a selected sample of *Chamelea* collected at Buggerru. Bright field (absorption) image (a) and LEXRF maps of Zn and Fe (b). Maps 1, size  $80 \times 80 \mu\text{m}^2$ , scan  $64 \times 64$  pixels; map 2, size  $80 \times 40 \mu\text{m}^2$ , scan  $64 \times 32$  pixels. Linear-combination analysis of the XANES spectra (c). Zn phosph (Zn phosphate), hdz (hydrozincite) and Zn-cyst (Zn cysteine). Contribution fractions (sum fixed to 100%) of the Zn phases identified by the LCA (uncertainty around 5–8%) (d)

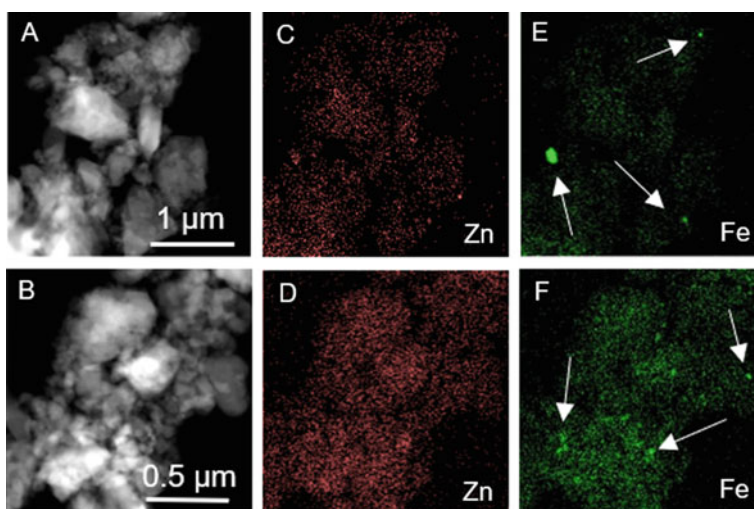


**Fig. 10.3** STEM images (a and b) with the EDS maps of Zn (c and d) and Fe (e and f) in bivalve shells. Arrows indicate Fe concentrated spots

= 0.12). Also, Fe can occur as concentrated spots, in agreement with the observed low correlation to Ca ( $\rho_{\text{Fe-Ca}} = 0.08$ ) (for the complete dataset of  $\rho$  values see Table 3 in [31]).

Zinc speciation in bivalve shells was investigated by XANES analysis in samples having the highest Zn concentration (*Lentidium*, *Donax* and *Chamelea* from Buggerru). Figure 10.2c shows bivalve shell spectra and the phases identified by the LCA. The XANES spectral features are smoother and broader with respect to the reference compounds, likely due to several Zn-phases and/or disordered Zn coordination environment in the shell samples. Comparing the Zn XANES spectral features of bivalve samples with those of the reference compounds, the similarity with the Zn phosphate spectrum is clear. LCA of XANES spectra was performed to determine the main Zn-phases present in these bivalve samples and the results are shown in Fig. 10.2c–d. In *Lentidium* and *Donax* the main contribution comes from the Zn phosphate (51–55%), followed by hydrozincite (22–25%) and Zn cysteine (23–24%) in similar amount. On the other hand, in *Chamelea*, characterized by the highest Zn content (81 mg/kg) in this study, Zn cysteine (56%) is the most abundant Zn species, followed by Zn phosphate (33%) and hydrozincite (11%), suggesting that cysteine synthesis in the investigated bivalves increases when the Zn uptake from the organism is higher and the excess of Zn is incorporated in the shell as a non-toxic form.

The  $\mu$ -XRF analysis was used to investigate Ca, Zn and Fe distribution in the foraminiferal shells (Fig. 10.4a). The distribution of Zn and Fe in foraminiferal shells shows clear differences in comparison with bivalve samples. Both Zn and Fe distributions depict spots and inhomogeneities, but Zn appears more broadly diffused in homogeneous halos on the *Q. seminula* specimens. The relatively high correlation between Zn and Fe  $\rho_{\text{ZnFe}} (> 50\%)$  in all samples (up to 70% for *E. aculeatum*) suggests that Fe and Zn tend to be co-located, while the low  $\rho_{\text{CaFe}} (< 15\%)$  in both foraminiferal taxa samples points out the Fe segregation in Fe-rich spots. Interestingly, the correlation between Ca and Zn is largely different in *E. aculeatum* being  $\rho_{\text{ZnCa}} < 30\%$  and in *Q. seminula* being  $\rho_{\text{ZnCa}} > 50\%$ . This finding quantifies the observation that Zn is mainly localized in *E. aculeatum* while it is more broadly distributed in *Q. seminula* shell.

The analysis of Zn K-edge XAFS spectra from bulk samples revealed a clear structural difference between average Zn environment in *E. aculeatum* and *Q. seminula*. XAFS spectrum of *E. aculeatum* depicts features similar to hydrozincite, whereas *Q. seminula* specimen shows XAFS features of a largely more disordered environment, similar to fourfold-coordinated Zn adsorbed on calcite ( $\text{Zn}_{4\text{c}}$ , see below) (Fig. 10.4b).

Since the  $\mu$ -XRF data highlighted a nonuniform Zn distribution within the calcite shell, we exploited the  $\mu$ -XANES as a tool to get further details about the coordination chemistry of Zn in the shells. We collected Zn K-edge  $\mu$ -XAS spectra at different spots in the samples, characterized by low (L), medium (M) and high (H) normalized fluorescence Zn/Ca intensity ratios  $R_N$  (see [32] for details) (Fig. 10.4c), and we exploited the LCA to individuate and quantify the Zn-phases in the shells (Fig. 10.4d). In a preliminary screening among the reference compounds, we found three main Zn containing phases in all the  $\mu$ -XANES spectra: Zn-hydrozincite, Zn/calcite and  $\text{Zn}_{4\text{c}}$ , the last associated to Zn adsorbed on calcite or hydroxyapatite (the spectra

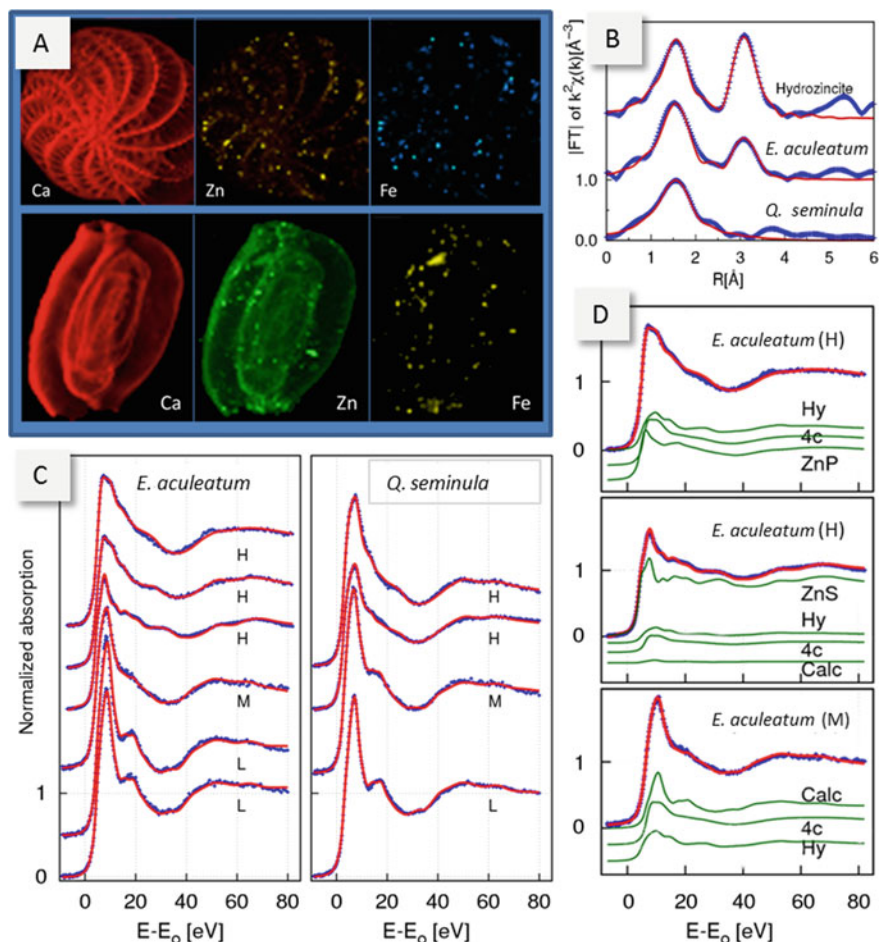


**Fig. 10.4** Results of  $\mu$ -XRF and  $\mu$ -XANES on foraminifera.  $\mu$ -XRF maps for *E. aculeatum* (top row) and *Q. seminula* (bottom row) at the Ca, Zn and Fe fluorescence lines (a). Moduli of the Fourier Transform (IFT) of Zn K-edge EXAFS spectra (blue points) measured for hydrozincite mineral reference and bulk samples (about 300 specimens) of *E. aculeatum* and *Q. seminula* (b). The IFT of EXAFS best fit procedures are shown as red lines for completeness. Experimental (blue points) and LCA best fit (red lines) of selected Zn K-edge  $\mu$ -XANES spectra on *E. aculeatum* (left column) and *Q. seminula* (right column) (c). Zn K-edge  $\mu$ -XANES were measured at selected points in the low (L), medium (M) and high (H) regions of the normalized fluorescence Zn/Ca intensity ratio  $R_N$  (see [32] for details). Experimental (blue points) and LCA best fit (red lines) of selected Zn K-edge  $\mu$ -XANES spectra on *E. aculeatum* (Hy—hydrozincite, 4c—fourfold-coordinated Zn adsorbed, ZnP— $Zn_3(PO_4)_2$ , ZnS—sphalerite, Calc—Zn-Ca solid solution) (d)

are very similar pointing out very similar Zn adsorption site geometry in calcite and hydroxyapatite).

Our analysis of  $\mu$ -XANES spectra suggests an intra-specimen variability related to the local Zn concentration. Particularly, high values of the hydrozincite fraction correspond to higher Zn concentration (Zn richer spots, frequent in *E. aculeatum* and rare in *Q. seminula*), while Zn/calcite and Zn<sub>4</sub>C phases are favored in regions having lower Zn concentration. Moreover, the Zn  $\mu$ -XANES features also showed the presence of other components such as Zn-sulphide (ZnS) and Zn-phosphate Zn<sub>3</sub>(PO<sub>4</sub>)<sub>2</sub> in some spots of the *Elphidium* spp. samples. Noticeably, further HR-TEM investigation on the same specimens revealed aggregates of Zn carbonate nanocrystals, having an individual size of ~5 nm. Based on the SAED pattern, we identified the main reflections of hydrozincite. In other areas of the *E. aculeatum* shell, we found Zn to be co-located with S, and the SAED pattern revealed the presence of nanocrystalline sphalerite, ZnS, confirming results obtained by  $\mu$ -XANES analysis.

## 10.5 Discussion and Conclusions

In our bivalve and foraminifera case-study, we found that large fraction of Zn occurs in independent phases such as Zn-phosphate, Zn-cysteine and even nanocrystalline hydrozincite. Peculiarly, Zn in bivalves does not seem to be incorporated into aragonite lattice or adsorbed onto the surfaces of Ca-carbonate (nano)crystals. This suggests that, under environmental stress, Zn incorporation in bivalve shells occurs with the biosynthesis of phases other than Ca-carbonate. These results point out that bivalves can use different biogeochemical reactions, involving cysteine molecule, phosphate or carbonate ions, to regulate trace element concentrations and their chemical speciation. At the present step of the research, we are not able to assess if these Zn-independent phases were formed as a by-product of the molecular machinery, exploited by the mollusks for the Ca-carbonate synthesis that could be activated also without Zn stress.

This study provided insight into the understanding of cellular control of biomineralization in foraminifera. Combining  $\mu$ -XRF and  $\mu$ -XAS techniques, we found that Zn occurs as a solid calcite solution or it is adsorbed onto calcite surfaces and inter-grain spaces due to foraminiferal cellular biosynthesis. Other Zn phases were also detected by XAS and TEM: specifically, hydrozincite was found along with a Zn/Ca solid solution and it is most likely produced during the primary biomineralization process. The occurrence of sphalerite crystals close to calcite aggregates and the presence of detectable amounts of S within the shells, element present in metallothioneins, often used by foraminifera for metal detoxification [61, 62], suggest that sphalerite could be a product of the biosynthesis process but further studies are required to exclude a post-mortem precipitation. Zinc speciation, size of crystal domains and distributions in the shells differ for the two investigated taxa. In calcite needles of *Q. seminula*, Zn is uniformly distributed, and it occurs in a less ordered

environment, indicating that Zn is incorporated more easily during the biologically controlled mineralization processes.

Application of synchrotron techniques such as STXM and  $\mu$ -XRF to the case-studies allowed us to identify colocalization and chemical distribution of Ca, Zn and Fe across the shells. Moreover, the elemental selectivity and coordination chemistry sensitivity of XAS technique were applied, allowing us to identify the chemical and mineral species of Zn. Understanding biomineralization processes, their structural properties, coordinative and chemical environment offers a unique opportunity to take steps forward in understanding geological record and environmental reconstruction. Paleothermometers and proxies based on elemental ratios and isotopes can be better developed and used when data on microscopic processes and structures are comprised in the models [28]. In this study, we provided relevant information for speciation and location of Fe and Zn in some biominerals. This new knowledge will be of future benefit for the understanding of isotopes fractionation and chemical distribution variability across biomineralization depending on foraminifera and bivalve species.

**Acknowledgements** We acknowledge CESA (grant number: E58C16000080003) from RAS, and RAS/FBS (grant number: F72F16003080002) grants, the POR FESR Sardegna 2014–2020 (project cluster Top-Down: TESTARE), and the CeSAR (Centro Servizi d'Ateneo per la Ricerca) of the University of Cagliari, Italy, for SEM analysis. The ESRF EV-94 and ES-540 proposals provided access to the BM23 micro-focus experiment. The authors acknowledge the CERIC-ERIC Consortium (grant numbers: 20152020, 20162061, 20167045, 20177041, and 20182100) for the access to experimental facilities and financial support and the Romanian Ministry of Education (through the Core Program, Project PN16-480102). XAFS (Elettra) 20160254 beamtime, Diamond SP16496 beamtime, and grant are acknowledged. The research leading to this result has been supported by the project CALIPSOplus under the Grant Agreement 730872 from the EU Framework Program for Research and Innovation HORIZON 2020. The Grant of Excellence Departments, MIUR (ARTICOLO 1, COMMI 314–337 LEGGE 232/2016), is gratefully acknowledged.

## References

1. E. Beniash, Biominerals—hierarchical nanocomposites: the example of bone. Wiley Interdiscip. Rev. Nanomed. Nanobiotechnol. **3**, 47–69 (2011). <https://doi.org/10.1002/wnan.105>
2. J. Yu, H. Elderfield, Benthic foraminiferal B/Ca ratios reflect deep water carbonate saturation state. Earth Planet. Sci. Lett. **258**, 73–86 (2007). <https://doi.org/10.1016/j.epsl.2007.03.025>
3. D.W. Lea, G.T. Shen, E.A. Boyle, Coralline barium records temporal variability in equatorial Pacific upwelling. Nature **340**, 373–376 (1989). <https://doi.org/10.1038/340373a0>
4. S.P. Bryan, T.M. Marchitto, Testing the utility of paleonutrient proxies Cd/Ca and Zn/Ca in benthic foraminifera from thermocline waters. Geochem. Geophys. Geosyst. **11**, Q01005 (2010). <https://doi.org/10.1029/2009GC002780>
5. A.L. Soldati, D.E. Jacob, P. Glatzel, J.C. Swarbrick, J. Geck, Element substitution by living organisms: the case of manganese in mollusc shell aragonite. Sci. Rep. **6**, 22514 (2016). <https://doi.org/10.1038/srep22514>
6. L. Chauvaud, A. Lorrain, R.B. Dunbar, Y.-M. Paulet, G. Thouzeau, F. Jean, J.-M. Guarini, D. Mucciarone, Shell of the Great Scallop *Pecten maximus* as a high-frequency archive of paleoenvironmental changes. Geochem. Geophys. Geosyst. **6**, 1–15 (2005). <https://doi.org/10.1029/2004GC000890>

7. M.H. Klünder, D. Hippler, R. Witbaard, D. Frei, Laser ablation analysis of bivalve shells—archives of environmental information. *Geol. Surv. Denmark Greenl. Bull.* **15**, 89–92 (2008)
8. A.J. Gooday, Benthic foraminifera (protista) as tools in deep-water palaeoceanography: environmental influences on faunal characteristics. *Adv. Mar. Biol.* **46**, 1–90 (2003). [https://doi.org/10.1016/S0065-2881\(03\)46002-1](https://doi.org/10.1016/S0065-2881(03)46002-1)
9. E. Arminot du Châtelet, J.-P. Debenay, R. Soulard, Foraminiferal proxies for pollution monitoring in moderately polluted harbors. *Environ. Pollut.* **127**, 27–40 (2004). [https://doi.org/10.1016/S0269-7491\(03\)00256-2](https://doi.org/10.1016/S0269-7491(03)00256-2)
10. G. Nehrke, H. Poigner, D. Wilhelms-Dick, T. Brey, D. Abele, Coexistence of three calcium carbonate polymorphs in the shell of the Antarctic clam *Laternula elliptica*. *Geochem. Geophys. Geosyst.* **13**, 1–8 (2012). <https://doi.org/10.1029/2011GC003996>
11. S. Weiner, H.A. Lowenstam, L. Hood, Characterization of 80-million-year-old mollusk shell proteins. *Proc. Natl. Acad. Sci. U. S. A.* **73**, 2541–2545 (1976). <https://doi.org/10.1073/pnas.73.8.2541>
12. A. Checa, A new model for periostracum and shell formation in Unionidae (Bivalvia, Mollusca). *Tissue Cell.* **32**, 405–416 (2000). <https://doi.org/10.1054/tice.2000.0129>
13. Z. Yao, M. Xia, H. Li, T. Chen, Y. Ye, H. Zheng, Bivalve shell: not an abundant useless waste but a functional and versatile biomaterial. *Crit. Rev. Environ. Sci. Technol.* **44**, 2502–2530 (2014). <https://doi.org/10.1080/10643389.2013.829763>
14. M. Suzuki, S. Sakuda, H. Nagasawa, Identification of chitin in the prismatic layer of the shell and a chitin synthase gene from the Japanese pearl oyster. *Pinctada Fucata*. *Biosci. Biotechnol. Biochem.* **71**, 1735–1744 (2007). <https://doi.org/10.1271/bbb.70140>
15. Y. Kong, G. Jing, Z. Yan, C. Li, N. Gong, F. Zhu, D. Li, Y. Zhang, G. Zheng, H. Wang, L. Xie, R. Zhang, Cloning and characterization of Prsilkin-39, a novel matrix protein serving a dual role in the prismatic layer formation from the oyster *Pinctada fucata*. *J. Biol. Chem.* **284**, 10841–10854 (2009). <https://doi.org/10.1074/jbc.M808357200>
16. R.A. Lutz, Bivalve Molluscs: biology, ecology and culture by Elizabeth Gosling. *Q. Rev. Biol.* **79**, 317 (2004). <https://doi.org/10.1086/425799>
17. L.J. De Nooijer, H.J. Spero, J. Erez, J. Bijma, G.J. Reichart, Biomineralization in Perforate Foraminifera. *Earth-Sci. Rev.* **135**, 48–58 (2014). <https://doi.org/10.1016/j.earscirev.2014.03.013>
18. S. Weiner, P.M. Dove, An overview of biomineralization processes and the problem of the vital effect. *Rev. Mineral. Geochem.* **54**, 1–29 (2003). <https://doi.org/10.2113/0540001>
19. B.R. Schöne, D.P. Gillikin, Unraveling environmental histories from skeletal diaries—advances in sclerochronology. *Palaeogeogr. Palaeoclimatol. Palaeoecol.* **373**, 1–5 (2013). <https://doi.org/10.1016/j.palaeo.2012.11.026>
20. J. Erez, The source of ions for biomineralization in Foraminifera and their implications for paleoceanographic proxies. *Rev. Mineral. Geochem.* **54**, 115–149 (2003). <https://doi.org/10.2113/0540115>
21. G.M. Henderson, New oceanic proxies for paleoclimate. *Earth Planet. Sci. Lett.* **203**, 1–13 (2002). [https://doi.org/10.1016/S0012-821X\(02\)00809-9](https://doi.org/10.1016/S0012-821X(02)00809-9)
22. M. Risk, M. Burchell, K. de Roo, R. Nairn, M. Tubrett, G. Försterra, Trace elements in bivalve shells from the Río Cruces, Chile. *Aquat. Biol.* **10**, 85–97 (2010). <https://doi.org/10.3354/ab00268>
23. J. Yu, H. Elderfield, B. Hönisch, B/Ca in planktonic foraminifera as a proxy for surface seawater pH. *Paleoceanography* **22**, PA2202 (2007). <https://doi.org/10.1029/2006PA001347>
24. J.E. Pietrzak, J.M. Bates, R.M. Scott, Constituents of unionoid extrapallial fluid. II. pH and metal ion composition. *Hydrobiologia* **50**, 89–93 (1976)
25. M. Zuykov, E. Pelletier, C. Belzile, S. Demers, Alteration of shell nacre micromorphology in blue mussel *Mytilus edulis* after exposure to free-ionic silver and silver nanoparticles. *Chemosphere* **84**, 701–706 (2011). <https://doi.org/10.1016/j.chemosphere.2011.03.021>
26. V. Yanko, A.J. Arnold, W.C. Parker, *Effects of Marine Pollution on Benthic Foraminifera—Modern Foraminifera* (Springer, Netherlands, Dordrecht, 2003)

27. R.J.P. Williams, J.J.R.F. da Silva, *The Natural Selection of the Chemical Elements* (Bath Press Ltd., Great Britain, 1996)
28. X.-M. Liu, L.C. Kah, A.H. Knoll, H. Cui, A.J. Kaufman, A. Shahar, R.M. Hazen, Tracing Earth's O<sub>2</sub> evolution using Zn/Fe ratios in marine carbonates. *Geochemical Perspect. Lett.* **2**, 24–34 (2016). <https://doi.org/10.7185/geochemlet.1603>
29. P.B. Tchounwou, C.G. Yedjou, A.K. Patlolla, D.J. Sutton, Heavy metal toxicity and the environment. *Exp. Suppl.* **101**, 133–164 (2012). [https://doi.org/10.1007/978-3-7643-8340-4\\_6](https://doi.org/10.1007/978-3-7643-8340-4_6)
30. R. Singh, N. Gautam, A. Mishra, R. Gupta, Heavy metals and living systems: An overview. *Indian J. Pharmacol.* **43**, 246–253 (2011). <https://doi.org/10.4103/0253-7613.81505>
31. D. Medas, I. Carlomagno, C. Meneghini, G. Aquilanti, T. Araki, D.E. Bedolla, C. Buosi, M.A. Casu, A. Gianoncelli, A.C. Kuncser, V.A. Maraloiu, G.D. Giudici, Zinc incorporation in marine bivalve shells grown in mine-polluted seabed sediments : a case study in the Malfidano mining area ( SW Sardinia, Italy ). *Environ. Sci. Pollut. Res.* (2018). <https://doi.org/10.1007/s11356-018-3504-y>
32. G. De Giudici, C. Meneghini, D. Medas, C. Buosi, P. Zuddas, A. Iadecola, O. Mathon, A. Cherchi, A.C. Kuncser, Coordination environment of Zn in foraminifera *Elphidium aculeatum* and *Quinqueloculina seminula* shells from a polluted site. *Chem. Geol.* **477**, 100–111 (2018). <https://doi.org/10.1016/j.chemgeo.2017.12.009>
33. T. Bechstädt, M. Boni, Sedimentological, stratigraphical and ore deposits field guide of the autochthonous Cambro-Ordovician of southwestern Sardinia: Servizio Geologico d'Italia Memorie Descrittive Carta Geologica d'Italia, v. 48, 434 p. (1994)
34. A. Marcello, S. Pretti, P. Valera, M. Agus, M. Boni, M. Fiori, Metallogeny in Sardinia (Italy): from the Cambrian to the Tertiary, in *32nd International Geological Congress, APAT 4*, ed. by L. Guerrieri, L. Rischia, L. Serva, pp. 14–36, Firenze (2004)
35. M. Boni, H.A. Gilg, G. Aversa, G. Balassone, The “Calamine” of Southwest Sardinia: geology, mineralogy, and stable isotope geochemistry of supergene Zn mineralization. *Econ. Geol.* **98**, 731–748 (2003). <https://doi.org/10.2113/gsecongeo.98.4.731>
36. P. Stara, R. Rizzo, G.A. Tanca, Iglesias-Arburese: Miniere e Minerali, Centrooffset, Siena (1996)
37. R. Bartole, S. De Muro, Acoustic facies and seabed features of the mixed carbonate-siliciclastic deposits of the last eustatic cycle in the La Maddalena Archipelago (North Sardinia, Italy). *Ital. J. Geosci.* **131**, 102–122 (2012). <https://doi.org/10.3301/IJG.2011.28>
38. M. Schintu, B. Marras, A. Maccioni, D. Puddu, P. Meloni, A. Contu, Monitoring of trace metals in coastal sediments from sites around Sardinia. Western Mediterranean. *Mar. Pollut. Bull.* **58**, 1577–1583 (2009). <https://doi.org/10.1016/j.marpolbul.2009.07.015>
39. V. Moschino, M. Schintu, A. Marrucci, B. Marras, N. Nesto, L. Da Ros, An ecotoxicological approach to evaluate the effects of tourism impacts in the Marine Protected Area of La Maddalena (Sardinia, Italy). *Mar. Pollut. Bull.* **122**, 306–315 (2017). <https://doi.org/10.1016/j.marpolbul.2017.06.062>
40. G. Salvi, C. Buosi, D. Arbutta, A. Cherchi, G. De Giudici, A. Ibba, S. De Muro, Ostracoda and foraminifera response to a contaminated environment: the case of the Ex-military arsenal of the la Maddalena Harbour (Sardinia, Italy). *Micropaleontology* **61**, 115–133 (2015)
41. W.R. Walton, Techniques for recognition of living foraminifera. *Contrib. Cushman. Found. Foraminifer. Res.* **3**, 56–60 (1952)
42. A.R. Loeblich Jr., H. Tappan, *Foraminiferal Genera and Their Classification* (Van Reinhold Company, New York, 1987)
43. F. Cimerman, M.R. Langer, Mediterranean Foraminifera. Ljubljana, Slovenska Akademija Znanosti in Umetnosti. *Academia Scientiarum et ArtiumSlovenica Cl. 4 Historia Naturalis* (1991)
44. L. Hottinger, E. Halicz, Z. Reiss, Recent Foraminiferida from the Gulf of Aqaba, Red Sea. *Ljubljana Academia Scientiarum et ArtiumSlovenica, Classis IV, Historia Naturalis* (1993)
45. F. Sgarrella, M. Moncharmont Zei, Benthic foraminifera of the Gulf of Naples (Italy): systematics and autoecology. *Boll. Soc. Paleontol. Ital.* **32**, 145–264 (1993)



46. D.E. Conners, S.M. Westerfield, A. Feyko, M.C. Black, Lead Accumulation in soft tissues and shells of asiatic clams (*Corbicula fluminea*), in *The 1999 Georgia Water Resources Conference*, ed. by K. J. Hatcher, pp. 597–600 (1999)
47. A. Gianoncelli, G.R. Morrison, B. Kaulich, D. Bacescu, J. Kovac, Scanning transmission x-ray microscopy with a configurable detector. *Appl. Phys. Lett.* **89**, 251117–251119 (2006). <https://doi.org/10.1063/1.2422908>
48. G.R. Morrison, A. Gianoncelli, B. Kaulich, D. Bacescu, J. Kovac, A fast readout CCD system for configured-detector imaging in STXM, in *Proceedings of the 8th International Conference X-ray Microscopy. IPAP Conference Series*, pp. 277–379 (2006)
49. A. Gianoncelli, B. Kaulich, R. Alberti, T. Klatka, A. Longoni, A. de Marco, A. Marcello, M. Kiskinova, Simultaneous soft X-ray transmission and emission microscopy. *Nucl. Instrum. Methods Phys. Res. Sect. A Accel. Spectrometers, Detect. Assoc. Equip.* **608**, 195–198 (2009). <https://doi.org/10.1016/j.nima.2009.06.035>
50. A. Gianoncelli, G. Kourousias, A. Stolfa, B. Kaulich, Recent developments at the TwinMic beamline at ELETTRA: an 8 SDD detector setup for low energy X-ray Fluorescence. *J. Phys. Conf. Ser.* **425**, 182001 (2013). <https://doi.org/10.1088/1742-6596/425/18/182001>
51. A. Gianoncelli, G. Kourousias, L. Merolle, M. Altissimo, A. Bianco, Current status of the TwinMic beamline at Elettra: a soft X-ray transmission and emission microscopy station. *J. Synchrotron Radiat.* **23**, 1526–1537 (2016). <https://doi.org/10.1107/S1600577516014405>
52. A. Gianoncelli, G. Kourousias, M. Altissimo, D.E. Bedolla, L. Merolle, A. Stolfa, H.-J. Shin, Combining multiple imaging techniques at the TwinMic X-ray microscopy beamline. *AIP Conf. Proc.* **1764**, 30002 (2016). <https://doi.org/10.1063/1.4961136>
53. B. Kaulich, D. Bacescu, J. Susini, C. David, E. Di Fabrizio, G.R. Morrison, P. Charalambous, J. Thieme, T. Wilhelm, J. Kovac, D. Cocco, M. Salome, O. Dhez, T. Weitkamp, S. Cabrini, D. Cojoc, A. Gianoncelli, U. Vogt, M. Podnar, M. Zangrando, M. Zacchigna, M. Kiskinova, *Proceeding 8th International Conference X-ray Microscopy IPAP Conference Series*. Presented at the (2006)
54. Numpy: <https://docs.scipy.org/doc/numpy-1.14.0/reference/generated/numpy.corrcoef.html>. Copyright 2008–2009, The Scipy community. Last updated on 11 May 2014
55. scipy: <https://docs.scipy.org/doc/scipy-0.14.0/reference/generated/scipy.stats.spearmanr.html>. Copyright 2008–2009, The Scipy community. Last updated on 11 May 2014
56. A. Di Cicco, G. Aquilanti, M. Minicucci, E. Principi, N. Novello, A. Cognigni, L. Olivi, Novel XAFS capabilities at ELETTRA synchrotron light source. *J. Phys. Conf. Ser.* **190**, 12043 (2009). <https://doi.org/10.1088/1742-6596/190/1/012043>
57. M. Benfatto, C. Meneghini, A close look into the low energy region of the XAS spectra: the XANES region, in *Synchrotron Radiation, Basic, Methods and Applications*, ed. by S. Mobilio, F. Boscherini, C. Meneghini (Springer-Verlag, Berlin, 2014), pp. 213–240
58. R. Torchio, C. Meneghini, S. Mobilio, G. Capellini, A. Garcia Prieto, J. Alonso, M.L. Fdez-Gubieda, V. Turco Liveri, A. Longo, A.M. Ruggirello, T. Neisius, Microstructure and magnetic properties of colloidal cobalt nano-clusters. *J. Magn. Magn. Mater.* **322**, 3565–3571 (2010). <https://doi.org/10.1016/j.jmmm.2010.07.008>
59. C. Meneghini, F. Bardelli, S. Mobilio, ESTRA-FitEXA: a software package for EXAFS data analysis. *Nucl. Instrum. Methods Phys. Res. Sect. B Beam Interact. Mater. Atoms.* **285**, 153–157 (2012). <https://doi.org/10.1016/j.nimb.2012.05.027>
60. O. Mathon, A. Beteva, J. Borrel, D. Bugnazet, S. Gatla, R. Hino, I. Kantor, T. Mairs, M. Munoz, S. Pasternak, F. Perrin, S. Pascarelli, The time-resolved and extreme conditions XAS (TEXAS) facility at the European Synchrotron Radiation Facility: the general-purpose EXAFS bending-magnet beamline BM23. *J. Synchrotron Radiat.* **22**, 1548–1554 (2015). <https://doi.org/10.1107/S1600577515017786>
61. C.K. Carney, S.R. Harry, S.L. Sewell, Detoxification biominerals, in *Biomineralization I. Topics in Current Chemistry*, ed. by K. Naka (Springer, Berlin, Heidelberg, 2007), pp. 155–185
62. V. Le Cadre, J.-P. Debenay, Morphological and cytological responses of Ammonia (foraminifera) to copper contamination: implication for the use of foraminifera as bioindicators of pollution. *Environ. Pollut.* **143**, 304–317 (2006). <https://doi.org/10.1016/j.envpol.2005.11.033>

# Chapter 11

## Insights into the Structure of Reaction Intermediates Through Coupled X-ray Absorption/UV-Vis Spectroscopy



Francesco Tavani, Andrea Martini, Francesco Sessa, Giorgio Capocasa, Giorgio Olivo, Osvaldo Lanzalunga, Stefano Di Stefano, and Paola D'Angelo

**Abstract** In this work, we propose a method for the structural characterization of chemical reaction intermediates. It allows one to analyze time-resolved coupled energy dispersive X-ray absorption spectroscopy (EDXAS) and UV-Vis reaction data through a matricial approach. Concentration profiles for the reaction key species are derived from the UV-Vis data and are used as mathematical constraints to extract their associated X-ray absorption near edge structure (XANES) spectra. The obtained XANES spectra are then quantitatively characterized by full multiple scattering (MS) calculations. We demonstrate the capabilities of this approach by applying it over a series of coupled EDXAS/UV-Vis spectra acquired in the reaction between  $\text{Fe}^{II}$ (tris(2-pyridylmethyl)amine) ( $[\text{Fe}^{II}(\text{TPA})(\text{CH}_3\text{CN})_2]^{2+}$ ) and  $\text{H}_2\text{O}_2$ . As a result, structural information for the elusive reaction key intermediate  $[\text{Fe}^{III}(\text{TPA})(\text{OOH})(\text{X})]^{2+}$  is derived and it is suggested that  $\text{X} = \text{CH}_3\text{CN}$  in opposition to  $\text{X} = \text{H}_2\text{O}$ .

---

F. Tavani · F. Sessa · G. Capocasa · G. Olivo · O. Lanzalunga · S. Di Stefano · P. D'Angelo (✉)  
Dipartimento di Chimica, Università di Roma La Sapienza, P.le A. Moro 5, 00185 Roma, Italy  
e-mail: [p.dangelo@uniroma1.it](mailto:p.dangelo@uniroma1.it)

F. Tavani  
e-mail: [francesco.tavani@uniroma1.it](mailto:francesco.tavani@uniroma1.it)

A. Martini  
Dipartimento di Chimica, Università degli Studi di Torino, Via Giuseppe Verdi, 8,  
10124 Torino, Italy

F. Sessa  
Department of Chemistry and Chemical Engineering, Chalmers University of Technology,,  
Kemigården 4, 412 96 Göteborg, Sweden

G. Capocasa · O. Lanzalunga · S. Di Stefano  
Istituto CNR di Metodologie Chimiche (IMC-CNR), Sezione Meccanismi di Reazione,  
P.le A. Moro 5, 00185 Roma, Italy

© Springer Nature Switzerland AG 2021

A. Di Cicco et al. (eds.), *Synchrotron Radiation Science and Applications*,  
Springer Proceedings in Physics 220, [https://doi.org/10.1007/978-3-030-72005-6\\_11](https://doi.org/10.1007/978-3-030-72005-6_11)

## 11.1 Introduction

Unveiling the structure of fleeting reaction intermediates is an important step along the way that leads to the full understanding of a chemical process. In fact, the quantitative geometrical characterization of these interchanging chemical species is a desirable support, although difficult to obtain, for the comprehension of the overall reaction mechanistic picture. Novel experimental and theoretical approaches have been developed to investigate the complex systems routinely dealt with by researchers and to acquire detailed structural information on the intermediates that are formed in a given chemical transformation, especially when the reaction timescales are inferior to the seconds.

Among the numerous spectroscopic techniques that may be used to follow the structural and electronic variations occurring during a chemical reaction, X-ray absorption spectroscopy (XAS) stands out as a powerful probe of the local environment pertaining to a selected photoabsorbing atom. An initial investigation made use of time-resolved energy dispersive X-ray absorption spectroscopy (EDXAS) synchronized with a stopped-flow apparatus to follow reactions of Ir, Fe and Ni complexes [1]. In a following study, UV-Vis spectroscopy and energy dispersive extended X-ray absorption fine structure (EXAFS) data were obtained through a stopped-flow experiment on an oxidative reaction of Pd complexes in solution occurring in the second time scale [2]. Additionally, radiation damage effects were highlighted during reactions of Cu containing samples through the combination of in-situ XAS/UV-Vis spectroscopies [3]. We have recently shown that by coupling EDXAS to UV-Vis spectroscopy it is possible to follow chemical processes occurring in solution with characteristic timescales ranging between seconds and milliseconds and to qualitatively identify the reaction intermediates [4]. Specifically, time-resolved XAS made it possible to identify the sequence of oxidation states in the reactions between the non-heme complex  $\text{Fe}^{II}(\text{tris}(2\text{-pyridylmethyl)amine})$  ( $[\text{Fe}^{II}(\text{TPA})(\text{CH}_3\text{CN})_2]^{2+}$ ) and two different oxidizing agents, hydrogen peroxide and peroxyacetic acid (AcOOH). In a subsequent investigation, through the time-resolved EDXAS technique pseudo-first order kinetic constants relative to fast oxidation reactions involving a non-heme oxo complex and a series of sulfides and alcohol substrates were obtained [5].

In time-resolved experiments a large series of spectra are measured, and every individual spectrum may be seen as the superposition of a small number of components weighed for their relative concentration [6]. In order to extract the spectra belonging to the pure components, a wide variety of methods can be applied. A common technique is the Linear Combination Fit (LCF), which is limited however by the necessity of knowing *a priori* the number of reference compounds and their spectra [7, 8]. Principal Component Analysis (PCA) has also been a widespread approach for the correct estimation of the number of pure species in complex matrices. PCA was used, for example, to identify the number of pure species in a series of X-ray absorption near edge structure (XANES) spectra of CuPd/KL zeolites measured in temperature-programmed reduction conditions and then the Iterative Target Transform Analysis (ITTTA) curve resolution algorithm was employed to extract

their spectra and concentration profiles [9]. In recent years, there has been increasing work regarding the analysis of XANES data by means of the Multivariate Curve Resolution Alternating Least Squares (MCR-ALS) method [10], an iterative algorithm that factorizes the experimental dataset in the product of a physically and chemically meaningful spectral matrix associated to the pure species and its relative concentration profile matrix [6]. Relying on MCR-ALS, investigations have been performed on lithium batteries containing doped  $V_2O_5$  [11], formation of Q-dots based on ZnO [12], the temperature-induced degradation of chlorine layered double hydroxide [13], and numerous other solid phase systems [14–20]. While the MCR-ALS mathematical approach is promising for the study of time- and space-resolved spectral series, its main disadvantage resides in the fact that the matricial decomposition does not provide unique solutions, which strongly depend on the algorithm initiation process. This problem may be addressed by imposing different mathematical, physical or chemical constraints [6, 21].

In this paper it is shown that the individuation of pure species and their chemical characterization in complex spectral mixtures may be achieved for chemical reactions occurring in solution on the millisecond time scale. In particular, a matricial approach has been applied to the coupled EDXAS/UV-Vis spectra relative to the reaction between  $[Fe^{II}(TPA)(CH_3CN)_2]^{2+}$  (**1**) and  $H_2O_2$  in order to extract the XANES spectra of the key reaction intermediates and to derive quantitative information on their geometrical structures.

## 11.2 Materials and Methods

### 11.2.1 Materials

The TPA (trispyridylmethylamine) and hydrogen peroxide solutions (50 wt. in  $H_2O$ , stored at  $4^\circ C$ ) used in this work were purchased from Sigma Aldrich.  $[Fe^{II}(TPA)(OTf)_2]$  ( $OTf = trifluoromethanesulfonate$ ) was obtained by metallation of the TPA ligand (Sigma Aldrich) in dry  $CH_3CN$  with  $Fe(OTf)_2 \times 2CH_3CN$ , previously prepared from anhydrous  $Fe(II)$  chloride (Sigma Aldrich), as described in the literature [22, 23]. All air-sensitive materials were prepared, handled and stored employing either standard Schlenk and vacuum line techniques or a glove-bag under  $N_2$  flux. Once the  $CH_3CN$  solvent dissolves complex  $[Fe^{II}(TPA)(OTf)_2]$ , complex  $[Fe^{II}(TPA)(CH_3CN)_2](OTf)_2$  is formed. From now on, only the  $[Fe^{II}(TPA)(CH_3CN)_2]^{2+}$  species will be mentioned.

## 11.2.2 Methods

**Reaction Details.** For all mixing experiments involving the stopped-flow, stock solutions of 70 mM  $[\text{Fe}^{II}(\text{TPA})(\text{CH}_3\text{CN})_2]^{2+}$  in  $\text{CH}_3\text{CN}$  and 140 mM  $\text{H}_2\text{O}_2$  in  $\text{CH}_3\text{CN}$  were injected into the reservoirs of the stopped-flow instrument. These solutions were mixed in a 1:1 volume ratio at room temperature to obtain final concentrations of 13 mM and 70 mM for  $[\text{Fe}^{II}(\text{TPA})(\text{CH}_3\text{CN})_2]^{2+}$  and  $\text{H}_2\text{O}_2$  respectively. In every experiment, 100  $\mu\text{L}$  of each solution were shot by the instrument into the cell.

**Energy dispersive x-ray absorption and UV-Vis measurements.** The coupled EDXAS/UV-Vis spectra were measured at the ID24 beam-line of the european synchrotron radiation facility [24] ESRF, in Grenoble. The detailed description of both the EDXAS and UV-Vis simultaneous data collection is provided in Reference [4]. The synchronized acquisition of the EDXAS and UV-Vis spectra was performed using a Bio-Logic SFM-400 stopped-flow device (whose dead time is about 2.0 ms for a flow rate of 8 ml/s) equipped with a flow-through quartz capillary cell (whose diameter and wall thickness were 1.3 mm and about 10  $\mu\text{m}$ , respectively).

**UV-Vis analysis and XANES spectra extraction.** It is known that, in  $\text{CH}_3\text{CN}$ ,  $\text{H}_2\text{O}_2$  oxidizes **1** to the species  $[\text{Fe}^{III}(\text{TPA})(\text{OOH})(\text{X})]^{2+}$  (**2**) [25, 26], which in turn has been suggested to evolve to the  $\mu$ -oxo dimer  $[\text{Fe}_2^{III}(\text{TPA})_2(\mu\text{-O})(\text{H}_2\text{O})_2]^{4+}$  (**3**) [27], as depicted in Fig. 11.1.

Herein, the relative concentrations of the principal reaction species are obtained by following the UV-Vis absorbance time evolution of the reaction  $\text{Fe}^{III}$  key intermediate. Such concentration profiles are then used to extract the XAS spectra that belong to the reaction intermediates by inverting the Lambert-Beer law written in matricial form applied to the time-resolved EDXAS experimental spectra. Finally, from the quantitative analysis of the derived XANES spectra, accurate information is acquired on the geometries of the reaction key species, in excellent agreement with the existent literature structural data for the already characterized coordination compounds, and providing new structural information for the elusive  $[\text{Fe}^{III}(\text{TPA})(\text{OOH})(\text{X})]^{2+}$  complex.

Figure 11.2a shows the absorbance evolution at  $\lambda = 524 \text{ nm}$  recorded during the course of the reaction of **1** (13 mM) with  $\text{H}_2\text{O}_2$  (70 mM) in  $\text{CH}_3\text{CN}/\text{H}_2\text{O}$  (99.8:0.2

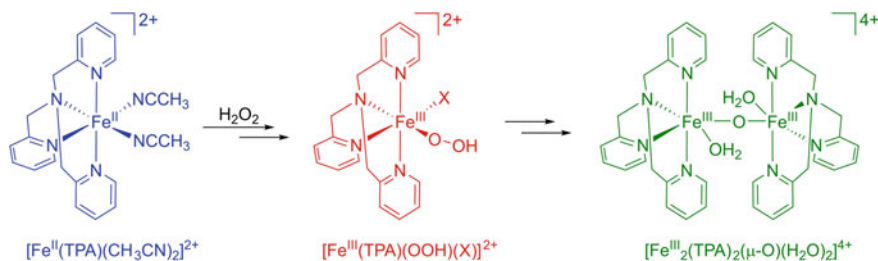


**Fig. 11.1** Proposed mechanism of the reaction between  $[\text{Fe}^{II}(\text{TPA})(\text{CH}_3\text{CN})_2]^{2+}$  and  $\text{H}_2\text{O}_2$  [28]

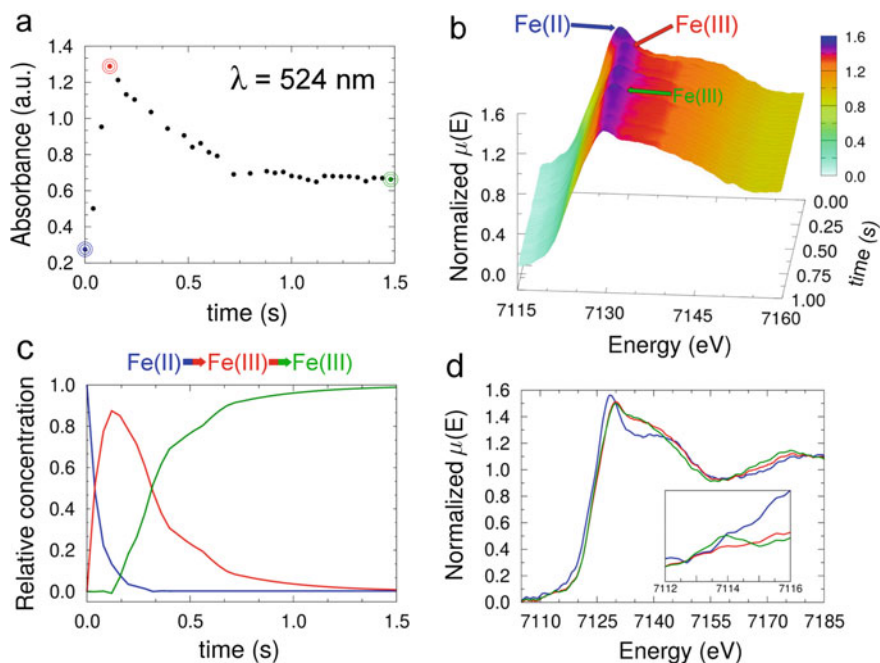


**Fig. 11.2** **a** Time evolution of the absorbance at  $\lambda = 524 \text{ nm}$  recorded for the reaction between  $[\text{Fe}^{\text{II}}(\text{TPA})(\text{CH}_3\text{CN})_2]^{2+}$  (13 mM) and  $\text{H}_2\text{O}_2$  (70 mM) in  $\text{CH}_3\text{CN}/\text{H}_2\text{O}$  (99.8:0.2(v/v)) at  $25^\circ\text{C}$ . **b** Time evolution of the Fe K-edge EDXAS spectra of the same reaction mixture. EDXAS and UV-Vis spectra were recorded contemporaneously in a stopped-flow cell. **c** Time evolution of the relative concentrations of  $[\text{Fe}^{\text{II}}(\text{TPA})(\text{CH}_3\text{CN})_2]^{2+}$  (blue),  $[\text{Fe}^{\text{III}}(\text{TPA})(\text{OOH}(\text{X}))_2]^{2+}$  (red) and  $[\text{Fe}^{\text{III}}(\text{TPA})_2(\mu\text{-O})(\text{H}_2\text{O})_2]^{2+}$  (green). **d** Isolated EDXAS spectra belonging to the corresponding same colored Fe complexes in panel (c). A magnification of the 1s  $\rightarrow$  3d transition region is shown in the inset

(v/v)) at  $25^\circ\text{C}$ . The initial increase in absorbance up to  $t=104 \text{ ms}$  is due to the formation of **2** ( $\lambda_{\text{max}} = 538 \text{ nm}$ ) and the subsequent absorbance decrease to the evolution of the latter to the dimeric species **3** [4]. Figure 11.2c shows the relative concentration profiles assigned to the three species. The relative concentration of **2** (red) follows the general trend given by the time evolution of the absorbance at  $\lambda = 524 \text{ nm}$ . Conversely, we postulate that the conversion of the  $\text{Fe}^{\text{II}}$  reactant to the  $\text{Fe}^{\text{III}}$  intermediate and that of the  $\text{Fe}^{\text{III}}$  intermediate to the  $\text{Fe}^{\text{III}}$  dimer take place between  $t=0 \text{ s}$  and  $t=104 \text{ ms}$ , and between  $t=104 \text{ ms}$  and  $t=2 \text{ s}$ , respectively. As a consequence, the relative concentration of the initial  $\text{Fe}^{\text{II}}$  complex (blue) is assumed to decrease to zero with the same rate as the absorbance at  $\lambda = 524 \text{ nm}$  increases to its maximum between  $t=0 \text{ s}$  and  $t=104 \text{ ms}$ . Further, it is suggested the concentration profile of the  $\text{Fe}^{\text{III}}$  dimeric product (green) increases towards a plateau with the same rate as the absorbance at  $\lambda = 524 \text{ nm}$  decays between  $t=104 \text{ ms}$  and  $t=2 \text{ s}$ . This general picture for the relative concentrations of the reaction components holds if one requires the

initial concentrations of both the  $\text{Fe}^{III}$  complexes to be zero and the two reaction steps to be independent and complete. Within these approximations, one can use the relative concentrations acquired by means of the UV-Vis detection as mathematical constraints for the analysis of the EDXAS reaction spectra registered with a time resolution of 40 ms, shown as a continuous evolution in Fig. 11.2b.

For the Lambert-Beer law [6], the three main reaction components contribute to each experimental EDXAS spectrum registered at time  $t$  with their own EDXAS spectra weighted for their relative concentration. One can thus write the matrix of the experimental EDXAS spectra  $\mathbf{D}$  as:

$$\mathbf{D} = \mathbf{S} \cdot \mathbf{C} \quad (11.1)$$

where each column of  $\mathbf{D}$  is an EDXAS spectrum measured at time  $t$ ,  $\mathbf{S}$  and  $\mathbf{C}$  are a  $m \times 3$  and a  $3 \times m$  matrix representing the EDXAS spectra and relative concentrations of the three reaction key species, respectively, that reproduce the data matrix  $\mathbf{D}$  ( $m$  is the number of measured EDXAS energy values). The sought spectral matrix  $\mathbf{S}$  is therefore given by:

$$\mathbf{S} = \mathbf{D} \cdot \mathbf{C}^T \cdot (\mathbf{C} \cdot \mathbf{C}^T)^{-1} \quad (11.2)$$

where  $\mathbf{C}$  is the  $3 \times m$  relative concentration matrix for the three reaction species obtained through UV-Vis spectroscopy and  $\mathbf{C}^T$  is the transpose of  $\mathbf{C}$ . One can note that the knowledge of  $\mathbf{S}$  is exactly determined by that of  $\mathbf{D}$  and of  $\mathbf{C}$ .

**XANES data analysis.** The MXAN code was used to perform the XANES data analysis [29–33]. MXAN employs a multiple scattering (MS) approach in the framework of the muffin tin (MT) approximation to calculate theoretical spectra. Within this method, a complex optical potential is used, based on the local density approximation [34–37] of the self-energy of the excited photoelectron. In this study, the Norman criterion was employed to calculate the MT radii. The Hedin-Lundqvist (HL) scheme accounts for the self-energy using solely the real portion of the HL potential, while an empirical strategy is employed to include the effects of inelastic losses. The amplitude of the plasmon,  $A_s$ , and the energy onset,  $E_s$ , are refined in the latter stage [38]. The core hole lifetime ( $\Gamma_c$ ) of Fe was kept fixed at a value of 1.25 eV in all analyses, while during the minimization procedures a Gaussian function was employed to optimize the experimental resolution ( $\Gamma_{res}$ ).

The analyses of the XANES spectra assigned to species **1** and **2** were carried out starting from the crystallographic structure of complex  $[\text{Fe}^{II}(\text{TPA})(\text{CH}_3\text{CN})_2]^{2+}$  [39] where the Fe atom is in an octahedral configuration. In this structure, four nitrogen atoms belonging to the TPA backbone ( $N_{TPA}$ ) and two  $\text{CH}_3\text{CN}$  solvent nitrogen atoms ( $N_{ACN}$ ) coordinate the Fe photoabsorber. During the minimization procedure of the **1** species, a Fe- $N_{TPA}$  distance with a multiplicity of four and a Fe- $N_{ACN}$  distance with a multiplicity of two were optimized, while the geometries of the TPA chain and of the  $\text{CH}_3\text{CN}$  molecules have been kept fixed to those in the crystallographic structure. The XANES analysis of **2** has been performed using two different coordination models. In the former (**2a**), one of the acetonitrile ligands

has been replaced by a hydroperoxyl group and the Fe-N<sub>ACN</sub> and Fe-O<sub>per</sub> distances have been optimized independently. In the latter (**2b**), both the acetonitrile molecules have been replaced by two different ligands, namely a hydroperoxyl group and a water molecule and the Fe-O<sub>per</sub> and Fe-O<sub>wat</sub> distances have been minimized during the fitting procedure. In the case of complexes **2a** and **2b** the orientation of the hydroperoxyl group was changed within a range of  $\pm 20^\circ$  if compared to the initial geometry.

The XANES spectrum assigned to complex **3** was analyzed starting from the crystallographic geometry of the  $\mu$ -oxo dimer  $[\text{Fe}_2\text{O}(\text{5-Et-TPA})_2(\text{OH})-(\text{H}_2\text{O})]^{3+}$  [40]. In this structure, two Fe atoms are present and are linked through a bridging oxygen atom (*O<sub>bridge</sub>*), while each metal cation is coordinated by a TPA ligand and a water molecule. Three distinct bond lengths (Fe-N<sub>TPA</sub>, Fe-O<sub>wat</sub> and Fe-O<sub>bridge</sub>) were optimized in the minimization procedure, owing to the symmetry of the two Fe sites. Calculations of the XANES spectrum associated to the  $\mu$ -oxo dimeric species were performed by including scatterers within 5 Å, 6 Å and 7 Å of a given Fe cation, and it was found that scattering atoms outside a cut-off radius of 6 Å do not contribute significantly to the theoretical curve. Hydrogen atoms have not been included in each of the theoretical calculations. During all the minimization procedures, five nonstructural parameters have been optimized:  $E_0$ , the threshold energy,  $E_F$ , the Fermi energy level,  $E_s$  and  $A_s$ , the energy and amplitude of the plasmon, and  $\Gamma_{res}$ . The reliability of fit has been estimated using the residual function,  $R_{sq}$  [29, 30, 34].

## 11.3 Results and Discussion

Figure 11.2d presents the EDXAS spectra isolated through Equation (11.2) and assigned to complexes **1** (blue), **2** (red) and **3** (green). It is possible to identify the oxidation states of the spectral components by the relative energy positions of their main absorption edges. In fact, the spectrum assigned to the Fe<sup>II</sup> initial species possesses a first inflection point that lies at approximately 1 eV lower than those of the spectra assigned to the Fe<sup>III</sup> complexes, which are almost overlapping. Interestingly, the  $\mu$ -oxo dimeric Fe<sup>III</sup> complex shows a feature located at approximately 7113 eV, identifiable as a 1s→3d transition. This feature is not present in the spectrum of the Fe<sup>II</sup> complex and is very weak in that of the Fe<sup>III</sup>-OOH species. The proposed identification of the three Fe species is further supported by such observation. It is known, in fact, that high- and low- spin Fe<sup>III</sup> complexes in an octahedral geometry and  $\mu$ -oxo complexes show 1s→3d transitions, whereas these are very weak if visible in Fe<sup>II</sup> octahedral symmetric complexes [43].

In previous studies, the Fe<sup>III</sup>-OOH complex has been trapped at  $-40^\circ\text{C}$  and characterized through UV-Vis and numerous other spectroscopic techniques. It was shown through Electron Paramagnetic Resonance (EPR) that the intermediate is an  $S=1/2$  Fe<sup>III</sup> center, while resonance Raman identified vibrations assigned to the  $\nu(\text{Fe-O})$  and  $\nu(\text{O-O})$  modes [26, 27, 42]. The identification was strongly supported by the presence of a dominant peak at  $m/z$  478 with mass and isotope distribution pattern



consistent with that of  $[\text{Fe}^{III}(\text{TPA})(\text{OOH})\text{ClO}_4]^+$  through ESI mass spectrometry [42]. However, the mass-spectrometric analysis could not provide any insight into the identity of the sixth ligand of the intermediate, required to achieve its low-spin  $\text{Fe}^{III}$  state. Therefore, it was suggested that the sixth coordination site could be occupied by a solvent molecule such as  $\text{H}_2\text{O}$  or  $\text{CH}_3\text{CN}$  due to its high predisposition to dissociate [26, 42].

Looking at Fig. 11.2d one may note the similarity but not perfect equivalence between the extracted XANES spectra of the two  $\text{Fe}^{III}$  complexes. In particular, the shift of the XANES oscillations at about 7145 and 7170 eV toward lower energies in the spectrum of the dimeric product indicates an increase in the bond distance of some ligands [4]. Such evidence supports the notion that the chemical environments around the Fe atom in **2** and **3** are not the same.

In order to gain quantitative structural information regarding the three coordination complexes, a full MS analysis was carried out on their extracted spectral components. The XANES spectrum assigned to the  $\text{Fe}^{II}$  species shows evident differences if compared to those of the  $\text{Fe}^{III}$  complexes. A theoretical XANES spectrum has been calculated starting from the crystallographic structure of complex **1** [39]. As mentioned above, four nitrogen atoms of the TPA backbone, that were placed at the same  $\text{Fe}-\text{N}_{\text{TPA}}$  distance, and two nitrogen atoms belonging to the  $\text{CH}_3\text{CN}$  solvent molecules are the nearest neighbours of the metal cation. The  $\text{Fe}-\text{N}_{\text{TPA}}$  and  $\text{Fe}-\text{N}_{\text{ACN}}$  distances were refined along with the nonstructural parameters in order to obtain the best agreement with the experimental spectrum. The best fit result is shown in Fig. 11.3a together with the molecular cluster the calculation was based upon. The agreement between the theoretical spectrum and the isolated component is excellent and Table 11.1 reports the refined structural parameters. One may note that the  $\text{Fe}-\text{N}_{\text{TPA}}$  and the  $\text{Fe}-\text{N}_{\text{ACN}}$  bond lengths coincide with the same crystallographic distances within the statistical errors. The nonstructural parameters resulting from the minimization are reported in Table 11.2.

Conversely, the MXAN analysis of the  $\text{Fe(III)-OOH}$  complex has been carried out employing two distinct geometric models. In the former (**2a**) an acetonitrile ligand has been replaced by a hydroperoxyl group, while maintaining the remaining structure as that of complex **1**. In this structure, the  $\text{Fe}-\text{N}_{\text{ACN}}$ , the  $\text{Fe}-\text{N}_{\text{per}}$  and the  $\text{Fe}-\text{N}_{\text{TPA}}$  distances have been optimized independently. Figure 11.3b presents the results of the calculations and Table 11.1 contains the refined structural parameters. In this case as well there is a very good agreement between the experimental and theoretical spectra (with an  $R_{sq}$  value of 1.3), suggesting that a  $\text{CH}_3\text{CN}$  molecule coordinates the metal cation in the structure of the  $\text{Fe(III)-OOH}$  complex.

This hypothesis was further strengthened by performing a second minimization using a different starting structural model for the  $\text{Fe(III)-OOH}$  intermediate, where the two  $\text{CH}_3\text{CN}$  ligands were replaced by a hydroperoxyl group and a water molecule. In this case the  $\text{Fe}-\text{O}_{\text{per}}$ , the  $\text{Fe}-\text{O}_{\text{wat}}$  and the  $\text{Fe}-\text{N}_{\text{TPA}}$  bond lengths have been optimized. Tables 11.1 and 11.2, respectively, list the resulting best fit structural and nonstructural parameters, while Fig. 11.4 presents the comparison between the theoretical and isolated XANES spectra together with the corresponding molecular cluster. The theoretical curve based on this structure has a worse agreement with the

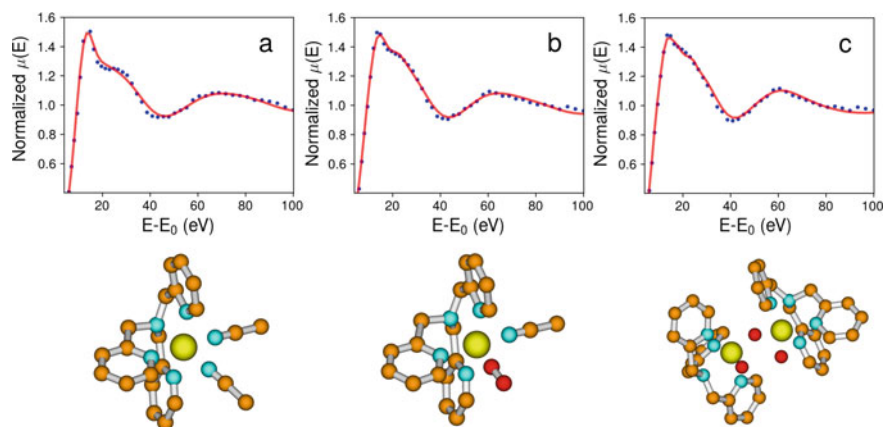


**Fig. 11.3** Fe K-edge XANES spectra (blue, dotted line) assigned to **1** (a), **2a** (b) and **3** (c) compared to the theoretical spectra (red, full line) calculated for optimized geometrical models. The best fit geometries are also shown, where the yellow, cyan, orange and red colors identify iron, nitrogen, carbon and oxygen atoms, respectively

**Table 11.1** Fe K-edge XANES structural parameters of **1**, **2a**, **2b** and **3** compared to literature X-ray crystallographic data reported for **1** and **3**.  $R_{Fe-N_{TPA}}$  and  $R_{Fe-N_{ACN}}$  are average distances between the metal cation and the TPA and solvent nitrogen atoms, respectively,  $R_{Fe-O_{per}}$  is the distance between the metal cation and the coordinating oxygen of the hydroperoxyl group in **2a** and **2b**,  $R_{Fe-O_{wat}}$  and  $R_{Fe-O_{bridge}}$  are the average distances between the metal cation and the water and bridging oxygen atoms in **3**, respectively. All distances are listed using Å as a unit

|   | $R_{Fe-N_{TPA}}$ | $R_{Fe-N_{ACN}}$ | $R_{Fe-O_{per}}$ | $R_{Fe-O_{wat}}$ | $R_{Fe-O_{bridge}}$ |
|---|------------------|------------------|------------------|------------------|---------------------|
| <b>1</b> <sup>a</sup> (crystallography) | 1.96(1)          | 1.92(1)          | –                | –                | –                   |
| <b>1</b> (this work)                    | 2.01(5)          | 1.96(5)          | –                | –                | –                   |
| <b>2a</b> (this work)                   | 2.08(5)          | 1.92(5)          | 1.92(5)          | –                | –                   |
| <b>2b</b> (this work)                   | 1.99(5)          | –                | 1.82(5)          | 2.10(5)          | –                   |
| <b>3</b> <sup>b</sup> (crystallography) | 2.18(1)          | –                | –                | 1.98(1)          | 1.80(1)             |
| <b>3</b> (this work)                    | 2.14(5)          | –                | –                | 1.96(5)          | 1.81(5)             |

<sup>a</sup>Ref. [41]

<sup>b</sup>Ref. [40]

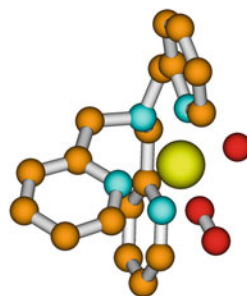
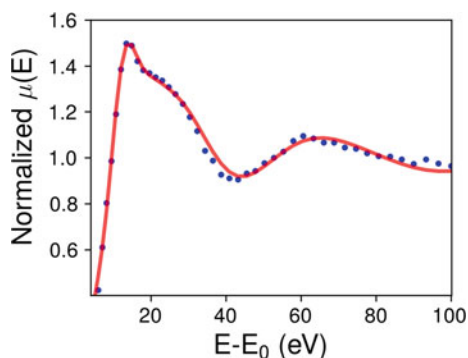
experimental spectrum ( $R_{sq}=1.8$ ), allowing one to suggest that the identity of the sixth ligand in the  $[\text{Fe}^{III}(\text{TPA})(\text{OOH})(\text{X})]^{2+}$  intermediate is  $\text{X} = \text{CH}_3\text{CN}$ .

The MS analysis of the Fe K-edge XANES spectrum assigned to complex Fe(III)-OH has provided structural insight for the elusive hydroperoxyl intermediate. In the intermediate  $\text{Fe}^{III}$  complex there is an expansion of the ligand cage around the Fe centre with an average  $\text{Fe-N}_{TPA}$  distance of 2.08(5) Å whereas the  $\text{Fe-N}_{ACN}$  and  $\text{Fe-O}_{per}$  average distances are 1.92(5) Å.

**Table 11.2** Nonstructural parameters obtained from the MXAN analysis of the Fe K-edge XANES spectra of **1**, **2a**, **2b** and **3**.  $E_0$  is the threshold energy,  $E_F$  is the Fermi energy level,  $E_s$  and  $A_s$  are the energy and amplitude of the plasmon,  $\Gamma_{res}$  is the experimental resolution,  $R_{sq}$  is the residual function

|           | $E_0(eV)$ | $E_F(eV)$ | $E_s(eV)$ | $A_s$ | $\Gamma_{res}(eV)$ | $R_{sq}$ |
|-----------|-----------|-----------|-----------|-------|--------------------|----------|
| <b>1</b>  | -4.1      | -1.1      | 15.8      | 13.7  | 2.0                | 1.4      |
| <b>2a</b> | -4.0      | -0.8      | 24.3      | 9.5   | 2.0                | 1.3      |
| <b>2b</b> | -4.0      | -4.0      | 15.7      | 9.8   | 1.7                | 1.8      |
| <b>3</b>  | -4.10     | -10.8     | 25.0      | 9.3   | 1.0                | 1.2      |

**Fig. 11.4** Fe K-edge XANES isolated spectrum relative to the  $[\text{Fe}^{III}(\text{TPA})(\text{X})(\text{OOH})]^{2+}$  complex (blue, dotted line) compared with the theoretical curve (red, full line) calculated for an optimized geometrical model where  $\text{X} = \text{H}_2\text{O}$ . The best fit geometry is also shown



Lastly, the analysis of the XANES spectrum belonging to complex **3** was performed starting from the crystal structure of the  $[\text{Fe}_2\text{O}(\text{5-Et-TPA})_2(\text{OH})-(\text{H}_2\text{O})]^{3+}$  dimer [40]. Throughout this calculation, the same coordination environment has been employed for the two  $\text{Fe}^{III}$  atoms present in the complex. It comprises the four nitrogen atoms of the TPA ligand, one water molecule and a bridging oxygen atom. The  $\text{Fe-N}_{\text{TPA}}$ ,  $\text{Fe-O}_{\text{wat}}$  and  $\text{Fe-O}_{\text{bridge}}$  bond lengths have been refined during the calculation, keeping the initial TPA structure fixed, and including all of the atoms within 6 Å of the metal cation. Figure 11.3c presents the results of this analysis where the experimental and theoretical spectra are shown together with the molecu-

lar cluster. One may note that the agreement between the two curves is excellent and that the structural results are equal to the crystallographic determinations within the statistical errors (Table 11.1).

This investigation demonstrates that coupled EDXAS/UV-Vis data relative to fast bimolecular reactions in solution may be employed to derive quantitative structural information on the chemical species involved in the process. In particular, the present study shows that UV-Vis spectroscopic information may be used as constraints to unambiguously extract the pure XANES spectra of the key reaction species from a set of time-resolved EDXAS data. This approach has enabled the geometrical characterization of an elusive intermediate such as the hydroperoxo complex  $\text{Fe}^{III}(\text{TPA})(\text{OOH})(\text{X})]^{2+}$ . The present work paves the way for the future application of advanced data analysis and theoretical techniques for the study of the mechanism of chemical reactions occurring in the millisecond time scale and for the structural assessment of their transient intermediates.

## References

1. M.B.B. Abdul Rahman, P.R. Bolton, J. Evans, A.J. Dent, I. Harvey, S. Diaz-Moreno, Application of stopped flow techniques and energy dispersive EXAFS for investigation of the reactions of transition metal complexes in solution: activation of nickel  $\beta$ -diketonates to form homogeneous catalysts, electron transfer reactions involving iron(III) and oxidative addition to iridium(I). *Faraday Discuss* **122**, 211–222 (2003). <https://doi.org/10.1039/B202833F>
2. G. Guilera, M.A. Newton, C. Polli, S. Pascarelli, M. Guino, K.K. Hii, In situ investigation of the oxidative addition in homogeneous Pd catalysts by synchronised time resolved UV-Vis/EXAFS. *Chem. Commun.* **41**, 4306–4308 (2006). <https://doi.org/10.1039/B606772G>
3. J.G. Mesu, A.M.J. van der Eerden, F.M.F. de Groot, B.M. Weckhuysen, Synchrotron radiation effects on catalytic systems as probed with a combined in-situ UV-Vis/XAFS spectroscopic setup. *J. Phys. Chem. B* **109**, 4042–4047 (2005). <https://doi.org/10.1021/jp045206r>
4. G. Olivo, A. Barbieri, V. Dantignana, F. Sessa, V. Migliorati, M. Monte, S. Pascarelli, T. Narayanan, O. Lanzalunga, S. Di Stefano, P. D'Angelo, Following a chemical reaction on the millisecond time scale by simultaneous X-ray and UV/Vis spectroscopy. *J. Phys. Chem. Lett.* **8**, 2958–2963 (2017). <https://doi.org/10.1021/acs.jpclett.7b01133>
5. G. Capocasa, F. Sessa, F. Tavani, M. Monte, G. Olivo, O. Lanzalunga Pascarelli, S. Di Stefano, P. D'Angelo, Coupled X-ray absorption/UV-vis monitoring of fast oxidation reactions involving a nonheme Iron-Oxo complex. *J. Am. Chem. Soc.* **141**, 2299–2304 (2019). <https://doi.org/10.1021/jacs.8b08687>
6. A. Martini, S.A. Guda, A.A. Guda, G. Smolentsev, A. Algasov, O. Usoltsev, M.A. Soldatov, A. Bugaev, Y. Rusalev, C. Lamberti, A.V. Soldatov, PyFitit: the software for quantitative analysis of XANES spectra using machine-learning algorithms. *Comput. Phys. Commun.* **107064** (2019). <https://doi.org/10.1016/j.cpc.2019.107064>
7. A.I. Frenkel, O. Kleinfeld, S.R. Wasserman, I. Sagi, Phase speciation by extended x-ray absorption fine structure spectroscopy. *J. Chem. Phys.* **116**, 9449–9456 (2002). <https://doi.org/10.1063/1.1473193>
8. A. Piovano, G. Agostini, A.I. Frenkel, T. Bertier, C. Prestipino, M. Ceretti, W. Paulus, C. Lamberti, Time resolved in situ XAFS study of the electrochemical oxygen intercalation in  $\text{SrFeO}_{2.5}$  brownmillerite structure: Comparison with the homologous  $\text{SrCoO}_{2.5}$  system. *J. Phys. Chem. C* **115**, 1311–1322 (2011). <https://doi.org/10.1021/jp107173b>

9. M. Fernandez-Garcia, C.M. Alvarez, G.L. Haller, XANES-TPR study of Cu-Pd bimetallic catalysts. Application of factor analysis. *J. Phys. Chem.* **99**, 12565–12569 (1995). <https://doi.org/10.1021/j100033a032>
10. J. Jaumot, A. De Juan, R. Tauler, MCR-ALS GUI 2.0: New features and applications. *Chemom. Intell. Lab. Syst.* **140**, 1–12 (2015). <https://doi.org/10.1016/j.chemolab.2014.10.003>
11. P. Conti, S. Zamponi, M. Giorgetti, M. Berrettoni, W.H. Smyrl, Multivariate curve resolution analysis for interpretation of dynamic Cu k-edge X-ray absorption spectroscopy spectra for a Cu doped V<sub>2</sub>O<sub>5</sub> lithium battery. *Anal. Chem.* **82**, 3629–3635 (2010). <https://doi.org/10.1021/ac902865h>
12. B.L. Caetano, V. Briois, S.H. Pulcinelli, F. Meneau, C.V. Santilli, Revisiting the ZnO Q-dot formation toward an integrated growth model: From coupled time resolved UV-Vis/SAXS/XAS data to multivariate analysis. *J. Phys. Chem. C* **121**, 886–895 (2017). <https://doi.org/10.1021/acs.jpcc.6b10062>
13. H.W.P. Carvalho, S.H. Pulcinelli, C.V. Santilli, F. Leroux, F. Meneau, V. Briois, XAS/WAXS time-resolved phase speciation of chlorine LDH thermal transformation: emerging roles of isoivalent metal substitution. *Chem. Mater.* **25**, 2855–2867 (2013). <https://doi.org/10.1021/cm401352t>
14. A. Martini, E. Alladio, E. Borfecchia, Determining Cu-speciation in the Cu-CHA zeolite atalyst: the potential of multivariate curve resolution analysis of in situ XAS data. *Top. Catal.* **61**, 1296–1407 (2018). <https://doi.org/10.1007/s11244-018-1036-9>
15. A. Rochet, B. Baubet, V. Moizan, E. Devers, A. Hugon, C. Pichon, E. Payen, V. Briois, Intermediate species revealed during sulfidation of bimetallic hydrotreating catalyst: a multivariate analysis of combined time-resolved spectroscopies. *J. Phys. Chem. C* **121**, 18544–18556 (2017). <https://doi.org/10.1021/acs.jpcc.7b03735>
16. A. Voronov, A. Urakawa, W. Van Beek, N.E. Tsakoumis, H. Emerich, M. Rønning, Multivariate curve resolution applied to in situ X-ray absorption spectroscopy data: An efficient tool for data processing and analysis. *Anal. Chim. Acta* **840**, 20–27 (2014). <https://doi.org/10.1016/j.aca.2014.06.050>
17. A. Martini, E. Borfecchia, K.A. Lomachenko, I.A. Pankin, C. Negri, G. Berlier, P. Beato, H. Falsig, S. Bordiga, C. Lamberti, Composition-driven Cu-speciation and reducibility in Cu-CHA zeolite catalysts: a multivariate XAS/FTIR approach to complexity. *Chem. Sci.* **8**, 6836–6851 (2017). <https://doi.org/10.1039/c7sc02266b>
18. W.H. Cassinelli, L. Martins, A.R. Passos, S.H. Pulcinelli, C.V. Santilli, A. Rochet, V. Briois, Multivariate curve resolution analysis applied to time-resolved synchrotron X-ray Absorption Spectroscopy monitoring of the activation of copper alumina catalyst. *Catal. Today* **229**, 114–122 (2014). <https://doi.org/10.1016/j.cattod.2013.10.077>
19. A. Rochet, B. Baubet, V. Moizan, C. Pichon, V. Briois, Co-K and Mo-K edges Quick-XAS study of the sulphidation properties of Mo/Al<sub>2</sub>O<sub>3</sub> and CoMo/Al<sub>2</sub>O<sub>3</sub> catalysts. *Comptes Rendus Chimie* **19**, 1337–1351 (2016). <https://doi.org/10.1016/j.crci.2016.01.009>
20. F. Tavani, M. Fracchia, N. Pianta, P. Ghigna, E. Quartarone, P. D'Angelo, Multivariate curve resolution analysis of operando XAS data for the investigation of the lithiation mechanisms in high entropy oxides. *Chem. Phys. Lett.* **760** (2020). <https://doi.org/10.1016/j.cplett.2020.137968>
21. C. Ruckebusch, L. Blanchet, Multivariate curve resolution: a review of advanced and tailored applications and challenges. *Anal. Chim. Acta* **765**, 28–36 (2013). <https://doi.org/10.1016/j.aca.2012.12.028>
22. A. Diebold, A. Elbouadili, K.S. Hagen, Crystal structures and solution behavior of paramagnetic divalent transition metal complexes (Fe, Co) of the sterically encumbered tridentate macrocycles 1,4,7-R<sub>3</sub>-1,4,7-triazacyclononane: coordination numbers 5 (R = i-Pr) and 6 (R = i-Bu). *Inorg. Chem.* **39**, 3915–3923 (2000). <https://doi.org/10.1021/ic000456h>
23. A. Diebold, K.S. Hagen, Iron(II) polyamine chemistry: variation of spin state and coordination number in solid state and solution with Iron(II) Tris(2-pyridylmethyl)amine complexes. *Inorg. Chem.* **37**, 215–223 (1998). <https://doi.org/10.1021/ic971105e>

24. S. Pascarelli, O. Mathon, T. Mairs, I. Kantor, G. Agostini, C. Strohm, S. Pasternak, F. Perrin, G. Berruyer, P. Chappellet, C. Clavel, M.C. Dominguez, The Time-resolved and Extreme-conditions XAS (TEXAS) facility at the European synchrotron radiation facility: the energy-dispersive X-ray absorption spectroscopy beamline ID24. *J. Synch. Rad.* **23**, 353–368 (2016). <https://doi.org/10.1107/S160057751501783X>
25. C. Kim, K. Chen, J. Kim, L. Que, Stereospecific alkane hydroxylation with H<sub>2</sub>O<sub>2</sub> catalyzed by an Iron(II)-Tris(2-pyridylmethyl)amine complex. *J. Am. Chem. Soc.* **119**, 5964–5965 (1997). <https://doi.org/10.1021/ja9642572>
26. K. Chen, M. Costas, J. Kim, A.K. Tipton, L. Que, Olefin Cis-dihydroxylation versus epoxidation by non-Heme Iron catalysts: two faces of an Fe<sup>III</sup>-OOH coin. *J. Am. Chem. Soc.* **124**, 3026–3035 (2002). <https://doi.org/10.1021/ja0120025>
27. A.M.P. Payeras, R.Y.N. Ho, M. Fujita, L. Que, The reaction of [Fe<sup>II</sup>(tpa)] with H<sub>2</sub>O<sub>2</sub> in acetonitrile and acetone-distinct intermediates and yet similar catalysis. *Chem. Eur. J.* **10**, 4944–4953 (2004). <https://doi.org/10.1002/chem.200400480>
28. Additional intermediates forming during the process, other than those shown in the reaction mechanism, were not considered in this investigation because of their labile nature
29. M. Benfatto, S. Della Longa, Geometrical fitting of experimental XANES spectra by a full multiple-scattering procedure. *J. Synchr. Rad.* **8**, 1087–1094 (2001). <https://doi.org/10.1107/S0909049501006422>
30. M. Benfatto, S. Della Longa, C.R. Natoli, The MXAN procedure: a new method for analysing the XANES spectra of metalloproteins to obtain structural quantitative information. *J. Synchr. Rad.* **10**, 51–57 (2003). <https://doi.org/10.1107/s0909049502018137>
31. F. Tavani, A. Martini, G. Capocasa, S. Di Stefano, O. Lanzalunga, P. D'Angelo, Direct mechanistic evidence for a nonheme complex reaction through a multivariate XAS analysis. *Inorg. Chem.* **59**, 9979–9989 (2020). <https://doi.org/10.1021/acs.inorgchem.0c01132>
32. F. Tavani, G. Capocasa, A. Martini, F. Sessa, S. Di Stefano, O. Lanzalunga, P. D'Angelo, Direct structural and mechanistic insights into fast bimolecular chemical reactions in solution through a coupled XAS/UV-Vis multivariate statistical analysis. *Dalton Trans.* **50**, 131–142 (2020). <https://doi.org/10.1039/D0DT03083J>
33. F. Tavani, G. Capocasa, A. Martini, F. Sessa, S. Di Stefano, O. Lanzalunga, P. D'Angelo, Activation of C-H bonds by a nonheme iron(IV)-oxo complex: mechanistic evidence through a coupled EDXAS/UV-Vis multivariate analysis. *Phys. Chem. Chem. Phys.* **23**, 1188–1196 (2020). <https://doi.org/10.1039/D0CP04304D>
34. P. D'Angelo, A. Zitolo, G. Aquilanti, V. Migliorati, Using a combined theoretical and experimental approach to understand the structure and dynamics of imidazolium-based ionic liquids/water mixtures. 2. EXAFS Spectroscopy. *J. Phys. Chem. B* **117**, 12516–12524 (2013). <https://doi.org/10.1021/jp404868a>
35. E. Burattini, P. D'Angelo, A. Di Cicco, A. Filipponi, N.V. Pavel, Multiple scattering x-ray absorption analysis of simple brominated hydrocarbon molecules. *J. Phys. Chem.* **97**, 5486–5494 (1993). <https://doi.org/10.1021/j100123a007>
36. K. Hayakawa, K. Hatada, P. D'Angelo, S. Della Longa, C.R. Natoli, M. Benfatto, Full quantitative multiple-scattering analysis of X-ray absorption spectra: application to Potassium Hexacyanoferrat(II) and -(III) complexes. *J. Am. Chem. Soc.* **126**, 15618–15623 (2004). <https://doi.org/10.1021/ja045561v>
37. P. D'Angelo, M. Benfatto, Effect of multielectronic configurations on the XAFS analysis at the Fe K edge. *J. Phys. Chem. A* **108**, 4505–4514 (2004). <https://doi.org/10.1021/jp0499732>
38. P. D'Angelo, V. Migliorati, Solvation structure of Zn<sup>2+</sup> and Cu<sup>2+</sup> ions in acetonitrile: a combined EXAFS and XANES study. *J. Phys. Chem. B* **119**, 4061–4067 (2015). <https://doi.org/10.1021/acs.jpcc.5b01634>
39. Y. Zang, J. Kim, Y. Dong, E.C. Wilkinson, E.H. Appelman, L. Que, Models for nonheme iron intermediates: structural basis for tuning the spin states of Fe(TPA) complexes. *J. Am. Chem. Soc.* **119**, 4197–4205 (1997). <https://doi.org/10.1021/ja9638521>
40. Y. Dong, H. Fujii, M.P. Hendrich, R.A. Leising, G. Pan, C.R. Randall, E.C. Wilkinson, Y. Zang, L. Que, A high-valent nonheme Iron intermediate. Structure and properties of [Fe<sub>2</sub>(μ-

- O)<sub>2</sub>(5-Me-TPA)<sub>2</sub>](ClO<sub>4</sub>)<sub>3</sub>. *J. Am. Chem. Soc.* **117**, 2778–2792 (1995). <https://doi.org/10.1021/ja00115a013>
41. Y. Zang, J. Kim, Y. Dong, E.C. Wilkinson, E.H. Appelman, L. Que, Models for nonheme Iron intermediates: structural basis for tuning the spin states of Fe(TPA) complexes. *J. Am. Chem. Soc.* **119**, 4197–4205 (1997). <https://doi.org/10.1021/ja9638521>
  42. W.N. Oloo, L. Que, Bioinspired nonheme Iron catalysts for C-H and C=C bond oxidation: insights into the nature of the metal-based oxidants. *Acc. Chem. Res.* **48**, 2612–2621 (2015). <https://doi.org/10.1021/acs.accounts.5b00053>
  43. T.E. Westre, P. Kennepohl, J.G. DeWitt, B. Hedman, K.O. Hodgson, E.I. Solomon, A multiplet analysis of Fe K-edge 1s→3d pre-edge features in Iron complexes. *J. Am. Chem. Soc.* **119**(27), 6297–6314 (1997). <https://doi.org/10.1021/ja964352a>

# Chapter 12

## Structural Profile of a MgO/Co/MgO Trilayer Using Soft X-ray Resonant Magnetic Reflectivity



Ilaria Carlomagno , Adriano Verna , Thomas Forrest, and Carlo Meneghini 

**Abstract** The physical properties of nanostructured thin films and multilayers depend crucially on their interfaces. The precise knowledge of the interface morphology at the atomic scale is mandatory to reliably understand their macroscopic response. These details become even more critical when dealing with magnetic thin films as the finest structural and/or compositional local changes may affect the magnetic coupling and alter the macroscopic response. Soft X-ray Resonant Magnetic Reflectivity (SXRMR) is a suitable technique in this field, combining specific aspects of x-ray absorption and x-ray scattering processes to simultaneously obtain complementary structural and magnetic information on thin films and multilayers. Here, we present a case study on a MgO/Co/MgO trilayer in which the combined use of SXRMR, x-ray absorption spectroscopy and x-ray magnetic circular dichroism has allowed to reconstruct the elemental and magnetic depth profiles with sub-nanometric resolution and to distinguish fine compositional defects at the Co-on-MgO and MgO-on-Co interfaces.

### 12.1 Introduction

The magnetic response of nanometer-sized systems depends on their structure and morphology as well as on their chemical state and local composition [1]. In thin films and multilayers, interface effects play a dominant role and the overall magnetic response can be affected by fine details enclosed in few atomic layers [2]. The problem of studying buried regions lying at few nm beneath the surface is commonly addressed with X-rays probes such as X-Ray Reflectivity (XRR) and Grazing Incidence X-ray Diffraction (GIXD), routinely employed to assess the structure of thin films

---

Present address: of I. Carlomagno Elettra Sincrotrone Trieste.

---

I. Carlomagno (✉) · A. Verna · C. Meneghini  
Dipartimento di Scienze, Università Roma Tre, Rome, Italy  
e-mail: [ilaria.carlomagno@elettra.eu](mailto:ilaria.carlomagno@elettra.eu)

T. Forrest  
Diamond Light Source, Didcot, UK



and multilayers with atomic resolution [3]. The energetic range to perform such experiments is chosen far from the absorption edges, where the effects of absorption and consequent fluorescence emission are minimised.

Whenever the X-ray energy is close to an absorption edge, the rapid variation of the resonant scattering factors modifies the contrast for a specific element and provides the resonant diffraction, XRR, and GIXD techniques with elemental sensitivity [4, 5]. X-ray Magnetic Circular Dichroism (XMCD) is based on the absorption of circularly polarized x-rays at the L edges of magnetic elements which depends on the photon helicity and on the relative orientation of the radiation wavevector  $\mathbf{k}$  and of the magnetization vector  $\mathbf{M}$  [6, 7]. Combining this technique with the previous ones, results into a further degree of freedom providing element-selective magnetic details to scattering and absorption spectroscopy techniques. These properties are at the heart of Soft X-ray Resonant Magnetic Reflectivity (SXRMR).

SXRMR exploits the relatively large variation of the resonant and magnetic scattering factors close to the  $L_{2,3}$  absorption edges of  $nd$  elements. In this energy region, the real and imaginary parts of the anomalous corrections to the atomic scattering factors  $f_1 + if_2$  strongly depend on the x-ray energy and on the magnetic state of the investigated material. For this reason, SXRMR patterns collected varying the incident photon energies across the L edges with different magnetization directions provide element specific information about the atomic and magnetic structure of complex systems. A non-exhaustive list of magnetic materials investigated through SXRMR are 5d/3d and 4d/3d transition-metal bilayers with magnetism induced by proximity effect [8, 9], metallic multilayers [10, 11], exchange bias heterostructures [12–14], interface of complex transition-metal oxides [15–17], superconductor/ferromagnet interfaces [18]. With respect to the alternative and more traditional Polarized Neutron Reflectometry [19], SXRMR gives the opportunity to analyze separately the spin distribution of the different magnetic elements present in the same sample [12–14] but requires a spectroscopic determination of the optical properties.

The SXRMR puts together independent datasets collected in reflectivity, absorption, and magnetic dichroism experiments performed on the same sample, to impose severe constraints to the models used for data refinement, enhancing the accuracy and the sensitivity to weak structural and magnetic effects that may escape when these techniques are considered individually. In this work, SXRMR capabilities were employed to investigate the details of the atomic and magnetic structure of a MgO/Co/MgO trilayer. MgO/Co/MgO trilayers possess the highest known tunnel magnetoresistance (TMR) at room temperature and are ideal candidates for magnetic tunnel junctions (MTJs). However, the TMR experimentally obtained may be different from the theoretical predictions and even one order of magnitude smaller, calling for more accurate investigations to understand the detrimental factors. In particular, the MgO/Co interfaces are known to heavily affect the TMR and the magnetic anisotropy of the electrode and have recently stimulated a debate regarding the existence of a magnetic dead layer at the interface between MgO and the magnetic electrode [20–25]. At the interfaces, Co-O orbital hybridization and the formation of Co oxide phases might occur depending on the thickness of the Co and MgO layers and on the use of annealing treatments that can affect at the atomic scale some of the

structural properties of the interface, such as the roughness. These structural modifications were found to be associated with drastic changes in coercivity and easy axis direction, thus confirming the primary role played by the interface effects on the overall magnetic response of these systems. In such framework, the importance of assessing the structural and the magnetic properties across the interfaces represents a critical and fundamental issue.

Here, the compositional, structural and magnetic properties of a MgO/Co/MgO multilayer were investigated combining SXRMR, X-ray Absorption Spectroscopy (XAS), and XMCD, focussing in particular at the buried interfaces between MgO and Co. Detailed information regarding the chemical profile, the elemental coordination chemistry, and the magnetic profile of the system has been achieved. The thorough description we present includes thickness and roughness of each interface, oxidation states of Co, charge transfer effects at the MgO/Co interfaces, and Co oxidation/reduction processes. In addition, we were able to account for a structural asymmetry between the Co-on-MgO and MgO-on-Co interfaces affecting the shape of the magnetization profile which results significantly less sharp on the MgO-on-Co upper interface.

## 12.2 Experimental Procedure

The investigated MgO/Co/MgO trilayer was grown on a Si (111) substrate using a RF ion beam source (Veeco 3 cm rf-source) operating at 1 keV with Ar<sup>+</sup> ions [25]. The deposition rates were 2.3 nm min<sup>-1</sup> for MgO and 5.6 nm min<sup>-1</sup> for Co, respectively. Laboratory XRR was used to determine the thickness and roughness of the trilayer, resulting in a MgO(10 nm)/Co(10 nm)/MgO(10 nm) system.

SXRMR measurements were carried out at the I06-01 beamline (Diamond Light Source, UK). The sample was placed in a magnetic field of 0.1 T oriented along the film plane, for 5 min, at room temperature, under ambient pressure. Then, it was loaded into an UHV chamber of base pressure  $\simeq 10^{-9}$  mbar.

Three kinds of measurements were carried out using right (+) and left (-) handed x-ray circular polarizations: (i) XMCD, collecting the XAS signal across the L<sub>2,3</sub> Co edges, (ii) SXRMR, measuring the reflectivity in  $\theta - 2\theta$  geometry at fixed incident energies, and (iii) energy dependent reflectivity at fixed  $\theta - 2\theta$  angles (“energy scans” in the following).

XMCD measurements were carried out at the Co L<sub>2</sub> and L<sub>3</sub> edges, with an incidence angle  $\theta = 30^\circ$ . The XAS spectra, collected in Total Electron Yield (TEY), are shown in Fig. 12.1. The average ( $\bar{I} = (I_+ + I_-)/2$ ) and dichroic ( $\Delta I = I_+ - I_-$ ) signals are reported in the same plot as black and green lines, respectively.

In order to carry out resonant XRR in  $\theta$ - $2\theta$  geometry, four different photon energies were selected in the range of the Co L<sub>2,3</sub> edges shown in Fig. 12.1: far below the edge ( $E = 765$  eV), close to L<sub>3</sub> maximum (779.5 eV), close to the L<sub>2</sub> maximum (795 eV), and far above the edge (810 eV). The energy values close to the absorption maxima and far from them, enhance the Co scattering contrast.  $\theta$ - $2\theta$

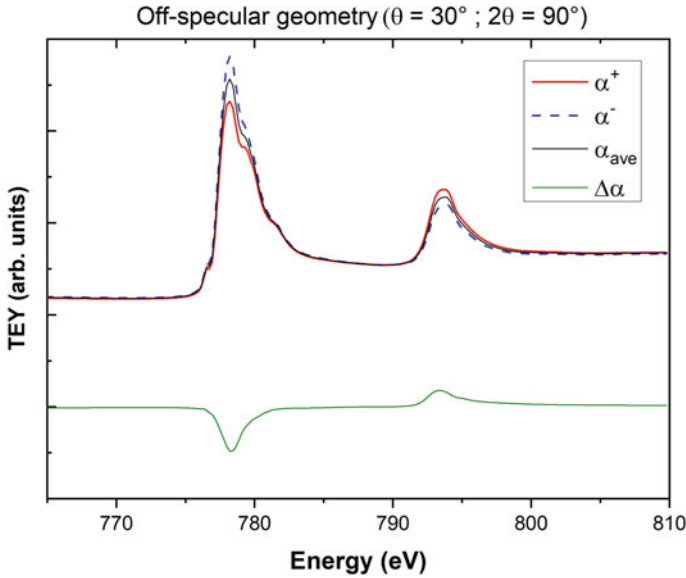


**Fig. 12.1** Absorption spectra collected in TEY around the Co  $L_{2,3}$  edges using right ( $\alpha^+$ , red solid line) and left ( $\alpha^-$ , blue dashed line) handed circular polarizations. The average signal (thin black line) is calculated as  $\bar{\alpha} = (\alpha^+ + \alpha^-)/2$ , the dichroic signal as  $\Delta\alpha = \alpha^+ - \alpha^-$

XRR measurements were carried out using left ( $I_-$ ) and right ( $I_+$ ) handed circularly polarized radiation. The sample was magnetized *ex-situ* with a field of about 0.1 T applied parallel to the sample surface. The measurements were consequently carried out with remanent magnetization parallel to the surface of the sample and contained in the scattering plane. The sample was kept at room temperature during the experiment. Data are shown in Fig. 12.2. The average signals  $(I_+ + I_-)/2$  and the asymmetry ratios  $\Delta I = (I_+ - I_-)/(I_+ + I_-)$  are also shown for the datasets collected at energies close to the Co  $L_{2,3}$  absorption edges (779.5 and 795.0 eV).

As expected, differences in the reflectance signal between the two polarizations are observed only when the photon energy matches the position of the absorption edge, i.e. when magnetic contribution to the scattering factors and the sensitivity to the local magnetic moment are maximized, such a difference reaches several tens of percents of the reflectance signal.

On the basis of the angular scans collected at the Co-L edges (779.5 eV and 795.0 eV scans in Fig. 12.2), we selected various incidence angles  $\theta$  in correspondence of which a large dichroic contrast was measured. For each of these selected angles  $\theta$ , energy scans in specular reflection across the Co  $L_{2,3}$  edges were collected reversing the x-ray beam polarization while simultaneously measuring the fluorescence signal at an emission angle  $\phi=90^\circ$ . Examples of the normalized reflectance from these energy scans  $\alpha = I_R/I_0$  are shown in Fig. 12.3. Noticeably, the shape of the

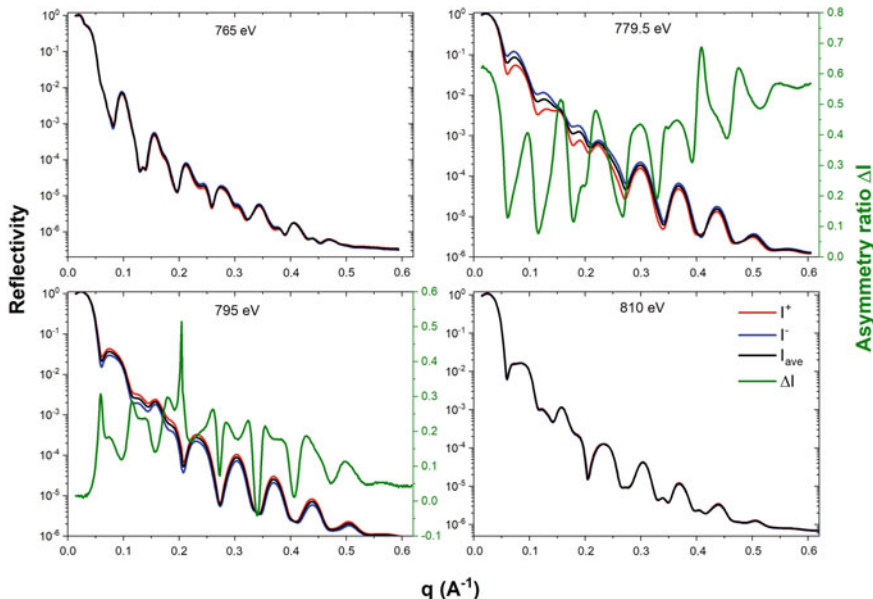


**Fig. 12.2**  $\theta$ - $2\theta$  XRR measurements collected at different photon energies for the two opposite circular polarizations. The reflectivity spectra are reported as a function of the exchanged momentum  $q = 4\pi/\lambda \cdot \sin \theta$ , where  $\lambda = c/\nu$  is the radiation wavelength. The asymmetry ratio, calculated as  $\Delta I = (I_+ - I_-)/(I_+ + I_-)$ , is shown only for the data collected at the L<sub>2</sub> and L<sub>3</sub> edges, which are those exhibiting a strong dichroic effect up to several tens of percents

reflected dichroic signal varies as a function of  $\theta$  grazing angle: these differences are related to the composition and magnetic structure of the multilayer and bring relevant information.

### 12.3 Data Analysis and Discussion

In transition metals, the white lines of the soft X-ray absorption spectra are largely affected by the coordination chemistry and the valence state of the absorber. For a given coordination and valence state, the white lines result from the contributions of complex multiplet components originating from the details of the crystal field around the absorber [26]. Despite the complex nature of the near edge region (XANES) the linear combination analysis (LCA) is a way to get accurate information about the composition in multiphase compounds [27, 28].

Here we reproduced the average TEY signal of Fig. 12.1 using a linear combination of reference absorption spectra relative to homogeneous systems with a single Co state. In this analysis, the magnetic contribution to the absorption coefficient was neglected. After the subtraction of the background (a linear pre-edge and a double

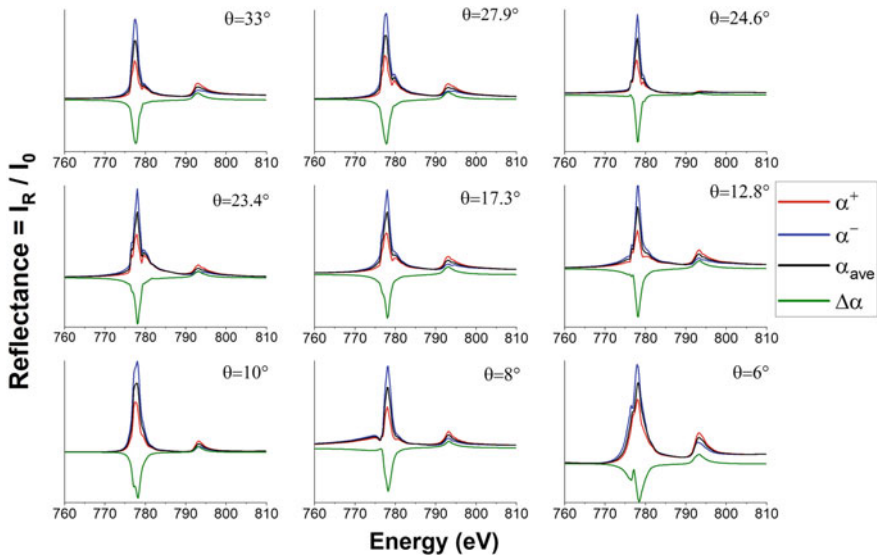
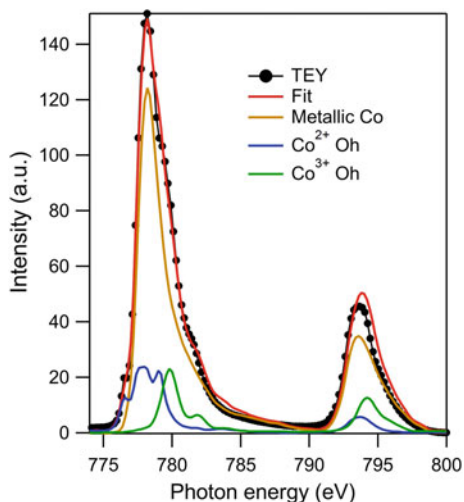


**Fig. 12.3** Energy scans across the Co  $L_{2,3}$  edges collected at selected  $\theta$  grazing angles in reflection geometry. The normalized reflectance signals  $\alpha = I_R/I_0$  recorded for right ( $\alpha^+$ , red) and left ( $\alpha^-$ , blue) handed polarizations are shown together with the average ( $\alpha_{ave}$ , black) and dichroic ( $\Delta\alpha$ , green line) signals

S-shaped function representing the transition to continuum states), the measured Co  $L_{2,3}$  edges resemble the typical absorption spectrum of metallic Co. However, comparing our experimental TEY data to the TEY reference spectrum of a pure Co foil (by Regan et al. [29]), a significant difference can be noticed in the high-energy region of the white line, suggesting the presence of oxidized Co component(s). Therefore, we carried out the LCA using three reference spectra: metallic  $\text{Co}^0$ , and oxidized  $\text{Co}^{2+}$  and  $\text{Co}^{3+}$ . For the metallic component we used the TEY spectrum by Regan et al. [29]. For the oxidized components, we had no experimental spectra, hence we considered the charge transfer multiplet (CTM) calculations reported by Morales et al. [30] for  $\text{Co}^{2+}$  and  $\text{Co}^{3+}$  ions in octahedral (Oh) coordination sites.

The presence of the  $\text{Co}^{2+}$  state alone, ascribable to the common CoO species, is not sufficient to explain the differences between our experimental TEY spectrum of the investigated multilayer and that of metallic Co, especially when it comes to the shoulder above the Co  $L_3$  white line. This feature requires a component having a maximum at higher energy, i.e.  $\text{Co}^{3+}$  in Oh symmetry must be used. The three reference spectra were normalized so that their integral is directly proportional to the number of 3d holes per atom,  $n_h$ . For the metallic phase, we consider  $n_h = 2.65$ , which is the average of the values 2.50 and 2.80 found by Stöhr and Siegmann from valence-band calculations with two different methods [31]. For  $\text{Co}^{2+}$  and  $\text{Co}^{3+}$ , we assumed 3 and 4 holes per atom, respectively. In Fig. 12.4, we show the experimental TEY spectrum after background subtraction together with the best fit obtained by the

**Fig. 12.4** Linear combination analysis of the average absorption spectrum reported in Fig. 12.1. The experimental spectrum (black circles) and the best fit (red line) are reported together with the three contribution used in the LCA



combination of the three components. The good agreement of the LCA supports the presence of oxidized Co phases. The relative concentrations obtained from LCA are 78(2) % for the metallic Co phase, 13(1)% for the  $\text{Co}^{2+}$  Oh state, and 9(1) % for the  $\text{Co}^{3+}$  Oh state. These values seem in contrast with previous results [25] and also with the SXRMR analysis. The apparent divergence is resolved taking into account the different surface sensitivity of TEY that may give systematic differences compared to the other techniques (see further discussion below). First of all, because TEY is a surface sensitive probe, having an average probing depth of 2–3 nm at the Co L edges [32], therefore it may not reflect the average composition of the whole Co film but only that of a limited region (see below for further details). In addition, the theoretical calculations we used for  $\text{Co}^{2+}$  and  $\text{Co}^{3+}$  assume an ideal coordination geometry that can differ from the actual situation due to distortions and defects [33, 34].

Aside from a precise quantification of the Co phases concentrations, the LCA indicates that: (i) most of the Co atoms are in metallic environment; (ii) a fraction of Co atoms is oxidized in a  $2^+/3^+$  mixed charge state ascribable to the formation of a  $\text{CoO}_x$  phase ( $x$  being the average Oxygen content in the oxidised Co) which is likely located at the interfaces with the MgO layers. Such information was relevant to tailor the trilayer model for the SXRMR analysis described below.

The average signals of the four angular scans in Fig. 12.2 were fitted simultaneously, using the ReMagX software [35]. The ReMagX code gives the possibility to fit the reflectivity patterns and the energy scans at the same time, refining the structural and magnetic parameters of the model that reproduces the investigated sample. The use of constraints among the fitting parameters improve the reliability of the model and enhances the sensitivity to weak structural and magnetic features.

As a first step, we took into account a model made up of three distinct and pure layers: MgO, Co, and MgO. The best fit, obtained by refining the thickness,  $t$ , and

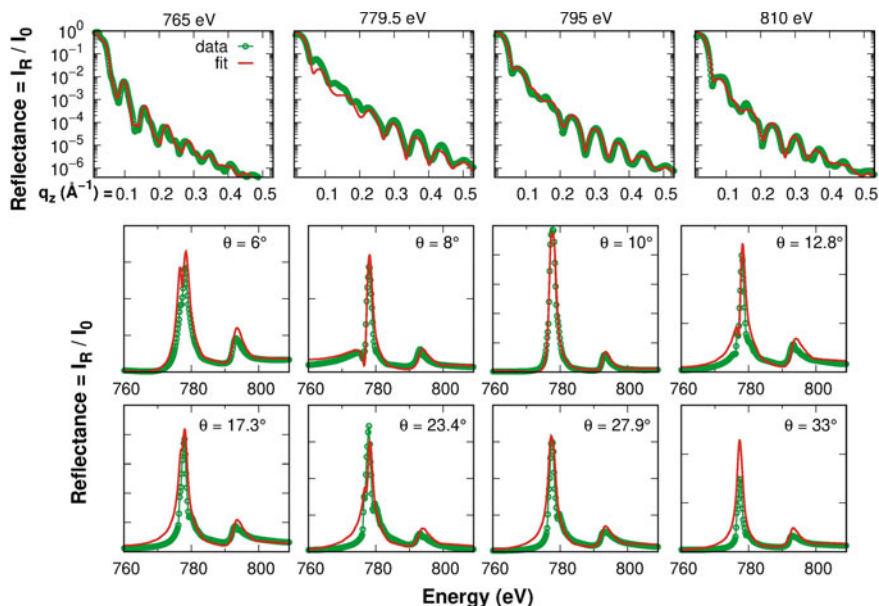


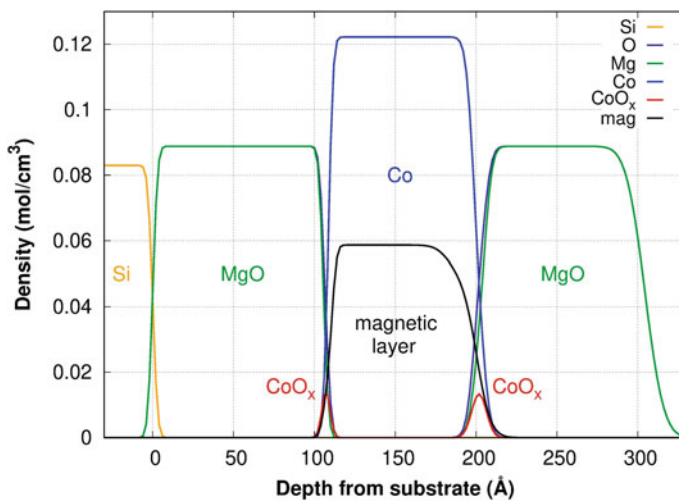
**Fig. 12.5** Experimental data (red) and best fit simulations (green) of the angular and energy scans performed in reflection geometry

the roughness,  $\sigma$ , of each layer, could not reproduce adequately the experimental observations, especially close to the resonance, suggesting a more complex structure. On the basis of the LCA results, the model was improved including two more layers accounting for the Co oxide phase, localized at the Co-on-MgO and MgO-on-Co interfaces. In this 5-layers model, the thickness  $t$ , roughness  $\sigma$ , and density  $\rho$  of each layer were refined. Once a good agreement was reached, the parameters were further refined in a second fitting procedure, involving not only the angular scans, but also the average signal from the energy scans at fixed  $\theta - 2\theta$  geometry in Fig. 12.3. The agreement between data and fits can be seen from Fig. 12.5, while the resulting structural parameters are reported in the left hand side of Table 12.1, and the depth profile is shown in the Fig. 12.6.

As anticipated above, the results in Table 12.1 seem to be in contrast with the oxidised Co fraction evaluated by LCA of the TEY spectrum. However, in order to reliably compare these results, the different penetration depths of the two techniques should be taken into account. Indeed, due to the mean free path  $\lambda$  of the electrons in the sample, the TEY intensity of a layer of thickness  $t$  is reduced by a factor:  $t/\lambda(1 - \exp(-t/\lambda))$ . In deeper layers a further  $\exp(-t/\lambda)$  reduction is required to account for the mean free path of photoelectrons through the  $t$  overlying layer. This is still an oversimplified model because the roughness of the layers makes the  $\text{CoO}_x$  buried into the metal layer (Fig. 12.6) so that the three layers cannot be strictly considered as a stack. Furthermore, the quite large roughness of  $\text{CoO}_x$  layers makes

**Table 12.1** Structural and magnetic parameters obtained from the best fit model. For the refined parameters uncertainties are reported in brackets

|                        | $t$<br>(Å) | $\sigma$<br>(Å) | $\rho$<br>$\left(\frac{\text{mol}}{\text{cm}^3}\right)$ | $t_M$<br>(Å) | $\sigma_M$<br>(Å) | $\rho_M$<br>$\left(\frac{\text{mol}}{\text{cm}^3}\right)$ |
|------------------------|------------|-----------------|---|--------------|-------------------|---|
| <b>MgO</b>             | 102.3 (5)  | 8.7 (2)         | 0.09 (2)  |              |                   |   |
| <b>CoO<sub>x</sub></b> | 0.7 (5)    | 3.3 (3)         | 0.05 (2)  | 0.1 (1)      | 6.9               | 0.09 (3)  |
| <b>Co</b>              | 93.1 (5)   | 3.3 (3)         | 0.13 (2)  | 85.9 (2)     | 6.9 (5)           | 0.06 (1)  |
| <b>CoO<sub>x</sub></b> | 2.7 (5)    | 2.5 (2)         | 0.03 (2)  | 5.3 (3)      | 2.3 (5)           | 0.02 (1)  |
| <b>MgO</b>             | 105.8 (5)  | 2.5             | 0.09  |              |                   |   |
| <b>Si(111)</b>         | –          | 2.4             | 0.08  |              |                   |   |

**Fig. 12.6** Density profile as a function of the distance from the Si(111) substrate of the model structure providing the best fit to experimental data

their effective thickness (i.e. their full width half maximum in Fig. 12.6) larger than the nominal  $t$  (Table 12.1). Standing these caveat, we evaluate the CoO<sub>x</sub> contribution to the TEY intensity on the basis of the SXRMR model assuming the thickness of CoO<sub>x</sub> at the MgO-on-Co interface around  $t + \sigma = 4\text{Å}$  (the bottom CoO<sub>x</sub> does not contribute significantly due to the overlying 9.3 nm-thick Co layer) obtaining about 15% of the CoO<sub>x</sub> contribution to the TEY signal, roughly in agreement with the experimental finding.

It is remarkable how our analysis, combining several independent datasets and exploiting the resonance effect, is sensitive to the thin interface layers at the Co-on-MgO and MgO-on-Co interfaces. Interestingly, such analysis allows one to appreciate structural differences between the Co-on-MgO and MgO-on-Co interfaces: the bottom Co-on-MgO appears sharper ( $\sigma = 2.5\text{Å}$ ) than the top MgO-on-Co ( $\sigma = 3.3\text{Å}$ ).



One has to keep in mind that the effective Co-oxide thickness results from the convolution of layer thickness  $t$  and interface roughness  $\sigma$ : despite lower CoO presents a larger  $t = 2.7 \text{ \AA}$ , the top CoO layer is indeed thicker (FWHM around 1 nm) resulting in a sharper transition of the Co-on-MgO interface, as shown in Fig. 12.6. As noticed above, the total Co-oxide layers resulting from the resonant reflectivity analysis represent only some percent of the total Co film and this seems in contrast with the LCA analysis (Fig. 12.4) showing about 20% of Co oxidized. However, considering that the surface sensitivity of TEY is  $2 \div 3 \text{ nm}$ , our results are consistent.

So far, we have discussed and analysed the average signals calculated from the two polarizations. This kind of data contains information on the structure of the sample but it is not sensitive to the magnetic nature of the system.

The magnetic sensitivity of SXRMR is related to the differences on the real ( $f_1$ ) and imaginary ( $f_2$ ) part of the anomalous corrections to the atomic scattering factors, as a function of the left(−) or right(+)-handed polarization direction with respect to the magnetic polarization at the Co site. This affects the x-ray absorption coefficient and reflected intensities. Therefore, the dichroic signals of the angular and energy scans contain element-selective information regarding the magnetic properties of the Co phases. To access this information, we started from the 5 layers model discussed above. The distribution of Co magnetic moments in the sample is given by the sum of the contribution of three distinct layers. The magnetic profile was obtained refining each magnetic layer thickness  $t_M$ , roughness  $\sigma_M$ , and density  $\rho_M$  until the simulated dichroic signals reproduced adequately the experimental reflectivity and fixed-angle energy scans. The parameters of the magnetic layer are reported in Table 12.1, on the right hand side. For sake of clarity, the magnetic depth profile of the best fit model is shown in Fig. 12.6 as a black line, together with the elemental profile represented by colored lines.

Interestingly, the different structure of the interfaces has an effect on the magnetic profile: it is evident how the bottom Co-on-MgO magnetic interface is quite sharper compared to the top one MgO-on-Co. The density of the magnetic layer starts to decrease before that of the “structural” Co (compare the purple and the black curves in Fig. 12.6). On the contrary, this is not observed at the bottom interface. This finding may suggest the presence of a thin magnetic dead layer arising from the broader transition from Co to MgO giving rise to a gradual intermixing between the magnetic and not magnetic phases. Fitting procedures with a single magnetic layer revealed to be ineffective in providing a magnetization depth profile that satisfactorily reproduced the dichroic reflectivity measurements (asymmetry ratios). In particular, the top magnetic layer with a very large  $\sigma_M$  value can properly modulate the decrease of magnetization at the MgO-on-Co interface.

## 12.4 Conclusions

We presented the structural and magnetic characterization of a MgO/Co/MgO trilayer obtained by SXRMR, combining the analysis of XRR (resonant and non-resonant) with XANES and XMCD at the Co  $L_{2,3}$  edges.

By simultaneously fitting reflectivity, absorption and dichroic Co L edge signals, a detailed and reliable description of the MgO/Co/MgO multilayer morphology was achieved. This analysis not only assesses each of the three layer (MgO-Co-MgO) but it also separately describes the top (MgO-on-Co) from the bottom interface (Co-on-MgO) in terms of chemical (electron density and Co oxide content), structural, and magnetic details (layer thickness and roughness).

The contemporary fitting of independent datasets has allowed us to achieve a high sensitivity to fine details of Co distribution and magnetic response, pointing out the relevance of combined XRR, XAS, XMCD analysis for the accurate understanding of these multilayers. In particular, it has been possible to reveal an asymmetry between the Co-on-MgO and MgO-on-Co interfaces and individuate thin Co-oxides phases located between MgO and Co layers that may result elusive to conventional, single-technique analysis. The element-selective magnetic sensitivity of SXRMR provides a description of the magnetic layer in our trilayer, presenting the asymmetry of the magnetic profile across the Co layer.

**Acknowledgments** The authors wish to acknowledge Diamond Light Source for time on I06-1 under proposal SI1658 and Dr. H. Hussain for the support provided during the experiment.

## References

1. C. Silva, A. Vovk, R. da Silva, P. Strichonavec, P. Algarabel, A. Casaca, C. Meneghini, I. Carlomagno, M. Godinho, M. Cruz, Influence of the substrate on structure and magnetic properties of con thin films. *J. Alloys Compounds* **633**, 470–478 (2015)
2. I. Carlomagno, J. Drnec, A.M. Scaparro, S. Cicia, S. Vlaic, R. Felici, C. Meneghini, Co-Ir interface alloying induced by thermal annealing. *J. Appl. Phys.* **120**, 195302 (2016)
3. I. Carlomagno, J. Drnec, S. Vlaic, N. Vinogradov, F. Carl, H. Isern, C. Meneghini, R. Felici, Co film stretching induced by lattice mismatch and annealing: The role of graphene. *Appl. Surface Sci.* **432**, 22–26 (2018)
4. A. Gupta, A. Paul, M. Gupta, C. Meneghini, U. Pietsch, K. Mibu, A. Maddalena, S. To, G. Principi, Structural characterization of epitaxial fe/cr multilayers using anomalous x-ray and neutron reflectivity. *J. Magnetism Magnetic Mater.* **272–276**, 1219–1220 (2004)
5. P. Centomo, P. Canton, C. Burato, C. Meneghini, M. Zecca, Resonant-xrd characterization of nanoalloyed au-pd catalysts for the direct synthesis of  $H_2O_2$ : quantitative analysis of size dependent composition of the nanoparticles. *Appl. Sci.* **9** (2019)
6. P. Carra, B. Thole, M. Altarelli, X. Wang, X-ray circular dichroism and local magnetic fields. *Phys. Rev. Lett.* **70**, 694 (1993)
7. B. Thole, P. Carra, F. Sette, G. van der Laan, X-ray circular dichroism as a probe of orbital magnetization. *Phys. Rev. Lett.* **68**(12), 1943 (1992)
8. J. Geissler, E. Goering, M. Justen, F. Weigand, G. Schütz, J. Langer, D. Schmitz, H. Maletta, R. Mattheis, Pt magnetization profile in a Pt/Co bilayer studied by resonant magnetic x-ray reflectometry. *Phys. Rev. B* **65** (2001)








9. D.-O. Kim, K.M. Song, Y. Choi, B.-C. Min, J.-S. Kim, J.W. Chon, D.R. Lee, Asymmetric magnetic proximity effect in a Pd/Co/Pd trilayer system. *Sci. Rep.* **6**, 25391 (2016)
10. J.M. Tonnerre, L. Sève, D. Raoux, G. Soullié, B. Rodmacq, P. Wolfers, Soft X-ray resonant magnetic scattering from a magnetically coupled Ag /Ni multilayer. *Phys. Rev. Lett.* **75**, 740–743 (1995)
11. P. Jonnard, K. Le Guen, J.-M. Andrè, R. Delaunay, N. Mahne, S. Nannarone, A. Verna, Z.-S. Wang, J. T. Zhu, S.K. Zhou, Determination of the magnetization profile of Co/Mg periodic multilayers by magneto-optic Kerr effect and X-ray magnetic resonant reflectivity. *J. Phys. Conf. Ser.* **417**, 012025 (2013)
12. S. Brück, G. Schütz, E. Goering, X. Ji, K.M. Krishnan, Uncompensated moments in the MnPd/Fe exchange Bias System. *Phys. Rev. Lett.* **101**, 126402 (2008)
13. E. Blackburn, C. Sanchez-Hanke, S. Roy, D. J. Smith, J.-I. Hong, K.T. Chan, A.E. Berkowitz, S.K. Sinha, Pinned Co moments in a polycrystalline permalloy/CoO exchange-biased bilayer. *Phys. Rev. B* **78**, 180408 (2008)
14. J.M. Tonnerre, M. De Santis, S. Grenier, H.C.N. Tolentino, V. Langlais, E. Bontempi, M. García-Fernández, U. Staub, Depth magnetization profile of a perpendicular exchange coupled system by soft-X-ray resonant magnetic reflectivity. *Phys. Rev. Lett.* **100**, 157202 (2008)
15. J.W. Freeland, K.E. Gray, L. Ozyuzer, P. Berghuis, E. Badica, J. Kavich, H. Zheng, J.F. Mitchell, Full bulk spin polarization and intrinsic tunnel barriers at the surface of layered manganites. *Nat. Mater.* **4**, 62–67 (2005)
16. A. Verna, B.A. Davidson, Y. Szeto, A.Y. Petrov, A. Mirone, G. Giglia, N. Mahne, S. Nannarone, Measuring magnetic profiles at manganite surfaces with monolayer resolution. *J. Magn. Magn. Mater.* **322**, 1212–1216 (2010)
17. S. Brück, M. Paul, H. Tian, A. Müller, D. Kufer, C. Praetorius, K. Fauth, P. Audehm, E. Goering, J. Verbeeck, G. Van Tendeloo, M. Sing, R. Claessen, Magnetic and electronic properties of the interface between half metallic Fe<sub>3</sub>O<sub>4</sub> and semiconducting ZnO. *Appl. Phys. Lett.* **100**, 081603 (2012)
18. S. Brück, S. Treiber, S. Macke, P. Audehm, G. Christiani, S. Solta, H.-U. Habermeier, E. Goering, J. Albrecht, The temperature-dependent magnetization profile across an epitaxial bilayer of ferromagnetic La<sub>2/3</sub>Ca<sub>1/3</sub>MnO<sub>3</sub> and superconducting YBa<sub>2</sub>Cu<sub>3</sub>O<sub>7δ</sub>. *New J. Phys.* **13**, 033023 (2011)
19. J.F. Ankner, G.P. Felcher, Polarized-neutron reflectometry. *J. Magn. Magn. Mater.* **200**, 741–754 (1999)
20. C. Tusche, H. Meyerheim, N. Jedrecy, G. Renaud, J. Kirschner, Growth sequence and interface formation in the Fe/MgO/Fe (001) tunnel junction analyzed by surface x-ray diffraction. *Phys. Rev. B* **74**, 195422 (2006)
21. S. Wang, G. Han, G. Yu, Y. Jiang, C. Wang, A. Kohn, R. Ward, Evidence for FeO formation at the Fe/MgO interface in epitaxial tmr structure by x-ray photoelectron spectroscopy. *J. Magnetism Magnetic Mater.* **310**, 1935–1936 (2007)
22. S. Döring, F. Schönbohm, U. Berges, R. Schreiber, D. E. Bürgler, C. M. Schneider, M. Gorgoi, F. Schäfers, C. Papp, B. Balke, et al., Hard x-ray photoemission using standing-wave excitation applied to the MgO/Fe interface. *Phys. Rev. B* **83**, 165444 (2011)
23. J.-W. Cai, S. Okamoto, O. Kitakami, Y. Shimada, Large coercivity and surface anisotropy in MgO/Co multilayer films. *Phys. Rev. B* **63**, 104418 (2001)
24. M. Sicot, S. Andrieu, F. Bertran, F. Fortuna, Electronic properties of Fe, Co, and Mn ultrathin films at the interface with MgO (001). *Phys. Rev. B* **72**, 144414 (2005)
25. P. Rajput, A. Singh, M. Kumar, M. Gupta, V. Reddy, N. Ramanan, S. Jha, D. Bhattacharyya, N. Sahoo, Investigation of local structural and magnetic properties of discontinuous to continuous layer of Co at Co/MgO interface in MgO/Co/MgO trilayer structure. *J. Alloys Compounds* **700**, 267–271 (2017)
26. F. de Groot, Multiplet effects in X-ray spectroscopy. *Coord. Chem. Rev.* **249**, 31–63 (2005)
27. M. Benfatto, C. Meneghini, A close look into the low energy region of the XAS spectra: the XANES region, in *Synchrotron Radiation*, ed. by S. Mobilio, F. Boscherini, C. Meneghini (Springer, Heidelberg, 2015)

28. T. Chakraborty, C. Meneghini, G. Aquilanti, R.S., Investigating the development of spurious magnetism in single crystalline  $\text{BaTi}_{0.95}\text{Fe}_{0.05}\text{O}_3$  with high  $\delta$  by local structural probes. *J. Phys.: Condens. Matter* **26**, 196001 (2014)
29. T.J. Regan, H. Ohldag, C. Stamm, F. Nolting, J.Lüning, J. Stöhr, R.L. White, Chemical effects at metal/oxide interfaces studied by x-ray-absorption spectroscopy. *Phys. Rev. B* **64**, 214422 (Nov 2001)
30. F. Morales, F.M.F. de Groot, P. Glatzel, E. Kleimenov, H. Bluhm, M. Hävecker, A. Knop-Gericke, B.M. Weckhuysen, In Situ X-ray absorption of Co/Mn/TiO<sub>2</sub> catalysts for Fischer-Tropsch synthesis. *J. Phys. Chem. B* **108**, 16201–16207 (2004)
31. J. Stöhr, H.C. Siegmann, *Magnetism: From Fundamentals to Nanoscale Dynamics*, vol. 152 of Springer Series in Solid-State Sciences (Springer, Heidelberg, 2006)
32. R. Nakajima, J. Stohr, Y. Idzerda, Electron-yield saturation effects in l-edge x-ray magnetic circular dichroism spectra of Fe, Co, and Ni. *Phys. Rev. B* **59**, 6421 (1999)
33. S.I. Csiszar, M.W. Haverkort, Z. Hu, A. Tanaka, H.H. Hsieh, H.-J.Lin, C. T.Chen, T. Hibma, L.H. Tjeng, Controlling orbital moment and spin orientation in CoO layers by strain. *Phys. Rev. Lett.* **95**, 187205 (2005)
34. M.W. Haverkort, *Spin and orbital degrees of freedom in transition metal oxides and oxide thin films studied by soft x-ray absorption spectroscopy*. PhD thesis, Universität zu Köln (2005)
35. S. Macke, A. Radi, J.E. Hamann-Borrero, A. Verna, M. Bluschke, S. Brück, E. Goering, R. Sutarto, F. He, G. Cristiani, M. Wu, E. Benckiser, H.-U. Habermeyer, G. Logvenov, N. Gauquelin, G.A. Botton, A.P. Kájdós, S. Stemmer, G.A. Sawatzky, M.W. Haverkort, B. Keimer, V. Hinkov, Element specific monolayer depth profiling. *Adv. Mater.* **26**, 6554–6559 (2014)

# Chapter 13

## Metal Coordination Core in Copper(II) Complexes Investigated by XAFS



Irene Schiesaro , Iole Venditti , Maura Pelli , Carlo Santini ,  
Luca Bagnarelli, Giovanna Iucci , Chiara Battocchio ,  
and Carlo Meneghini 

**Abstract** In recent years the biomedical research has focused on new metal-based anticancer drugs. Among them Cu-based antitumor agents are arising some attention based on the observation that endogenous metals appear to be less toxic toward normal cells with respect to cancer ones. Conjugating the Cu(II) complexes with hydrophilic gold nanoparticles (Au-NPs) appears a promising way, suitable to improve the complexes solubility and stability in water and to raise their bioavailability. In this context, we investigated the valence state and coordination chemistry of Cu for a selection of Cu-complexes suitable for grafting on Au-NPs. The Cu K-edge XAFS data were analysed in the near edge (XANES) and extended (EXAFS) regions to obtain preliminary characterization aimed at understanding local coordination chemistry and electronic structure of Cu.

### 13.1 Introduction

Copper coordination compounds are being explored as a valid alternative to Pt(II) coordination compounds for cancer therapies [1]. Copper is in fact an essential trace element in human organisms having a key role in numerous physiological cellular processes such as redox chemistry, growth and development and interestingly it appears more toxic for cancer cells respect to normal cells [2, 3]. Noticeably altered levels of Cu are associated with a disease state, allowing to distinguish healthy cells from malignant ones that can be targeted by anticancer agents. For these reasons coordination compounds are stimulating the research interest aimed at understanding and optimizing their anticancer activity [1–3]. The quest of suitable ligands for copper based anticancer agents has been focused on Cu(II) complexes of bis(pyrazol-1-yl)-acetate functionalized with biomolecules [4–6]. These compounds present low

---

I. Schiesaro (✉) · I. Venditti · G. Iucci · C. Battocchio · C. Meneghini  
Department of Science, University Roma Tre, Viale G. Marconi 446, Rome, Italy  
e-mail: [irene.schiesaro@uniroma3.it](mailto:irene.schiesaro@uniroma3.it)

M. Pelli · C. Santini · L. Bagnarelli  
School of Science and Technology, Chemistry Division, University of Camerino,  
Camerino, MC, Italy

solubility in water, but when conjugated with hydrophilic gold nanoparticles (AuNPs) they seem to overcome this problem as demonstrated by previous studies addressed at investigating the loading and release of different Cu-based antitumor complexes, giving promising results [7]. In particular the Cu(II) complexes assembled with AuNP demonstrated to allow for slow and controlled release of the carried drugs into the target cell. The deep knowledge of this system at the molecular scale, in particular in the region of active Cu(II) site, is crucial to understand the bio-chemical activity of the complexes and finely tailor the release mechanisms. The chemical selectivity and local order sensitivity of XAFS (X-Ray Absorption Fine Structure) technique is very suitable to this aim [8]. In this work the Cu(II) local coordination chemistry in different Cu-bis(pyrazol-1-yl)-acetate complexes has been characterized looking at the Cu K-edge XAFS (X-ray absorption fine structure) in the near edge (XANES) and extended (EXAFS) regions.

## 13.2 Materials and Methods

### 13.2.1 Experimental Procedure

Copper(II) complexes of bis(pyrazol-1-yl)acetate heteroscorpionate ligands studied in this work were synthesized in accordance with the procedure detailed in Refs [4, 5]. As general procedure, in a round-bottom flask, the ligands were dissolved in CH<sub>3</sub>CN; then a CH<sub>3</sub>CN solution of CuCl<sub>2</sub> · 2H<sub>2</sub>O was added and the resulting solutions were stirred at room temperature overnight. The chemical structures of Cu-complexes (a)-(f) are shown in Fig. 13.1.

The Cu K-edge ( $E_{Cu} = 8980$  eV) X-ray absorption spectroscopy (XAS) measurements were carried out in transmission geometry at room temperature, at the XAFS beamline of the Elettra synchrotron radiation facility (Trieste, Italy) [9]. The Cu-complexes dried powders were mixed with PVP inert matrix (approximately 1:5 weight ratio) and pressed in order to obtain suitable homogeneous pellets. The Incident ( $I_0$ ) and transmitted ( $I_t$ ) X-ray intensities were measured using ionization chambers and the XAS signal was calculated as  $\alpha = \ln(I_0/I_t)$ . A Cu metal foil was placed after the  $I_t$  ionization chamber, the transmitted intensity ( $I_2$ ) was measured and the  $\alpha_{ref} = \ln(I_t/I_2)$  signal was used for precise X-ray beam energy calibration. For each sample several (at least 3) scans were measured, checked for energy calibration and data averaged up in order to improve the data statistics.

### 13.2.2 Data Treatment and Analysis

The raw spectra  $\alpha(E)$  were treated along the standard procedures [10] for XAFS data analysis subtracting a linear pre-edge background and normalizing for the edge jump in order to calculate the normalized absorption signals  $\mu(E)$  shown in Fig. 13.2.

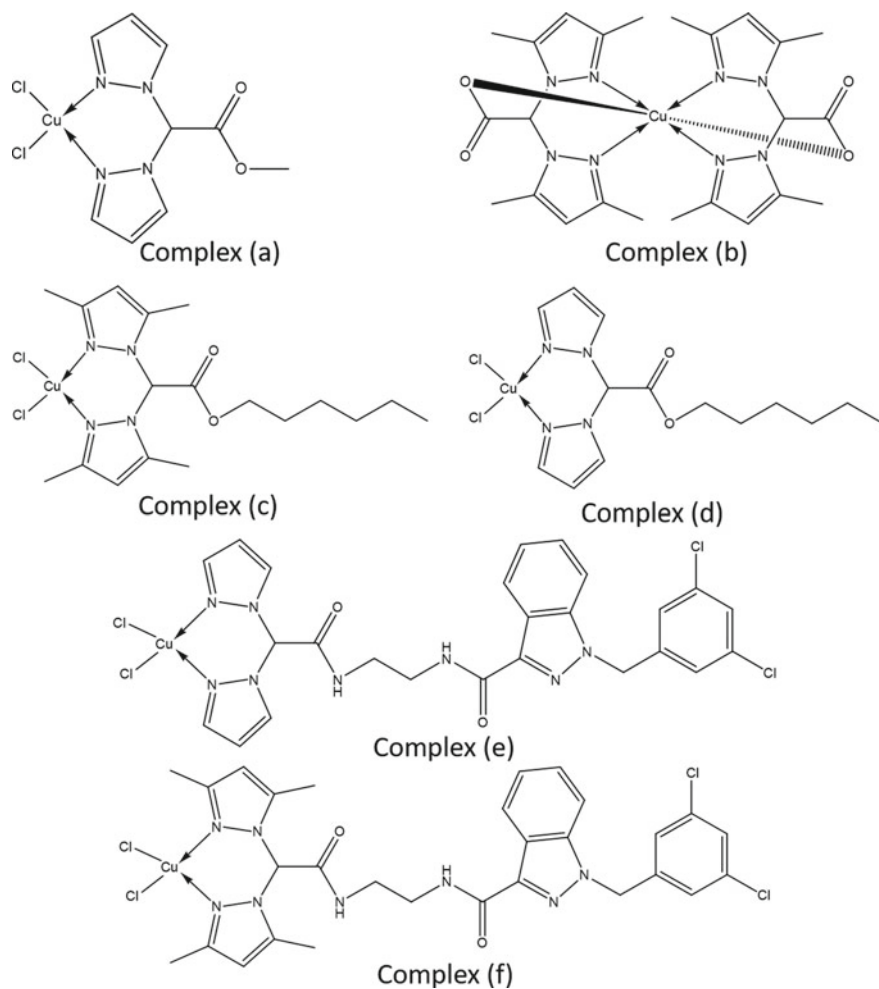


**Fig. 13.1** Structure of Copper(II) complexes (a–f)

The extended fine structural signal (EXAFS)  $\chi(k) = (\mu - \mu_o)/\mu_o$  has been calculated subtracting to the absorption signal  $\mu(E)$  the bare atom absorption background  $\mu_o(E)$  calculated as a polynomial spline through the normalized spectra. The origin of the photoelectron energy scale  $E_{Cu}$  that defines the photoelectron wavevector  $k = \sqrt{\frac{2m_e}{\hbar^2} (E - E_{Cu})}$  (being  $m_e$  the electron mass) was chosen at the maximum of the first derivative of  $\mu(E)$  and refined during the data fit.

The XANES features have been interpreted comparing the normalized experimental spectra  $\mu(E)$  of our complexes with the literature Cu XANES spectra of reference compounds [11]. Moreover, to better understand the local coordination geometry around Cu in our complexes we made ab-initio full multiple scattering (FMS)

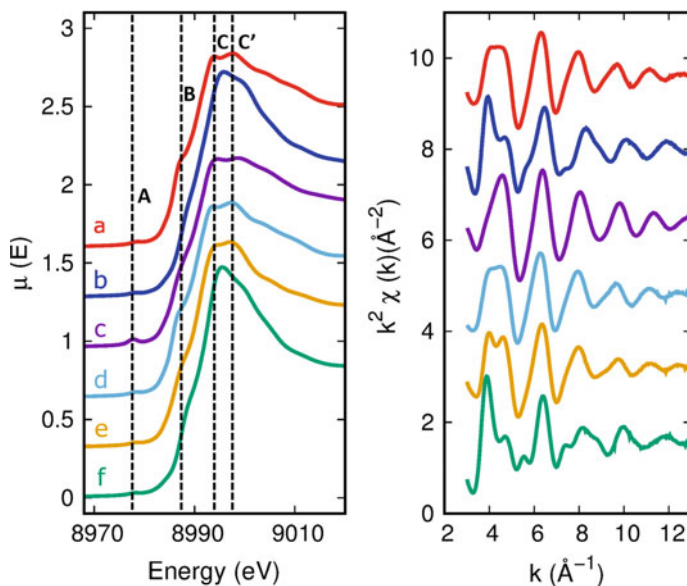


**Fig. 13.2** (Left) XANES region of the normalized absorption coefficient for all the samples investigated, vertically shifted for sake of comparison. The pre-edge peak at low energy A, the pre-edge shoulder B and the double peak C-C' are indicated. (Right) EXAFS oscillation in  $k$  space

XANES calculation for small Cu atomic clusters restricted to the nearest neighbour shells, using the FEFF 8.2 program [12] in order to relate the differences among the experimental XANES spectra on our complexes, to local structure distortions. The Hedin-Lundqvist model was used for the exchange-correlation potential [13] calculated in self consistent mode. It is important to point out here that in the last years Cu(II) coordination and ligand geometry in organic and hydrated complexes is a widely discussed question, which is still matter of debate (see Ref [14] and references therein), in which advanced methods for XAFS (XANES and EXAFS) data analysis [15–17] play a major role to understand the finest details of Cu-coordination geometry. In this work the very simple *nearest neighbour* models neglect the finest details coming from the far away next neighbour arrangement but allow to individuate the main features related to distortions in the local geometry while keeping calculation times shorter (few minutes in standard desktop PC) than those required in more extended clusters (that may reach several hours also on dedicated workstations) and can be used as starting models for more sophisticated calculations. The quantitative analysis in the extended (EXAFS) region of the spectra was carried out using the FITEXA program [10]. The data analysis has been carried out fitting the  $k^2$  weighted experimental spectra  $k^2\chi^{exp}(k)$ , to the model curve  $k^2\chi^{th}(k)$ , following a non linear least-square data refinement procedure in the reciprocal space, in the 3–15  $\text{\AA}^{-1}$   $k$ -range. The  $\chi^{th}$  curve was calculated as a sum of partial contributions (shells)  $\chi^{th} = \sum_i \chi_i^{th}$ , each  $\chi_i^{th}$  being calculated using the standard EXAFS model



function [18], assuming a Gaussian neighbour distribution characterized by three structural parameters being the average coordination distance  $R_i$ , the shell multiplicity  $N_i$  and the variance (mean-square relative displacement, MSRD)  $\sigma_i^2$ . We tried to apply the cumulant expansion model [8, 18] of the EXAFS function in order to take account of deviations from Gaussian distribution but we found this model does not improve the best fit quality while worsening the reliability of the fit due to a strong correlation between the parameters, in particular  $C_1$  (distance) and  $C_3$  (skewness) well above the 90 at %.

The theoretical amplitude, phase and mean free path functions required for the standard EXAFS formula were calculated using the FEFF 8.2 program [12].

### 13.3 XANES Results

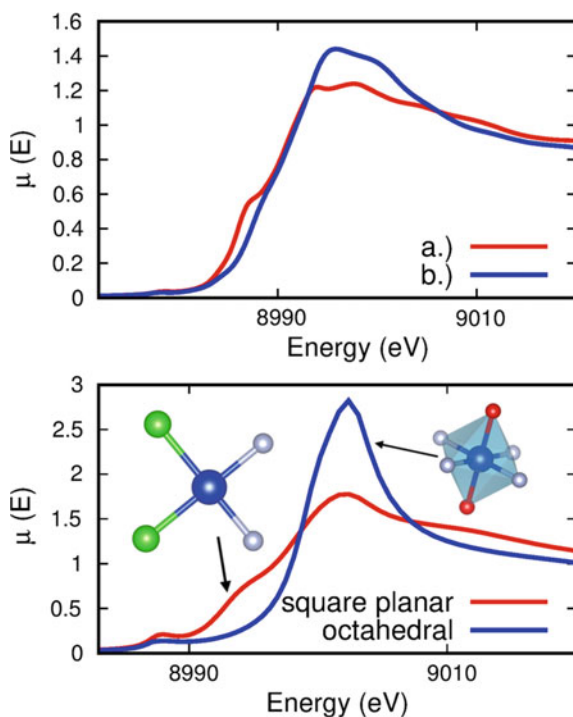
In Fig. 13.2 the XANES regions of the normalized absorption coefficient  $\mu(E)$  for all the investigated samples are reported. Similar features can be identified in all the spectra from complex (a) to complex (f): they present a weak pre-edge peak at low energy A (around 8980 eV), a pre-edge shoulder B and a double peak C-C' in the "white line" region.

The XANES features provide information about the oxidation state of the absorber and its local coordination geometry [8, 18]. In order to understand the local coordination geometry around Cu in these complexes a first qualitative interpretation of the XANES features has been made comparing the experimental data with the literature, in particular the large number of XANES spectra reported in Refs [11, 19]. Accordingly to the literature the main edge position and shape allow to identify valence state of Cu as 2+ in all the investigated complexes. In particular the pre-edge peak A and the shoulder B can be associated respectively to the transitions  $1s \rightarrow 3d$  [20] and  $1s \rightarrow 4p$  [19]. The transition  $1s \rightarrow 3d$  in fact is absent in Cu(I) because it is a  $d^{10}$  species and the orbitals are all occupied, moreover the  $1s \rightarrow 4p$  transition is more intense and at lower energy [21].

Differences can be noticed in the normalized XANES spectra. Complex (b) and complex (f) have the most intense C peak and weaker C', the shoulder B is the most intense in complex (a) spectrum and almost absent in complex (b) spectrum. Differences among the spectra of Cu in different complexes are also evident looking at the  $k^2$ -weighted EXAFS spectra reported in Fig. 13.2 especially in the region of the first main oscillation around  $4\text{--}5 \text{ \AA}^{-1}$ .

Comparison with literature data [11] also suggests copper four coordinated to glycine-like molecules in our complexes with roughly planar geometry, in particular for complexes (a), (c), (d) and (e). In order to obtain more details on local coordination geometry around Cu, we focused on the spectrum of complex (b) to understand if the differences in the region of the shoulder B could derive from different coordination geometry as the chemical structure in Fig. 13.1 suggests. In Fig. 13.3 the spectra

**Fig. 13.3** (Top) XANES spectra of complex (a) and complex (b). (Bottom) Results of the XANES simulation: complex (a) and complex (b) were modeled in a simplified way respectively in a square planar arrangement with 2 Cl and 2 N around Cu and in an octahedral arrangement with 4 N and 2  $\Omega$  around Cu



of complexes (a) and (b) are reported for sake of comparison highlighting that in complex (b) the pre-edge shoulder B disappears while the white-line is clearly higher than complex (a).

In order to understand the structural origin of such a difference we performed *ab-initio* XANES simulations for different local coordination geometries in a simplified model considering only the nearest neighbour coordination around the Cu absorber: respectively 2 Cl and 2 N arranged in a square planar geometry for complex (a), and 4 N and 2  $\Omega$  in a slightly elongated octahedral arrangement for complex (b) (the neighbour coordination distances were kept from the EXAFS analysis). In the bottom panel of Fig. 13.3 the XANES calculated from these models are reported: it is evident that the pre-edge shoulder B is associated to the planar structure while it is absent in the octahedral coordination geometry which, on the contrary, depicts higher white line in qualitative agreement with our experimental data.

In order to understand the coordination geometry of Cu in the different complexes another couple of samples was considered: complex (c) and complex (d) having very similar structure except for the methyl groups bonded to the pyrazole rings present only in the complex (c). As evident in Figs. 13.2 and 13.4 their Cu K-edge XANES behaves quite differently: the pre-edge shoulder B of complex (c) is less pronounced and also the shape of the main peak is broadened and less intense. Moreover, looking at the EXAFS oscillation in *k* space (Fig. 13.2) other differences are evident as the

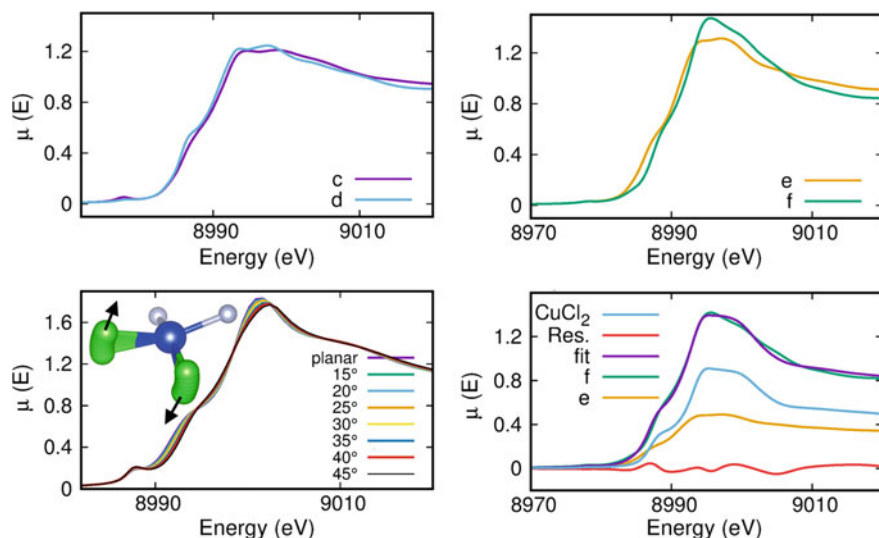


**Fig. 13.4** Panel (a) - XANES spectra of complex (c) and complex (d). Panel (b): Results of the XANES simulation: complex (c) and complex (d) were modeled considering 2 Cl and 2 N bounded to a central Cu in a planar configuration. The XANES curves were computed while the Cl atoms are tilted out of the Cu-2N plane at different angles (see the model on the top left of the figures). The tilt angles goes from planar configuration  $0^\circ$ , till  $45^\circ$  (black) tilt. As the two atoms of Cl progressively tilting going out of plane the main peak goes down and the pre-edge shoulder become less evident. Panel (c): XANES spectra of complex (e) and complex (f). Panel (d): Results of the linear combination fit for complex (f) obtained combining the experimental data for complex (e) and  $\text{CuCl}_2$ , the residual is shown in red

the intensity of the main oscillation at around  $4\text{\AA}^{-1}$  being weaker in complex (c). Also in this case we built a simple model for the Cu local coordination considering 2 Cl and 2 N bounded to a central Cu in a planar configuration. Then XANES spectra were calculated rotating the 2 Cl out of the Cu- $\text{N}_2$  plane so that the square planar structure progressively evolves toward a tetrahedral geometry. The evolution of the calculated XANES features as a function of tilt angle reveals an interesting behavior: as the two Cl atoms progressively tilt out of the Cu- $\text{N}_2$  plane, the main white line peak broadens and decreases, slightly shifting toward high energies. At the same time the pre-edge shoulder B becomes less pronounced and weaker. This behaviour closely resembles the difference observed comparing the experimental Cu K-edge XANES spectra of complex (c) and complex (d). This finding suggests the Cu in the complex (d) has a square planar coordination geometry, while Cu has a tilted square coordination in the complex (c). The two complexes just differ for the presence of the methyl groups bounded to the pyrazole rings in complex (c) absent in the complex (d). Therefore the distorted coordination is likely related to a steric effect induced by the methyl groups of the complex (c).

Finally also the XANES spectra of complex (e) and complex (f) appear largely different despite the quite similar chemical structure around the Cu site (Fig. 13.1).

In this case the steric effect due to the methyl groups bounded to the pyrazole rings in complex (f) does not seem enough to justify the observed differences between complex (e) and (f). In order to understand why such a difference we modeled the complex (f) as a linear combination of Cu bonded to complex (e) and  $\text{CuCl}_2$  XANES spectra (linear combination analysis, LCA). The good agreement of the LCA (Fig. 13.4) suggests that the complex (f) data may result from a mixture of Cu in different coordination environment: partially in complex (e) and partially still linked to chlorine in a separate phase, which likely originates from precursor reagents, suggesting some defect in the purification procedure.

## 13.4 EXAFS Results

The preliminary qualitative analysis of the XANES region, carried out comparing the experimental spectra to each other and with simple models ab-initio XANES calculations, provides relevant information about the Cu coordination geometry and sample purity. The analysis of the EXAFS region of the spectra allows to achieve further details about the average local atomic structure around the absorber in terms of neighbour coordination shells. In particular the interatomic distances are quantitative details we used to tailor the parameters for the XANES models. Moreover the analysis of the next neighbour contributions to the EXAFS signal can be used to validate the coordination model in this case of complex molecules [22–24].

The best fit results are shown in the reciprocal ( $k$ ) and real ( $R$ ) spaces for complex (c) in Fig. 13.5 for sake of example, along with the partial contributions used in the analysis to the model  $\chi^{th}(k)$  function. The first shell, that corresponds to the main peak of the FT (uncorrected for the phase shift), is assigned both to 2 atoms of Cl and 2 atoms of N bounded to the central Cu around 2 Å. In the analysis of complex (b) data we had to consider an octahedral coordination. Due to the very similar backscattering amplitude and phase shift functions for C, O and N we considered a single shell made by 4 N (or 6 N for the complex (b)) as the results do not change within the uncertainty using oxygen or carbon neighbour shells.

The second shell consists of the contribution coming from the Cu-N(2) bond at around 3 Å while the weak contribution visible around 4 Å in the Fourier transform is associated to the single (SS) and multiple scattering (MS) to C(2) atoms through N, in particular the MS contributions are relevant due to the almost aligned configuration. We applied the same model to all the samples with similar quality of the data, except for complex (f) that the XANES results suggests not properly purified.

In Table 13.1 the complete structural details resulting from the quantitative analysis of complex (c) and complex (d) EXAFS spectra are reported, including the next neighbour shells details. The complex (c) has shorter distances and less disorder with respect to complex (d), likely due to the steric constraints we recognized from the XANES analysis, making the complex (c) structure more rigid. For all the samples the structural parameters concerning the first two coordination shells are resumed in Table 13.2. The obtained interatomic distances of the complexes agree with the

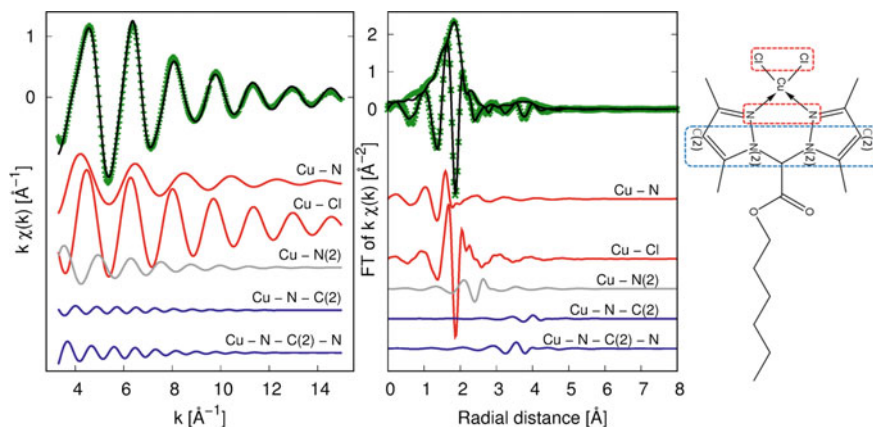


**Fig. 13.5** Cu K-edge EXAFS data fitting for complex (c): (left panel) experimental data (green crosses) and best fit (black line) are reported, together with the partial contributions, vertically shifted for sake of clarity. (right panel) The modulus ( $|FT|$ ) and imaginary part ( $Imm(FT)$ ) of the Fourier transforms of experimental (green crosses) and best fit (black lines) are shown, the  $Imm(FT)$  of the contributions used in the fit are also shown, vertically shifted for sake of clarity. The model molecule structure is shown on the right side, highlighting the neighbour shells used in the analysis

**Table 13.1** Best fit results for Cu K-Edge XAFS data analysis of complex (c) and complex (d)

|                   | Complex(c) |                                      | Complex(d) |                                      |
|-------------------|------------|--------------------------------------|------------|--------------------------------------|
|                   | R(Å)       | $\sigma^2 \cdot 10^{-2}(\text{Å}^2)$ | R(Å)       | $\sigma^2 \cdot 10^{-2}(\text{Å}^2)$ |
| Cu - N            | 1.948(5)   | 0.48(2)                              | 2.002(5)   | 0.52(3)                              |
| Cu - Cl           | 2.200(5)   | 0.29(1)                              | 2.256(5)   | 0.55(3)                              |
| Cu - N(2)         | 2.95(1)    | 0.93(5)                              | 2.96(1)    | 1.10(6)                              |
| Cu - N - C(2)     | 4.22(1)    | 0.91(5)                              | 4.68(1)    | 0.55(3)                              |
| Cu - N - C(2) - N | 4.57(1)    | 1.20(6)                              | 4.25(1)    | 0.95(5)                              |

**Table 13.2** Best fit results for Cu K-edge XAFS Data Analysis of samples from complex (a) to complex (e)

|             | Cu - N   |                                      | Cu - Cl  |                                      |
|-------------|----------|--------------------------------------|----------|--------------------------------------|
|             | R(Å)     | $\sigma^2 \cdot 10^{-2}(\text{Å}^2)$ | R(Å)     | $\sigma^2 \cdot 10^{-2}(\text{Å}^2)$ |
| Complex (a) | 1.961(5) | 0.48(2)                              | 2.224(5) | 0.41(3)                              |
| Complex (b) | 1.987(5) | 0.32(3)                              |          |                                      |
| Complex (c) | 1.948(5) | 0.48(2)                              | 2.200(5) | 0.29(1)                              |
| Complex (d) | 2.002(5) | 0.52(3)                              | 2.256(5) | 0.55(3)                              |
| Complex (e) | 1.956(5) | 0.39(2)                              | 2.222(5) | 0.52(3)                              |

values expected from the chemical structures. A comparison between complex (a) and complex (d) is relevant because they depict the very similar nearest neighbour structure around Cu but differ in the outermost shells (see Fig. 13.1). As it can be seen in Fig. 13.2 the XANES of the two complexes, depending solely on the local structure are very similar but the interatomic distances are greater in complex (d), this likely reflecting the interaction of the carbon tail with the inner shells around Cu.

## 13.5 Conclusion

We exploited Cu K-edge XAFS data analysis to probe in detail the local coordination geometry of Cu(II) bonded in complexes of bis(pyrazol-1-yl)-acetate heteroscorpionates.

The edge position confirmed the oxidation state Cu(II) in all the investigated samples. The analysis of XANES achieved comparing the experimental spectra among them and with *ab-initio* calculated XANES models has provided relevant details: complex (a) and complex (b) present respectively a planar and an octahedral geometry. Comparing the XANES shape of complex (c) and complex (d) revealed the deformation of Cu coordination geometry originating from the methyl groups bounded to the pyrazole rings in the molecule. Furthermore the linear combination analysis has highlighted purification defects in complex (f), indicating that LCA is an important tool for sample quality screening.

The quantitative analysis of the EXAFS region of the spectra allowed to explore the next neighbour shell coordination around copper and validate the Cu coordination in these complexes in accordance with that expected from the synthesis. Interestingly for complex (c) the steric hindrance of methyl groups induces a clear effect on the coordination mode squeezing the nearest neighbour coordination distances.

This analysis is an essential preliminary step toward a deep understanding of the Cu(II) complexes, mandatory for the next issue being the reliable and precise understanding of nanoassemblies obtained by conjugating Cu(II) coordination compounds to hydrophilic AuNPs surfaces.

## References

1. F. Tisato, C. Marzano, M. Porchia, M. Pellei, C. Santini, *Med. Res. Rev.* **30**, 708–749 (2010)
2. V. Gandin, M. Porchia, F. Tisato, A. Zanella, E. Severini, A. Dolmella, C. Marzano, *J. Med. Chem.* **56**, 7416–7430 (2013)
3. A. Hussain, M.F. AlAjmi, M.T. Rehman, S. Amir, F.M. Husain, A. Alsalmeh, M.A. Siddiqui, A.A. AlKhedhairi, R.A. Khan, *Sci. Rep.* **9**, 5237 (2019)
4. M. Pellei, V. Gandin, L. Marchiò, C. Marzano, L. Bagnarelli, C. Santini, *Molecules* **24**, 1761 (2019)
5. S. Gabrielli, M. Pellei, I. Venditti, I. Fratoddi, C. Battocchio, G. Iucci, I. Schiesaro, C. Meneghini, A. Palmieri, E. Marcantoni, L. Bagnarelli, R. Vallesi, C. Santini, *Dalton Trans.* **49**, 15622–15632 (2020). <https://doi.org/10.1039/D0DT02952A>

6. M. Pellei, V. Gandin, C. Cimarelli, W. Quaglia, N. Mosca, L. Bagnarelli, C. Marzano, C. Santini, J. Inorg. Biochem. **187**, 33–40 (2018)
7. I. Fratoddi, I. Venditti, C. Battocchio, L. Carlini, S. Amatori, M. Porchia, F. Tisato, F. Bondino, E. Magnano, M. Pellei, C. Santini, Nanomaterials **9**, 772 (2019)
8. G. Bunker, *Introduction to XAFS* (Cambridge University Press, Cambridge, UK, 2010)
9. A. Di Cicco, G. Aquilanti, M. Minicucci, E. Principi, N. Novello, A. Cognigni, L. Olivi, J. Phys.: Conf. Ser. **190**, 012043 (2009)
10. C. Meneghini, F. Bardelli, S. Mobilio, Nucl. Instrum. Methods B **285**, 153 (2012)
11. J. Chaboy, A. Muñoz-Páez, F. Carrera, P. Merkling, E. Sánchez Marcos, Phys. Rev. B **71**, 134208 (2005)
12. A.L. Ankudinov, B. Ravel, J. Rehr, S.D. Conradson, Phys. Rev. B. **58**, 7565 (1998)
13. L. Hedin, B.I. Lundqvist, J. Phys. C: Solid State Phys. **4**, 2064 (1971)
14. I. Persson, D. Lundberg, É.G. Bajnóczi, K. Klementiev, J. Just, C. Sigfridsson, G.V. Kajsas, Inorg. Chem. **59**, 9538–9550 (2020)
15. P. D'Angelo, E. Bottari, M.R. Festa, H.-F. Nolting, N.V. Pavel, J. Chem. Phys. **107**, 2807 (1997)
16. M. Benfatto, P. D' Angelo, S. Della Longa, N.V. Pavel, Phys. Rev. B: Condens. Matter Mater. Phys. **65**, 174205 (2002)
17. G. Marco, S. Tonelli, A. Zanelli, G. Aquilanti, M. Pellei, C. Santini, Polyhedron **48**, 174–180 (2012)
18. P. Fornasini, Introduction to X-ray absorption Spectroscopy; M. Benfatto, C. Meneghini, A close look into the Low Energy Region of the XAS spectra: The XANES Region; in Synchrotron Radiation, ed. by S. Mobilio, F. Boscherini, C. Meneghini (Springer, Heidelberg, 2015)
19. L. Kau, D.J. Spira-Solomon, J.E. Penner-Hahn, K.O. Hodgson, E.I. Solomon, J. Am. Chem. Soc. **109**, 6433–6442 (1987)
20. G. Aquilanti, M. Giorgetti, M. Minicucci, G. Papini, M. Pellei, M. Tegoni, A. Trasatti, C. Santini, Dalton Trans. **40**, 2764–2777 (2011)
21. M. Giorgetti, L. Guadagnini, S.G. Fiddy, C. Santini, M. Pellei, Polyhedron **28**, 3600–3606 (2009)
22. C. Meneghini, L. Leboffe, M. Bionducci, G. Fanali, M. Meli, G. Colombo, M. Fasano, P. Ascenzi, S. Mobilio, PloS One **9**, 8 (2014)
23. C. Meneghini, S. Morante, Biophys. J. **75**, 1953–1963 (1998)
24. C. Nicolafrancesco, F. Porcaro, I. Pis I3, S. Nappini, L. Simonelli, C. Marini, E. Frangipani, D. Visaggio, P. Visca, S. Mobilio, C. Meneghini, I. Fratoddi, G. Iucci, C. Battocchio, Inorg. Chem. **58**, 4935–4944 (2019)
25. V. Gandin, F. Tisato, A. Dolmella, M. Pellei, C. Santini, M. Giorgetti, C. Marzano, M. Porchia, J. Med. Chem. **57**(11), 4745–4760 (2014)
26. C. Battocchio, C. Meneghini, I. Fratoddi, I. Venditti, M.V. Russo, G. Aquilanti, C. Maurizio, F. Bondino, R. Matassa, M. Rossi, S. Mobilio, G. Polzonetti, J. Phys. Chem. C **116**, 19571–19578 (2012)

# Chapter 14

## Structural Fluctuations at Nanoscale in Complex Functional Materials



Gaetano Campi

**Abstract** Outstanding structure-function relationships of modern complex functional materials, are often due their dynamic heterogeneous structure and composition. These materials are characterized by weak competing interactions between structural units, giving rise to ultrastructure presenting different supramolecular configurations at nanoscale. The fluctuations between these different configurations play a central role in the understanding of both the basic properties of materials and their functionality. The visualization and the understanding of the dynamic fluctuations at nanoscale require experimental techniques suitable to provide appropriate spatial and temporal resolution, jointly to advanced modelling and statistical tools for data analysis. Examples of complex functional materials can be found in different fields ranging from material science to biology. Here we review connections between new geometries arising from structural fluctuations at nanoscale with the emerging macroscopic properties in some simple model systems in different fields.

### 14.1 Introduction

Modern Complex Functional Materials (CFMs) show composition and structure that vary over different length scale [1]. This inhomogeneity causes structural fluctuations at the nanoscale that play a fundamental role in the CFMs functionality.

CFMs can be found in different fields including colloids [2, 3], biomaterials [4], and strongly correlated materials [5]. Some example of CFMs are illustrated in Fig. 14.1a. Steel [6] and cement [7] are the most common materials with high environmental impact. Their mechanical and thermal properties are dramatically affected by the assembly and packing of structural units at micro and nanoscale. Inhomogeneous CFMs are typical of biology where membranes [8] and fibers [9] are the most important constituent of tissues and their structure at nanoscale fluctuates following specific physical principles to allow vital functions [10–12]. Scaling down at atomic

---

G. Campi (✉)  
Institute of Crystallography CNR, 00015 Monterotondo Rome, Italy  
e-mail: [gaetano.campi@ic.cnr.it](mailto:gaetano.campi@ic.cnr.it)



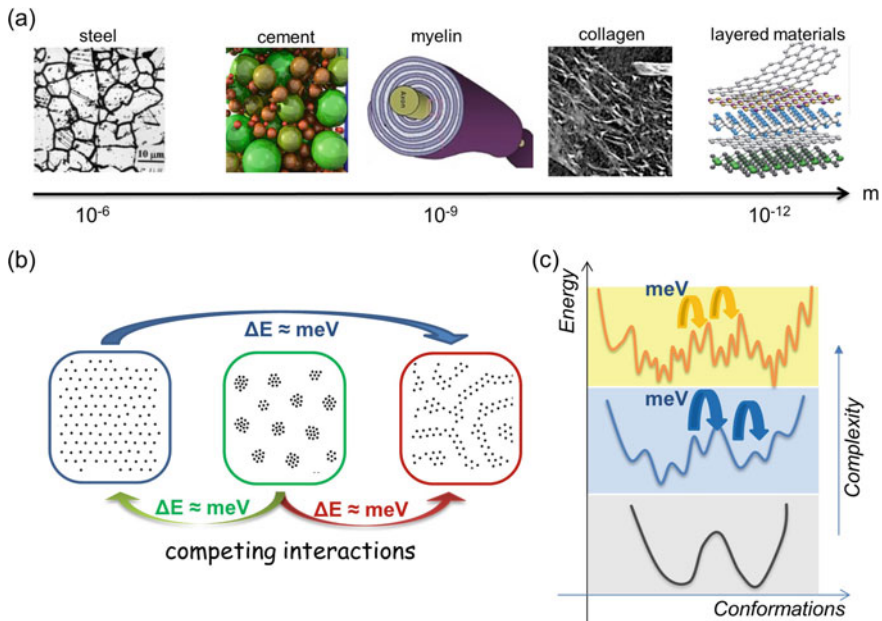


**Fig. 14.1** **a** Complex functional materials with structural packing at different length scale. **b** Pictorial view of different spatial patterns arising from different competing interactions. **c** Energy-conformational diagram. The different spatial patterns produce an energy landscape where the transitions between different conformations involve energy values down to few meV. The complexity increases with both increasing number of conformations and decreasing of differences between energy levels

level, electronic inhomogeneity is found in strongly correlated and quantum materials such as High  $T_c$  Superconductors (HTS), characterized by assembly of 2D like atomic structures with the formation of competing lattice, charge and spin conformational states [13–15]. The competition between different states with similar energies leads to the spontaneous formation of fluctuating supra-molecular conformations playing a central role in the understanding of both the basic properties of CFMs and their functionality, as represented in Fig. 14.1b. The transition between different spatial patterns associated to competing supramolecular configurations can occur at energy scale down to few meV. These energy values are typical of soft and biological matter (see Fig. 14.1c) but, as we'll describe here below can involve short range and weak competing interactions in the hard matter.

The visualization of fluctuating structural conformations (see Fig. 14.1c) requires high spatiotemporal resolution tools. At this aim we used a methodological approach based on the statistical physics applied to scanning synchrotron X-ray micro diffraction measurements.

In this paper we visualize fluctuations at nanoscale in a couple of significant cases studies belonging to different research fields. In Sect. 14.2 we describe this methodology. In Sect. 14.3.1 we apply this methodology to characterize the structural

fluctuations at nanoscale of myelin both in functional and in aged degraded state. In Sect. 14.3.2 we show structural fluctuations in a cuprate superconductor where electronic patches at nanoscale coexist with defect quenched disorder. Our findings show how structural fluctuations at nanoscale, affecting and determining the macroscopic functionality, are a general feature in the physics of complex matter.

## 14.2 Methods

### 14.2.1 Scanning X-ray Diffraction Measurements

The visualization of the structural dynamic fluctuations at nanoscale requires experimental techniques suitable to provide appropriate spatial resolution, jointly to advanced modelling and statistical tools for data analysis. A typical experimental space-resolved X-ray scattering setup in transmission and in reflection mode is shown in Fig. 14.2a, b respectively. It includes an in-vacuum undulator as primary source, an

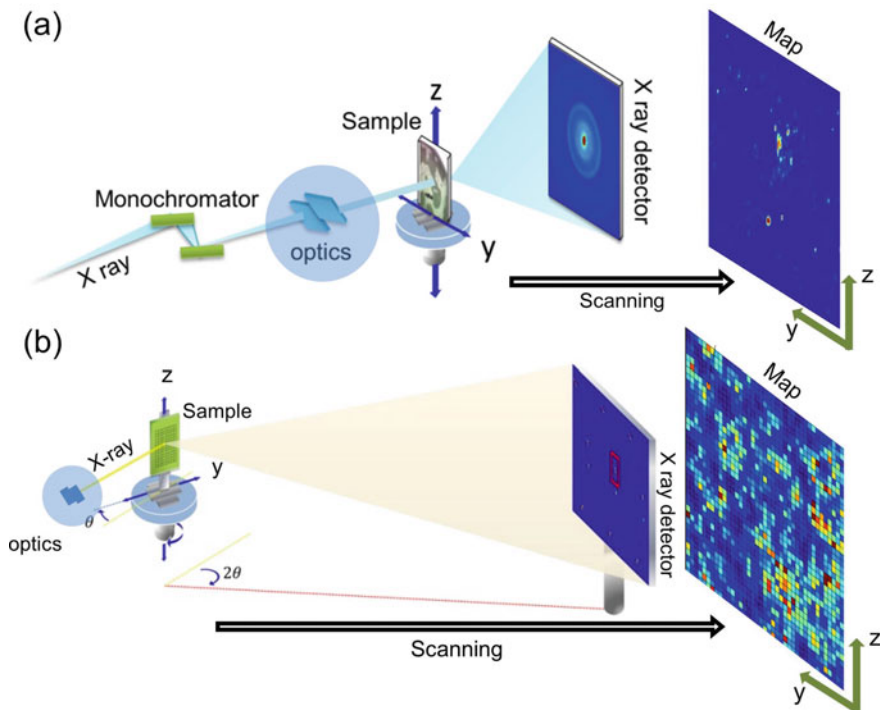


**Fig. 14.2** Schematic of experimental setup for space resolved scanning X-ray diffraction in **a** transmission and **b** reflection mode

monochromators for energy selection and focusing optics providing different beam spot sizes ranging from 50 nm to few microns.

The scanning micro X-ray diffraction measurements of HTS and myelin of frog's sciatic nerve were performed on the ID13 beamline of the European Synchrotron Radiation Facility, ESRF, France. The experimental methods were carried out in "accordance" with the approved guidelines. Adult female frogs (*Xenopus laevis*; 12 cm length, 180–200 g weight, *Xenopus express*, France) were housed and euthanized at the Grenoble Institute of Neurosciences with kind cooperation of Dr. Andre Popov. The local committee of Grenoble Institute of Neurosciences approved the animal experimental protocol. We used an X-ray beam of  $\lambda = 12.6$  keV focused on a  $1 \mu\text{m}^2$  spot. The sample holder allowed both horizontal (y) and vertical (z) translation stages with  $0.1 \mu\text{m}$  repeatability. A Fast Readout Low Noise (FReLoN) camera ( $1024 \times 1024$  pixels of  $100 \times 100 \mu\text{m}^2$ ) was used for data collection at room temperature. We chose an exposure time of 300 ms for minimizing the radiation damage and for keeping a good sensitivity at the same time. 2-D diffraction patterns with the expected arc-rings corresponding to the Bragg diffraction orders  $h = 2, 3, 4, 5$  were measured. The electron density profiles were extracted by diffraction intensities using Fourier analysis [11].

Diffraction measurements on  $\text{HgBa}_2\text{CuO}_{4+y}$  (Hg1201) single crystals were performed on the ID13 beamline at ESRF. We moved the sample under a  $1 \mu\text{m}^2$  focused beam with energy 13 keV using an x-y translator with step of  $1 \mu\text{m}$ , scanning a sample area of  $65 \times 80 \mu\text{m}^2$ , at 100 K.

## 14.2.2 Statistical Physics and Big-Data Sets Analysis

The large quantity of collected data have been analyzed by using a dedicated software written in Matlab [15]. It allows to select specific features of each single diffraction pattern and to analyze them to extract several parameters of interest, e.g. reflection width, intensity or position in reciprocal space. Once extracted, these parameters are used to build spatial maps analyzed by spatial statistical tools such as the probability density function, spatial correlation function, clustering degree, tessellation and percolation [15–17].

## 14.3 Results

### 14.3.1 Structural Fluctuations at Nanoscale and Correlated Disorder in Myelin

Myelin represents a simple and important example of biological ultrastructure. The scheme of its multilamellar ultrastructure, shown in Fig. 14.3a, is made of the stacking

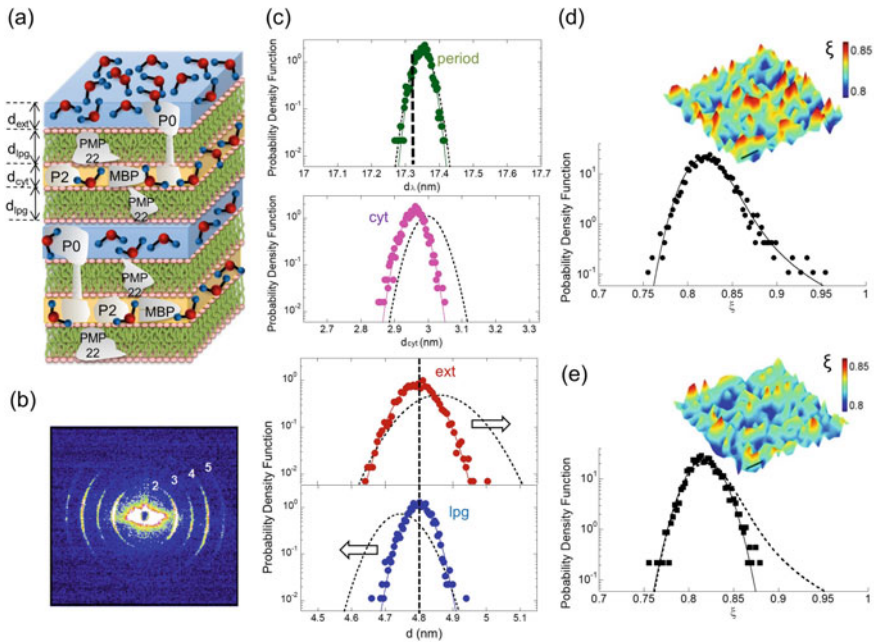


**Fig. 14.3** **a** Scheme of multilamellar structure of myelin. **b** Typical X-ray diffraction image of myelin with Bragg diffraction orders  $h = 2, 3, 4, 5$  corresponding to the concentric rings produced by the layered structure of the myelin. **c** Probability density function of myelin layers thicknesses representing the structural fluctuations of (full circles) aged nerve and (dotted lines) functional nerve. Probability Density Function and maps of conformational parameter,  $\xi$ , for the **d** functional and **e** aged state. We observe the presence of the “functional tail” characterizing the dynamic correlated disorder in the living nerve

of (i) cytoplasmatic (cyt), (ii) lipidic (lpg), (iii) extracellular (ext) and (iv) another lipidic (lpg) layer [18, 19]. The individual thickness of each layer named  $d_\lambda$ ,  $d_{cyt}$ ,  $d_{lpg}$ ,  $d_{ext}$ , measured in a  $1 \mu\text{m}^2$  spot area, has been extracted from electron density profiles computed by Fourier analysis of the diffraction patterns (see Fig. 14.3b), as described in details in Campi et al. [11].

The structural fluctuations in myelin have been investigated by calculating the Probability Density Function of the  $d_\lambda$ ,  $d_{cyt}$ ,  $d_{lpg}$ ,  $d_{ext}$  thicknesses in both the functional (dotted lines) and aged nerve (full circles), measured after 18 h from dissection (Fig. 14.3c).

Despite the stability of the period, the aged nerve is characterized by decreasing fluctuations and decreasing spatial correlations between fluctuations. Indeed, in the functional nerve, larger values of external membrane thickness,  $d_{ext}$ , are compensated by smaller values of lipidic thickness,  $d_{lpg}$ , as indicated by the arrows in the last two panels of Fig. 14.3c. This ability goes lost in the aged nerve, where fluctuations and their spatial correlations are reduced, as indicated by the probability functions.

These structural fluctuations and their spatial correlations can be quantified by introducing the conformational parameter,  $\xi$ , given by the ratio between hydrophilic and hydrophobic layers:

$$\xi = (d_{\text{ext}} + d_{\text{cyt}})/2d_{\text{lipg}} \quad (14.1)$$

Typical maps of  $\xi$  measured on a  $100 \times 100 \mu\text{m}^2$  ROI of a nerve in the functional living phase and in the aged resting phase are shown in the insets of Fig. 14.3d, e, respectively. The red spots represent areas where hydrophilic layers are larger, while in the blue spots they become smaller and the thickness of the hydrophobic layer increases.

The Probability Density Function of  $\xi$  in the living phase shows a skewed line shape modelled by using Levy stable distributions (see Fig. 14.3d). The Levy stable distribution provide a general statistical description of complex signals deviating from normal behavior [20]. On the other hand, in the aged phase, the structural fluctuations are frozen, losing the correlated disorder; here,  $\xi$  distribution changes to a Gaussian line shape function, which is peculiar of a static state approaching the thermodynamic equilibrium. This means that the aged system acquires rigidity and static order, losing correlated dynamic disorder that determines the functionality of living systems.

### ***14.3.2 Structural Fluctuations at Nanoscale and Non-euclidean Geometry in a Cuprate Superconductor***

High temperature superconducting perovskites are heterostructures at the atomic limit composed of active layers (copper oxide in the case of cuprates) sandwiched between rock-salt layers. The sample we studied is the layered perovskite  $\text{HgBa}_2\text{CuO}_{4+y}$  (Hg1201) with optimum doping ( $y = 0.12$ ), tetragonal symmetry (P4/mmm), lattice parameters  $a = b = 0.387480(5)$  nm,  $c = 0.95078(2)$  nm at  $T = 100$  K and superconducting temperature  $T_c = 95$  K. The layered atomic structure is composed of electronically active  $\text{CuO}_2$  planes intercalated with  $\text{HgO}_y$ -BaO layers. The X-ray diffraction measurements show diffuse streaks below the onset temperature  $T_{\text{O-i}} = 350$  K (see Fig. 14.4b) crossing the Bragg peaks due to oxygen interstitials (O-i) forming atomic stripes in the  $\text{HgO}_y$  layers [21, 22]. Alongside the oxygen ordering, the electronic modulations, namely charge density waves (CDW), have been identified by satellite peaks at  $q_{\text{CDW}} = 0.23\mathbf{a}^*, 0.16\mathbf{c}^*$  (where  $\mathbf{a}^*$ ,  $\mathbf{b}^*$  and  $\mathbf{c}^*$  are the reciprocal lattice units with  $\mathbf{b}^*=0$ ) around the (1 0 8) Bragg peaks, below the onset temperature  $T_{\text{CDW}} = 240$  K (see Fig. 14.4b) [14].

This shows how small changing in the energy landscape of the system, corresponding e.g. to few kelvin degrees, lead to different structural conformations. The

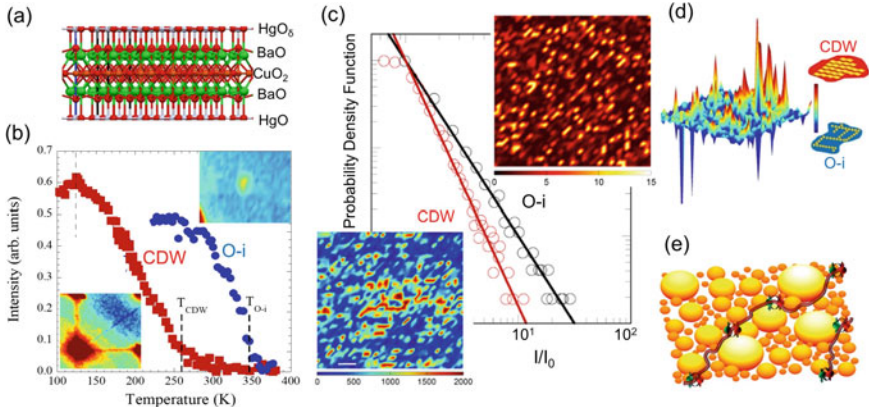


**Fig. 14.4** **a** Layered structure of Hg1201. **b** Temperature evolution of CDW peak and O-i diffuse streaks. The insets show the 2D diffraction images of both the CDW peak and the diffuse streaks of O-i. **c** Maps of normalized intensity of Charge Density Waves (CDW)-peak and O-i- streaks intensity. The scale bar corresponds to 5  $\mu\text{m}$ . Also shown are the probability density functions calculated from the O-i streaks and CDW intensity maps. **d** Difference map between CDW and O-i intensity showing the negative spatial correlation. The CDW puddles and O-i rich regions give rise to the positive (red) and negative (yellow) zones, respectively. **e** Picture of CDW puddles whose spatial arrangement gives rise to non-euclidean complex geometries

maps with Probability Density Functions of the normalized intensity of CDW peaks and oxygen O-i diffuse streaks at room temperature are shown in Fig. 14.4c.

Both maps clearly show spatial inhomogeneity described by the power-law behavior of the Probability Density Function of the normalized intensity  $x = I/I_0$

$$P(x) \sim Cx^{-\alpha} \quad (14.2)$$

with different critical exponent of  $\alpha = 1.8 \pm 0.1$  and  $\alpha = 2.2 \pm 0.1$  for the O-i and CDW, respectively. The other interesting feature is the spatial interplay between CDW rich regions and O-i rich regions. We find a negative spatial correlation between CDW peaks and O-i, as shown by the ‘difference map’ in Fig. 14.4d. The poor CDW regions on the  $\text{CuO}_2$  basal plane correspond to O-i rich regions on the  $\text{HgO}_y$  layers.

Thus, the CDW puddles introduce a topological change in the available space for the free electrons of Cooper pairs flowing in the interstitial space outside of CDW electronic patches that do not crystallize at low temperatures. In this landscape, shown in Fig. 14.4e, Cooper pairs can take different paths running in the interfacial space outside of the CDW puddles that cannot be topologically deformed one into the other. These paths create non-trivial geometries for electrons which can be mapped into a hyperbolic space for a system of nanodomains with power law distribution [23].

## 14.4 Conclusions

We have discussed the key role of structural fluctuations at nanoscale as a general feature in physics promoting functionality in out-of-equilibrium conditions in different materials. We considered here high-temperature Superconductors ( $\text{HgBa}_2\text{CuO}_{4+y}$ ) and myelin as simple model systems in the field of quantum materials and biological matter, respectively.

In the myelin the nanoscale ultrastructure is due to the stacking of membrane layers. The fluctuations of ultrastructure are characterized by the correlated dynamics of cytosolic and lipid biological membranes, following the Levy statistics and ensuring the physiological condition for the electrical transmission in nervous system. In cuprate high-temperature superconductors, nanoscale ultrastructure is formed by the stacking of  $\text{CuO}_2$  planes alternating with insulators layers. Here fluctuations of the ultrastructure give rise to phase separation with filamentary superconductivity developing in hyperbolic space.

These studies have been possible thanks to the new advanced features of the latest generation synchrotron sources. The different statistical physics found in these out-of-equilibrium systems tells us that the visualization of fluctuations can provide fundamental information about functionality in new advanced materials. These results open new venues in the double-handed issue pertaining both to technology, relative to the controlled fabrication of superconducting devices and to basic physics dealing with the formation and evolution of spatial patterns and quantum coherence at the nanoscale in inhomogeneous complex matter.

**Acknowledgements** The author thanks Alessandro Ricci, Nicola Poccia, Manfred Burghammer, Luisa Barba, Michael di Gioacchino, Stella Caporale, Michela Fratini and Antonio Bianconi for the long-standing precious collaboration.

## References

1. E. Longo, F.D.A. La Porta, Recent advances in complex functional materials, in *Recent Advances in Complex Functional Materials* (Springer International Publishing AG, Cham, 2017)
2. J.M. Brader, R. Evans, M. Schmidt, Statistical mechanics of inhomogeneous model colloid-polymer mixtures. *Mol. Phys.* **101**(23–24), 3349–3384 (2003)
3. G. Campi, A. Mari, H. Amenitsch, A. Pifferi, C. Cannas, L. Suber, Monitoring early stages of silver particle formation in a polymer solution by in situ and time resolved small angle X-ray scattering. *Nanoscale* **2**(11), 2447–2455 (2010)
4. A. Kaushik, M.A. Mujawar, K. Sharma, State-of art functional biomaterials for tissue engineering. *Front. Mater.* **6**, 172 (2019)
5. E. Morosan, D. Natelson, A.H. Nevidomskyy, Q. Si, Strongly correlated materials. *Adv. Mater.* **24**(36), 4896–4923 (2012)
6. T. Liu, M.J. Long, D.F. Chen, H.M. Duan, L.T. Gui, S. Yu et al., Effect of coarse TiN inclusions and microstructure on impact toughness fluctuation in Ti micro-alloyed steel. *J. Iron Steel Res. Int.* **25**(10), 1043–1053

7. S.A. Fennis, J.C. Walraven, Using particle packing technology for sustainable concrete mixture design. *Heron* **57**(2012), 2 (2012)
8. H. Lodish, A. Berk, S.L. Zipursky, P. Matsudaira, D. Baltimore, J. Darnell, *Molecular Cell Biology*, 4th edn. (National Center for Biotechnology Information, Bookshelf, 2000)
9. P.H. Cooke, F.S. Fay, Correlation between fiber length, ultrastructure, and the length-tension relationship of mammalian smooth muscle. *J. Cell Biol.* **52**(1), 105–116 (1972)
10. G. Campi, M. Fratini, I. Bukreeva, G. Ciasca, M. Burghammer, F. Brun et al., Imaging collagen packing dynamics during mineralization of engineered bone tissue. *Acta Biomater.* **23**, 309–316 (2015)
11. G. Campi, M. Di Gioacchino, N. Poccia, A. Ricci, M. Burghammer, G. Ciasca, A. Bianconi, Nanoscale correlated disorder in out-of-equilibrium myelin ultrastructure. *ACS Nano* **12**(1), 729–739 (2017)
12. G. Campi, F. Cristofaro, G. Pani, M. Fratini, B. Pascucci, P.A. Corsetto et al., Heterogeneous and self-organizing mineralization of bone matrix promoted by hydroxyapatite nanoparticles. *Nanoscale* **9**(44), 17274–17283 (2017)
13. G. Campi, N. Poccia, B. Joseph, A. Bianconi, S. Mishra, J. Lee et al., Direct visualization of spatial inhomogeneity of spin stripes order in  $\text{La}_{1.72}\text{Sr}_{0.28}\text{NiO}_4$ . *Condensed Matter* **4**(3), 77 (2019)
14. G. Campi, A. Bianconi, N. Poccia, G. Bianconi, L. Barba, G. Arrighetti et al., Inhomogeneity of charge-density-wave order and quenched disorder in a high-Tc superconductor. *Nature* **525**(7569), 359–362 (2015)
15. G. Campi, A. Bianconi, Evolution of complexity in out-of-equilibrium systems by time-resolved or space-resolved synchrotron radiation techniques. *Condensed Matter* **4**(1), 32 (2019)
16. I. Bukreeva, G. Campi, M. Fratini, R. Spanò, D. Bucci, G. Battaglia et al., Quantitative 3D investigation of neuronal network in mouse spinal cord model. *Sci. Rep.* **7**, 41054 (2017)
17. N. Poccia, M. Chorro, A. Ricci, W. Xu, A. Marcelli, G. Campi, A. Bianconi, Percolative superconductivity in  $\text{La}_2\text{CuO}_{4.06}$  by lattice granularity patterns with scanning micro x-ray absorption near edge structure. *Appl. Phys. Lett.* **104**(22), 221903 (2014)
18. R.L. Avila, B.R. Tevlin, J.P. Lees, H. Inouye, D.A. Kirschner, Myelin structure and composition in zebrafish. *Neurochem. Res.* **32**(2), 197–209 (2007)
19. M. Di Gioacchino, G. Campi, N. Poccia, A. Bianconi, Correlated disorder in myelinated axons orientational geometry and structure. *Condensed Matter* **2**, 29 (2017)
20. A.V. Chechkin, V.Y. Gonchar, J. Klafter, R. Metzler, Fundamentals of Lévy flight processes. *Adv. Chem. Phys.* **133**, 439–496 (2006)
21. M. Izquierdo, S. Megtert, D. Colson, V. Honkimäki, A. Forget, H. Raffy, R. Comès, One dimensional ordering of doping oxygen in  $\text{HgBa}_2\text{CuO}_{4+\delta}$  superconductors evidenced by X-ray diffuse scattering. *J. Phys. Chem. Solids* **72**(5), 545–548 (2011)
22. G. Campi, A. Ricci, N. Poccia, L. Barba, G. Arrighetti, M. Burghammer et al., Scanning micro-x-ray diffraction unveils the distribution of oxygen chain nanoscale puddles in  $\text{YBa}_2\text{Cu}_3\text{O}_{6.33}$ . *Phys. Rev. B* **87**(1), 014517 (2013)
23. G. Campi, A. Bianconi, High-temperature superconductivity in a hyperbolic geometry of complex matter from nanoscale to mesoscopic scale. *J. Supercond. Novel Magn.* **29**(3), 627–631 (2016)



# Chapter 15

## Structural Properties of Porous Silicon Nanowires: A Combined Characterization by Advanced Spectroscopic Techniques



Seyed Javad Rezvani, Yimin Mijiti, Federico Galdenzi, Luca Boarino, Roberto Gunnella, Augusto Marcelli, Nicola Pinto, and Andrea Di Cicco

**Abstract** Advanced characterization techniques including synchrotron radiation have been used to investigate the structural and electronic properties of doped silicon nanowires (NWs). Si L-edge, O K-edge and F K-edge XAS (x-ray absorption spectroscopy) spectra of silicon NWs at different doping levels have been collected at the BEAR beamline of the ELETTRA synchrotron radiation facility. XAS results show that the NWs structures are modified changing the type and level of doping and by the etching process. Optical Raman spectroscopy of NWs shows shifted and broadened first order optical mode, corresponding to a decrease in size of the crystallite domains inside the nanowires. The observed Raman shifts are compatible with the occurrence of a larger crystallite size in p-type NWs and smaller one in n-type NWs, in line with XAS results. Fabricated low-doped p-type NWs were also pressurized up to 24 GPa in a diamond anvil cell at room temperature and Raman scattering was recorded at selected pressures. The Si diamond crystal structure (dc-Si) is observed to persist up to  $\sim 22$  GPa, much higher than the phase transition onset ( $\sim 11$  GPa) occurring in bulk silicon in the same experiment.

---

S. J. Rezvani (✉) · Y. Mijiti · R. Gunnella · N. Pinto · A. Di Cicco  
School of science and technology, Physics division, University of Camerino,  
Via Madonna delle Carceri 9, 62032 Camerino, Italy  
e-mail: [sj.rezvani@unicam.it](mailto:sj.rezvani@unicam.it)

S. J. Rezvani · L. Boarino  
Advanced Materials Metrology and Life Science Division,  
INRiM (Istituto Nazionale di Ricerca Metrologica), 10135 Turin, Italy

S. J. Rezvani · F. Galdenzi · A. Marcelli  
INFN—Laboratori Nazionali di Frascati, Via Enrico Fermi 54, 00044 Frascati, RM, Italy

F. Galdenzi  
University of Roma Tre, Largo S. Leonardo Murialdo 1, 00146 Rome, Italy

A. Marcelli  
International Center for Material Science Superstripes, RICMASS,  
via dei Sabelli 119A, 00185 Rome, Italy

CNR - Istituto Struttura della Materia and Elettra-Sincrotrone Trieste, Basovizza Area Science Park, 34149 Trieste, Italy

© Springer Nature Switzerland AG 2021

A. Di Cicco et al. (eds.), *Synchrotron Radiation Science and Applications*,  
Springer Proceedings in Physics 220, [https://doi.org/10.1007/978-3-030-72005-6\\_15](https://doi.org/10.1007/978-3-030-72005-6_15)

## 15.1 Introduction

Nanoscale materials are known to have physico-chemical properties that differ from those of their bulk counterparts. In the recent years semiconducting nanowires (NWs) such as silicon NWs have been extensively investigated due to their unique chemical and physical properties that makes them perfect candidates for applications in nano-electronics, opto-electronics, solar cells and sensors exploiting their quantum confinement [1–3]. Porous silicon nanowires (PSNWs) have recently attracted a lot of attention because of their intense photoluminescence due to strong quantum confinement effects within pores.[1, 4]. However, the electronic transport properties of these semi-insulating materials reduce the electro-luminescence efficiency [5]. PSNWs can also be used in optics and electro-optics due to their unique properties such as tunable refractive index and high internal surface [6, 7]. However, the electronic properties of nanowires are strongly dependent on their surface and core structures which is dependent on the fabrication parameters.

Crystalline nanowires are usually synthesized in ultra high vacuum using vapor solid liquid [VLS] technique in a chemical vapor deposition or molecular beam epitaxy systems [8, 9]. On the other hand, the porous nanowires are usually fabricated by Metal Assisted catalytic Etching [MAcE] [10, 11]. While VLS method is rather costly and complicated, recent studies showed that single Ge crystalline wires could be synthesized with particular geometries by adatom flux dynamics modulation achieved via growth temperature [12, 13].

It is also shown that in the MAcE process, silicon nanowires with pre-designed structures can be engineered tuning the etching mechanism used and the substrate doping type and level [10, 14]. However, the structural and electronic properties of synthesized wires are neither completely investigated nor understood. For example, in doped germanium nanowires the conventional compensation occurs not by the addition of a substituting counter-dopant impurity inside the crystal lattice but due to the presence of the surface traps [9]. Furthermore, the occurrence of different silicon structures such as r8 or bc8, usually obtained under high pressure, could have strong impact on the properties of the nanowires. Thus, it is also interesting to study the structural transformations occurring in porous silicon nanowires at extreme conditions, as it is also discussed in recent works [15, 16].

Here, we characterize the structural and electronic properties of doped Si nanowires, synthesized by MAcE with different structures using X-ray absorption and Raman spectroscopy techniques. X-ray absorption spectroscopy (XAS) is a powerful element selective technique with strong sensitivity to the local geometrical structure, allows targeting the evolution of the local structures using tunable synchrotron radiation [17–20]. Moreover, XAS spectroscopy in the soft x-ray range also have surface sensitivity when different detection techniques (with different probing depths) are combined. The total electron yield (TEY) and the total fluorescence yield (TFY) techniques exhibit effective probing depths (EPD) of 2–10 nm and 50–100 nm, respectively, allowing a depth dependent analysis [21, 22]. Being complementary to the XAS technique, Raman is also a very sensitive probe of local atomic

environments in semiconducting materials. Raman spectroscopy can be used as a convenient tool to identify different phases as well as the phase transitions of various nano-structures, determining, which domains are amorphous or crystalline, whether there are defects, determining the sizes (diameter, lateral dimensions, etc.) of various types of nanomaterials [23]. Here, we have applied Raman spectroscopy to different NWs under ambient conditions, and studied the transitions occurring at high pressures (up to about 24 GPa) for a selected p-doped NWs sample in a diamond anvil cell.

## 15.2 Experimental

Samples of silicon nanowires were fabricated by metal assisted chemical etching using colloidal lithography [10]. We studied Si(100) substrates with different p-(B doped) and n-(P doped) doping level, and resistivity of 10–30  $\Omega$ cm and 0.01–0.02  $\Omega$ cm, respectively. The substrates were initially cleaned with acetone and deionized water, then dipped in 10% HF solution to remove the surface oxide. A suitable amount of polystyrene nano-spheres, with an initial size of 140 nm, were deposited on the substrate. The plasma etching was later used to reduce the size to a mean value of 90 nm followed by the deposition of an Au layer of 20 nm thick. In a further step, the nano-spheres were removed by sonication. The silicon substrates were etched in a solution of HF:H<sub>2</sub>O<sub>2</sub>:H<sub>2</sub>O, using 50% HF and 30% H<sub>2</sub>O<sub>2</sub> for six minutes. The MACE process was performed at room temperature and in the dark to avoid photo-generated carriers.

X-ray absorption spectroscopy experiments at Si L-, F K- and O K- edges were carried out at the BEAR beamline of the Elettra synchrotron radiation facility (Trieste, Italy). The synchrotron was working at the energy of 2 GeV with typical currents around 300 mA. The beamline operates in the photon energy range of 2.8–1600 eV with an intense photon beam of selectable polarization. The optical layout is based on the Plane Mirror Grating Mirror configuration (see Fig. 15.1). The BEAR beamline can work with three monochromators working in different energy ranges; the normal-incidence GNIM from 2.7 to 50 eV, the grazing incidence G1200 from 40 to 1200 eV and the G1800 for the range 600–1600 eV. In the present study, we have used only the G1200 monochromator working at grazing incidence and delivering a flux of  $\sim 10^{11}$  photons/sec (at around 100 eV) with a resolving power of about 3000 (at 400 eV).

Micro-Raman spectra were collected at the INFN-LNF laboratory using the Jasco NRS-5100 confocal Raman microscope, equipped with a 523 nm (green) laser with a 100 $\times$  magnification objective. Exposure time for laser illumination was set to 10 s and spectra were collected 10 times for each point of measure and then averaged.

Raman spectroscopy measurements were carried out also under high pressures using a membrane diamond anvil cell (similar to the one described in detail in Ref [24]) which was equipped with type IIa ultralow fluorescence diamond anvils of 300  $\mu$ m culet. These measurements were carried out using a solid-state green

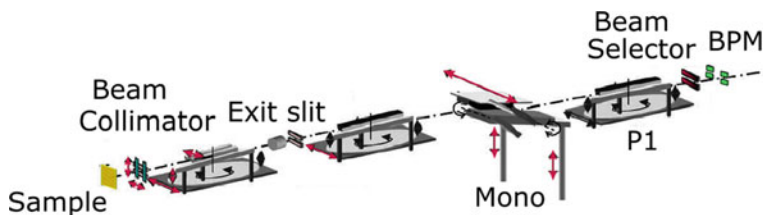


**Fig. 15.1** Sketch of the BEAR beamline set up. The beam position is monitored via a photon beam position monitor (BPM) at the beginning of the beamline, measuring the photocurrent from four Mo plates prior to the beamline optics. The beam polarization is modulated by a vertically moving double slit that customizes the vertical acceptance of the bending magnet output. The beamline Plane Mirror Grating (PMPG) configuration consists of a first parabolic mirror which focalizes the emitted photons, a monochromator working with a parallel beam, a second parabolic mirror focusing the dispersed beam through the experimental chamber exit slit, and finally an elliptical mirror collimating the photons on the sample position. The beamline exploits two grazing channel monochromators: G1200 and G1800 with 1200 and 1800 lines/mm, respectively. The G1200 is adapted for the energy range 40–1400 eV and G1800 is optimized for the energy range 600–1600 eV. The variations of the incident photon beam is also monitored by collecting the plane mirror current and the intensity of the incident beam is recorded by photo-detectors installed in the experimental chamber

laser (50 mW, 523 nm) exploiting the micro-Raman open-space spectroscopy instrument at the University of Camerino. The Raman scattering signal was collected in back-scattering geometry using a 50X objective installed on an Olympus BXFM microscopy, filtered and sent into a Horiba iHR320 optical spectrometer (equipped with a 1800 lines  $\times$  mm<sup>-1</sup> grating, and with a Peltier-cooled CCD detector).

The sample for Raman measurements under pressure was obtained by loading a tiny amount of low p-doped SiNWs in a stainless steel gasket with a central hole of 100  $\mu$ m, which was pre-indented to a thickness of 40  $\mu$ m. Methanol–ethanol mixture (4:1 ratio) was used as a pressure transmitting medium, while the standard ruby fluorescence technique was used as the in situ pressure measurements [25]. Raman measurements were collected at selected increasing pressures up to about 24 GPa.

### 15.3 Results and Discussion

Fabricated silicon nanowires using the MacE method can show distinct morphologies depending on etching solutions ratios, metal catalysts and doping types and levels (detailed information can be found in Ref [10, 14]). Here we have focused our attention on the structural properties of Si NWs for different doping types and level, and on the structural evolution of a selected type of NWs (low-doped p-type) at high pressures.

### 15.3.1 X-ray Absorption Spectroscopy

X-ray absorption spectra of porous Si NWs fabricated using different doping type and level of the silicon substrates are shown in Fig. 15.2. The spectra were collected in Total Electron Yield (TEY) mode using the photo-emitted drain current measured from the sample.

Si L-edge, O K-edge, and F K-edge XAS spectra of selected nanowires samples with different doping type and doping level are shown in Fig. 15.2. All samples were etched in the 2:1:3 ratio of the etching solution of HF:H<sub>2</sub>O<sub>2</sub>:H<sub>2</sub>O (H<sub>2</sub>O<sub>2</sub> is the oxidizing agent and HF the etching agent). A single low B doped Si etched in the 2:3:1 ratio of the etching solution of HF:H<sub>2</sub>O<sub>2</sub>:H<sub>2</sub>O is also included for comparison.

In particular, the Si L-edge and O K-edge spectra reported in Fig. 15.2a, b are related to (from bottom to top): highly ( $\sim 10^{18}$ atm/cm<sup>3</sup>) boron (p-type) doped Si (P<sup>+</sup>, lower curve); low ( $\sim 10^{15}$ atm/cm<sup>3</sup>) boron doped Si (P, second curve from the bottom); low ( $\sim 10^{15}$ atm/cm<sup>3</sup>) boron doped Si, but etched using a different catalytic solution concentration using a large ratio of the oxidizing agent H<sub>2</sub>O<sub>2</sub> (third curve from the bottom); highly phosphorous doped (n-type) Si (n<sup>+</sup>, upper curve).

The Si L-edge XAS spectra show several components at around 100 eV (A), 105.6 eV (C), 108.1 eV (D) and 112.4 eV (E). These features correspond to the a1(3s), t2(3p), e( $\epsilon$ d) and t2+e ( $\epsilon$ d) of 3s, 2p and 3d-like excitations, respectively. The A feature is characteristic of crystalline silicon and is almost negligible in all the spectra with the exception of the highly n-type doped sample that shows also an additional feature around 104 eV, which may be related to the spin-orbit splitting of the core excitation state of silicon oxide falling in the 104–106 eV range of [26, 27]. This feature is also observed as a shoulder (B) in the spectrum of sample P<sup>+</sup>. Furthermore, the sample synthesized with a higher oxidizing agent ratio shows a

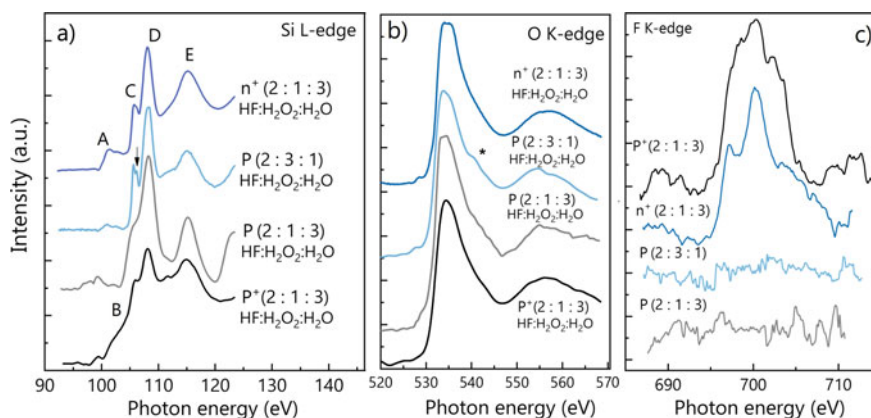


**Fig. 15.2** X-ray absorption spectra of Si NWs fabricated by MACe process, with different doping type (p and n) and doping level as described in the text. The Si L-edge, O K-edge and F K-edge x-ray absorption spectra of the nanowires are shown in panels (a), (b), and (c) respectively

peak splitting at around 105 eV (see arrow in figure), which might be associated to the formation of other oxides with different stoichiometry or valence [14]. The distribution of non-stoichiometric oxides in these samples might be the origin of the absence of the spin-orbit splitting [28–30].

The oxygen K-edge spectra of the samples under consideration show mainly SiO<sub>2</sub> features in all samples with a slight broadening. This broadening is in agreement with the presence of small amounts of other oxide phases (e.g., SiO, SiO<sub>x</sub>) and different stoichiometries. The sample synthesized with a higher oxidant agent ratio, on the other hand, shows the possible presence of a second component (labeled \*) which may be associated with the observed splitting in the Si-L edge spectrum mentioned above. On the other hand, the bulk oxide phase is relatively similar in all samples.

The Si L-edge and O K-edge XAS results clearly demonstrate the sensitivity of the surface chemistry either to doping type and level or to the catalytic solution used in the etching process. NWs fabricated in solution with a higher ratio of the oxidant agent exhibit a higher degree of oxidation as well as the presence of different oxide stoichiometry and different valence states. On the other hand, NWs synthesized using a highly n-doped silicon substrate show distinct features (A) indicating a larger fraction of Si crystallites in the porous structure, as compared to p-doped NWs.

The F K-edge spectra shown in Fig. 15.2c were recorded for all samples to monitor the presence of residual fluorine after the etching procedure. We have found that only highly doped samples (P or n) show a detectable signal of F atoms embedded in the structure. However, the quality of the measured spectra did not allow us to derive precise information about the chemical environment around F ions. The presence of the fluorinated species in highly doped nanowires have been also observed previously and is suggested to be correlated with the depletion of the surface charge region with the F atoms during the tunneling process across this region [10]. This tunneling is suggested to be also responsible for modifications of the nanowires internal structures.

### 15.3.2 Raman spectroscopy

Raman spectra of fabricated samples using different doping types and levels with similar etching solution ratios are shown in Fig. 15.3a, using the same nomenclature used above (n for n-doped, P for p-doped, + for high doping levels). The typical Raman spectrum of bulk silicon, showing the strong first-order optical phonon peak in the Stokes band around 520 cm<sup>-1</sup>, is also reported in the figure (bottom curve) as a reference. For all of the NWs samples, the Raman spectra show a broadened peak (main band located between 500 and 520 cm<sup>-1</sup>) and a clear shift to lower wavenumbers compared with the corresponding feature in crystalline bulk Si. This shift can be assigned to the decrease of the average silicon crystallite size, embedded within the porous structure of the nanowires. In fact, for nano-crystalline or disordered systems, the Raman active modes are not limited to those defined by the  $q \sim 0$  condition in a bulk crystal and this results in an asymmetric peak shifted to lower wavenumbers

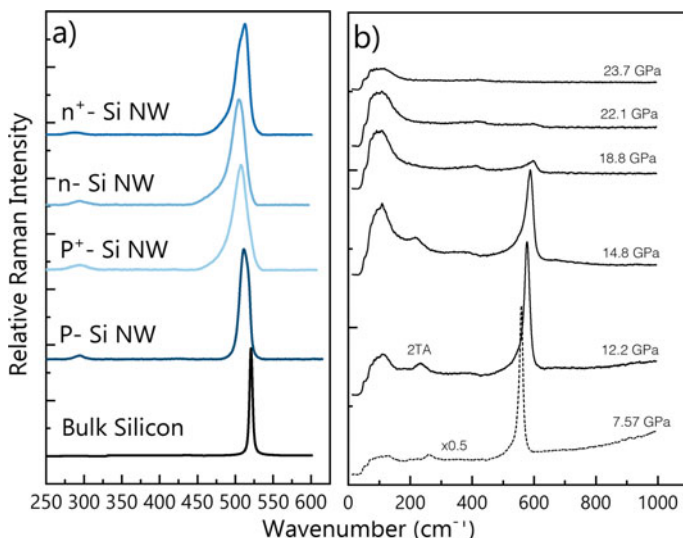


**Fig. 15.3** **a** Raman spectra of porous Si NWs with different doping type and level, synthesized using MAcE process with catalytic solution of HF:H<sub>2</sub>O<sub>2</sub>:H<sub>2</sub>O with the 2:1:3 ratio (see text). **b** Raman spectra of the low p-doped nanowires collected in the diamond anvil cell for increasing pressures (from bottom to top)

[31]. Generally speaking, for smaller crystalline grains we expect larger asymmetry, broadening and frequency shifts in Raman spectra. The shifts observed in our spectra suggest that larger Si crystallites are found in p-type NWs while smaller ones are typical of n-type NWs, in line with the XANES results discussed in the previous section.

Apart from the low-doped sample (P), all other Raman spectra evidence a broad asymmetry of the peak with components around  $476\text{ cm}^{-1}$  and  $484\text{ cm}^{-1}$  that can be correlated either to the quantum confinement of the Si crystallites inside the wires or to the presence of structural defects (typical of porous silicon) as reported in Refs [14, 32–34]. The small additional component appearing at  $\sim 300\text{ cm}^{-1}$ , which remains similar in intensity in all the samples, is assigned to the second-order 2TA band associated with two transverse acoustic phonons [31, 34].

A preliminary high-pressure experiment was carried out collecting Raman spectra of low p-doped nanowires at selected pressures up to 23.7 GPa and room temperature, as presented in Fig. 15.3(b). It has been previously reported that the nanomaterials can exhibit distinct phase transformations in comparison to their bulk counter parts [35]. It has been also suggested that the modified transitions could be related to the shape and dimension of the nanostructures [36]. In particular, silicon shown several metastable phases occurring at high pressures with interesting properties that, when combined with the modified properties in typical nanostructures, could be exploited in several applications.

As shown in Fig. 15.3b, we can observe that the main TO Raman mode at  $517.5\text{ cm}^{-1}$  shows a blue shift with the increase of pressure as a direct consequence of lattice volume decrease (contraction of average interatomic distances), in agreement with previously reported results on bulk silicon at high pressure [37] and with previous recent experiments on nanowires [15]. Moreover, it is also possible to observe a gradual increase in the width of the TO peak at increasing pressures up to 14.8 GPa. This fact can be tentatively interpreted as the effect of induced strains on the NWs which also gradually increase the level of disorder under high pressure. Interestingly, the transition from a cubic diamond type phase (dc-Si) to the metallic white tin ( $\beta$ -Sn-Si, or Si-II) ones is observed at pressures higher than about 22 GPa. This onset pressure results to be significantly higher than the expected value of the bulk silicon being around 11–12 GPa [38] and observed also in the present experiment, and also higher than the onset pressure (19 GPa) of the undoped SiNWs of similar size that were synthesized in a hot wall CVD reactor by the VLS growth mechanism [15].

The modification of the pressure onset for the phase transition in porous silicon nanowires can be assigned to the hindrance of the metallic phase nucleation as mainly due to the size effect (e.g., small crystallite domain) in these nanowires. This possibly indicates that phase transitions in elemental Si are not only affected by crystallite size but also by the morphology of the nanocrystalline system and possible presence of impurities including doping levels. However, further investigations are certainly necessary to better understand the effects of shape, morphology, crystallite sizes, and impurities on the phase behavior of the porous silicon nanowires.

## 15.4 Conclusions

In this work, several microstructural properties of Si NWs synthesized by metal assisted etching have been investigated by using x-ray absorption spectroscopy and Raman scattering techniques. The nanowires were synthesized using different doping type and levels as well as using different catalytic solutions. Our results show that the NWs structures can be modified by different preparation procedures. For example, the quantity of oxidizing agent used in the etching method is found to alter the fraction of Si crystallites inside the synthesized wires and may result in a different oxide stoichiometry. Raman spectroscopy of NWs showed in shifted and broadened first order optical modes, corresponding to the decrease of the crystallite domain size inside the nanowires. Based on Raman results, we infer that the smaller crystallite sizes are contained in n-doped Si NWs. The phase transformation of a low p-doped Si NWs sample was also investigated by Raman scattering versus pressure, showing that the onset of the diamond to  $\beta$ -Sn transformation is shifted up to about 22 GPa. These results demonstrate the unique role of advanced synchrotron radiation techniques like x-ray absorption spectroscopy, for nanomaterial characterization, in particular when combined with other state-of-the-art techniques available at most laboratories such as Raman scattering.



## References

1. L.T. Canham, Silicon quantum wire array fabrication by electrochemical and chemical dissolution of wafers. *Appl. Phys. Lett.* **57**(10), 1046–48 (1990)
2. Z. Kang, C. Tsang, N. Wong, Z. Zhang, S. Lee, Silicon quantum dots: a general photocatalyst for reduction, decomposition, and selective oxidation reactions. *J. Am. Chem. Soc.* **129**(40), 12090–12091 (2007)
3. L. Pavesi, L. Dal Negro, C. Mazzoleni, G. Franzo, F. Priolo, Optical Gain in Silicon Nanocrystals **408**(6811), 440–444 (2000)
4. V. Lehmann, U. Gosele, Porous silicon formation: a quantum wire effect. *Appl. Phys. Lett.* **58**, 856–858 (1991)
5. S. Borini, L. Boarino, G. Amato, Coulomb blockade tuned by NO<sub>2</sub> molecules in nanostructured silicon. *Adv. Mater.* (2006). <https://doi.org/10.1002/adma.200600198>
6. A. Loni, T. Defforge, E. Caffull, G. Gautier, L. Canham, Porous silicon fabrication by anodisation: progress towards the realisation of layers and powders with high surface area and micropore content. *Microporous Mesoporous Mater.* **213**, 188–191 (2015)
7. S. Carturan, G. Maggioni, S. Rezvani, R. Gunnella, N. Pinto, M. Gelain, D. Napoli, Wet chemical treatments of high purity Ge crystals for  $\gamma$ -ray detectors: Surface structure, passivation capabilities and air stability. *Mater. Chem. Phys.* **161**, 116–122 (2015). <https://doi.org/10.1016/j.matchemphys.2015.05.022>. <https://linkinghub.elsevier.com/retrieve/pii/S0254058415300821>
8. R.S. Wagner, W.C. Ellis, Vapor-liquid-solid mechanism of single crystal growth. *Appl. Phys. Lett.* **4**(5), 89 (1964)
9. N. Pinto, S.J. Rezvani, L. Favre, I. Berbezier, M. Fretto, L. Boarino, Geometrically induced electron-electron interaction in semiconductor nanowires. *Appl. Phys. Lett.* (2016). <https://doi.org/10.1063/1.4962893>
10. S.J. Rezvani, R. Gunnella, D. Neilson, L. Boarino, L. Croin, G. Aprile, M. Fretto, P. Rizzi, D. Antonioli, N. Pinto, Effect of carrier tunneling on the structure of Si nanowires fabricated by metal assisted etching. *Nanotechnology* (2016). <https://doi.org/10.1088/0957-4484/27/34/345301>
11. S.J. Rezvani, N. Pinto, L. Boarino, Rapid formation of single crystalline Ge nanowires by anodic metal assisted etching. *CrystEngComm* **18**(40), 7843–7848 (2016). <https://doi.org/10.1039/C6CE01598K>
12. S.J. Rezvani, N. Pinto, L. Boarino, F. Celegato, L. Favre, I. Berbezier, Diffusion induced effects on geometry of Ge nanowires. *Nanoscale* **6**(13), 7469–7473 (2014). <https://doi.org/10.1039/C4NR01084A>
13. S.J. Rezvani, L. Favre, F. Celegato, L. Boarino, I. Berbezier, N. Pinto, Supersaturation state effect in diffusion induced Ge nanowires growth at high temperatures. *J. Crystal Growth* (2016). <https://doi.org/10.1016/j.jcrysgro.2015.11.029>
14. S.J. Rezvani, N. Pinto, R. Gunnella, A. D’Elia, A. Marcelli, A. Di Cicco, Engineering porous silicon nanowires with tuneable electronic properties. *Condensed Matter* **5**(4), 57 (2020). <https://doi.org/10.3390/condmat5040057>. <https://www.mdpi.com/2410-3896/5/4/57>
15. L. Huston, A. Lugstein, J. Williams, J. Bradby, The high pressure phase transformation behavior of silicon nanowires. *Appl. Phys. Lett.* **113**(12), 123, 103 (2018). <https://doi.org/10.1063/1.5048033>
16. Y. Xuan, L. Tan, B. Cheng, F. Zhang, X. Chen, M. Ge, Q. Zeng, Z. Zeng, Pressure-induced phase transitions in nanostructured silicon. *J. Phys. Chem. C* **124**(49), 27089–27096 (2020). <https://doi.org/10.1021/acs.jpcc.0c07686>
17. M. Pasqualini, S. Calcaterra, F. Maroni, S. Rezvani, A.D. Cicco, S. Alexander, H. Rajantie, R. Tossici, F. Nobili, Electrochemical and spectroscopic characterization of an alumina-coated LiMn<sub>2</sub>O<sub>4</sub> cathode with enhanced interfacial stability. *Electrochimica Acta* **258**, 175–181 (2017). <https://doi.org/10.1016/j.electacta.2017.10.115>
18. S.J. Rezvani, M. Ciambè, R. Gunnella, M. Minicucci, M.A. Muñoz, F. Nobili, M. Pasqualini, S. Passerini, C. Schreiner, A. Trapananti, A. Witkowska, A. Di Cicco, Local structure and

- stability of SEI in graphite and ZFO electrodes probed by as K-Edge absorption spectroscopy. *J. Phys. Chem. C* **120**(8), 4287–4295 (2016). <https://doi.org/10.1021/acs.jpcc.5b11798>
19. S. Rezvani, M. Pasqualini, A. Witkowska, R. Gunnella, A. Birrozzi, M. Minicucci, H. Rajantie, M. Copley, F. Nobili, A.D. Cicco, Binder-induced surface structure evolution effects on Li-ion battery performance. *Appl. Surface Sci.* **435**, 1029–1036 (2018). <https://doi.org/10.1016/j.apsusc.2017.10.195>
  20. A. Bianconi, A. Marcelli, Surface X-ray absorption near-edge structure: XANES, in *Synchrotron Radiation Research* (Springer US, Boston, MA, 1992), pp. 63–115. [https://doi.org/10.1007/978-1-4615-3280-4\\_2](https://doi.org/10.1007/978-1-4615-3280-4_2)
  21. A. Di Cicco, A. Giglia, R. Gunnella, S.L. Koch, F. Mueller, F. Nobili, M. Pasqualini, S. Passerini, R. Tossici, A. Witkowska, SEI growth and depth profiling on ZFO electrodes by soft X-ray absorption spectroscopy. *Adv. Energy Mater.* **5**(18), 1500, 642 (2015). <https://doi.org/10.1002/aenm.201500642>
  22. S.J. Rezvani, F. Nobili, R. Gunnella, M. Ali, R. Tossici, S. Passerini, A. Di Cicco, SEI dynamics in metal oxide conversion electrodes of Li-Ion batteries. *J. Phys. Chem. C* **121**(47), 26379–26388 (2017). <https://doi.org/10.1021/acs.jpcc.7b08259>
  23. G. Gouadec, P. Colombar, Raman spectroscopy of nanomaterials: how spectra relate to disorder, particle size and mechanical properties. *Prog. Crystal Growth Characterization Mater.* **53**(1), 1–56 (2007). <https://doi.org/10.1016/j.pcrysgrow.2007.01.001>. URL <https://linkinghub.elsevier.com/retrieve/pii/S0960897407000022>
  24. Y. Mijiti, M. Perri, J. Coquet, L. Nataf, M. Minicucci, A. Trapananti, T. Irifune, F. Baudelet, A. Di Cicco, A new internally heated diamond anvil cell system for time-resolved optical and x-ray measurements. *Rev. Sci. Instruments* **91**(8), 085, 114 (2020)
  25. A. Dewaele, M. Torrent, P. Loubeyre, M. Mezouar, Compression curves of transition metals in the mbar range: experiments and projector augmented-wave calculations. *Phys. Rev. B* **78**, 104, 102 (2008). <https://doi.org/10.1103/PhysRevB.78.104102>
  26. G.R. Harp, Z.L. Han, B.P. Tonner, Spatially-resolved X-ray absorption near-edge spectroscopy of silicon in thin silicon-oxide films. *Physica Scripta* (1990). <https://doi.org/10.1088/0031-8949/1990/T31/003>
  27. F.J. Himpsel, F.R. McFeely, A. Taleb-Ibrahimi, J.A. Yarnoff, G. Hollinger, Microscopic structure of the SiO<sub>2</sub>/Si interface. *Phys. Rev. B* **38**(9), 6084–6096 (1988). <https://doi.org/10.1103/PhysRevB.38.6084>
  28. G.R. Harp, Z.L. Han, B.P. Tonner, X-ray absorption near edge structures of intermediate oxidation states of silicon in silicon oxides during thermal desorption. *J. Vacuum Sci. Technol. Vacuum Surfaces Films* (1990). <https://doi.org/10.1116/1.576737>
  29. Dien Li, X-ray absorption spectroscopy of silicon dioxide (SiO<sub>2</sub>) polymorphs: the structural characterization of opal. *Am. Mineralogist* **76**, 622–632 (1994)
  30. G.R. Harp, Z.L. Han, B.P. Tonner, Spatially-resolved X-ray absorption near-edge spectroscopy of Silicon in thin Silicon-oxide Films. *Physica Scripta* **T31**, 23–27 (1990). <https://doi.org/10.1088/0031-8949/1990/T31/003>. <http://stacks.iop.org/1402-4896/1990/i=T31/a=003?key=crossref.b75c22d111667e768da9f9416b837c5c>
  31. B. Li, D. Yu, S.L. Zhang, Raman spectral study of silicon nanowires. *Phys. Rev. B* **59**, 1645–1648 (1999). <https://doi.org/10.1103/PhysRevB.59.1645>
  32. G.G. Siu, X.L. Wu, Y. Gu, X.M. Bao, Ultraviolet and blue emission from crystalline SiO<sub>2</sub> coated with In<sub>2</sub>O<sub>3</sub> and Li<sub>2</sub>O<sub>3</sub>. *Appl. Phys. Lett.* **74**(13), 1812–1814 (1999). <https://doi.org/10.1063/1.1230943/1.123094>
  33. M. Khorasaninejad, J. Walia, S.S. Saini, Enhanced first-order Raman scattering from arrays of vertical silicon nanowires. *Nanotechnology* **23**(27), 275, 706 (2012). <https://doi.org/10.1088/0957-4484/23/27/275706>
  34. S. Zhang, X. Wang, K. Ho, J. Li, P. Diao, S. Cai, Raman spectra in a broad frequency region of p type porous silicon. *J. Appl. Phys.* **76**(5), 3016–3019 (1994). <https://doi.org/10.1063/1.3575043/1.357504>
  35. R. Vajtai, *Springer Handbook of Nanomaterials* (Springer, Heidelberg, 2013). <https://doi.org/10.1007/978-3-642-20595-8>

36. S.H. Tolbert, A.B. Herhold, L.E. Brus, A.P. Alivisatos, Pressure-induced structural transformations in Si nanocrystals: surface and shape effects. *Phys. Rev. Lett.* **76**(23), 4384–4387 (1996). <https://doi.org/10.1103/PhysRevLett.76.4384>
37. J.Z. Hu, L.D. Merkle, C.S. Menoni, I.L. Spain, Crystal data for high-pressure phases of silicon. *Phys. Rev. B* **34**(7), 4679–4684 (1986). <https://doi.org/10.1103/PhysRevB.34.4679>
38. R.O. Piltz, J.R. Maclean, S.J. Clark, G.J. Ackland, P.D. Hatton, J. Crain, Structure and properties of silicon XII: a complex tetrahedrally bonded phase. *Phys. Rev. B* **52**(6), 4072–4085 (1995). <https://doi.org/10.1103/PhysRevB.52.4072>

# Chapter 16

## The Use of Synchrotron-Based X-ray Microtomography for the Pore Network Quantitative and Computational Fluid Dynamics Experiments on Porous Carbonate Rocks



Miller Zambrano, Lucia Mancini, and Emanuele Tondi

**Abstract** In carbonates rocks, the textural properties of the pore network (e.g., pores size distribution, pores shape, pores connectivity and tortuosity), and therefore the porosity and permeability, are highly variable due to primary depositional conditions, diagenesis processes and deformation. For this reason, the quantitative characterisation of carbonate reservoirs, in terms of porosity and permeability, is challenging. This study presents a methodology for investigating the pore network in carbonate rocks using high-resolution synchrotron X-ray computed microtomography (SR micro-CT). This could be combined with computational fluid dynamics (CFD) simulations for obtaining information about fluid transport and calculated the permeability of the samples. Using key samples from rocks corresponding to porous and tight carbonates exposed in south and central Italy, the methodology has been applied to three different study cases: rapid characterisation of porous carbonate reservoirs (Abruzzo, central Italy), quantitative analysis of deformed porous carbonates (Sicily, south Italy), and pore-scale assessment of fractures hosted in tight carbonates (Murge, south Italy). Some samples may contain deformation structures (i.e. deformation bands, fractures) or may be altered by diagenesis (e.g., cementation, dissolution). The pore space can be filled by a single fluid phase (i.e. air) or multiple (i.e. bitumen and trapped gas). The selected rock samples were scanned by means of phase-contrast synchrotron SR micro-CT at the SYRMEP beamline of the Elettra synchrotron in Trieste (Italy). The tomographic images were acquired using a multi-resolution approach with a pixel size variable in the range of 1.0–2.4  $\mu\text{m}$  depending on the grain size distribution of the rock sample. After reconstruction, images were filtered and segmented for characterising the pore phase. The resulting images were used for both performing

---

M. Zambrano (✉) · E. Tondi

School of Science and Technology - Geology Division, University of Camerino, Camerino, Italy  
e-mail: [miller.zambrano@unicam.it](mailto:miller.zambrano@unicam.it)

L. Mancini

Elettra-Sincrotrone Trieste S.C.p.A, Basovizza, Trieste 34149, Italy

LINXS—Lund Institute of Advanced Neutron and X-ray Science, Lund 22370, Sweden

© Springer Nature Switzerland AG 2021

A. Di Cicco et al. (eds.), *Synchrotron Radiation Science and Applications*,

Springer Proceedings in Physics 220, [https://doi.org/10.1007/978-3-030-72005-6\\_16](https://doi.org/10.1007/978-3-030-72005-6_16)

203

a quantitative pore network analysis of the studied rock samples and CFD experiments (multiple relaxation times lattice-Boltzmann method, MRT-LBM) using the open source software PALABOS.

## 16.1 Introduction

The characterisation of carbonate reservoirs is challenging due to the variability at the pore-scale driven by primary depositional conditions, diagenesis processes and deformation. The fluid migration and recovery rates are controlled in part by the pore architecture properties such as, porosity, pores size distribution, pores shape, and tortuosity [1, 2]. The multivariable control on the permeability is revealed by important scattering permeability–porosity cross plots. For this reason, different attempts have been made to relate and estimate the value of permeability from the pore-network properties using empirical or analytical solutions, such as the Kozeny-Carman equation [3]. However, the implementation of such equation, is limited to certain circumstances, such as low cementation, well-sorting, and well-connectivity [1].

In the case of fractured carbonate rocks, fluid storage and migration can be enhanced or depend entirely on the fracture network [2, 4]. The permeability of a fractured reservoir depends on the geometrical properties of the fracture network, such as fracture connectivity and hydraulic aperture. The first one, controlled by fracture length distribution, orientation, and intensity, determines for instance whether the fluid can pass through different mechanical boundaries, such as single beds, bed package and bed packages associations [5–8]. The hydraulic aperture is controlled by the pore space between the opposite walls of the fracture, the mismatch between both surfaces, and the roughness [9–11].

The fluid phenomena in different types of rocks (volcanic, siliciclastic and carbonate rocks) at the pore scale can be better understood by integrating three-dimensional (3D) imaging techniques like X-ray [12–21] or Neutron computed microtomography [22–26] with direct fluid simulations [27, 28]. This combined approach can also help to develop accurate predictive equations for both porous and fracture carbonate reservoirs. Computed tomography techniques is used for characterising the pores and framework of different materials such as cement and concrete [29, 30], building stones [31–34], porous asphalt [35], extra-terrestrial rocks [36, 37], and cultural heritage artefacts [38–41]. X-ray microtomography is used for describing complex processes crystallisation processes [42–46], pore structure modification inside natural building stones [47], pyrolysis and gasification of coal [48], microcracking in cement due to leaching or temperature [49, 50].

In this study, a methodology for assessing the pore network in carbonate rocks using synchrotron X-ray computed microtomography (SR micro-CT) is presented. Obtained images can be used for performing quantitative analysis of different phase of interest (grains, pores, fluid content). This kind of analysis could be integrated with computational fluid dynamics (CFD) with the objective of investigating the

control exerted by the pore network on the storage and migration capacity in carbonates characterised by different texture, porosity, degrees and types of deformation (granular flow-deformation bands, brittle-fractures), and diagenesis (cementation, dissolution).

The methodology has been applied to three different study cases: rapid characterisation of porous carbonate reservoirs (Abruzzo, central Italy), quantitative analysis of deformed porous carbonates (Sicily, south Italy), and pore-scale assessment of fractures hosted in tight carbonates (Murge, south Italy). Samples pertain to actual reservoir carbonate rocks from Abruzzo where the lithofacies control the in-situ hydrocarbon distribution [51–57]. The porous carbonates sample from Sicily contains deformation bands, previous studies have reported significant variabilities regarding the porosity and permeability for these deformation features with respect to the host rock [58, 59]. Sample from Murge contains natural microfractures [55] characterised by partial cementation and variable mechanical aperture. The SR micro-CT images were acquired at the Elettra synchrotron facility (Basovizza, Trieste, Italy) and processed and analysed as described by Arzilli et al. [15] and Zambrano et al. [16]. The permeability of deformed porous carbonate rocks was computed via CFD using the PALABOS open source library [60].

Regardless the wide application of this methodology in previous studies, here we applied it to carbonates rock of extremely diverse architecture from highly porous to extremely tight. The advantages of the presented methodology are that can be used for detailed investigations of quantitative analysis and fluid flow or to rapid determination of reservoirs rocks matrix porosity.

## 16.2 Methods

### 16.2.1 Samples

With the objective of showing different scenarios, a total of four key samples corresponding to carbonate rocks exposed in different areas of Italy were selected. Samples were cut in cylinders of near 3.0 mm of diameter to guarantee the best penetration of X-rays.

The first two samples correspond to an actual exposed bitumen reservoir (exploited since Roman times) known as Roman Valley Quarry located at Maiella Mountain (Abruzzo). Two lithofacies are investigated, a pervious lithofacies (Au) and an impervious lithofacies (E). The sample of lithofacies Au is a *Lepidocyclina* grainstone with a porosity of 28.1% and a permeability of  $8.2 \times 10^{-14} \text{ m}^2$  and  $1.6 \times 10^{-13} \text{ m}^2$ , vertical and horizontal component respectively [53, 54]. The lithofacies E correspond to planktonic foraminifera wackestones and mudstones with a porosity of 28.6% and a permeability of near  $8.4 \times 10^{-17} \text{ m}^2$  [53, 54]. This difference in permeability is expressed by the distribution of bitumen in the different lithofacies, where Au is

highly saturated of bitumen and E is dry (without bitumen). The dissimilar distribution of bitumen regardless the similar porosity was related to the pore sizes since lithofacies E are characterised by microporosity. However, a further investigation is needed to better understand the control of both storage (hydrocarbon distribution) and migration (permeability).

The third sample corresponds to a deformation band hosted in San Vito lo Capo grainstone (Sicily). This sample has been previously investigated by SR micro-CT using a monochromatic X-ray beam at medium resolution using an isotropic voxel size of  $9.0 \mu\text{m}$  [16]; the authors indicate that permeability within the deformation band is present only in the parallel components since most of the flow is going through the slip surface. Since the spatial resolution in the present study is higher, we could verify if other areas of the deformation band may contribute to flow as well. Here, we tested the capability of imaging small pores, below  $10 \mu\text{m}$  in diameter, within the cataclastic zone.

The fourth sample corresponds to a tight platform carbonate from Murge (Italy) characterised by a negligible matrix porosity and the presence of microfractures. Laboratory analysis indicates a porosity below 2% and a permeability below  $1.0 \times 10^{-15} \text{ m}^2$  [61]. These rocks have been previously characterised also in terms of macroscopic fractures [5, 7, 7, 62].

The objectives of investigating this sample are: (i) testing the capability of investigating rocks with extremely low matrix porosity, and (ii) to characterise natural microfractures.

## **16.2.2 *Synchrotron Radiation Computed Microtomography (SR Micro-CT)***

The SR micro-CT imaging experiments were performed at the SYRMEP beamline of the Elettra Sincrotrone Trieste laboratory. This beamline is characterised by a nearly parallel geometry and high spatial coherence of the X-ray beam [63] allowing propagation-based phase-contrast effects to enhance the visibility of interfaces corresponding to abrupt phase changes in the sample [64]. Compared with absorption mode, phase images will appear sharper and small details can be detected (also smaller than the pixel size of the detector) and objects with similar linear attenuation coefficients could be detected and analysed. The SYRMEP beamline has been already used to obtain 3D images of carbonate rocks allowing extracting valuable information about pores morphology, connectivity, and permeability at the pore scale [12, 13, 15]. In this study, SR micro-CT experiments and 3D image processing and analysis were performed following the methodology described by Arzilli et al. [15] and Zambrano et al. [16] using a white beam configuration [65].

For the experiments, the X-ray beam was filtered with 1.5 mm Si + 1.0 mm of Al corresponding to a mean energy of 27 keV. The sample-to-detector distance was set at 150 mm and 200 mm (depending on the sample microstructure). For each sample,

1800 projections were acquired over a total scan angle of  $180^\circ$  with an exposure time/projection between 2.0 and 3.0 s (depending on the signal-to-noise ratio in the projection images). The detector consisted of a 16-bit, air-cooled, sCMOS camera (Hamamatsu C11440-22C) with a  $2048 \times 2048$ -pixel chip. The effective pixel size of the detector was set in a range from 1.0 to 2.4  $\mu\text{m}$  (depending on the sample). The tomographic slice reconstruction was performed using the SYRMEP Tomo Project software developed at Elettra [66] and powered by the ASTRA tomography toolbox [67] and TomoPy [68]. To increase the reliability of quantitative morphological analysis and enhance the contrast between pores, different filling fluid phases and rocks, a single-distance phase-retrieval algorithm [69] was applied to the projections prior to the reconstruction procedure.

The post-processing, including filtering and segmentation, and the quantitative analysis were performed by using the Pore3D software library custom developed at Elettra [70]. A 3D bilateral filter [71] was applied to the reconstructed data for smoothing the images and preserving edges [18]. After this step, 3D images were segmented (extracting of phase of interest, pores) by the automatic multiphase k-means clustering algorithm [72, 73], setting 3–4 classes of objects, depending on the sample. After this, the tool ‘Find Connected Structures’ of the Fiji software [74] was used for dividing the pore space into two components: (i) connected pores and (ii) isolated pores. In the case of dual-phase fluid content in pores two components were segmented: (i) bitumen-filled and (ii) gas-filled. The composition of the gas is unknown since no further test were made.

In addition, we performed CFD experiments using the open-source software PALABOS, which is based on lattice-Boltzmann method (LBM). This methodology [27, 28] consists of imposing a single-phase fluid flow through the segmented 3D images by maintaining a fixed pressure gradient between the inlet and outlet faces of the volume, the rest of the faces were padded. The interface pores-voids was converted to bounce-back boundary conditions. It was used a Multiple Relaxation Times (MRT) approach [75] with a D3Q19 lattice. This method generates viscosity-independent results of permeability. The permeability of the volume was calculated using Darcy’s law once steady conditions were reached. To evaluate anisotropy, the results of permeability and the pore network properties were calculated in three orientations.

### 16.3 Results and Discussions

The raw results of X-ray microtomographic experiments consist of reconstructed grey-scale virtual slices of the studied rocks (Fig. 16.1). Different rock elements (grains made of calcite or siliceous minerals and voids-pores), and eventually fluid content (e.g. hydrocarbon bitumen, gas) are observed and can be labelled by different colours. In the images, whitish colours represent calcite, pores filled with gas are the darkest phase, pores filled with bitumen are relatively less dark, whereas intermedium



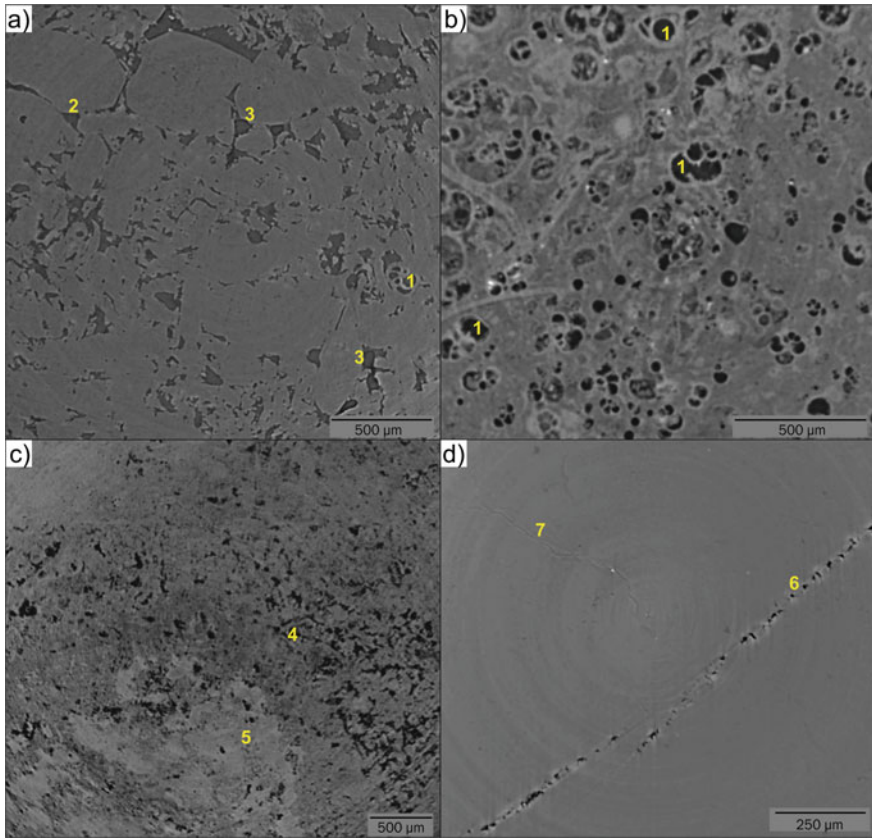


**Fig. 16.1** SR micro-CT images (slices) of the studied rock samples: **a** Lithofacies Au (reservoir from Cava Romana) at  $1.8\ \mu\text{m}$  voxel size, **b** lithofacies E (seal from Cava Romana) at  $1.4\ \mu\text{m}$  voxel size, **c** Deformation Band (San Vito lo Capo, Sicily) at  $2.4\ \mu\text{m}$  voxel size, and **d** Tight carbonate rock from Murge (Italy) at  $1.0\ \mu\text{m}$  voxel size. Notes: (1) isolated intragranular pores, (2) intergranular pores impregnated with bitumen, (3) trapped gas, (4) zone characterised by cataclasis, (5) zone characterised by cementation, (6) natural fractures partially open with aperture up to  $8\ \mu\text{m}$ , (7) microfractures with apertures near  $2\ \mu\text{m}$

grey could be either siliceous minerals or unresolved pores. Exceptionally, bright spots are present in the images that are interpreted as possible oxides.

For the case of porous carbonate reservoirs samples of Abruzzo (Maiella Mountain, Italy), the tomographic images show two quite different textures. The sample corresponding to lithofacies Au, is characterised by an important presence of intergranular pores and in minor proportion intragranular pores within bioclast (Fig. 1a). Two fluid phases filling the pores are distinguished corresponding to bitumen and unknown gas (possibly hydrocarbon volatiles). The bitumen is impregnating the rock

occupying almost the entire pore space, whereas the gas is trapped in the viscous bitumen. In the case of lithofacies E, the sample is characterised by an important presence of intragranular pores within bioclasts, intergranular space is almost absent likely due to the calcite cement (Fig. 1b).

A 3D rendering of the sample and the connected pores may explain in a simple way the hydrocarbon distribution in the analysed lithofacies exposed in Majella Mountain (Fig. 16.2). Here we can observe that, regardless the similar total porosity measured in laboratory (near 28%), the evaluated rocks present totally dissimilar storage and migration capabilities [54]. The 3D X-ray images reveal that pervious Lithofacies Au (Lepidocyclus grainstone, gas permeability near to  $5 \times 10^{-13} \text{ m}^2$ ) are highly connected (Fig. 2a), whereas impervious Lithofacies E (Planktonic foraminifera wackestones to mudstones, gas permeability near to  $8.4 \times 10^{-17} \text{ m}^2$ ) are characterised by isolated porosity (Fig. 2b).

Our results indicate that the porosity is near to 13.0% (isolated) and 14.3% (well-connected) for lithofacies E and Au, respectively. Whereas the bitumen saturation is 0.952 for the lithofacies Au. Differences of porosity with laboratory analysis can be explained as undetected pores with size likely below the achievable spatial resolution or corresponds to macrofractures not detected on the analysed volume. In the case

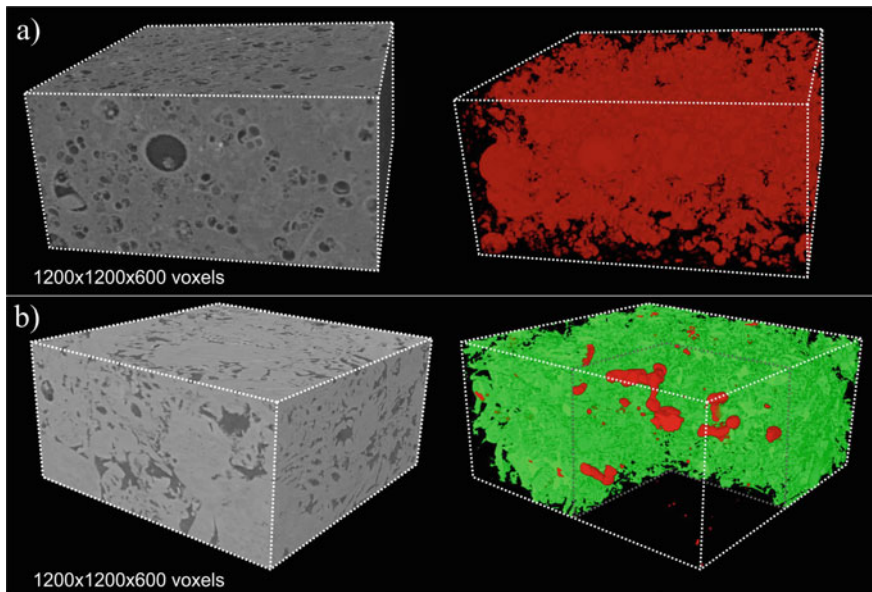


**Fig. 16.2** Volume renderings of SR micro/CT data obtained from samples of Cava Romana (Abruzzo, Italy) showing grey scale raw images and segmented pores: **a** Lithofacies E (seal from Cava Romana), isotropic voxel size =  $1.4 \mu\text{m}$  (isolated pores in red) and **b** lithofacies Au (reservoir from Cava Romana), isotropic voxel size =  $1.8 \mu\text{m}$ . In image **b** the bitumen-filled pores (green) were made transparent in a cubic portion of the volume to permits the observation of the trapped gas (red)

of small pores (below 10  $\mu\text{m}$  of diameter), their contribution to fluid maybe be quite negligible [28] due to a high friction to fluid flow or the presence of irreducible water (water trapped in micropores or bound to clay minerals affecting both effective porosity and permeability of reservoir rocks). Despite this the difference in porosity results are consistent with field observations where the lithofacies Au are likely a good reservoir, whereas Lithofacies E represent an excellent seal [54]. Thus, these results highlight the main control of the connectivity on the pore network for the fluid as it has been previously discussed by other authors [15, 16]. Since the applied methodology only needs small samples, a few millimetres thick, it can be used for rapid analysis of drill cuttings from oil exploration wells, providing fast volumetric information about the porosity, permeability, and texture of subsurface rocks.

In deformed porous carbonate samples from San Vito lo Capo (Sicily, Italy), results of high-resolution phase-contrast SR micro-CT (isotropic voxel size = 2.4  $\mu\text{m}$ ) allowed to detect very narrow pores within cataclastic zones of deformation bands (Fig. 1c). The pores across the deformation band (Fig. 3a) are generally

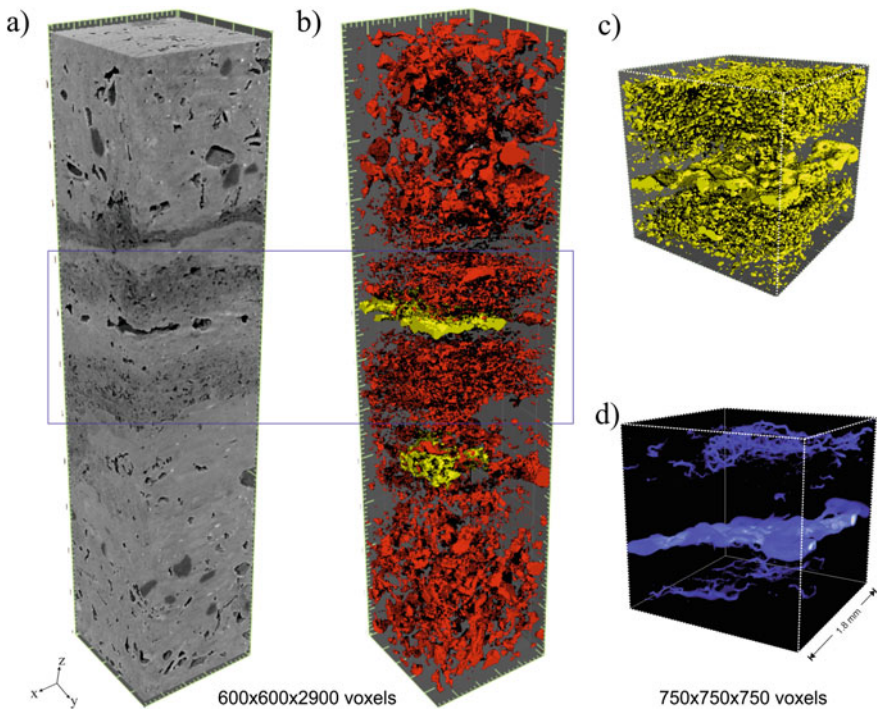


**Fig. 16.3** Volume renderings of a sample featuring deformation band hosted in a porous grainstone (San Vito lo Capo, Italy): **a** Gray scale raw SR micro-CT image obtained at an isotropic voxel size of 2.4  $\mu\text{m}$ , **b** the same volume with segmented pores (in red isolated pores, in yellow connected pores), **c** Segmented pores within a sub-volume corresponding to the core of the deformation band, **d** Velocity field computed by Lattice-Boltzmann simulations (lower velocities in blue, higher velocities in orange) within the sub-volume represented in **c**)

isolated as it is observed in the segmented image (Fig. 3b). However, some connected pores are related to the space within the fault surfaces generated by the mismatch of the surfaces due to displacement [9], surface wearing and dissolution (Fig. 3c). In addition, solution-enlarged stylolites can also create some a limited number of small connected pores. The pore space related to the mismatch of the fault surfaces and the solution-enlarged stylolites (preferentially connected parallelly to the deformation band) generates a significant anisotropy because fluid can flow only in the directions parallel to the deformation band (Fig. 3d). In the case of permeability, the results of Lattice-Boltzmann simulations are highly consistent with the data reported by previous authors using field [58, 59] or laboratory techniques [54, 76, 77]. Moreover, the implemented methodology permits investigating narrow zones (a few millimetres in size) within the deformation bands providing unique information.

Results indicate that deformation and diagenetic processes may have an important impact on the pore network properties and therefore on storage (porosity) and migration (permeability) capacity of the studied rocks. The reduction of the effective porosity within the DBs may be related to diagenesis or deformation processes. Grain size reduction (increment of specific surface), helped by intergranular pressure solution [78], generates an important effective porosity reduction due to both the accommodation of fine-grained residual material space and the precipitation of solved solids in the adjacent pore space [79]. In the first case, pore size may decrease and eventually the micropores may have (minor) contribution to the flow. The second case, cementation, is a preemptory mechanism for the occlusion and isolation.

The same methodological approach was also used to characterise tight carbonate samples (Murge, Italy). In this case, the images were reconstructed with an isotropic voxel size of  $1.0\ \mu\text{m}$  to detect micropores and microfractures (Fig. 1d). The evaluated sample is characterised by isolated pores with a diameter near to  $4\ \mu\text{m}$  and may present some multi-segment microfractures with aperture up to  $6\ \mu\text{m}$  (Fig. 16.4). In this sample, the permeability of a single fracture was calculated by using the MRT-LBM method. The resulting permeability value is near  $2.0 \times 10^{-17}\ \text{m}^2$ . Using the equation for smooth parallel plates of Snow [80], where permeability depends on the square of the hydraulic aperture divided by the value (12), it is straightforward the estimation of the corresponding hydraulic aperture ( $0.001\ \mu\text{m}$ ). This difference of three orders of magnitude between the mechanical aperture and the hydraulic aperture can be attributed to the connectivity of the pore network, the mismatch between surfaces, and the roughness of the fracture walls [9, 81].

As have been demonstrated, this methodology can be applied to a wide range of carbonate rocks lithofacies for characterizing their porosity and connectivity. The main advantages are (1) the accuracy of results, which is reached thanks to the phase contrast and high spatial resolution provided by the SR micro-CT technique, (2) the rapid determination of reservoirs rocks matrix porosity, which can be used for analysing of drill cuttings from oil exploration wells, and (3) the possibility to re-evaluate the samples using different resolution conditions, since it is a non-destructive approach. Similar approach can be applied to different kind of materials, such as terrestrial and extra-terrestrial rocks, construction materials, and cultural heritage artefacts.

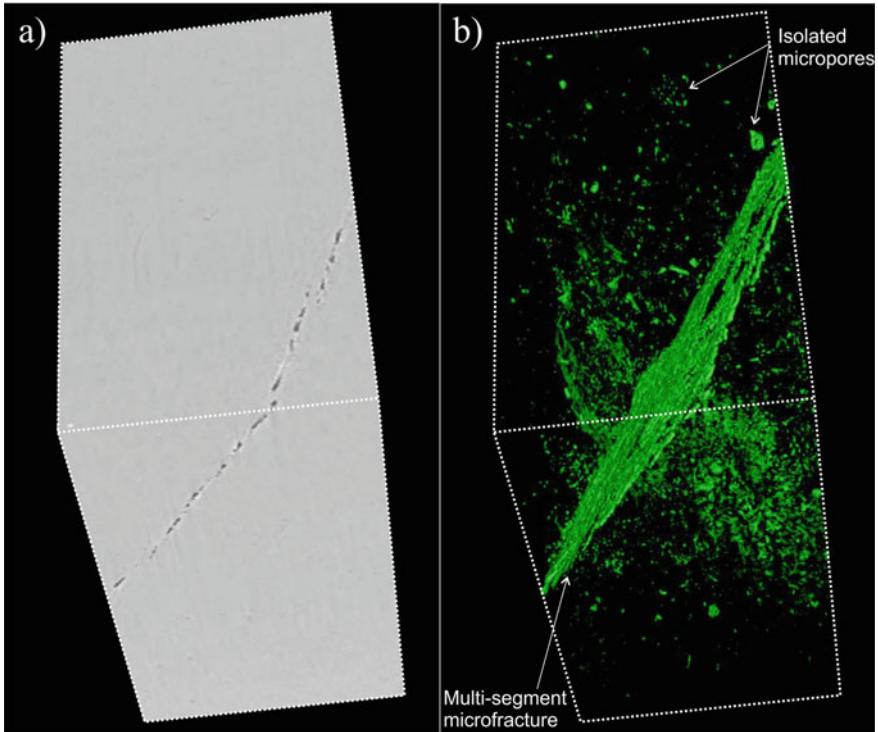


**Fig. 16.4** Volume renderings of a tight carbonate rock from Murge (Italy): **a** Gray scale raw SR micro-CT image is constructed with an isotropic voxel size of  $1.0\ \mu\text{m}$ , **b** The same volume with segmented pores including a multi-segment microfracture and isolated micropores. Volume dimension are  $1100 \times 1100 \times 600\ \mu\text{m}$

## 16.4 Conclusions

In this work, a synchrotron-based X-ray computed microtomography technique has been used for assessing the pore network of carbonate rocks, computing their permeability and textural properties. The same technique has been employed to investigate and explain field observations and laboratory results of permeability. The obtained results have permitted to deepen our understanding of diagenetic processes and their impact on permeability. To summarise:

- SR micro-CT is quite versatile for investigating millimetric zones of rock volumes with specific characteristics. Since small samples are required, the methodology can be also applied for fast investigations of drill cuttings representing a useful tool for exploration geology. The application of this approach can be extended to different of materials including extra-terrestrial rocks, and building stones.

- High spatial resolution phase-contrast SR micro-CT permits differentiating grains with different mineralogical content (i.e., calcite and siliceous minerals), micropores, microfractures and sometimes multiple fluid phases (i.e., bitumen, gas) within the pores.
- The experiments showed how deformation and diagenesis processes can locally change the capacity of both storage and migration of fluid in carbonates. X-ray micro CT provides valuable information about the pore-network connectivity and degree of cementation in reservoir samples explaining important differences in permeability despite similar porosity values of some samples.

**Acknowledgements** We acknowledge Elettra Sincrotrone Trieste for providing access to its synchrotron radiation facilities and the use of the software Pore3D. We thank Gabriele Lanzafame (now at University of Catania, Italy), and Fabio Arzilli (now at Manchester University, UK) for assistance in using beamline SYRMEP.

## References

1. F.A.L Dullien, *Porous Media: Fluid Transport and Pore Structure* (Academic Press, 2012)
2. F.J. Lucia, *Carbonate Reservoir Characterization: An Integrated Approach* (Springer Science & Business Media, 2007)
3. J. Kozeny, *Über Kapillare Leitung des Wassers im Boden* (Aufstieg Versicherung hnd Anwendung auf die Bemassung (Sitzungsber, Akad Wiss, 1927)
4. R. Nelson, *Geologic Analysis of Naturally Fractured Reservoirs* (Elsevier, 2001)
5. E. Panza, F. Agosta, A. Rustichelli et al., Fracture stratigraphy and fluid flow properties of shallow-water, tight carbonates: the case study of the Murge Plateau (southern Italy). *Mar. Pet. Geol.* **73** (2016). <https://doi.org/10.1016/j.marpetgeo.2016.03.022>
6. L. Massaro, A. Corradetti, F. Vinci et al., Multiscale fracture analysis in a reservoir-scale carbonate platform exposure (sorrento peninsula, Italy): implications for fluid flow. *Geofluids* **2018** (2018)
7. M. Zambrano, E. Tondi, I. Korneva et al., Fracture properties analysis and discrete fracture network modelling of faulted tight limestones, Murge Plateau, Italy. *Ital. J. Geosci.* **135**, 55–67 (2016)
8. J.N. Mendez, Q. Jin, M. González et al., Fracture characterization and modeling of karsted carbonate reservoirs: a case study in Tahe oilfield, Tarim Basin (western China). *Mar. Pet. Geol.* **112**, 104104 (2020)
9. M.Zambrano, A.D. Pitts, A. Salama, et al., Analysis of fracture roughness control on permeability using SFM and fluid flow simulations: implications for carbonate reservoir characterization. *Geofluids* **2019** (2019). <https://doi.org/10.1155/2019/4132386>
10. S.R. Ogilvie, E. Isakov, C.W. Taylor, P.W.J. Glover, *Characterization of Rough-Walled Fractures in Crystalline Rocks*, vol. 214, Special Publications (Geological Society, London, 2003), pp. 125–141
11. S.R. Ogilvie, E. Isakov, P.W.J. Glover, Fluid flow through rough fractures in rocks. II: a new matching model for rough rock fractures. *Earth Planet. Sci. Lett.* **241**, 454–465 (2006)
12. M.J. Blunt, B. Bijeljic, H. Dong et al., Pore-scale imaging and modelling. *Adv. Water Resour.* **51**, 197–216 (2013)
13. A. Cilona, D.R. Faulkner, E. Tondi et al., The effects of rock heterogeneity on compaction localization in porous carbonates. *J. Struct. Geol.* **67**, 75–93 (2014)

14. Y. Ji, S.A. Hall, P. Baud, T. Wong, Characterization of pore structure and strain localization in Majella limestone by X-ray computed tomography and digital image correlation. *Geophys. J. Int.* **200**, 701–719 (2015)
15. F. Arzilli, A. Cilona, L. Mancini, E. Tondi, Using synchrotron X-ray microtomography to characterize the pore network of reservoir rocks: a case study on carbonates. *Adv. Water Resour.* **95**, 254–263 (2016)
16. M. Zambrano, E. Tondi, L. Mancini et al., 3D Pore-network quantitative analysis in deformed carbonate grainstones. *Mar. Pet. Geol.* **82** (2017). <https://doi.org/10.1016/j.marpetgeo.2017.02.001>
17. P. Baud, U. Exner, M. Lommatzsch et al., Mechanical behavior, failure mode, and transport properties in a porous carbonate. *J. Geophys. Res.: Solid Earth* **122**, 7363–7387 (2017)
18. M. Voltolini, D. Zandomenighi, L. Mancini, M. Polacci, Texture analysis of volcanic rock samples: quantitative study of crystals and vesicles shape preferred orientation from X-ray microtomography data. *J. Volcanol. Geoth. Res.* **202**, 83–95 (2011)
19. H. Riegel, M. Zambrano, F. Balsamo et al., Petrophysical properties and microstructural analysis of faulted heterolithic packages: a case study from Miocene turbidite successions, Italy. *Geofluids* **2019** (2019). <https://doi.org/10.1155/2019/9582359>
20. H.L. Ramandi, R.T. Armstrong, P. Mostaghimi, Micro-CT image calibration to improve fracture aperture measurement. *Case Stud. Nondestruct. Test. Eval.* **6**, 4–13 (2016). <https://doi.org/10.1016/j.cnsdt.2016.03.001>
21. G. Pratesi, S. Caporali, F. Loglio et al., Quantitative study of porosity and pore features in moldavites by means of X-ray micro-CT. *Materials* **7**, 3319–3336 (2014)
22. E. Stavropoulou, E. Andò, A. Tengattini et al., Liquid water uptake in unconfined Callovo Oxfordian clay-rock studied with neutron and X-ray imaging. *Acta Geotech.* **14**, 19–33 (2019)
23. F.C. de Beer, M.F. Middleton, Neutron radiography imaging, porosity and permeability in porous rocks. *S. Afr. J. Geol.* **109**, 541–550 (2006)
24. B. Schillinger, E. Calzada, C. Eulenkamp et al., Dehydration of moulding sand in simulated casting process examined with neutron radiography. *Nucl. Instrum. Methods Phys. Res., Sect. A* **651**, 312–314 (2011)
25. S.A. Hall, Characterization of fluid flow in a shear band in porous rock using neutron radiography. *Geophys. Res. Lett.* **40**, 2613–2618 (2013)
26. M. Zambrano, F. Hameed, K. Anders et al., Implementation of dynamic neutron radiography and integrated X-ray and neutron tomography in porous carbonate reservoir rocks. *Front. Earth Sci.* **7** (2019). <https://doi.org/10.3389/feart.2019.00329>
27. W. Degruyter, A. Burgisser, O. Bachmann, O. Malaspinas, Synchrotron X-ray microtomography and lattice Boltzmann simulations of gas flow through volcanic pumices. *Geosphere* **6**, 470–481 (2010)
28. M. Zambrano, E. Tondi, L. Mancini et al., Fluid flow simulation and permeability computation in deformed porous carbonate grainstones. *Adv. Water Resour.* **115** (2018). <https://doi.org/10.1016/j.advwatres.2018.02.016>
29. E. Gallucci, K. Scrivener, A. Groso et al., 3D experimental investigation of the microstructure of cement pastes using synchrotron X-ray microtomography ( $\mu$ CT). *Cem. Concr. Res.* **37**, 360–368 (2007)
30. Í.B. da Silva, X-ray Computed Microtomography technique applied for cementitious materials: a review. *Micron* **107**, 1–8 (2018)
31. V. Cnudde, J.P. Cnudde, C. Dupuis, P.J.S. Jacobs, X-ray micro-CT used for the localization of water repellents and consolidants inside natural building stones. *Mater. Charact.* **53**, 259–271 (2004)
32. F. Hameed, B. Schillinger, A. Rohatsch et al., Investigations of stone consolidants by neutron imaging. *Nucl. Instrum. Methods Phys. Res., Sect. A* **605**, 150–153 (2009)
33. F. Hameed, A. Rohatsch, J. Weber et al., *Investigation of Calcareous Arenites From St. Stephan's Cathedral* (NIST, Vienna Gaithersburg, MD, 2006)
34. E. Possenti, C. Colombo, C. Conti et al., Consolidation of building materials with a phosphate-based treatment: Effects on the microstructure and on the 3D pore network. *Mater. Charact.* **154**, 315–324 (2019)

35. A. du Plessis, W.P. Boshoff, A review of X-ray computed tomography of concrete and asphalt construction materials. *Constr. Build. Mater.* **199**, 637–651 (2019)
36. D.S. Ebel, M.L. Rivers, Meteorite 3-D synchrotron microtomography: methods and applications. *Meteorit. Planet. Sci.* **42**, 1627–1646 (2007)
37. H. Liu, T. Xiao, H. Xie et al., Nondestructive material characterization of meteorites with synchrotron-based high energy X-ray phase micro-computed tomography. *J. Phys. D Appl. Phys.* **50**, 055301 (2017)
38. N. Sodini, D. Dreossi, A. Giordano et al., Comparison of different experimental approaches in the tomographic analysis of ancient violins. *J. Cult. Herit.* **27**, S88–S92 (2017)
39. A. Fedrigo, M. Strobl, A.R. Williams et al., Neutron imaging study of ‘pattern-welded’ swords from the Viking Age. *Archaeol. Anthropol. Sci.* **10**, 1249–1263 (2018)
40. F. Bernardini, C. Tuniz, F. Zanini, X-ray computed microtomography for paleoanthropology, archaeology, and cultural heritage, in *Nanotechnologies and Nanomaterials for Diagnostic, Conservation and Restoration of Cultural Heritage* (Elsevier, 2019) pp. 25–45
41. B. Schillinger, A. Beaudet, A. Fedrigo et al., Neutron imaging in cultural heritage research at the FRM II reactor of the Heinz Maier-Leibnitz center. *J. Imag.* **4**, 22 (2018)
42. M. Polacci, F. Arzilli, G. la Spina et al., Crystallisation in basaltic magmas revealed via in situ 4D synchrotron X-ray microtomography. *Sci. Rep.* **8**, 1–13 (2018)
43. F. Arzilli, L. Mancini, M. Voltolini et al., Near-liquidus growth of feldspar spherulites in trachytic melts: 3D morphologies and implications in crystallization mechanisms. *Lithos* **216**, 93–105 (2015)
44. G. Lanzafame, C. Ferlito, S. Donato, Combining chemical and X-ray microtomography investigations on crustal xenoliths at Mount Etna: evidence of volcanic gas fluxing. *Ann. Geophys.* **61**, 672 (2019)
45. A. Viani, G. Lanzafame, D. Chateigner et al., Microstructural evolution and texture analysis of magnesium phosphate cement. *J. Am. Ceram. Soc.* **103**, 1414–1424 (2020)
46. G. Lanzafame, G. Iezzi, L. Mancini et al., Solidification and turbulence (non-laminar) during magma ascent: insights from 2D and 3D analyses of bubbles and minerals in an Etnean dyke. *J. Petrol.* **58**, 1511–1533 (2017)
47. J. Dewanckele, T. de Kock, M.A. Boone et al., 4D imaging and quantification of pore structure modifications inside natural building stones by means of high resolution X-ray CT. *Sci. Total Environ.* **416**, 436–448 (2012)
48. J.P. Mathews, Q.P. Campbell, H. Xu, P. Halleck, A review of the application of X-ray computed tomography to the study of coal. *Fuel* **209**, 10–24 (2017)
49. T. Rougelot, N. Burlion, D. Bernard, F. Skoczylas, About microcracking due to leaching in cementitious composites: X-ray microtomography description and numerical approach. *Cem. Concr. Res.* **40**, 271–283 (2010)
50. K.Y. Kim, T.S. Yun, K.P. Park, Evaluation of pore structures and cracking in cement paste exposed to elevated temperatures by X-ray computed tomography. *Cem. Concr. Res.* **50**, 34–40 (2013)
51. F. Agosta, M. Alessandrini, E. Tondi, A. Aydin, Oblique normal faulting along the northern edge of the Majella Anticline, central Italy: inferences on hydrocarbon migration and accumulation. *J. Struct. Geol.* **31**, 674–690 (2009)
52. A. Rustichelli, E. Tondi, F. Agosta et al., Development and distribution of bed-parallel compaction bands and pressure solution seams in carbonates (Bolognana formation, Majella Mountain, Italy). *J. Struct. Geol.* **37**, 181–199 (2012)
53. A. Rustichelli, E. Tondi, F. Agosta et al., Sedimentologic and diagenetic controls on pore-network characteristics of Oligocene-Miocene ramp carbonates (Majella Mountain, central Italy). *AAPG Bull.* **97**, 487–524 (2013)
54. T. Volatili, M. Zambrano, A. Cilona et al., From fracture analysis to flow simulations in fractured carbonates: the case study of the Roman Valley Quarry (Majella Mountain, Italy). *Mari. Petrol. Geol.* **100** (2019). <https://doi.org/10.1016/j.marpetgeo.2018.10.040>
55. E. Panza, E. Sessa, F. Agosta, M. Giorgioni, Discrete fracture network modelling of a hydrocarbon-bearing, oblique-slip fault zone: Inferences on fault-controlled fluid storage and migration properties of carbonate fault damage zones. *Mar. Pet. Geol.* **89**, 263–279 (2018)



56. V. Romano, S. Bigi, F. Carnevale, et al., Hydraulic characterization of a fault zone from fracture distribution. *J. Struct. Geol.*, p. 104036 (2020)
57. F. Agosta, M. Alessandrini, M. Antonellini et al., From fractures to flow: a field-based quantitative analysis of an outcropping carbonate reservoir. *Tectonophysics* **490**, 197–213 (2010)
58. M. Antonellini, A. Cilona, E. Tondi et al., Fluid flow numerical experiments of faulted porous carbonates, Northwest Sicily (Italy). *Mar. Pet. Geol.* **55** (2014). <https://doi.org/10.1016/j.marpetgeo.2013.12.003>
59. E. Tondi, A. Rustichelli, A. Cilona et al., Hydraulic properties of fault zones in porous carbonates, examples from central and southern Italy. *Italian J. Geosci.* **135**, 68–79 (2016)
60. J. Latt, O. Malaspinas, D. Kontaxakis et al., Palabos: parallel Lattice Boltzmann solver. *Comput. Math. Appl* (2020). <https://doi.org/10.1016/j.camwa.2020.03.022>
61. E. Panza, F. Agosta, A. Rustichelli et al., Meso-to-microscale fracture porosity in tight limestones, results of an integrated field and laboratory study. *Mar. Pet. Geol.* **103**, 581–595 (2019)
62. I. Korneva, E. Tondi, F. Agosta et al., Structural properties of fractured and faulted Cretaceous platform carbonates, Murge Plateau (southern Italy). *Mar. Pet. Geol.* **57**, 312–326 (2014)
63. G. Tromba, R. Longo, A. Abrami et al., The SYRMEP beamline of Elettra: clinical mammography and bio-medical Applications, in *AIP Conference Proceedings* (American Institute of Physics), pp. 18–23 (2010)
64. P. Cloetens, R. Barrett, J. Baruchel et al., Phase objects in synchrotron radiation hard x-ray imaging. *J. Phys. D Appl. Phys.* **29**, 133 (1996)
65. D.R. Baker, L. Mancini, M. Polacci et al., An introduction to the application of X-ray microtomography to the three-dimensional study of igneous rocks. *Lithos* **148**, 262–276 (2012)
66. F. Brun, S. Pacilè, A. Accardo et al., Enhanced and flexible software tools for X-ray computed tomography at the Italian synchrotron radiation facility Elettra. *Fund. Inform.* **141**, 233–243 (2015)
67. W.J. Palenstijn, K.J. Batenburg, J. Sijbers, Performance improvements for iterative electron tomography reconstruction using graphics processing units (GPUs). *J. Struct. Biol.* **176**, 250–253 (2011)
68. D. Gürsoy, F. de Carlo, X. Xiao, C. Jacobsen, TomoPy: a framework for the analysis of synchrotron tomographic data. *J. Synchrotron Radiat.* **21**, 1188–1193 (2014)
69. D. Paganin, S.C. Mayo, T.E. Gureyev et al., Simultaneous phase and amplitude extraction from a single defocused image of a homogeneous object. *J. Microsc.* **206**, 33–40 (2002)
70. F. Brun, L. Mancini, P. Kasae et al., Pore3D: a software library for quantitative analysis of porous media. *Nucl. Instrum. Methods Phys. Res., Sect. A* **615**, 326–332 (2010)
71. C. Tomasi, R. Manduchi, Bilateral filtering for gray and color images, in *Sixth International Conference on Computer Vision* (IEEE Cat. No. 98CH36271). IEEE, pp. 839–846 (1998)
72. J.A. Hartigan, M.A. Wong, Algorithm AS 136: a k-means clustering algorithm. *J. Roy. Stat. Soc.: Ser. C (Appl. Stat.)* **28**, 100–108 (1979)
73. J.A. Hartigan, *Clustering Algorithms* (Wiley, New York, NY, 1975)
74. J. Schindelin, I. Arganda-Carreras, E. Frise et al., Fiji: an open-source platform for biological-image analysis. *Nat. Methods* **9**, 676–682 (2012)
75. D. d’Humières, Multiple-relaxation-time lattice Boltzmann models in three dimensions. *Philos. Trans. R. Soc. London, Ser. A* **360**, 437–451 (2002)
76. R.P. Sekti, *3-D Stratigraphy and Fracture Characterization in Late Cretaceous Carbonates* (Madonna della Mazza Italy, 2010)
77. P. Marchesini, Visualization and quantification of fluid dynamics in fractured carbonates using 4D ground penetrating radar (4D GPR) (2015)
78. E. Tondi, Nucleation, development and petrophysical properties of faults in carbonate grainstones: evidence from the San Vito Lo Capo peninsula (Sicily, Italy). *J. Struct. Geol.* **29**, 614–628 (2007)
79. V. Vajdova, P. Baud, L. Wu, T. Wong, Micromechanics of inelastic compaction in two allochemical limestones. *J. Struct. Geol.* **43**, 100–117 (2012)

80. D.T. Snow, A parallel plate model of fractured permeable media. Ph.D. Thesis, University of California (1965)
81. M. Zambrano, T. Volatili, L. Mancini, A. Pitts, M. Giorgioni, E. Tondi, Pore-scale dual-porosity and dual-permeability modeling in an exposed multi-facies porous carbonate reservoir. *Marine Petrol. Geol.* **128**, 105004 (2021)

# Chapter 17

## V K-Edge XANES Full Multiple Scattering Study of V-Bearing Phosphate Glasses



Federico Benzi , Eleonora Paris , Stefano Della Longa ,  
Consuelo Mugoni , Cristina Siligardi , and Gabriele Giuli 

**Abstract** In this contribution we analyzed the Vanadium speciation and structural local environment in two V-bearing Na-phosphate glasses by means of V K-edge X-ray Absorption Spectroscopy. The two glasses have starting molar proportions  $\text{Na}_2\text{O}:\text{V}_2\text{O}_5:\text{P}_2\text{O}_5$  equal to 45:10:45 (NaPV10) and 10:80:10 (NaPV80). Accurate analysis of the pre-edge peak of the two glasses allowed to determine the presence of  $^{[4]}\text{V}^{5+}$  and  $^{[5]}\text{V}^{5+}$  in NaPV80 and of  $^{[5]}\text{V}^{4+}$  and  $^{[6]}\text{V}^{4+}$  in NaPV10. EXAFS derived V–O distances for the two glasses are in agreement with literature data for the above mentioned V species. The determined V local geometries and the EXAFS derived bond distances have been used to build four structural models for  $^{[4]}\text{V}^{5+}$ ,  $^{[5]}\text{V}^{5+}$ ,  $^{[5]}\text{V}^{4+}$  and  $^{[6]}\text{V}^{4+}$  in the studied glasses; these models have been in turn used to calculate theoretical XANES spectra by means of the MXAN code. The partial contributions of each V species have been summed in order to fit the experimental XANES spectra of the two glasses. Iterative fitting of the structural parameters of each structural model resulted in a good agreement between experimental and theoretical XANES data. The analysis strategy used in the present work allowed to gain information of V speciation and on the structural local environment of the  $^{[4]}\text{V}^{5+}$ ,  $^{[5]}\text{V}^{5+}$ ,  $^{[5]}\text{V}^{4+}$  and  $^{[6]}\text{V}^{4+}$  species present in the analyzed glasses. Combined use of different spectral regions and data analysis routines allowed to successfully simulate XANES spectra and to gain an in depth knowledge of V local environment even in a complex system like amorphous glass containing different V species.

---

F. Benzi · E. Paris · G. Giuli (✉)

School of Science and Technology–Geology Division, University of Camerino, 62032 Camerino, Italy

e-mail: [gabriele.giuli@unicam.it](mailto:gabriele.giuli@unicam.it)

S. Della Longa

Department of Life, Health and Environmental Science, University of L'Aquila, 67100 Coppito, AQ, Italy

C. Mugoni · C. Siligardi

Department Engineering Enzo Ferrari, University of Modena and Reggio Emilia, 41125 Modena, Italy

## 17.1 Introduction

Glasses containing transition metals find applications in technological fields like power cells [1] and high power laser devices [2] because of their peculiar optical, electronic and magnetic properties. The semiconductive behavior and properties of glasses containing transition elements, and in particular Vanadium phosphate glasses, have long been known [3], but it was only after the theoretical studies by Sir Nevil Francis Mott [4–6], that the scientific community started to be interested in the possibility to exploit the properties of those kind of glasses for technological applications.

Among several glass matrices, phosphate glasses are interesting due to their easy preparation at low temperatures, strong glass forming role, high ionic conductivities and several applications [7–11]. The properties of phosphate glasses can be change by the addition of modifier halides or oxides of alkali, alkaline earth and transition metals into the glassy network [12–16]. Moreover glasses containing transition metal (TM) such as  $V_2O_5$  are especially attractive because of their applications as cathode materials in batteries, memory switching, electrical threshold and optical switching devices [17–19].

The electrical conductivity of these glasses containing different amounts of  $V_2O_5$  depends on the presence of two different valence states ( $V^{5+}$  and  $V^{4+}$ ) [20, 21]. The electronic conductivity is due to by small polaron hopping between such ions while the alkali oxide ( $Li^+$  or  $Na^+$ ) when added into a glass, can contribute to the charge transport and mixed conductivity to be observed. Generally, ionic conductivity depends on alkali concentration and ion mobility and if we assume that the motion of alkali ions and polarons are independent, the electrical conductivity can increase with increasing alkali content. Glasses containing transition metals and alkali, however, exhibit highly variable behavior—from strong conductivity anomalies to conductivity only slightly dependent on alkali content in the glass [22, 23].

## 17.2 Materials and Methods

### 17.2.1 Glass Synthesis

Two Na-V phosphate glasses have been synthesized with molar proportions  $Na_2O:V_2O_5:P_2O_5$  equal to 45:10:45 (NaPV10) and 10:80:10 (NaPV80) by mixing appropriate amounts of ammonium metavanadate ( $NH_4VO_3$ ), ammonium dihydrogen orthophosphate ( $NH_4H_2PO_4$ ) and sodium carbonate ( $Na_2CO_3$ ), and heating the mixture in a muffle furnace up to 450 °C. The powders were maintained at this temperature for 3 h in order to decompose  $NH_4H_2PO_4$  and  $NH_4VO_3$ . After that the mixtures were melted at 1000 °C for 30 min. The melt was then quickly quenched on a graphite mold at room temperature and annealed for 2 h near the Glass Transition

(T<sub>g</sub>) temperature (300 and 230 °C for NaPV10 and NaPV80 respectively) in order to relieve mechanical stresses.

### 17.2.2 XAS Data Collection and Analysis

XAS spectra of the two glass samples have been collected at the XAFS beamline of the ELETTRA storage ring, operated at 2.4 GeV in top-up mode with a typical current of 160 mA and a maximum current of 300 mA. The monochromator was equipped with a pair of Si(111) crystals. Harmonic were rejected using a pair of Pt-coated mirrors. Spectra were collected in transmission mode and the intensities of the incident and transmitted beams have been measured with two ionization chambers.

The raw XAS spectra have been subject to background subtraction and to normalization of the edge jump to one by using the Athena package [24].

Pre-edge peak data of the XANES spectra have been examined according to the procedure already used in [25–27] in order to determine V oxidation state and local coordination geometry. EXAFS data have been analyzed by means of the Horae package, which gives a graphical interface to the IFEFFIT procedure.

Calculation of theoretical XANES spectra have been performed thanks to the MXAN package [28, 29], that uses a Real Space Multiple Scattering (RSMS) method in the Green function formalism to calculate the final states of the Dyson equation in the framework of the muffin tin approximation for the Coulomb part of the potential. The RSMS is the one contained in the CONTINUUM code [30], the self energy can be chosen according to the Hedin-Lundqvist and the  $X_{\alpha}$ ; the damping of the XAFS oscillations is taken into account using a plasmon resonance model. No thermal displacement model is used.

A remarkable advantage of this code is the possibility to fit structural parameters (e.g. bond distances and bond angles) together with non-structural parameters, like muffin-tin spheres overlap, and fermi energy, with a least square method in order to obtain a best fit between experimental and theoretical spectra. However, this package does not use a Self Consistent Field method to calculate the potentials and charge densities, so that variables like interstitial potentials must be input. This choice (explained in details in [29]) has been made in order to save computational time and perform a fit in a reasonable time without losing physical rigor.

This procedure has already been successfully used to calculate XANES theoretical spectra in a set of vanadium model compounds with different V oxidation states and coordination geometries [31], resulting in good agreement between experimental and theoretical spectra.

## 17.3 Results

### 17.3.1 V K-Edge XANES Pre-edge Peak

The XANES spectra of the two glasses are shown in Fig. 17.1: clear differences are visible in the raw intensity of the pre-edge peak and in its energy position, indicating the predominance of different V oxidation states and coordination geometries in these two samples. Also marked differences in the EXAFS oscillation are evidence of different V–O distances.

In order to determine quantitatively the importance of different V species in the samples, the pre-edge peak has been compared to those of V model compounds with different oxidation states and coordination geometries according to the procedure described in [25, 27]. The pre-edge peak of sample NaPV80 can be adequately modeled by a linear combination of the pre-edge peak of Vanadinite and  $V_2O_5$  (containing  $V^{5+}$  respectively in tetrahedral coordination and in square pyramidal coordination). It is thus evident, that this glass contains dominantly  $V^{5+}$  with two different coordination geometry in almost similar amounts: 40 mol %  $[4]V^{5+}$  and 60 mol %  $[5]V^{5+}$  (where the term in square brackets represents the coordination number).

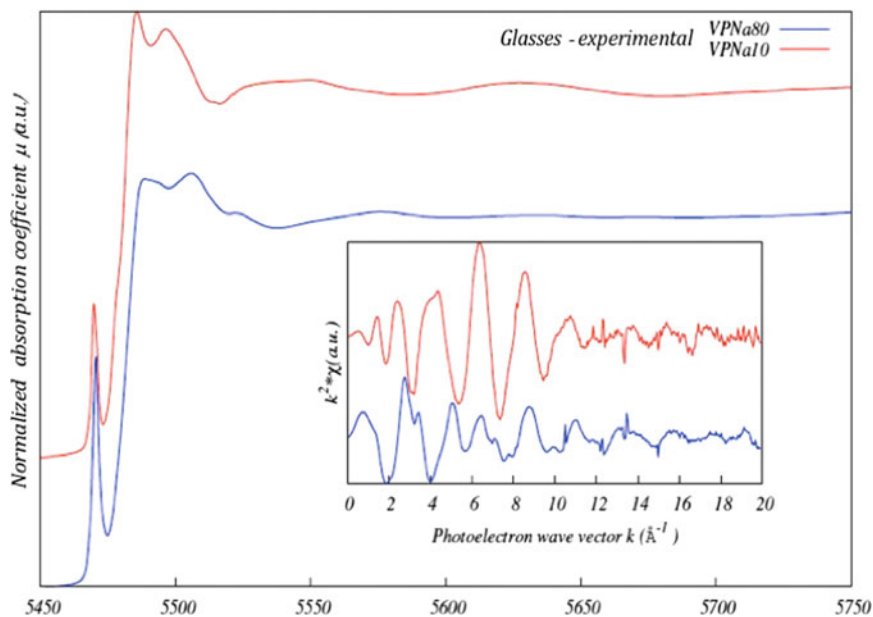


**Fig. 17.1** V K-edge XAS spectra of the two glasses studied. The two spectra have been vertically offset for clarity. In the inset, the EXAFS signal is shown as a function of the photoelectron wave vector

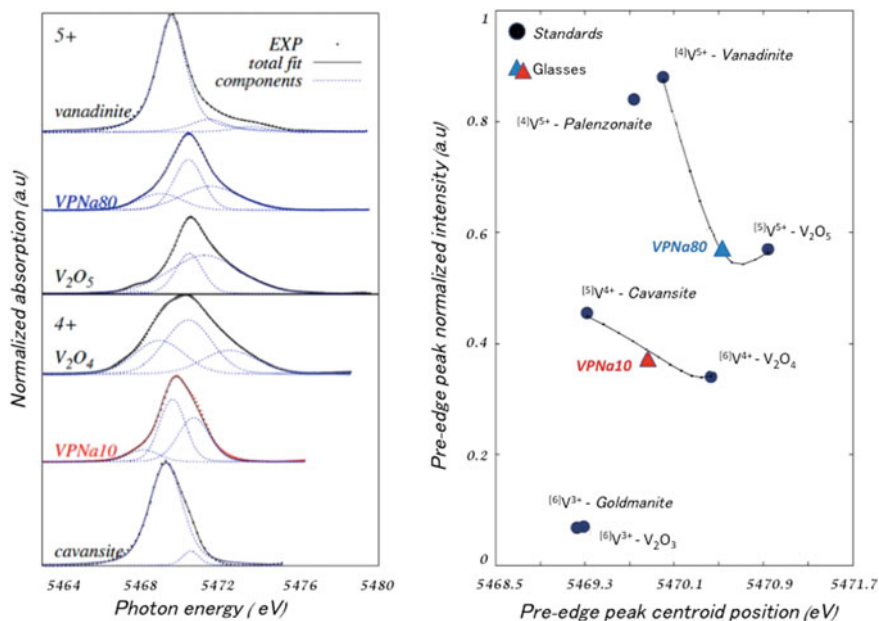


**Fig. 17.2** Background subtracted pre-edge peak of the 2 glass samples, compared with selected V model compounds (left panel); IN the right panel are shown the pre-edge peak normalized intensity and centroid energy of the 2 studied glasses, compared to those of V model compounds with known V oxidation state and coordination environment. NaPV80 displays the presence of pentavalent Vanadium in tetrahedral and square pyramidal coordination, whereas NaPV10 displays the presence of tetravalent V in square pyramidal and in octahedral coordination

On the other hand, the pre-edge peak of sample NAPV10 displays normalized Intensity and centroid Energy intermediate between those of cavansite and V<sub>2</sub>O<sub>4</sub> (containing V<sup>4+</sup> respectively in square pyramidal and octahedral coordination). This samples thus displays predominantly the presence of V<sup>4+</sup> with 2 different coordination geometries in very similar proportions: 45 mol % [6]V<sup>4+</sup> and 55 mol % [5]V<sup>4+</sup> (Fig. 17.2).

### 17.3.2 V K-Edge EXAFS

From the data obtained, we built 4 different clusters with V bonded to 4, 5 or 6 oxygens, choosing appropriate V–O distances according to literature data for [4]V<sup>5+</sup>, [5]V<sup>5+</sup>, [5]V<sup>4+</sup> and [6]V<sup>4+</sup> species. These starting clusters were used in order to calculate single- and multiple-scattering paths to be used for EXAFS data analysis.

The two clusters used for NaPV10 consist of:

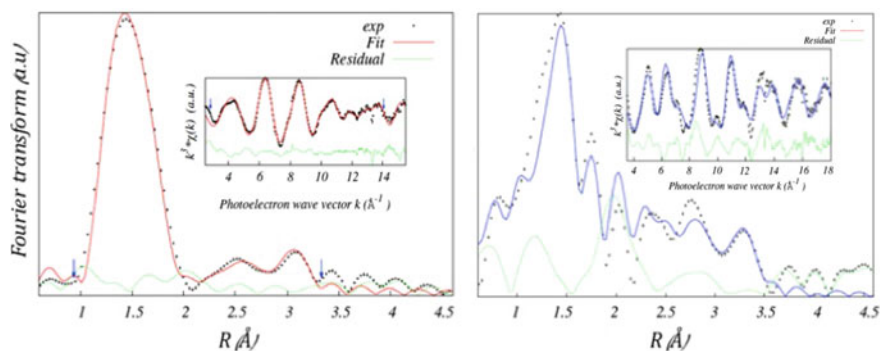


**Fig. 17.3** Fit results for the V K-edge EXAFS spectra of the NaPV10 (left) and NaPV80 (right) glasses studied

- (i) V in fivefold coordination, with a vanadyl V–O bond at 1.6 Å, 4 basal V–O bonds at 1.95 Å with 4 O–P bonds at 1.53 Å (so at 3.48 Å from the central V) and an unbonded oxygen at 2.9 Å;
- (ii) V in a regular sixfold coordination with 6 symmetric V–O bonds at 1.95 Å (average value from literature data) and 6 O–P bonds at 1.53 Å (at 3.48 Å from the central V).

The two clusters used for NaPV80 consist of:

- (i) V in fivefold coordination, with a vanadyl V–O bond at 1.58 Å, 4 basal V–O bonds at distances ranging from 1.78 to 2.05 Å with 4 O–P bonds at 1.53 Å;
- (ii) V in a regular tetrahedral coordination with 4 V–O bonds at 1.71 Å and 6 O–P bonds at 1.53 Å (at 3.48 Å from the central V).

Single scattering amplitude and phase have been calculated for every V–O, V–V, and V–P distance. EXAFS data analysis included fitting these distances, a global amplitude factor, the ratio between  $^{4}\text{V}^{5+}$  and  $^{5}\text{V}^{5+}$  (for NaPV80) or  $^{5}\text{V}^{4+}$  and  $^{6}\text{V}^{4+}$  species (for NaPV10), and two different edge energies (each relative to a different V species) for each spectrum.

The results of the fit are shown in Fig. 17.3, whereas the fitted distances are reported in Table 17.1.

### 17.3.3 Theoretical V K-Edge XANES Spectra

The results of the EXAFS fit have been used in order to modify the initial structural model used to calculate EXAFS contribution; these, in turns have been used in order



**Table 17.1** Results of the EXAFS data fit.

|  | NaPV10     |       |             |
|--|------------|-------|-------------|
| Square pyramid                                   |            |       | Octahedron  |
| V–O <sub>Vanadyl</sub>                           | 1.60(1) Å  | ⟨V–O⟩ | 1.90(2) Å   |
| ⟨V–O⟩  | 2.01(1) Å  | ⟨V–P⟩ | 3.22(3) Å   |
| ⟨V–P⟩  | 3.47(7) Å  |       |             |
| V–O <sub>unbonded</sub>                          | 2.90(2) Å  |       |             |
| $[^6]V^{4+}/([^5]V^{4+} + [^6]V^{4+}) = 0.27(2)$ |            |       |             |
|  | NaPV80     |       |             |
| Square pyramid                                   |            |       | Tetrahedron |
| V–O <sub>Vanadyl</sub>                           | 1.61(3) Å  | ⟨V–O⟩ | 1.82(2) Å   |
| ⟨V–O⟩  | 1.99(1) Å  |       |             |
| ⟨V–P⟩  | 3.45(73) Å |       |             |
| V–O <sub>unbonded</sub>                          | 2.86(2) Å  |       |             |
| ⟨V–V⟩  | 3.09(4) Å  |       |             |
| $[^5]V^{5+}/([^4]V^{5+} + [^5]V^{5+}) = 0.80(2)$ |            |       |             |

The numbers in parenthesis represent uncertainty in the last digit

to calculate XANES theoretical spectra. Follows the description of the structural model used for the calculation of the theoretical XANES spectra.

### NaPV10 V<sup>4+</sup> in octahedral coordination

According to literature data [32, 33] <sup>[6]</sup>V<sup>4+</sup> commonly has a shorter bond length (not necessarily a vanadyl, i.e. a double V=O bond), a long trans bond opposed to it and 4 equatorial bonds with intermediate bond lengths. In particular the vanadyl bond is in the range 1.48–1.74 Å, the trans bond in the range 2–2.6 Å and the equatorial bonds in the range 1.86–2.16 Å. Our choice was thus to refine 3 individual distances: a vanadyl distance, a trans distance and one individual distance for the 4 equatorial bonds. The bond angles were optimized in couples using the same fit variable for opposite couples of atoms. The P atoms were linked to the respective O atoms. Since the refinement of V<sub>2</sub>O<sub>4</sub> in [31] was not accurate enough, the muffin-tin fit parameters, i.e. the overlap and the interstitial potential, were let to move almost freely.

### NaPV10 V<sup>4+</sup> in square pyramidal coordination

In this case from literature data [33, 34] we know that V has a short vanadyl double bond V=O, 4 basal bonds and sometimes a trans bond that can be considered unbonded. The vanadyl bond distance is in the range 1.48–1.66 Å, the basal bond distances in the range 1.86–2.12 Å and the trans oxygen distance (to the opposite site of the vanadyl bond) is at about 2.9 Å. The fit variables were thus chosen as in the case of the octahedral part: one distance for the vanadyl bond, one for the trans bond, one for all the 4 basal bonds. Again, the bond angles were optimised coupling opposite atoms. The P atoms were linked to the respective O atoms and the MT

variables were again chosen from the values found in [31] and let free to slightly vary (a few percent) around the starting value.

### NaPV10 optimization of the theoretical XANES spectrum

The fit of the experimental spectrum was performed by summing two contributions, so that the structural and non structural parameters of one contribution are fitted every time, keeping fixed the other contribution. The relative importance of each contribution (i.e. the value  $^{[5]}\text{V}^{5+}/(^{[4]}\text{V}^{5+} + ^{[5]}\text{V}^{5+})$ ) was initially chosen according to the values determined by the pre-edge peak (i.e. 0.5). This value has been then refined during each optimization cycle. Since there is no possibility to refine the relative quantity of the two contributions and the relative energy shift, to estimate those quantities we adopted this strategy.

MXAN allows to add a previously calculated spectrum and fit the difference; If we want to fit a spectrum in which two components are predominant so that  $S = \nu A + (1 - \nu)B$ , we can consider the case  $0.5 < \nu < 1$  (i.e., the case with a dominant A species). We can first calculate the theoretical spectra for each V species ( $A_0$  and  $B_0$ ), then we can fix B to  $B_0$  (because, the less important contribution is thought to influence the least the spectrum) and refine A; the fit result ( $A_1$ ), can be then fixed and we can do a second cycle of refinements, this time fixing  $A_1$  and refining  $B_0$ . This procedure can be repeated several times until the residual of the fit does not change significantly.

We performed 10 optimization cycles, checking the value of the residual until we got a stable value of the disagreement index. We will not report all of the procedure, but only show the final results. The best fit is shown in Fig. 4a, while the best fit parameters are displayed in Table 17.2. The calculated spectrum is in very good agreement with the experimental one. All the features of the experimental spectrum are reproduced in the theoretical spectrum, with the correct energy position and intensity. In particular the resonance peaks “a” and “b” are present and accurately reproduced. This is an indication that the MS is accurately calculated. The small discrepancy in the position and intensity of peak “c” can be due to (i) a badly estimated broadening of the spectrum and (ii) the presence of Na which is not included in the structural model used for the calculation of the theoretical spectrum. The refined bond distances are in good agreement with those determined by the EXAFS analysis and so an overall agreement with bond distances is found in tetravalent V. For the octahedrally coordinated V we have found that a better fit is obtained if the 6 distances are not all regular, but distorting the polyhedron. This is in good agreement also with literature data, both for crystalline structures [26, 33] and for V phosphate glasses [35].

The result of this procedure is reported in Table 17.2.

From the calculations we found out that the ratio  $^{[6]}\text{V}/^{[5]}\text{V} + ^{[6]}\text{V}$  is around 0.3, i.e. closer to the value found in the EXAFS refinement (0.27) than that found in the pre-edge peak analysis (0.45). We believe that the actual value is so somewhere

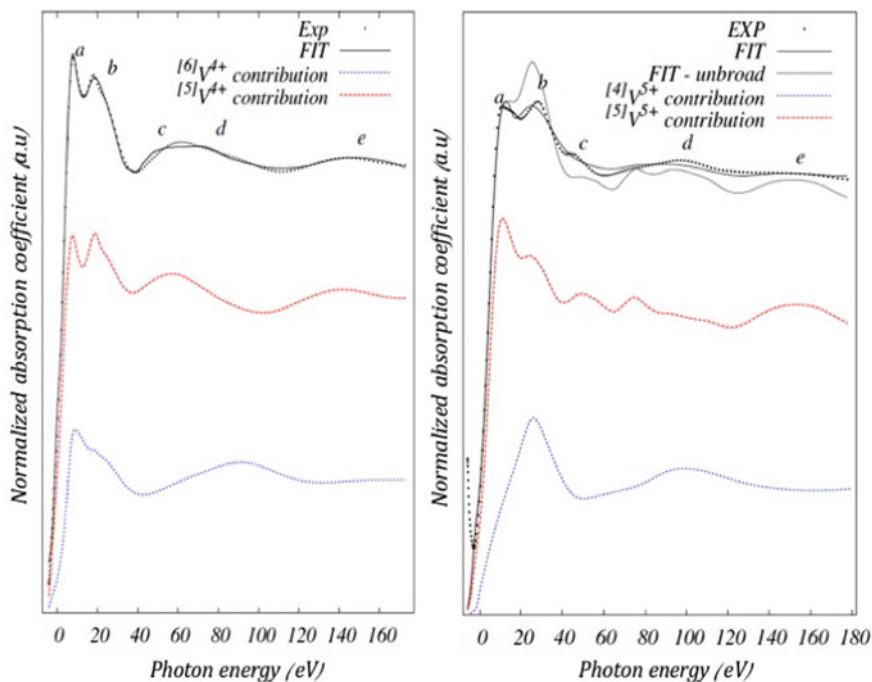


**Fig. 17.4** Fit results for the V K-edge XANES spectra of the NaPV10 (left) and NaPV80 (right) glasses. The black dotted lines represent the experimental spectra, whereas the black continuous lines the weighted sum of the theoretical spectra calculated for each Vanadium species (colored dotted lines)

**Table 17.2** Parameters used for the XANES fit

|             |                                     |                |            |  |  |
|-------------|-------------------------------------|----------------|------------|--|--|
|             | NaPV10                              |                |            |  | $[6]V^{4+}/([5]V^{4+} + [6]V^{4+}) = 0.30$ |
| Overlap (%) | V MuffinTin radius ( $\text{\AA}$ ) | $V_{0in}$ (eV) | $E_0$ (eV) |  | coordination                               |
| 24 (2)      | 1.094                               | -9 (1)         | 5477.5     |  | $[5]V^{4+}$                                |
| 25 (4)      | 1.297                               | -9 (3)         | 5477.6     |  | $[6]V^{4+}$                                |
|             | NaPV80                              |                |            |  | $[5]V^{5+}/([4]V^{5+} + [5]V^{5+}) = 0.70$ |
| Overlap (%) | V MuffinTin radius ( $\text{\AA}$ ) | $V_{0in}$ (eV) | $E_0$ (eV) |  | coordination                               |
| 25 (2)      | 1.146                               | -11 (2)        | 5478.9     |  | $[4]V^{5+}$                                |
| 257 (2)     | 1.072                               | -12.5 (6)      | 5477.4     |  | $[5]V^{5+}$                                |

intermediate between 0.3 and 0.45, i.e. intermediate between the pre-edge peak determination, the EXAFS fit and the XANES fit.

### NaPV80 optimization of the theoretical XANES spectrum

The fit procedure was the same of NaPV10, and a convergence was achieved after 6 cycles, even though, as exposed before, for the fivefold coordinated V some further refinements were necessary. The best fit, as determined by the residual, is shown in Fig. 4b, while the fit parameters are displayed in Table 17.2.

The calculated spectrum is in very good agreement with the experimental one. For clarity, in Fig. 4b we also displayed a calculation without the plasmon broadening (the energy dependent part of the broadening, see Sect. 17.2.2). This has been shown because some features (“c” and “d”) are a bit less prominent after the broadening.

It is interesting to notice that those peaks have analogues in the  $V_2O_5$  spectrum, in particular the peaks “d” and “f” in [31]. MXAN slightly underestimated the same peaks in  $V_2O_5$  as in NaPV80. This can be an indication that using a similar atomic configuration for the two samples was a good choice. The “a” and “b” peaks, that correspond to the strongest MS contribution, are less accurately determined for NaPV80 than for NaPV10. This could possibly happen due to the presence of V in the second coordination shell, which leads to stronger multiple scattering that is less accurately calculated by MXAN at low energy [30]. The V–O bond distances in the fourfold coordinated contribution are shorter than those calculated with the EXAFS refinement, but closer to the average of the V–O distances in the literature (1.72 Å [33]). All of the bond distances found in the square pyramidal contribution were slightly longer with respect to those found in EXAFS, with the exception of the trans V–O bond, that we found to be shorter (2.52 Å vs. 2.86 Å of EXAFS). The XANES distances are anyway compatible to the EXAFS distances within the error bars.

As for NaPV10, after the fit we tried to optimize the energy shift and the ratio  $a = {}^{51}V/{}^{51}V + {}^{41}V$  by calculating the residual as a function of  $a$  and Energy shift. The results are summarized in Table 17.2. In this case the lower residual for the  $a$  parameter (0.7) was found to be closer to that calculated with the pre-edge peak analysis (0.60) than to that determined by the EXAFS analysis. Anyway, the XANES value falls in the limit of the error bar, so probably the actual value is somewhere intermediate between those obtained from the EXAFS and the XANES calculations. The determined relative energy shift was found to be 1.5 eV.

### NaPV80 $V^{5+}$ in tetrahedral coordination

From the EXAFS analysis we were able to determine only the first coordination shell of atoms, i.e. the 4 neighbouring oxygens. For the XANES analysis we kept as starting parameters this configuration, according to literature data [36]. We also considered the tetrahedron to be regular for the bond distances, using a single fit variable for the 4 V–O distances. We refined the 4 bond angles independently.

The MT parameters were chosen from the model compounds analysis and let free to slightly vary around the values found for  ${}^{41}V^{5+}$  in [31] i.e. 0.2 for the MT overlap and  $-13$  eV for the interstitial potential.

### NaPV80 V<sup>5+</sup> in square pyramidal coordination

In this case the EXAFS analysis did not give us a clear answer about the V local structure, so we performed several trials with different atomic configurations to determine the most suitable one according to the residual. The details will not be reported here, but the trials involved (i) the removal of the P atom with an eventual substitution of a V atom at opportune distance determined by the V<sub>2</sub>O<sub>5</sub> structure (the three configurations being thus with a P atom in the second coordination shell, a V atom in the second coordination shell and no atoms in the second coordination shell); (ii) the removal of some of the V atoms in the second coordination shell. The best configuration was found to be: (i) a vanadyl bond; (ii) a trans bond opposed to it; (iii) a basal bond with two V atoms in the corner (a configuration already found in V<sub>2</sub>O<sub>5</sub>, see [37] and [31]); (iv) a basal bond with a P atom opposed to it; (v) two basal bonds bended towards the 2 V atoms in the second coordination shell. The fit was performed in different steps:

first we varied the structural parameters in groups (basal oxygens, second shell atoms, vanadyl and trans oxygens) to check the behaviour of those parameters on the theoretical spectrum; after reaching a configuration that was satisfactory we have released all the variables as previously done for <sup>51</sup>V<sup>4+</sup> in NaPV10: one common fit parameter for the basal oxygen atoms, one for the vanadyl and one for the trans oxygen. The bond angles were varied in couples, the P atom was linked again to the corresponding O atom. The V atoms coordinates in the second coordination shell were independent and free to move.

## 17.4 Conclusions

In both cases we have shown how the combined analysis of all the regions of the absorption spectrum can lead to a deep knowledge on the V local structure of phosphate glasses, even in complex cases when several different Vanadium species are present. The pre-edge peak analysis was able to give us precious information about (i) the coordination geometries and (ii) oxidation states of the glasses. In systems like V-bearing glasses, in which V can be in a variety of coordination geometries and oxidation states, this procedure provided important information: in fact, by determining the V coordination geometries we were able to build the starting cluster, while by determining the V oxidation state we were able to estimate if the bond distances determined by ab-initio calculations were reasonable. Through EXAFS analysis we were able to refine the bond distances obtaining a radial distribution function that at the end we geometrically refined by means of MS geometrical fits of the XANES region.

The analysis performed on the different parts of the spectra converged to the same results, even though some questions, like the Na structural role in these glasses and the long V–O bond distances in the <sup>51</sup>V<sup>5+</sup> component of NaPV80, are still unsolved.

## References

1. Y. Sakurai, J. Yamaki, Correlations between microstructure and electrochemical behaviour of amorphous  $V_2O_5$ - $P_2O_5$  in lithium cells. *J. Electrochem. Soc.* **135**(4), 791–796 (1988)
2. J. Campbell, T. Suratwala, Nd-doped phosphate glasses for high-energy/high-peak-power lasers. *J. Non-Cryst. Solids* **263–264**, 318–341 (2000)
3. M. Munakata, Electrical conductivity of high vanadium phosphate glass. *Solid-State Electron.* **1**, 159–163 (1960)
4. N. Mott, Electrons in disordered structures. *Adv. Phys.* **16**(61), 49–144 (1967)
5. N. Mott, Conduction in glasses containing transition metal ions. *J. Non-Cryst. Solids* **1**(1), 1–17 (1968)
6. I. Austin, N. Mott, Polarons in crystalline and non-crystalline materials. *Adv. Phys.* **18**(71), 41–102 (1969)
7. P.A. Tick, Water durable glasses with ultra low melting temperatures. *Phys. Chem. Glasses* **25**(6), 149–154 (1984)
8. H.S. Liu, P.Y. Shih, T.S. Chin, Low melting  $PbO$ - $ZnO$ - $P_2O_5$  glasses. *Phys. Chem. Glasses* **37**(6), 227–235 (1996)
9. R.K. Brow, Review: the structure of simple phosphate glasses. *J. Non-Cryst Solids* **263–264**, 1–28 (2000)
10. H. Yung, P.Y. Shih, H.S. Liu, T.S. Chin, Nitridation effect on properties of stannous-lead phosphate glasses. *J. Am. Ceram. Soc.* **80**, 2213 (1997)
11. C.M. Shaw, J.E. Shelby, The effect of stannous oxide on the properties of stannous fluorophosphate glasses. *Phys. Chem. Glasses* **29**, 87 (1988)
12. R.K. Brow, Nature of alumina in phosphate glass: I, properties of sodium aluminophosphate glass. *J. Am. Ceram. Soc.* **76**, 91 (1993)
13. S. Kabi, A. Ghosh, Dynamics of  $Ag^+$  ions and immobile salt effect in  $CdI_2$  doped silver phosphate glasses. *Solid State Ion.* **187**, 39 (2011)
14. A. Shaw, A. Ghosh, Influence of immobile ions on the length scale of ion transport in conducting phosphate glasses. *J. Phys. Chem. C* **116**, 24255 (2012)
15. C. Mugoni, M. Montorsi, C. Siligardi, H. Jain, *J. Non-Cryst. Solids* **383**, 137–140 (2014)
16. C. Mugoni, H. Jain, M. Montorsi, M. Montecchi, A. Kovalskiy, C. Siligardi, Structural origin of electrical conductivity of copper lithium metaphosphate glasses. *J. Non-Cryst. Solids* **447**, 91–97 (2016)
17. A. Ghosh, Memory switching in bismuth-vanadate glasses. *J. Appl. Phys.* **64**, 2652 (1988)
18. J. Livage, J.P. Jollivet, E. Tronc, Electronic properties of mixed valence oxide gels. *J. Non-Cryst. Solids* **121**, 35 (1990)
19. Y. Sakurai, J. Yamaki,  $V_2O_5$ - $P_2O_5$  glasses as cathode for lithium secondary battery. *J. Electrochem. Soc.* **132**, 512 (1985)
20. S. Jayaseelan, P. Muralidharan, M. Venkateswarlu, N. Satyanarayan, Ion transport and relaxation studies of silicovanadotellurite glasses at low temperatures. *Mater. Chem. Phys.* **87**(2–3), 370–377 (2004)
21. Y. Dimitriev, V. Dimitrov, M. Arnaudov, D. Topalov, IR-spectral study of vanadate vitreous systems. *J. Non Cryst. Solids* **57**(1), 147–156 (1983)
22. G.D.L.K. Jayasinghe, M.A.K.L. Dissanayake, P.W.S.K. Bandaranayake, J.L. Souquet, D. Foscallo, *Solid State Ionics* **93**, 291 (1997)
23. J.R. Macdonald D.R. Franceschetti, Impedance spectroscopy emphasising solid materials and systems, in ed. by JR Macdonald (Wiley, New York, 1987), p. 98.
24. B. Ravel, M. Newville, ATHENA, ARTEMIS, HEPHAESTUS: data analysis for X-ray absorption spectroscopy using IFEFFIT. *J. Synchrotron Radiat.* **12**(4), 537–541 (2005)
25. G. Giuli, E. Paris, J. Mungall, C. Romano, D. Dingwell, V oxidation state and coordination number in silicate glasses by XAS. *Am. Miner.* **89**(11–12), 1640–1646 (2004)
26. J. Wong, F.W. Lytle, R.P. Messmer, D.H. Maylotte, K-edge absorption spectra of selected vanadium compounds. *Phys. Rev. B* **30**, 5596–5610 (1984)

27. A. Moretti, G. Giuli, F. Nobili, A. Trapananti, G. Aquilanti, R. Tossici, R. Marassi, Structural and electrochemical characterization of vanadium-doped  $\text{LiFePO}_4$  cathodes for lithium-ion batteries. *J. Electrochem. Soc.* **160**(6), A940–A949 (2013)
28. M. Benfatto, S. Della Longa, Geometrical fitting of experimental XANES spectra by a full multiple-scattering procedure. *J. Synchrotron Rad.* **8**(4), 1087–1094 (2001).
29. M. Benfatto, S. Della Longa MXAN: new improvements for potential and structural refinement. *J. Phys.: Conf. Ser.* **190**(1), 012031, (2009)
30. C. Natoli, M. Benfatto, A unifying scheme of interpretation of x-ray absorption spectra based on the multiple scattering theory. *J. Phys. Colloques* **47**(C8), 11–23 (1986)
31. F. Benzi, G. Giuli, S. Della Longa, E. Paris, Vanadium K-edge XANES in vanadium-bearing model compounds: a full multiple scattering study. *J. Synchrotron Rad.* **23**(4), 947–952 (2016)
32. K.D. Rogers, An x-ray diffraction study of semiconductor and metallic vanadium dioxide. *Powder Diffr.* **8**, 240–244 (1993)
33. M. Schindler, F.C. Hawthorne, W.H. Baur, Crystal chemical aspects of vanadium: polyhedral geometries, characteristic bond valences, and polymerization of  $(\text{VO}_n)$  polyhedra. *Chem. Mater.* **12**(5), 1248–1259 (2000)
34. R. Danisi, T. Armbruster, B. Lazic, In situ dehydration behavior of zeolite-like cavansite: a single-crystal X-ray study. *Am. Miner.* **97**, 1874–1880 (2012)
35. U. Hoppe, N. Wycko, M. Schmitt, R. Brow, A. Schöps, A. Hannon, Structure of  $\text{V}_2\text{O}_5\text{-P}_2\text{O}_5$  glasses by X-ray and neutron diffraction. *J. Non-Cryst. Solids* **358**(2), 328–336 (2012)
36. M. Nagashima, T. Armbruster, Palenzonaite, berzeliite, and manganberzeliite:  $(\text{As}^{5+}, \text{V}^{5+}, \text{Si}^{4+})\text{O}_4$  tetrahedra in garnet structures. *Mineral. Mag.* **76**(5), 1081–1097 (2012)
37. V. Shklover, T. Haibach, F. Ried, R. Nesper, P. Novak, Crystal structure of the product of  $\text{Mg}^{2+}$  insertion into  $\text{V}_2\text{O}_5$  single crystals. *J. Solid State Chem.* **123**(2), 317–323 (1996)